Anisotropy and Spin Relaxation in the Condensed Phase

by

Jennifer Handsel

A thesis submitted to

University of Oxford

in partial fulfillment of the requirements for the degree of

Doctor of Philosophy

in

Physical and Theoretical Chemistry

Trinity Term 2016

Physical and Theoretical Chemistry Laboratory

and

St Cross College

This thesis is dedicated to R. E. Merrifield.

Only three people have ever really understood the Schleswig-Holstein business – the Prince Consort, who is dead – a German professor, who has gone mad – and I, who have forgotten all about it. — Lord Palmerston

Abstract

Anisotropy and Spin Relaxation in the Condensed Phase

Jennifer Handsel

A thesis submitted for the degree of Doctor of Philosophy

Trinity Term 2016

Physical and Theoretical Chemistry Laboratory and *St Cross College*

Chapter 1 introduces the concept of spin, how spins interact, and how the spin state in a radical pair can affect the outcome of a chemical reaction between the unpaired electrons. The computational methodology for simulating such radical pairs is also discussed.

Chapter 2 discusses anisotropy in the singlet recombination yield of a radical pair in a carotenoid-porphyrin-fullerene triad, containing many hyperfine couplings. The singlet yield was calculated as a function of the direction of an applied magnetic field, using symmetry in the molecule to reduce the size of the problem. The symmetry reduction was partially successful, however it was not possible to include all the hyperfine couplings in the molecule.

Chapter 3 introduces a radical pair located on a flavin ligand and a tryptophan residue in the protein cryptochrome, and discusses the spin-relaxation mechanism of singlet-triplet dephasing. Magnetic field effect curves, describing the formation of a secondary radical pair as a function of applied magnetic field, were found to be broader in longer-lived radical pairs, due to dephasing caused by spin-selective recombination to the singlet ground state. Additional singlet-triplet dephasing may

occur due to hopping of one of the unpaired electrons, between a zone of strong exchange interaction and a zone of negligible exchange interaction, although this is an incomplete description of the spin-relaxation.

Chapter 4 discusses the effect of rotational tumbling on spin-relaxation in the flavin-tryptophan radical pair in cryptochrome. Simulations indicated that the resulting modulation of anisotropic hyperfine couplings contributed modestly to spin-relaxation during transient absorption measurements, but was insufficient to explain the lack of an experimental low-field effect, or to explain the width of the experimental magnetic field effect curves as a function of magnetic field strength.

Chapter 5 discusses magnetic field effects on the mutual annihilation of a pair of triplet excitons in tetracene and anthracene crystals. The experimental singlet recombination yield was found, for the first time, to be modulated as a function of the direction of a applied magnetic field as weak as 2 mT. Simulations indicated that this anisotropy arose due to the zero field splitting of the electronic state in each triplet exciton. The direction of the external magnetic field altered the singlet component of the eigenstates of the Hamiltonian, and therefore altered the time-average of the singlet probability of a triplet exciton pair. This is different to the already established mechanism under a strong magnetic field, where the anisotropy arises from level crossings of eigenstates.

Acknowledgements

K. J. Tan, Riccardo Montis, and Mark Oxborrow of Imperial College, London: for providing zone refined anthracene and sublimation flakes of tetracene

Till Biskup, Kiminori Maeda, Kevin Henbest and Jing Li: for providing the experimental measurements in chapters 3 and 4

The electronics teams in the ICL and PTCL: in particular, Nen, for advice on electrical grounding and shielding, and Neville, for aid in constructing the AMELIA experiment

Dr Christiane Timmel: for providing the idea and equipment to build the AMELIA device

Professor Peter Hore: for his endless patience and understanding

Ilya Kuprov, Leonard Suskind, and Gilbert Strang: for their excellent online lecture series

Hore and Timmel group members, past and present: Till and Daniel, for the late night conversations; Jason, for your architectural expertise; Hamish and Susannah, for being good travel companions; Kevin for your kindness and generosity; Marcin, for your deep conversations on the ontology of lock-in amplifiers

Comrades at Oxford Wudang: for the hard training and good beer. Sean and Dave, this work would not have been possible without you.

Fellow collegians at St Cross: DK for all the fun and baking, Sabine, for your Teutonic stoicism, and Syntrophissa Patta for keeping the flame burning

My parents: for providing me with the opportunity and encouragement to cultivate my mind

Contents

Chapter 1

Introduction

This chapter will introduce the quantum mechanical concept of spin, and discuss in detail the magnetic interactions, both isotropic and anisotropic, between particles with non-zero spin. It will also describe how the spin state of a pair of radicals can affect the outcome of a chemical reaction.

Two types of spin-chemical reaction will be discussed in this thesis. Chapters 2 through 4 will discuss reactions between radical pairs in an organic molecule, and Chapter 6 will discuss reactions between pairs of triplet excitons in a crystal lattice. Particular attention will be paid to the effect of an external magnetic field on the outcome of these reactions, with regard to both strength and direction of the field. Spin relaxation will also be discussed in detail, as will the potential implications for a biological magnetosensor based on the radical-pair mechanism.

1.1 The Discovery of Spin

The quantum property of spin does not have a classical analogue, so was not discovered until relatively recently. The way in which spin was discovered illustrates its fundamental properties and implications.

The idea of electron spin was proposed by Goudsmit and Uhlenbeck in 1925, in order to explain anomalous fine structure in the atomic spectrum of hydrogen and

ionized helium [64]. This spectrum, measured by Paschen, appeared to show a

$$2^2\mathrm{S} \longrightarrow 1^2\mathrm{S}$$

transition[1], which is forbidden by the selection rule

$$\Delta\ell = \pm 1\,,$$

where ℓ is the orbital angular momentum quantum number[2]. Goudsmit and Uhlenbeck proposed an additional angular momentum associated with spin of the electron, $s = \frac{1}{2}$. The spin angular momentum could be combined with the orbital angular momentum by vector addition to give the total angular momentum j:

$$|s - \ell| \leq j \leq s + \ell\,.$$

This suggested that there were in fact two states with P character, $2^2\mathrm{P}_{3/2}$ and $2^2\mathrm{P}_{1/2}$, which are energetically distinct due to spin-orbit coupling [9]. Both of these states have allowed transitions to the ground state $1^2\mathrm{S}$, which explains Paschen's anomalous result.

Initially, the electron's spin angular momentum was thought to correspond to physical rotation in space, as would be expected of a spinning charged particle [177]. However, this leads to paradoxical conclusions – if the electron were a classical particle with volume, its surface velocity would have to exceed the speed of light, and if the electron is a point particle, as we now believe, rotation in space is a nonsensical concept. Moreover, Bloch and Alvarez demonstrated in 1940 that neutrons also possess a magnetic moment, despite having zero electrical charge [7].

Furthermore, the half-integer nature of electron spin is incompatible with rotations in physical space. Orbital angular momentum can be understood as arising

[1] S represents a state with zero orbital angular momentum.

[2] This selection rule arises as a photon is a spin-one particle, and total angular momentum must be conserved.

from the shape of atomic orbitals, which are solutions of Schrödinger's equation for a single electron in a coulombic potential. These orbitals are the spherical harmonics, $Y_\ell^m(\hat{r})$, which are also eigenfunctions of the angular momentum operators $\hat{L}^2 = \hat{L}_x^2 + \hat{L}_y^2 + \hat{L}_z^2$ and $\hat{L}_z$ (where z is some arbitrarily chosen axis that determines the directionality of the harmonics)[3]:

$$\begin{aligned} \hat{L}^2\, Y_\ell^m &= \ell(\ell+1) Y_\ell^m \\ \hat{L}_z\, Y_\ell^m &= m Y_\ell^m \,. \end{aligned} \tag{1.1}$$

The parameter ℓ is the orbital angular momentum, and m is the projection of the angular momentum onto the z axis. The only allowed values of ℓ are integers, for $\ell \geq 0$. This means that $s = \frac{1}{2}$ for an electron cannot be derived from the concept of angular momentum.

Nothing is known about the composition of the electron – it is currently assumed to be a fundamental particle, so the origin of the electron's spin is unknown. However, we do know that spin and orbital angular momentum are linked, as orbital angular momentum and photon spin are interconverted when a photon is absorbed by or emitted from an atom.

Within a molecular orbital, Pauli's exclusion principle means that two electrons cannot have a symmetric spin state. The only state they can have, therefore, is the singlet state, where the two spins are antiparallel in an antisymmetric configuration (the singlet state will be defined more rigorously further on). This means that the reaction of a pair of radicals to form a singlet ground state molecule must be spin-allowed. In essence, the quantum state of the radical pair must have a singlet component for the reaction to proceed.

The fact that electrons have spin, in addition to orbital angular momentum, means that organic radicals are paramagnetic — without electron spin, the low symmetry of most organic molecules would preclude a magnetic moment arising from orbital angular momentum. This means that in organic radicals, there are

[3]Here, and throughout this thesis, we work in units where the fundamental unit of angular momentum $\hbar = 1$.

interactions between the spin of the unpaired electron and any nuclear spins, and all of these spins interact with an external magnetic field. These interactions cause oscillations in the spin-state of a pair of radicals, and can therefore alter the singlet product yield from a reaction between the two radicals.

1.2 Properties of Spin

In order to perform theoretical calculations, spin must be defined more rigorously. In practice, the spin state is represented by a complex vector in what is called Hilbert space, while observables are represented by matrix operators, which act upon the state vector. In this formalization, the state vector is represented by a ket $|\psi\rangle$. The expected value of an operator $\hat{O}$ can be calculated with

$$\langle\psi|\hat{O}|\psi\rangle$$

where

$$\langle\psi| = |\psi\rangle^{\dagger} \ .$$

The spin properties of a particle are determined by its spin quantum number s. For electrons, $s = \frac{1}{2}$ in all cases. Like the electron, nuclei may also exhibit spin. This is because neutrons and protons are each made of three quarks (a spin-half particle), which makes the neutron and proton both spin-half particles. The spin of the nucleons is added constructively or destructively to determine the spin of the nucleus, which can take values

$$s = 0,\ \frac{1}{2},\ 1,\ \frac{3}{2},\ 2, \ldots$$

The projection of the spin of a given particle on an arbitrary chosen z axis can take values

$$m_s = -s,\ -s+1, \ldots, s-1,\ s\,.$$

With these two quantities, we can define a set of orthonormal basis states of the form $|s, m_s\rangle$, with the following properties:

$$\hat{S}^2 |s, m_s\rangle = s(s+1) |s, m_s\rangle$$
$$\hat{S}_z |s, m_s\rangle = m_s |s, m_s\rangle$$

The operator $\hat{S}^2 = \hat{S}_x^2 + \hat{S}_y^2 + \hat{S}_z^2$, while $\hat{S}_p$ is the operator corresponding to the projection of spin along axis p. The spin of a particle is a conserved quantity, therefore the commutator

$$\left[\hat{S}^2, \hat{S}_p\right] = 0$$

However, the $\hat{S}_p$ operators do not commute with each other:

$$\begin{aligned} \left[\hat{S}_x, \hat{S}_y\right] &= i\hat{S}_z \\ \left[\hat{S}_y, \hat{S}_z\right] &= i\hat{S}_x \\ \left[\hat{S}_z, \hat{S}_x\right] &= i\hat{S}_y \end{aligned} \tag{1.2}$$

This means that the x, y, and z components of the spin cannot be specified simultaneously.

A spin operator for any arbitrary direction in space can be constructed with $\hat{n} \cdot \vec{S}$, where $\hat{n}$ is some unit vector, and

$$\vec{S} = \begin{pmatrix} \hat{S}_x \\ \hat{S}_y \\ \hat{S}_z \end{pmatrix} .$$

These spin operators can be used to describe the interaction between spins, or the interaction between a spin and a magnetic field, so are fundamental for simulating spin-chemical reactions. Together, they can be applied to the state ket, to describe the coherent evolution of the spin state through time. Other operators can be constructed that describe reactivity, and spin relaxation, and will be described later on.

1.3 The Spin-Half Particle

Spin-half particles are very common in spin chemistry, so will be discussed in detail. For a spin-half particle, such as an electron or a proton, we can choose two basis states, representing spin up and spin down along the arbitrarily chosen z axis:

$$|u\rangle = \begin{pmatrix} 1 \\ 0 \end{pmatrix}$$
$$|d\rangle = \begin{pmatrix} 0 \\ 1 \end{pmatrix} .$$

Any possible spin state can be constructed as a linear combination of these two basis states. The two basis states are eigenstates of the $\hat{S}_z$ operator,

$$\hat{S}_z |u\rangle = \frac{1}{2} |u\rangle$$
$$\hat{S}_z |d\rangle = -\frac{1}{2} |d\rangle$$

where

$$\hat{S}_z = \begin{pmatrix} \frac{1}{2} & 0 \\ 0 & -\frac{1}{2} \end{pmatrix} .$$

This means that our basis states have a definite component of spin along the z axis. All other states, which are a linear combination of the two basis states,

$$|\psi\rangle = c_1 |u\rangle + c_2 |d\rangle ,$$

have no definite component of spin along the z axis. Experimentally, this means that if one wishes to measure the component of spin along the z axis, the system must be forced into one of our two basis states. The two coefficients are complex numbers with normalization condition $|c_1|^2 + |c_2|^2 = 1$. The value of $|c_1|^2$ is the probability of measuring spin-up, while $|c_2|^2$ is the probability of measuring spin-down.

The above basis states are not eigenstates of the $\hat{S}_x$ and $\hat{S}_y$ operators, as can be seen from the commutation relations in **equation 1.2**. These operators take the

form

$$\hat{S}_x = \begin{pmatrix} 0 & \frac{1}{2} \\ \frac{1}{2} & 0 \end{pmatrix}$$
$$\hat{S}_y = \begin{pmatrix} 0 & -\frac{i}{2} \\ \frac{i}{2} & 0 \end{pmatrix} ,$$

and have their own pairs of eigenstates that correspond to definite components of spin along the x and y axes, respectively.

Particles with a higher spin can be described in a similar way, but with a larger number of basis states. In this thesis, the only higher spin treaded is nitrogen-14. Nitrogen-14 is spin-one, as it has an odd number of neutrons and an odd number of protons. The state vector therefore has three basis states rather than two, and operators are 3×3 matrices.

The fact that spin is described by a state vector distinguishes it as a quantum property. A classical state cannot be considered to be a linear combination of other states, and all properties can be measured simultaneously, to arbitrary precision, in classical physics.

1.4 Treating Multiple Spins

A single, isolated, spin is not a realistic system. In organic radicals, unpaired electrons are coupled to neighboring magnetic nuclei, such as hydrogen and nitrogen-14, which must be excluded explicitly in calculations. Moreover, a spin-chemical reaction involves at least two unpaired electrons.

The state vector of a pair of spins, one with state vector $|\psi_1\rangle$ and the second with state vector $|\psi_2\rangle$, can be constructed by taking the direct product

$$|\psi_1\rangle \otimes |\psi_2\rangle \ .$$

In the same way, an operator that acts on the first spin in the combined spin space

can be constructed as

$$\hat{O}_1 = \hat{O} \otimes \hat{\mathbb{1}}\,,$$

where $\hat{O}$ is some matrix operator in the Hilbert space of $|\psi_1\rangle$, and $\hat{\mathbb{1}}$ is the identity matrix in the Hilbert space of $|\psi_2\rangle$. Conversely, an operator acting on the second spin is

$$\hat{O}_2 = \hat{\mathbb{1}} \otimes \hat{O}\,.$$

This follows from the mathematical identity

$$(\boldsymbol{A} \otimes \boldsymbol{B})(\vec{a} \otimes \vec{b}) = (\boldsymbol{A}\vec{a}) \otimes (\boldsymbol{B}\vec{b})$$

For a system composed of N spins, a matrix operator $\hat{O}_n$ acting on the n^{th} spin in the combined spin space is

$$\hat{O}_n = \hat{\mathbb{1}}_1 \otimes \hat{\mathbb{1}}_2 \otimes \cdots \otimes \hat{\mathbb{1}}_{n-1} \otimes \hat{O} \otimes \hat{\mathbb{1}}_{n+1} \otimes \cdots \otimes \hat{\mathbb{1}}_N$$

where $\hat{\mathbb{1}}_k$ is the identity matrix in the Hilbert space of the k^{th} spin.

Once a spin system and its operators have been built, the spin evolution can be simulated by describing spin interactions with a Hamiltonian operator, and a spin-chemical reaction can be modeled.

1.5 Spin-Chemical Reactions

Spin-chemical reactions are distinct from other chemical reactions in that, in addition to energetic considerations, the system must be in an appropriate spin state for the reaction to proceed. A primary characteristic of such reactions is that they can be affected by the strength and direction of an applied magnetic field.

This thesis focuses on three different spin-chemical reactions; singlet recombination in an organic bi-radical, a similar reaction in a protein, and triplet exciton annihilation in an organic crystal. These reactions broadly follow a similar scheme,

as all involve recombination to form a singlet ground state. These recombination reactions are necessarily spin-selective, as Pauli's exclusion principle constrains a pair of electrons in an orbital to be in a singlet spin state. Therefore, in the reactions relevant to this work, a pair of electrons or excitons can only react if their spin-state is singlet.

Radical Pairs must be Spin-Correlated for a Magnetic Field Effect to be Measurable

Spin-chemistry deals with reactions between species that have non-zero spin. For the reaction to be affected by an external magnetic field in an observable way, the two species must be spin-correlated. A common mechanism to create such a state is the photoexcitation of a molecule, which then oxidizes or reduces a neighboring molecule to create a radical pair:

$$^{\mathrm{S}}\mathrm{A}^{*} + \mathrm{B} \longrightarrow {}^{\mathrm{S}}[\mathrm{A}^{\cdot+}\mathrm{B}^{\cdot-}]$$

or

$$^{\mathrm{S}}\mathrm{A}^{*} + \mathrm{B} \longrightarrow {}^{\mathrm{S}}[\mathrm{A}^{\cdot-}\mathrm{B}^{\cdot+}]\,.$$

In practice, a radical pair created in this way is not always in a singlet state. In certain reactions, the photoexcited state has a long lifetime compared to the rate of electron transfer, such that inter-system crossing (often caused by the presence of a heavy atom) generates a triplet excited state. In these reactions, the excited singlet state quickly fluoresces back to the ground state, such that the subsequent electron transfer produces a radical pair in a triplet state [161]:

$$^{\mathrm{T}}\mathrm{A}^{*} + \mathrm{B} \longrightarrow {}^{\mathrm{T}}[\mathrm{A}^{\cdot+}\mathrm{B}^{\cdot-}]$$

or

$$^{\mathrm{T}}\mathrm{A}^{*} + \mathrm{B} \longrightarrow {}^{\mathrm{T}}[\mathrm{A}^{\cdot-}\mathrm{B}^{\cdot+}]\,.$$

Triplet-born radical pairs are common in dilute solutions, as there is time for inter-system crossing before the excited molecule meets a reaction partner. The radical pairs studied in this thesis all have an initial singlet state, as they are bi-radicals within a molecule or protein. As a result, after photoexcitation, electron transfer occurs on a timescale such that intersystem-crossing is negligible.

Oxidation, by O_2, of a molecule with a singlet ground state is another common mechanism that creates a radical pair in a triplet state, as O_2 has a triplet ground state. Other mechanisms that produce a spin correlated radical pair include hydride transfer and bond homolysis [161].

Magnetic field effects can be observed on reactions between free radicals, despite the fact that two free radicals have a random spin state when they encounter each other. Initially, a randomly chosen pair of free radicals has a probability of $1/4$ of being in a singlet state, and a probability of $3/4$ of being in a triplet state. However, on a first encounter, the pairs with a singlet state are much more likely to react than the pairs in a triplet state, leaving a spin-polarized ensemble of triplet radical pairs.

Radical Pairs undergo Spin-Selective Reactions

According to Pauli's exclusion principle, no pair of fermions can have the same state. Furthermore, in a molecular orbital, the spacial wavefunction is symmetric, so the rules of parity mean that the spin wavefunction must be antisymmetric [151]. Two electrons in the same molecular orbital are therefore constrained to a singlet spin state. This means that, for a radical pair to react and form a ground state molecule, the pair must be in a singlet state[4], as spin is conserved.

This thesis will focus on reactions between singlet-born radical pairs created by photoexcitation and subsequent electron transfer. In these reactions, the radical pair can either recombine to the singlet ground state, or form a long-lived secondary product. Hyperfine interactions with nuclei in each radical drive singlet-triplet interconversion, such that the initial singlet state is not retained. The radical pair

[4]Unless the product has a triplet ground state, which is uncommon.

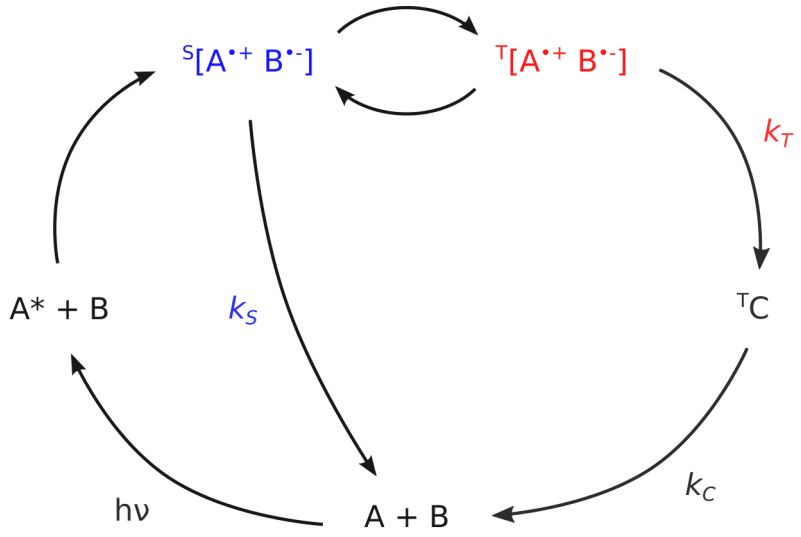

Figure 1.1: Example of a singlet-born radical pair reaction with two spin-selective reactivity channel. The rate k_S represents recombination to the ground state, and can only occur when the radical pair is in a singlet state, while k_T is the rate of formation of a long-lived triplet product C. The rate $k_C \ll k_S, k_T$.

can either recombine to form the singlet ground state, or form a secondary product (either by chemical reaction, or simply by diffusing apart). The singlet recombination is always spin-selective, while the formation of the secondary product may be triplet selective (**figure 1.1**) or not spin-selective (**figure 1.2**).

As spin is a magnetic property, an external magnetic field can alter the spin state of the radical pair. The field can alter the singlet/triplet probability over the lifetime of the radical pair, and therefore influence the ratio of the products [161]. Even a magnetic field whose strength is smaller than that of the hyperfine couplings (generally $\leq 1\,\mathrm{mT}$) can have a substantial effect, by splitting degeneracies and therefore causing increased oscillation away from the initial spin state.

The radical pair is an example of a dissipative system, *i.e.* a transient system extremely far from equilibrium. Such systems also exist in classical physics, with a simple example being a pendulum. If the pendulum is pushed with the exact amount of energy required to make it rotate through 180° and stop vertically, any infinitesimal force is sufficient to make the pendulum fall one way or the other. This is in contrast to the equilibrium state of a pendulum hanging at rest, where

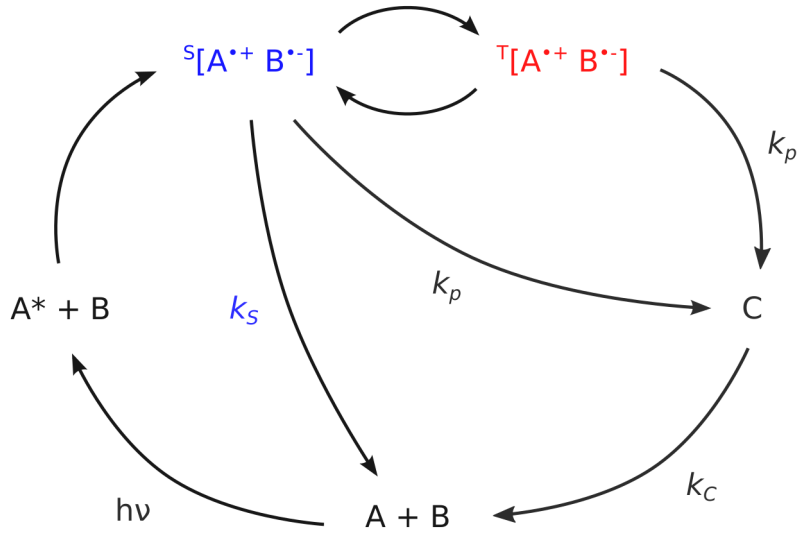

Figure 1.2: Example of a singlet-born radical pair reaction with one spin-selective reactivity channels. The rate k_S represents recombination to the ground state, and can only occur when the radical pair is in a singlet state. The rate k_p represents a non spin-selective reaction that forms a long-lived radical pair, for example by proton transfer. The rate $k_C \ll k_S, k_p$.

the infinitesimal force would have negligible effect. The dissipative pendulum was originally conceived as a system where the idea of the Newtonian trajectory could not be applied, and instead had to be treated probabilistically [145].

Chapter 2 will discuss a carotenoid-porphyrin-fullerene biradical, with both singlet and triplet selective reaction pathways. **Chapters 3–4** will discuss a radical pair between flavin adenine dinucleotide (FAD) and tryptophan (Trp), where only the singlet recombination is spin selective, and a secondary, long-lived, radical pair forms by proton transfer. **Chapter 5** will discuss the reaction between a pair of triplet excitons rather than a radical pair.

1.6 Spin Interactions

The coherent evolution of a spin state depends on the interaction between each spin and the external magnetic field (the Zeeman interaction), and the interactions between spins. Interactions between spins include a contribution from each spin's magnetic dipole, and an isotropic contribution from the overlap of each spin's spacial

wavefunction. The initial spin state is a linear combination of eigenfunctions of the spin Hamiltonian, whose phases oscillate at frequencies determined by the spin interactions, resulting in evolution away from the original state.

The time evolution of a quantum state $\psi(t)$ is governed by Schrödinger's equation,

$$\frac{d\psi(t)}{dt} = -i\hat{H}\psi(t)\,, \tag{1.3}$$

where $\hat{H}$ is the Hamiltonian operator, corresponding to the energy of the system. As we are using units of $\hbar = 1$, the Hamiltonian has units of frequency.

Since magnetic interactions are generally much weaker than electronic interactions, the spin Hamiltonian can be treated as a perturbation

$$\hat{H} = \hat{H}_0 + \hat{H}_{\text{spin}}\,.$$

In the same way, the full wavefunction can be considered to be the direct product of the electronic wavefunction and the spin wavefunction:

$$\psi(t) = \psi_0(t) \otimes \psi_{\text{spin}}(t)\,.$$

The electronic wavefunction was therefore neglected, and henceforth all Hamiltonians and quantum states will refer to the spin contribution only. The Hamiltonian therefore represents a Hermitian matrix operating on a complex state vector $|\psi\rangle$. Schrödinger's equation then becomes

$$\frac{d}{dt}\,|\psi(t)\rangle = -i\hat{H}\,|\psi(t)\rangle\ ,$$

with solution

$$\begin{aligned} |\psi(t)\rangle &= e^{-i\hat{H}t}\,|\psi(0)\rangle \\ &= \hat{U}(t)\,|\psi(0)\rangle\ , \end{aligned}$$

where $\hat{U}$ is a unitary matrix known as the propagator.

The form of the spin Hamiltonian depends on the interactions between nuclei, electrons, and any external magnetic field. The interactions found in an organic radical are discussed below.

1.6.1 The Zeeman Interaction

The energy of a magnetic dipole in a magnetic field is [50]

$$E = -\vec{\mu} \cdot \vec{B}\,, \tag{1.4}$$

where μ is the magnetic moment of the dipole and $\vec{B}$ is the applied magnetic field[5]. For an electron,

$$\begin{aligned} \vec{\mu} &= -\frac{eg}{2m_e}\vec{S} \\ \vec{\mu} &= -\gamma_e \vec{S}\,, \end{aligned} \tag{1.5}$$

where e is the elementary charge (here defined to be positive), $g = 2.002319$ is the electronic g-factor [124], m_e is the mass of the electron, $\vec{S}$ is the vector of electronic spin operators, and $\gamma_e = 1.761 \times 10^{11}\,\mathrm{s^{-1}\,T^{-1}}$ is the electron's gyromagnetic ratio [124]. Combining **equations 1.4** and **1.5** gives the Zeeman interaction, with Hamiltonian [50]

$$\hat{H} = \gamma_e \vec{S} \cdot \vec{B}\,. \tag{1.6}$$

Trivially, this has eigenstates of spin up and spin down along the applied magnetic field vector, with energy separation $\gamma_e B$.

A nuclear Zeeman interaction also exists, but was neglected for the purposes of this thesis. This is because the proton's gyromagnetic ratio ($\gamma_p = 2.657 \times 10^{8}\,\mathrm{s^{-1}\,T^{-1}}$) is negligible compared to the electron's [124], and because all simulations in the current work assumed zero initial nuclear polarization. Furthermore, this approximation is justified empirically by its use in many past studies [161].

[5] That is, the energy is minimized when the magnetic moment is aligned with the field.

1.6.2 Exchange Interaction

The exchange interaction arises due to constraints on the spacial wavefunction of a pair of electrons. In the triplet state, there is zero probability of the two electrons occupying the same point in space, while in the singlet state this probability is enhanced [151]. This results in an isotropic magnetic interaction in the singlet state, giving rise to a Hamiltonian of the form

$$\hat{H} = -2J\vec{S}_1 \cdot \vec{S}_2 \,, \tag{1.7}$$

where $\vec{S}_p$ is the vector of spin operators of electron p. This Hamiltonian splits the spin eigenstates into a triplet subspace of degenerate states, and a singlet state, with energy separation $2J$. The addition of a dipolar interaction between electrons lifts degeneracies in the triplet subspace, with the exact form of the triplet eigenstates depending on the relative orientation of the electrons.

In the solid state, the Dzyaloshinskii-Moriya interaction can lead to both symmetric and antisymmetric anisotropy in the exchange interaction of the form

$$\hat{H} = \vec{S}_1 \cdot \boldsymbol{J} \cdot \vec{S}_2 + \vec{J} \cdot \left(\vec{S}_1 \times \vec{S}_2 \right) \,, \tag{1.8}$$

where $\boldsymbol{J}$ is a symmetric tensor and $\vec{J}$ is an axial vector, and the cross product describes the anti-symmetry [54]. This anisotropic interaction has only been observed in spin glasses with significant spin-orbit coupling [49], and has therefore been considered inconsequential to the spin systems in the present work.

1.6.3 Dipolar Interaction

The dipolar interaction arises due to the interaction of a pair of electrons' dipoles. Its Hamiltonian takes the form

$$\hat{H} = \vec{S}_1 \cdot \boldsymbol{D} \cdot \vec{S}_2 \,, \tag{1.9}$$

where $\boldsymbol{D}$ is the traceless, symmetric, dipolar interaction tensor [105]. For a pair of motionless electrons,

$$D_{pq} = \frac{\mu_0 \gamma_1 \gamma_2 \hbar}{4\pi r^3} \left(\delta_{pq} - 3e_p e_q\right) . \tag{1.10}$$

where

$$p\,,\, q = x\,,\, y\,,\, z\,, \tag{1.11}$$

μ_0 is the magnetic permeability of a vacuum, γ_j is the gyromagnetic ratio of electron j, r is the separation of the electrons, and $\vec{e}$ is the unit vector pointing from one electron to the other. Since electrons are most commonly studied in molecular orbitals, **equation 1.10** can be averaged over the relative positions of each electron to give

$$D_{pq} = \frac{\mu_0 \gamma_1 \gamma_2 \hbar}{4\pi} \left\langle \frac{\delta_{pq} - 3e_p e_q}{r^3} \right\rangle . \tag{1.12}$$

If the eigenvalues of tensor $\boldsymbol{D}$ are ordered such that

$$|d_1| \leq |d_2| \leq |d_3| \tag{1.13}$$

the tensor can be characterized by its axiality,

$$\begin{aligned} \Delta D &= 2d_3 - (d_1 + d_2) \\ \Delta D &= 3d_3\,, \end{aligned} \tag{1.14}$$

and its rhombicity [181, 149],

$$\delta D = d_1 - d_2\,. \tag{1.15}$$

Careful examination of **equations 1.10** and **1.12** reveal that there is no rhombicity for motionless electrons, and that this property arises when the symmetry of the inter-electron separation distribution is less than cylindrical.

In the basis where $\boldsymbol{D}$ is diagonalized to

$$\boldsymbol{D} = \begin{pmatrix} d_1 & 0 & 0 \\ 0 & d_2 & 0 \\ 0 & 0 & d_3 \end{pmatrix} \tag{1.16}$$

(*i.e.* with the z axis aligned with the inter-electron vector $\vec{e}$), the dipolar eigenstates are

$$\begin{aligned} |S\rangle &= |\uparrow\downarrow\rangle - |\downarrow\uparrow\rangle \ , \quad \omega_S = 0 \\ |T_0\rangle &= |\uparrow\downarrow\rangle + |\downarrow\uparrow\rangle \ , \quad \omega_0 = -\frac{d_3}{2} \\ |T_-\rangle &= |\uparrow\uparrow\rangle - |\downarrow\downarrow\rangle \ , \quad \omega_- = -\frac{d_1}{2} \\ |T_+\rangle &= |\uparrow\uparrow\rangle + |\downarrow\downarrow\rangle \ , \quad \omega_+ = -\frac{d_2}{2} \, . \end{aligned} \tag{1.17}$$

As expected, the singlet state has no dipolar interaction energy due to it having zero total spin. The triplet states do have a dipolar interaction, with the parallel states lower in energy than the antiparallel state (d_1 and d_2 are positive, while d_3 is negative according to **equation 1.12**). The parallel spin states are degenerate when $\delta D = 0$. With the addition of an exchange interaction, the relative energies of the singlet state and the triplet subspace are affected, but the form of the triplet eigenstates is not.

In an isotropic liquid, the dipolar interaction cancels out at short range, due to rapid molecular motion [105]. However, at longer ranges, there is incomplete cancellation – since spin is generally negligibly coupled to molecular rotation, distant spins would have to diffuse at a greater speed for the dipolar magnetic field to average to zero [95]. However, since the dipolar interaction has a r^{-3} dependence, the long range dipolar interaction is negligible unless the spins have very large magnetic moments (*e.g.* in transition metals) [36].

1.6.4 Hyperfine Interaction

The hyperfine interaction is essentially the exchange and dipolar interactions between an electron and a nucleus.

$$\hat{H} = a\vec{S}_1 \cdot \vec{S}_2 + \vec{S}_1 \cdot \boldsymbol{A} \cdot \vec{S}_1 \, , \tag{1.18}$$

where a is the isotropic hyperfine coupling constant, and $\boldsymbol{A}$ is the traceless, symmet-

ric, anisotropic hyperfine coupling tensor. Because the anisotropic tensor represents a dipolar interaction, it can be characterized by its axiality,

$$\Delta A = 2a_3 - (a_1 + a_2) \tag{1.19}$$

and its rhombicity,

$$\delta A = a_1 - a_2 \,. \tag{1.20}$$

as introduced in the previous section.

In the case of an electron coupled with a spin-half nucleus, the isotropic component energetically isolates the (electron-nucleus) singlet state from the triplet subspace, while the anisotropic component splits the triplet subspace into non-degenerate states.

Hyperfine interactions can be measured with electron paramagnetic resonance, or calculated with quantum chemical methods. In the latter case it is important to use numerical slater orbitals, or a contracted Gaussian basis set [12], otherwise the probability of the electron being at the same location as the nucleus will be underestimated.

An antisymmetric contribution to the hyperfine interaction has been reported in certain systems containing heavy nuclei [8, 150], following the Dzyaloshinskii-Moriya mechanism described above. However, this contribution has only been observed in ordered systems in the solid state, which have significant spin-orbit coupling brought on by heavy atoms. The author knows of no example where an antisymmetric hyperfine interaction has been observed in the organic molecules treated in the present work.

1.6.5 Zero Field Splitting

Zero field splitting is essentially a dipolar interaction between two electrons whose spacial wavefunctions overlap, such that they cannot be considered to be individual particles. The laws of addition of spin allow such an electron pair to behave as a

spin-zero or a spin-one particle [151]. In the case of the spin-one particle, the spin Hamiltonian is

$$\begin{aligned} \hat{H} &= \vec{S} \cdot \boldsymbol{D} \cdot \vec{S} \\ \hat{H} &= \vec{S} \cdot \begin{pmatrix} E - \frac{D}{3} & 0 & 0 \\ 0 & -E - \frac{D}{3} & 0 \\ 0 & 0 & \frac{2D}{3} \end{pmatrix} \cdot \vec{S}, \end{aligned} \tag{1.21}$$

where $\vec{S}$ is the vector of spin operators for a spin-one particle. The zero field splitting tensor, $\boldsymbol{D}$, is traceless, as in the triplet state there is zero probability of finding the two electrons in the same point of space, and as such there can be no isotropic contribution [151]. The parameters E and D can be measured with electron paramagnetic resonance.

The zero field splitting tensor can alternatively be expressed as

$$\boldsymbol{D} = \begin{pmatrix} E & 0 & 0 \\ 0 & -E & 0 \\ 0 & 0 & D \end{pmatrix} \tag{1.22}$$

by adding the unit matrix multiplied by $\frac{D}{3}$ - this simply shifts the energy of each of the Hamiltonian's eigenstates by an identical value, which is inconsequential to the spin dynamics of the electron pair if there is no mixing between the triplet subspace and the singlet state. In this case the Hamiltonian's eigenstates are

$$\begin{aligned} |\psi_1\rangle &= |0\rangle \\ |\psi_2\rangle &= \frac{1}{\sqrt{2}} \left(|1\rangle - |{-1}\rangle \right) \\ |\psi_3\rangle &= \frac{1}{\sqrt{2}} \left(|1\rangle + |{-1}\rangle \right), \end{aligned} \tag{1.23}$$

with corresponding energies

$$\begin{aligned} \omega_1 &= 0 \\ \omega_2 &= D - E \\ \omega_3 &= D + E \end{aligned} \tag{1.24}$$

1.6.6 Spin-orbit Coupling

A Charge Moving Relative to an Observer Exhibits a Magnetic Field

A charged particle, when observed in its rest frame, does not exhibit a magnetic field. However, an observer in an inertial frame moving at velocity $\vec{v}$ with respect to the charged particle[6], experiences a magnetic field according to the Joules-Bernoulli equation [30],

$$\vec{B} = \gamma_L \frac{\vec{E} \times \vec{v}}{c^2}\,, \tag{1.25}$$

where $\vec{E}$ is the electric field from the charged particle, c is the speed of light, and $\gamma_L = \frac{1}{\sqrt{1-\frac{v^2}{c^2}}}$ is Lorentz's factor.

The electric potential of a nucleus with charge Ze is

$$V_E = \frac{Ze}{4\pi\epsilon_0 r}\,, \tag{1.26}$$

where Z is the atomic number of the nucleus, e is the elementary charge, ϵ_0 is the permittivity of a vacuum to an electric field, and r is the distance from the nucleus. Taking the negative Laplacian of the electric potential, the electric field experienced by an electron at position r is then[7]

$$\vec{E} = \frac{\vec{r}}{r}\frac{Ze}{4\pi\epsilon_0 r^2}\,. \tag{1.27}$$

Returning to the rest frame of the electron, the magnetic field experienced by the electron due to nuclear motion (assuming $v \ll c$) is, classically,

$$\begin{aligned}
\vec{B} &= \frac{Ze}{4\pi\epsilon_0 c^2 r^3}\vec{r} \times \vec{v} \\
\vec{B} &= \frac{Ze}{4\pi\epsilon_0 c^2 m_e r^3}\vec{r} \times \vec{p} \\
\vec{B} &= \frac{\mu_0 Ze}{4\pi m_e r^3}\vec{l}\,,
\end{aligned} \tag{1.28}$$

[6] *i.e.* the charged particle is moving away from the observer at velocity $-\vec{v}$

[7] Assuming the contribution from the repulsion of other electrons averages to zero

where μ_0 is the permeability of a vacuum to a magnetic field, m_e is the mass of the electron, $\vec{p}$ is the linear momentum of the electron, and $\vec{l}$ is the angular momentum of the electron.

An Electron's Orbital Angular Momentum and Spin Interact

When treated quantum mechanically, the magnetic field experienced by the electron (**equation 1.28**) becomes

$$\vec{B} = \frac{\mu_0 Ze}{8\pi m_e r^3}\vec{L}\,, \tag{1.29}$$

where $\vec{L}$ is now the orbital angular momentum operator of the electron, and an extra factor of $\frac{1}{2}$ has been gained due to Thomas' precession [9].

Combining **equations 1.4** (p. 14) and **1.29**, the electron's spin interacts with the magnetic field arising from its orbital angular momentum with Hamiltonian

$$\begin{aligned}\hat{H}_{\text{so}} &= \frac{\mu_0 Ze\gamma_e}{8\pi m_e r^3}\vec{L}\cdot\vec{S} \\ &= \xi(\vec{r})\vec{L}\cdot\vec{S}\,.\end{aligned} \tag{1.30}$$

The spin-orbit coupling function, $\xi(\vec{r})$, can then be averaged over the orbital wavefunction, which for an atomic orbital gives[8]

$$\lambda = \langle nlm_l \,|\, \xi(r) \,|\, nlm_l\rangle = -\frac{\mu_0\gamma_e Z^4 e}{8\pi m_e n^3 a_0^3 l(l+1/2)(l+1)}\,, \tag{1.31}$$

where a_0 is the Bohr radius. The spin-orbit coupling can then be expressed more simply in terms of the averaged coupling constant,

$$\hat{H}_{\text{so}} = \lambda\vec{L}\cdot\vec{S}\,. \tag{1.32}$$

Due to the quartic dependence of the spin-orbit coupling constant on Z, spin-orbit coupling is significant in heavy species such as bromine, iodine and the transition

[8] This expression does not apply for $l = 0$, as the s orbital has non-zero probability at the nucleus, so the r^{-3} dependence of $\xi(r)$ is non-integrable. However in this case $\vec{L}_q\,|\psi\rangle = 0$, so there is no spin-orbit coupling. Furthermore, the Z^4 dependence only applies to an atom with a single electron.

metals[9] [175, 93], but can often be ignored in lighter species.

Certain small molecules, such as superoxide and the hydroxyl radical [94], have orbital angular momentum in the ground state. This is due to degenerate π^* antibonding orbitals. This means that any linear combination of the two orbitals is also a valid ground state orbital, allowing complex orbitals, which have a non-zero component of angular momentum along the bonding axis [9, 119].

However, organic radicals generally do not have an orbitally degenerate ground state, as they lack the axial symmetry of the aforementioned species. This is certainly the case for flavin and tryptophan radicals, and triplet excitons in polyacene crystals, which are treated in the current work. Therefore the only contribution to spin orbit coupling in these species comes from mixing of the ground state with electronically excited states. This can be treated as a second order perturbation [9],

$$E_2 = \sum_n \frac{\langle 0|\hat{H}|n\rangle \langle n|\hat{H}|0\rangle}{\Delta E_n}\,, \tag{1.33}$$

where $|0\rangle$ is the ground state, $|n\rangle$ is the n^{th} excited state, ΔE_n is their energy separation, and $\hat{H}$ is the full spin Hamiltonian, including explicit spin-orbit coupling terms. The result of this perturbation is that the electronic g-factor, previously included in the electron's gyromagnetic ratio,

$$\gamma_e = \frac{eg}{2m_e} = \frac{g\mu_B}{\hbar}\,, \tag{1.34}$$

is treated as a tensor. The Zeeman Hamiltonian thus becomes

$$\hat{H} = -\frac{\mu_B}{\hbar}\vec{S}\cdot\boldsymbol{G}\cdot\vec{B}_0\,. \tag{1.35}$$

Even if the spin-orbit coupling is isotropically averaged by molecular tumbling, such that the g-factor can be represented as a constant, the latter generally differs from the g-factor of a free electron.

[9] In even heavier species, Lorentz's factor can no longer be approximated as 1, which results in even stronger spin-orbit coupling.

A Particle's Spin can Interact with a Second Particle's Orbital Angular Momentum

This can occur between a nuclear spin and an electron's orbital angular momentum[10], and can be thought of as a contribution to the hyperfine Hamiltonian. This interaction has the form

$$\hat{H}_{\text{so}} = -\frac{\mu_0 \gamma_2 e}{4\pi m_e r^3} \vec{L}_1 \cdot \vec{S}_2 \,, \tag{1.36}$$

where $\vec{L}_1$ is the angular momentum operator of the electron, $\vec{S}_2$ is the spin operator of the nucleus, and γ_2 is the gyromagnetic ratio of the nucleus [65]. A similar expression can be derived for the interaction between an electron's spin and a second electron's orbital angular momentum, where it can be thought of as an addition to the dipolar Hamiltonian.

Analogously to **equation 1.35**, these interactions can be accounted for by including a G-tensor into the hyperfine and electron-electron dipolar Hamiltonians. The net result is that the dipolar and hyperfine coupling tensors lose their symmetry, and gain an isotropic component.

G-tensor Anisotropy was Considered Negligible

In principle, G-tensor anisotropy could lead to spin relaxation in a radical pair tumbling in solution. However, measured anisotropy for flavin and tryptophan radicals bound to proteins occurs in the third decimal place of the G-tensors' principal values (**table 1.1**).

Table 1.1: Principal values of the G-tensor of flavin and tryptophan radicals [136, 56, 18]. The charged flavin was measured in glucose oxidase, the neutral flavin in DNA photolyase, and the tryptophan in ribonucleotide reductase. The number in parentheses is the error in the last digit.

	$FAD^{\cdot -}$	$FADH^{\cdot}$	$TRP^{\cdot}$
g_{xx}	2.00429(3)	2.00431(5)	2.0033(1)
g_{yy}	2.00389(3)	2.00360(5)	2.0024(1)
g_{zz}	2.00216(3)	2.00217(7)	2.0021(1)

[10]The reasoning is the same as outlined above, except one must consider the magnetic field generated by movement of the electron in the rest frame of the nucleus.

Assuming that these values are applicable to the systems studied in the present work, at the weak applied magnetic fields used, the anisotropy from the G-tensor is negligible compared to the anisotropy in the hyperfine coupling, so the anisotropy in the G-tensor was ignored.

In the case of tetracene and anthracene crystals, no G-tensor anisotropy has been observed in the limit of experimental error [187].

Difference in g-factor Was Considered Negligible

A difference in the g-factor experienced by each electron can contribute to the spin dynamics of a radical pair, notably inducing interconversion between S and T_0 states. Experimental studies give $g = 2.0034$ for an anionic flavin radical [118, 136], which is within experimental error of Bleifuss's g-factor for a neutral tryptophanyl radical ($g_e = 2.0030 \pm 0.0004$) in a protein [18]. Assuming that these g-factors are applicable to the radical pairs studied in this thesis, $\Delta g \approx 10^{-4}$. Given that the hyperfine couplings studied in the present work have been calculated to be of the order 1 mT [78], the applied magnetic field would need to be 1000 mT for Δg to significantly affect the spin dynamics. Even assuming $\Delta g \approx 10^{-3}$, the applied field would need to be of the order 100 mT to be significant, far higher than the field strengths treated in this thesis.

1.6.7 Nuclear Quadrupole Interaction

Nuclei with $S > \frac{1}{2}$ have an electric quadrupole moment, which can interact with a local electric field gradient. This contributes to the spin Hamiltonian, as the orientation of the quadrupole moment depends on the nuclear spin state. This interaction was ignored, however, as a previous study suggested that it has negligible effect on the spin dynamics of a flavin-tryptophan radical pair [38]. This is because the electric field gradient in the organic radicals is quite small.

1.6.8 Summary

The spin interactions deemed most important to the organic systems studied in the present work are the hyperfine, and electron-electron dipolar and exchange interactions. The hyperfine interaction is responsible for coherent conversion between singlet and triplet states in a radical pair, which can be modified by an external magnetic field. The electron-electron interactions, if dominant, hinder a magnetic field effect on a radical pair, as the singlet state is their eigenstate. However, in triplet exciton systems, the zero field splitting is responsible for the coherent interconversion and magnetic field effect.

1.7 The Density Matrix

The density matrix is a well-established method of describing a spin system. It is commonly used for simulating both electron-paramagnetic resonance and nuclear magnetic resonance experiments, as well as spin-chemical reactions. The advantage of a density matrix over a vectorial quantum state is that the former can represent a statistical ensemble of different states.

A density matrix describes the statistical properties of an ensemble of spin systems with identical interactions. It combines the quantum probability amplitudes of a set of state vectors with the classical probability of a given spin system *being* in one of the states[11]. If the ensemble is known to be made up of states

$$|\psi_1\rangle\,,|\psi_2\rangle\,,|\psi_3\rangle\,,\ldots,|\psi_n\rangle$$

with corresponding (classical) probabilities

$$p_1\,,\,p_2\,,\,p_3\,,\,\cdots\,,\,p_n$$

[11]Emphasis here to avoid confusion with the act of *measuring* some observable property of the spin system, which would force the system into an eigenstate of the operator corresponding to the observable.

then a density matrix can be constructed as

$$\hat{\rho} = p_1 \left|\psi_1\right\rangle \left\langle\psi_1\right| + p_2 \left|\psi_2\right\rangle \left\langle\psi_2\right| + p_3 \left|\psi_3\right\rangle \left\langle\psi_3\right| + \cdots + p_n \left|\psi_n\right\rangle \left\langle\psi_n\right| \ . \tag{1.37}$$

The probability of measuring a given state $|\phi\rangle$ is

$$\left\langle\phi\right| \hat{\rho} \left|\phi\right\rangle \ ,$$

or equivalently the trace

$$\mathrm{Tr}\left[\hat{P}_\phi \, \hat{\rho}\right] \ ,$$

where the projection operator $\hat{P}_\phi$ can be constructed as

$$\hat{P}_\phi = \left|\phi\right\rangle \left\langle\phi\right| \ .$$

Diagonal elements of the density matrix are probabilities of finding the system in the corresponding state. Off-diagonal elements indicate that the ensemble is spin-polarized into an effective state that is a coherent superposition of the two corresponding states. It is important to note that many different ensembles of spin states can be described by the same density matrix. For example, a density matrix of the form

$$\begin{aligned} \hat{\rho} &= 0.5 \begin{pmatrix} \alpha \\ \beta \end{pmatrix} \begin{pmatrix} \alpha^* & \beta^* \end{pmatrix} + 0.5 \begin{pmatrix} \alpha \\ -\beta \end{pmatrix} \begin{pmatrix} \alpha^* & -\beta^* \end{pmatrix} \\ &= \begin{pmatrix} |\alpha|^2 & 0 \\ 0 & |\beta|^2 \end{pmatrix} \end{aligned} \tag{1.38}$$

is identical to the density matrix constructed of two orthogonal states,

$$\begin{aligned} \hat{\rho} &= |\alpha|^2 \begin{pmatrix} 1 \\ 0 \end{pmatrix} \begin{pmatrix} 1 & 0 \end{pmatrix} + |\beta|^2 \begin{pmatrix} 0 \\ 1 \end{pmatrix} \begin{pmatrix} 0 & 1 \end{pmatrix} \\ &= \begin{pmatrix} |\alpha|^2 & 0 \\ 0 & |\beta|^2 \end{pmatrix} . \end{aligned} \tag{1.39}$$

This indicates that both ensembles of spins have identical statistical properties.

Precise knowledge of the density matrix does not give precise knowledge of the spin states in the ensemble, unless the matrix is singular, in which case the system can be described equally well with a single state vector.

It is always possible to decompose the density matrix into eigenstates,

$$\hat{\rho} = \sum_{n=1}^{N} p_n \left|\psi_n\right\rangle \left\langle\psi_n\right| \tag{1.40}$$

where $|\psi_n\rangle$ form an orthonormal basis and N is the dimension of the density matrix. The orthonormal decomposition is the simplest possible set of states with the statistical properties of the density matrix in question, however, as is evident in **equations 1.38** and **1.39**, it is possible that *none* of the actual spins in the ensemble are in any of the eigenstates.

The Density Matrix can be Propagated with the Liouville-von Neumann Equation

The Liouville-von Neumann equation is a differential equation governing the coherent evolution of a density matrix [80]. It takes the form

$$\begin{aligned} \frac{d\hat{\rho}}{dt} &= -i[\hat{H}, \hat{\rho}] \\ &= -i(\hat{H}\hat{\rho} - \hat{\rho}\hat{H})\,. \end{aligned} \tag{1.41}$$

If the Hamiltonian is stationary, the above equation can be solved to give

$$\hat{\rho}(t) = e^{-i\hat{H}t}\,\hat{\rho}(0)\,e^{i\hat{H}t}\,. \tag{1.42}$$

This follows from **equation 1.37**. For a given state, $|\psi\rangle$, Schrödinger's equation gives

$$|\psi(t)\rangle = e^{-i\hat{H}t}\,|\psi(0)\rangle$$

Therefore the contribution to the density matrix is

$$|\psi(t)\rangle \langle\psi(t)| = e^{-i\hat{H}t} |\psi(0)\rangle \langle\psi(0)| e^{i\hat{H}t}$$

Initial Nuclear States were Assumed to be at Equilibrium

It is convenient to describe a system at thermodynamical equilibrium with a density matrix proportional to the identity matrix. In this case,

$$\begin{aligned} \frac{d\hat{\rho}}{dt} &= -i\left(\hat{H}\hat{\rho} - \hat{\rho}\hat{H}\right) \\ &= -\frac{i}{N}\left(\hat{H}\hat{\mathbb{1}} - \hat{\mathbb{1}}\hat{H}\right) \\ &= 0 \end{aligned} \tag{1.43}$$

where N is the dimension of the density matrix. A density matrix proportional to the identity matrix signifies that one has no information about the spin state of the spin system; when performing a measurement all allowed results are equally likely. This can be verified by the fact that the identity matrix is the identity in any basis. Any deviation from the identity means that there is some degree of spin polarization, and diagonalization of the density matrix will reveal the basis in which the polarization is most easily detected.

This initial density matrix of all nuclei included in simulations was assumed to be proportional to the identity matrix. This is strictly incorrect in the presence of a magnetic field, as at equilibrium, there is a slight spin-polarization along the magnetic field's axis. For a spin-half nucleus, the ratio between populations at equilibrium is

$$\frac{p_2}{p_1} = e^{\Delta E/k_B T},$$

where k_B is Boltzmann's constant, and T is the absolute temperature. Given that the energy splitting

$$\Delta E = g\mu_B B_0,$$

(where μ_B is Bohr's magneton, and B_0 is the applied field strength) then at 30 mT,

$$\frac{p_2}{p_1} \approx 1.0001$$

Since the spin systems discussed in the present work involve an initial fully singlet electronic state (*i.e.* a singlet/triplet polarization of infinity), the equilibrium nuclear polarization is negligible.

The density matrix approach has been used successfully for decades to describe nuclear magnetic resonance and electron paramagnetic resonance [105]. It can also be applied to the describe the polarization state of photons [19]. However, it does not describe the noise that spontaneously arises in an ensemble of spins. This noise can be described with Fields' *modified spin-density* approach [52, 51].

1.8 Spin Relaxation and Reactivity

So far, time evolution has been described deterministically, meaning that an ensemble of spins can be propagated either forward or backward in time infinitely, with no loss of certainty in the state of the system. This does not correspond with experimental observation – an initially pure spin state soon becomes mixed, and thereafter tends to thermodynamic equilibrium. Furthermore, the history of an ensemble at equilibrium cannot be determined. This progression towards thermodynamic equilibrium is known as spin relaxation.

Realistic treatment of a spin system therefore requires a modification of the Liouville-von Neumann equation to take into account spin relaxation as well as reactivity. This is done by including appropriate superoperators into the differential equation of motion of the density matrix, giving

$$\frac{d\hat{\rho}}{dt} = -i\left[\hat{H}, \hat{\rho}\right] - \hat{\hat{K}}\hat{\rho} - \hat{\hat{R}}\hat{\rho}\,. \tag{1.44}$$

$\hat{\hat{K}}$ and $\hat{\hat{R}}$ are the reactivity and relaxation superoperators, respectively. Superoper-

ators can be expressed in matrix form as

$$\hat{\hat{O}}\hat{\rho} \rightarrow \sum_n \hat{O}_n^{(1)} \hat{\rho}\, \hat{O}_n^{(2)}\,, \tag{1.45}$$

where $\hat{O}_n^{(k)}$ is some operator in Hilbert space. The form of the reactivity and relaxation superoperators will be defined in the relevant chapters.

In this thesis, irreversible reactivity will be considered, such that the product states can be omitted from the density matrix – under such conditions, reactivity decays the trace of the density matrix. Furthermore, spin-selective reactivity contributes to spin relaxation by decaying coherent superpositions of singlet and triplet states, which will be discussed further in **chapter 3**.

1.8.1 Liouville Space

When relaxation and asymmetric reactivity are considered, **equation 1.44** becomes very difficult to solve. Fortunately, it is possible to transform the matrix operators into a more soluble form. We can define an operator, vec(), that reshapes a matrix row-wise into a column vector,

$$\mathrm{vec}(\boldsymbol{A}) = \vec{A}\,.$$

The following correspondence exists

$$\begin{aligned} \boldsymbol{BAC} &\leftrightarrow \boldsymbol{B} \otimes \boldsymbol{C}^{\mathrm{T}}\, \mathrm{vec}(\boldsymbol{A}) \\ \boldsymbol{BAC} &\leftrightarrow \boldsymbol{B} \otimes \boldsymbol{C}^{\mathrm{T}}\, \vec{A} \end{aligned} \tag{1.46}$$

We can therefore apply vec() to the density matrix,

$$\mathrm{vec}(\hat{\rho}) = \vec{\rho}$$

converting it from a matrix in Hilbert space to a vector in what is known as Liouville space. The operators acting on the density matrix in **equation 1.44** are converted

to superoperators in Liouville space by means of the transformation in **equation 1.46**. The general superoperator in **equation 1.45** therefore has the form

$$\hat{\hat{O}} = \sum_n \hat{O}_n^{(1)} \otimes \hat{O}_n^{(2)\mathrm{T}}$$

In order to treat coherent evolution, a Hamiltonian superoperator is defined with

$$-i\left(\hat{H}\hat{\rho} - \hat{\rho}\hat{H}\right) \leftrightarrow -i\left(\hat{H} \otimes \hat{\mathbb{1}}^{\mathrm{T}} - \hat{\mathbb{1}} \otimes \hat{H}^{\mathrm{T}}\right)\vec{\rho},$$

where $\mathbb{1}$ is the identity matrix in Hilbert space, and the Hamiltonian superoperator is

$$\hat{\hat{H}} = \hat{H} \otimes \hat{\mathbb{1}}^{\mathrm{T}} - \hat{\mathbb{1}} \otimes \hat{H}^{\mathrm{T}}\,. \tag{1.47}$$

Relaxation and reactivity superoperators can be constructed in the same way, and will be defined in the relevant chapters. The end result is a differential equation involving

$$\begin{aligned}\frac{d\vec{\rho}}{dt} &= -i\hat{\hat{H}}\vec{\rho} - \hat{\hat{K}}\vec{\rho} - \hat{\hat{R}}\vec{\rho} \\ &= -\hat{\hat{L}}\vec{\rho}\end{aligned} \tag{1.48}$$

where $\hat{\hat{L}}$ is known as the Liouvillian. As long as the Liouvillian is time independent, the equation of motion of the density matrix is

$$\vec{\rho}(t) = e^{-\hat{\hat{L}}t}\,\vec{\rho}(0)\,. \tag{1.49}$$

Calculations in Liouville space allow spin-relaxation effects to be included in the simulation of spin-chemical reactions. Appropriate relaxation effects make simulations more realistic, as experimental spin systems relax on timescales much faster than the $\sim 1\,\mu s$ lifetime of the radical pairs discussed in the current work.

1.9 Magnetic Field Effects on Radical Pair Reactions

The theory described in the previous sections can be used for simulating spin-chemical reactions. In this thesis, it will be used primarily to simulate the singlet recombination yield from a reaction between a pair of radicals, which are created in a singlet state.

We have already discussed that radical pairs must be spin-correlated for a magnetic field effect to be observable. Another criterion is that there must be a large enough distance between the electrons such that exchange and dipolar interactions are minimal. This is because these two interactions have a singlet eigenstate, so singlet-triplet interconversion is halted if these two interactions are dominant.

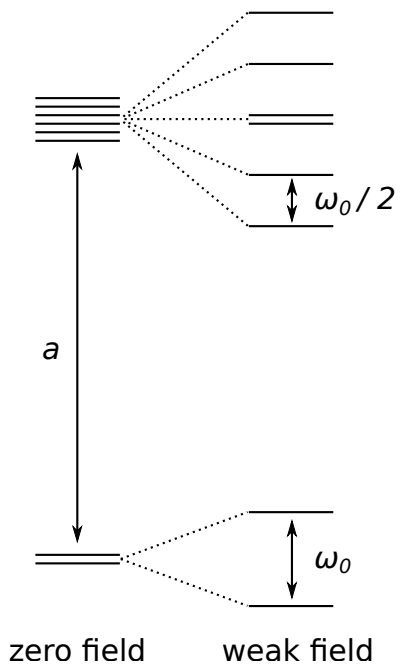

Figure 1.3: Eigenstates of a radical pair with a single proton coupled to one of the electrons, with hyperfine coupling constant a. The effect of a weak magnetic field, ω_0, is also shown, where $\omega_0 \ll a$. For a sufficiently long-lived radical pair, the splitting of degeneracies by the application of a weak field results in an increase in spin evolution away from an initial singlet state, lowering the average singlet probability over the lifetime of the pair.

The electronic singlet state is not an eigenstate of the hyperfine interaction,

however, so hyperfine couplings drive singlet-triplet interconverstion. The addition of an external magnetic field changes the identity and energy of eigenstates of the spin-Hamiltonian, which modifies singlet/triplet probability over the lifetime of a radical pair. The applied field therefore affects the singlet recombination yield.

Magnetic field effects can understood qualitatively by the energy levels in a radical pair with a single proton coupled to one of the electrons[12], where the hyperfine coupling constant is a. In the absence of an applied magnetic field, there are degenerate eigenstates of the spin-Hamiltonian with singlet component. A weak magnetic field ($\omega_0 \ll a$) lifts these degeneracies, resulting in an increase in coherent evolution away from an initial singlet state, compared to the zero field case (**figure 1.3**).

At very high fields ($\omega_0 \gg a$), the $T_\pm$ electronic spin states are effectively eigenstates of the Hamiltonian, with eigenvalues $\lambda \approx \pm\omega_0$, due to the dominant electronic Zeeman interaction:

$$\left.\begin{array}{r} |\alpha\uparrow\uparrow\rangle \\ |\beta\uparrow\uparrow\rangle \end{array}\right\} \quad \lambda \approx \omega_0$$

$$\left.\begin{array}{r} |\alpha\downarrow\downarrow\rangle \\ |\beta\downarrow\downarrow\rangle \end{array}\right\} \quad \lambda \approx -\omega_0\,,$$

where the nuclear spin state is represented by α/β, and the electronic spin state by $\uparrow/\downarrow$. The hyperfine interaction can be treated as a small perturbation of the Zeeman interaction, such that the remaining eigenstates are

$$\left.\begin{array}{r} |\psi_1\rangle = |\alpha\uparrow\downarrow\rangle \\ |\psi_{1'}\rangle = |\beta\downarrow\uparrow\rangle \end{array}\right\} \quad \lambda \approx \frac{a}{2}$$

$$\left.\begin{array}{r} |\psi_2\rangle = |\alpha\downarrow\uparrow\rangle \\ |\psi_{2'}\rangle = |\beta\uparrow\downarrow\rangle \end{array}\right\} \quad \lambda \approx -\frac{a}{2}\,.$$

The $T_\pm$ states are therefore energetically isolated from the T_0 and S states, so

[12]It is important to note, however, that a single proton radical pair is unrealistic, and cannot be used to quantitatively simulate more complicated spin systems.

the former two states are not populated if the initial state is singlet. Furthermore, in the eigenbasis of the Hamiltonian,

$$|S\rangle = \frac{1}{\sqrt{2}}\left(|\psi_1\rangle - |\psi_2\rangle\right)$$
$$|T_0\rangle = \frac{1}{\sqrt{2}}\left(|\psi_1\rangle + |\psi_2\rangle\right)$$

which results in interconversion between S and T_0 at the hyperfine frequency, a (**figure 1.4**). The energetic isolation of the $T_\pm$ states results in a larger singlet recombination yield than in the low field case.

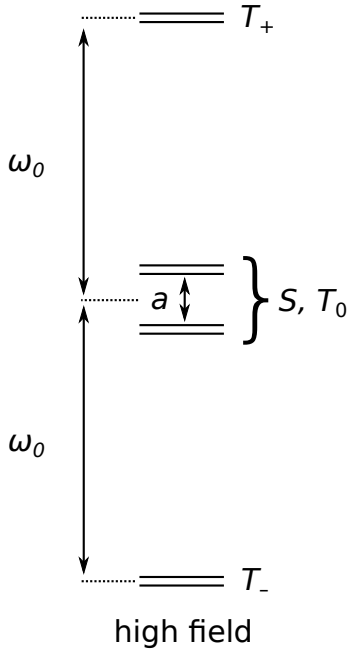

Figure 1.4: Eigenstates of a radical pair with a single proton coupled to one of the electrons, with hyperfine coupling constant a, and strong applied magnetic field ω_0, where $\omega_0 \gg a$. The eigenstates in the electronic $\{S, T_0\}$ subspace are $|S\rangle + |T_0\rangle$ and $|S\rangle - |T_0\rangle$, such that an initial singlet state interconverts completely with the T_0 state. The energetic isolation of the T_+ and T_- states ensures that the these two states are not populated.

A magnetic field effect can also be observed due to differences in g-factor between the electrons in a radical pair, which works very similarly to the hyperfine mechanism at high applied fields. However, the g-factor mechanism can only be observed for very strong magnetic fields ($> 200\,\mathrm{mT}$), so will not be considered in this thesis.

1.10 Calculation of Singlet Recombination Yield

Like spin-relaxation, reactions between spins are modeled probabilistically. One of the outcomes of a radical pair or a triplet exciton pair reaction is recombination to the singlet ground state. This recombination is described by applying the singlet projection operator to the density matrix, and decaying this singlet component at an appropriate rate. The most conceptually simple method of calculating the final singlet yield is therefore to propagate the spin system until decay is complete, storing the cumulative singlet yield at each timestep.

Reaction to form a triplet product can be described in a similar way, while non spin selective reactivity can be simulated by decaying the density matrix without applying a projection operator.

1.10.1 Singlet Yield in Liouville Space

When working in Liouville space, the singlet yield can be calculated by solving the inverse of the Liouvillian applied to the initial density array.

If the singlet recombination yield as a function of time is Φ_S, its time dependence is governed by

$$\frac{d}{dt}\Phi_S(t) = +k_S\, p_S(t)\,,$$

where k_S is the singlet recombination rate constant, and p_S is the singlet probability of the radical pair. The singlet probability can be expanded as

$$p_S(t) = \vec{P}_S^{\dagger}\, \vec{\rho}(t)$$

where $\vec{P}_S$ is the singlet projection operator in Liouville space. This follows from the mathematical identity

$$\mathrm{vec}(\boldsymbol{A}) \cdot \mathrm{vec}(\boldsymbol{B}) = \mathrm{Tr}[\boldsymbol{A}^{\mathrm{T}}\boldsymbol{B}]\,,$$

which, combined with the fact that the singlet projection operator is Hermitian,

gives

$$\mathrm{vec}(\hat{P}_S)^\dagger \,\mathrm{vec}(\hat{\rho}) = \mathrm{Tr}[\hat{P}_S\,\hat{\rho}]\,.$$

The singlet yield after the complete decay of the radical pair is

$$\begin{aligned}
\Phi_S &= k_S \int_0^\infty p_S(t)\,dt \\
&= k_S \int_0^\infty \vec{P}_S^\dagger\,\vec{\rho}(t)\,dt \\
&= k_S\,\vec{P}_S^\dagger \int_0^\infty \vec{\rho}(t)\,dt \\
&= k_S\,\vec{P}_S^\dagger \int_0^\infty e^{-\hat{\hat{L}}t}\,\vec{\rho}(0)\,dt \\
&= k_S\,\vec{P}_S^\dagger\,\hat{\hat{L}}^{-1}\,\vec{\rho}(0)
\end{aligned} \tag{1.50}$$

In practice, the inversion of the Liouvillian was not calculated explicitly, rather $\hat{\hat{L}}^{-1}\vec{\rho}(0)$ was calculated with Matlab's \ operator. As all simulations in this thesis assumed an initial singlet state, $\vec{\rho}(0)$ is proportional to the singlet projection operator.

In Hilbert space,

$$\begin{aligned}
\hat{P}_S &= |S\rangle\langle S| \otimes \hat{\mathbb{1}}_{\mathrm{nuc}} \\
&= \frac{1}{4}\mathbb{1} - \vec{S}_1 \cdot \vec{S}_2
\end{aligned}$$

where $\vec{S}_i$ is the vector of x, y and z spin operators for electron i. The initial singlet state

$$\hat{\rho}(0) = \frac{\hat{P}_S}{M}\,,$$

where M is the number of nuclear spin states, which serves to make the trace of the initial density matrix, and hence the initial population, equal to 1.

1.10.2 The Exponential Model

It is difficult to simulate large spin systems efficiently in Liouville space, due to the memory requirements of storing the Liouvillian, and the time taken to solve its

inversion. Large spin systems can instead be described with the exponential model,[13] which allows calculation of the singlet yield by diagonalizing the spin-Hamiltonian in Hilbert space. This saves time and memory at the expense of using a simplified description of the spin-chemical reaction.

The exponential model describes a radical pair undergoing coherent evolution, where the singlet and triplet electronic states react to form distinct products (**figure 1.1**, p. 11), and both reactions occur at the same rate. This model simplifies the calculation of the singlet product yield; however, in addition to the assumption of equal decay rates, the simplification comes at the price of neglecting spin relaxation. However, this model is useful for simulating large spin systems that would be otherwise intractable, and therefore gives a qualitative understanding of the properties of the spin system.

In the density matrix representation, the probability of measuring the electron pair in the singlet state is

$$\begin{aligned} p_s(t) &= \mathrm{Tr}\left[\hat{P}_S\hat{\rho}(t)\right] \\ &= \sum_{m=1}^{4M} \langle m|\hat{P}_S\hat{\rho}(t)|m\rangle \\ &= \sum_{m=1}^{4M}\sum_{n=1}^{4M} \langle m|\hat{P}_S|n\rangle \langle n|\hat{\rho}(t)|m\rangle \ , \end{aligned} \tag{1.51}$$

where $\hat{P}_S$ is the singlet projection operator, M is the number of nuclear states, and the resolution of the identity has been inserted in the third line. According to **equation 1.42** (p. 27), in the absence of spin-relaxation and reactivity,

$$\begin{aligned} \hat{\rho}(t) &= e^{-i\hat{H}t}\hat{\rho}(0)e^{i\hat{H}t} \\ &= \frac{1}{M}e^{-i\hat{H}t}\hat{P}_S e^{i\hat{H}t} \ , \end{aligned} \tag{1.52}$$

with an initial singlet state. Expanding the exponential contributions in terms of

[13] It is called exponential because the density matrix decays exponentially with time.

eigenstates $|n'\rangle$ of the Hamiltonian,

$$e^{-i\hat{H}t} = \sum_{n'=1}^{4M} e^{-i\omega_{n'}t} |n'\rangle \langle n'| \,, \tag{1.53}$$

and choosing basis states, $|m\rangle$ and $|n\rangle$, to be the eigenstates of the Hamiltonian, the second multiplicand in the last line of **equation 1.51** can be re-expressed as

$$\begin{aligned} \langle n|\hat{\rho}(t)|m\rangle &= \frac{1}{M} e^{-i\omega_n t} \langle n|\hat{P}_S|m\rangle e^{i\omega_m t} \\ &= \frac{1}{M} \hat{P}_S^{(nm)} e^{i(\omega_m - \omega_n)t} \\ &= \frac{1}{M} \hat{P}_S^{(nm)} e^{i\omega_{mn} t} \,, \end{aligned} \tag{1.54}$$

where ω_n is the n^{th} eigenvalue of the Hamiltonian, and $\omega_{mn} = \omega_m - \omega_n$. Inserting the above result back into **equation 1.51**,

$$\begin{aligned} p_s(t) &= \sum_{m=1}^{4M} \sum_{n=1}^{4M} \hat{P}_S^{(mn)} \hat{P}_S^{(nm)} e^{i\omega_{mn} t} \,, \\ &= \sum_{m=1}^{4M} \sum_{n=1}^{4M} |\hat{P}_S^{(mn)}|^2 \cos(\omega_{mn} t) \,, \end{aligned} \tag{1.55}$$

where we have used the fact that the singlet projection operator is Hermitian, and the exponential term has been replaced by a *cosine* term as the singlet probability must be real.

If it is assumed that the electronic singlet and triplet states react at the same rate, k, all density matrix elements decay at the same rate, and the singlet product yield is

$$\Phi_s = k \int_0^\infty p_s(t) e^{-kt} dt \,. \tag{1.56}$$

With the singlet probability from **equation 1.55**, the above equation can be solved to give [172]

$$\Phi_s = \frac{1}{M} \sum_{m=1}^{4M} \sum_{n=1}^{4M} |\hat{P}_S^{(mn)}|^2 \frac{k^2}{k^2 + \omega_{mn}^2} \,. \tag{1.57}$$

1.11 Aims and Objectives

The aim of this thesis is to explore anisotropic effects and spin relaxation in spin-chemical reactions. Here, anisotropy refers to a change in the outcome of the reaction as a function of magnetic field orientation. Two relaxation mechanisms, rotational tumbling, and singlet-triplet dephasing, will be studied in depth, in order to clarify their effect both *in vitro* and *in vivo*.

A biradical in a carotenoid-porphyrin-fullerene molecule will be studied theoretically, in order to assess the viability of measuring anisotropy at weak magnetic field strengths. This biradical will be studied in Hilbert space without spin relaxation, as the large number of hyperfine couplings prevent a more realistic simulation. A second radical pair, in the protein cryptochrome, will be simulated in order to assess whether rotational tumbling and singlet-triplet dephasing are significant relaxation mechanisms. This radical pair will be simulated in Liouville space, in order to facilitate the inclusion of the relaxation effects. For these radical pair reactions, hyperfine interactions (both isotropic and anisotropic) and the exchange interaction will be simulated. Electron-electron dipolar interactions will be neglected, due to the large separation between the radicals.

Anisotropy at low fields ($< 10mT$) will be studied experimentally in anthracene and tetracene crystals, as a proof-of-concept of the AMELIA apparatus (Angle Modulated Experiment for Lock-In Detection of Anisotropy), and to gain an improved understanding of the spin chemistry of these crystals. The experiments will also be simulated, which will give an estimate of the kinetics of triplet exciton annihilation. In these triplet exciton reactions, the proximity of the two electrons in each exciton makes zero-field splitting the dominant interaction. Dipolar interactions between a pair of excitons also exist, but will be neglected in this thesis as they are far smaller than the zero field splitting.

Chapter 2

Sensitivity of Singlet Yield Calculation in CPF Triad

2.1 Introduction

Carotenoid-porphyrin-fullerene (CPF) triad molecules were originally synthesized as a model for a photosynthetic reaction center [98]. Magnetic field effects were then found on electron recombination reactions in triad K (**figure 2.1**), after excitation with green light [111].

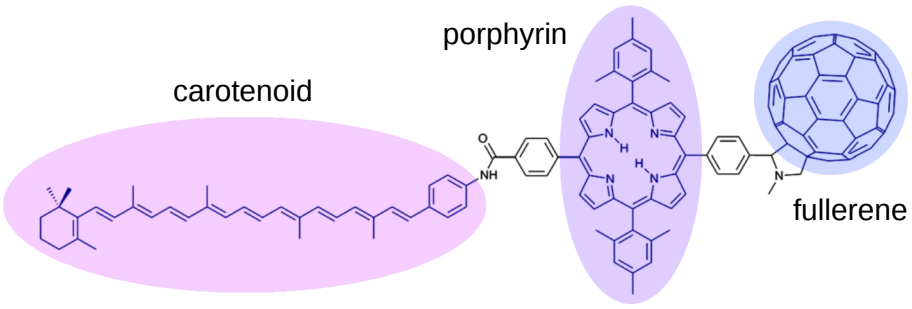

Figure 2.1: The carotenoid-porphyrin-fullerene (CPF) triad studied in the present chapter. After photoexcitation of the porphyrin, a biradical is formed by electron transfer, with the anion located on the fullerene, and the cation loacted on the carotenoid. This molecule is also known as triad K.

The photochemistry of triad K is not fully understood. It is known that on excitation of the porphyrin moiety with a 532 nm laser pulse, the fullerene gains an

electron from the porphyrin, and the carotenoid loses an electron to the porphyrin, to create a biradical (**figure 2.2**). This process occurs on a ns timescale [162, 115]. The resulting biradical can be monitored with a probe beam of 975 nm infrared radiation, which is absorbed by both the carotenoid cation and the fullerene anion [162].

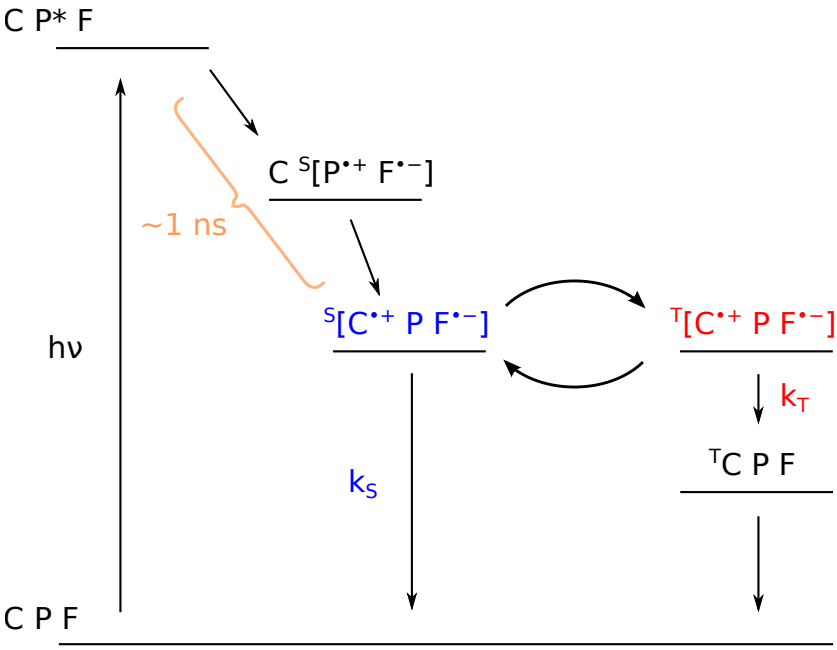

Figure 2.2: Photochemistry of the CPF triad K. The porphyrin moiety is excited with a green laser, and subsequent charge transfer results in a biradical, with one unpaired electron on the carotenoid moiety, and the second unpaired electron on the fullerene moiety. The biradical can either recombine to the singlet ground state, or form a long-lived triplet state located on the carotenoid.

The biradical is thought to be created in a state with overwhelmingly singlet character, and both coherent and incoherent spin evolution drive singlet-triplet interconversion [115]. There are thought to be two, spin dependent, reaction pathways. The first is a return to the electronic ground state, which is only possible when the biradical is in a singlet state. The second pathway is believed to be electron transfer from the fullerene to the carotenoid, leading to a long-lived, uncharged, triplet state. This second pathway is possible only when the biradical is in a triplet state (**figure 2.2**).

The rate constants of these two processes are heavily dependent on temperature.

At 110 K, in 2-methyltetrahydrofuran, k_S has been measured to be $1.8 \times 10^7\,\mathrm{s}^{-1}$, while k_T was found to be negligible [115]. On the other hand, at room temperature and using the same solvent, k_S has been found to be negligible, while k_T was measured to be $1.8 \times 10^7\,\mathrm{s}^{-1}$ [98].

The motivation behind the current work was to attempt a proof-of-concept quantum mechanical simulation of the spin dynamics of the CPF triad. This was done by treating similar hyperfine couplings in the carotenoid moiety as identical. For the sake of simplicity, no attempt was made to include asymmetric decay kinetics from the singlet and triplet states, which is clearly an unrealistic assumption. In addition, spin relaxation was wholly neglected. The latter assumption may not be unreasonable, as Maeda has fitted the spin relaxation rate to be 10^5 to $10^6\,\mathrm{s}^{-1}$ [114], at 123 K and an applied field of 4 mT, which is significantly slower than the measured decay kinetics.

The CPF's Spin System is too Large to be Fully Simulated using Quantum Mechanics

The anionic radical on the fullerene moiety does not, in the majority of cases[1], have any hyperfine couplings, as carbon-12 does not have a magnetic moment. However, the carotenoid cation has 46 protons, most of which have non-negligible hyperfine couplings to the unpaired electron (**figure 2.3**, p. 43).

It was not possible to include all 46 protons in the carotenoid moiety in the calculation of the spin dynamics of the biradical, due to the large amount of memory required. With 48 spin-half particles (including the two electrons), the full calculation would require a $2^{48} \times 2^{48}$ density matrix. Using single precision floating point (*i.e.* 32 bit per float), would require 2.95×10^{20} GB of memory to store the full matrix. Even using sparse linear algebra, the density matrix would have to be just 3.47×10^{-16} % dense for the whole density matrix to fit in the memory of a 1 TB shared memory supercomputer. Clearly the calculation is not feasible with the

[1] Carbon-13 has a natural abundance of 1.1 %, so 49 % of the C_{60} molecules in an ensemble are expected to have one or more carbon-13 atoms, which do have a magnetic moment.

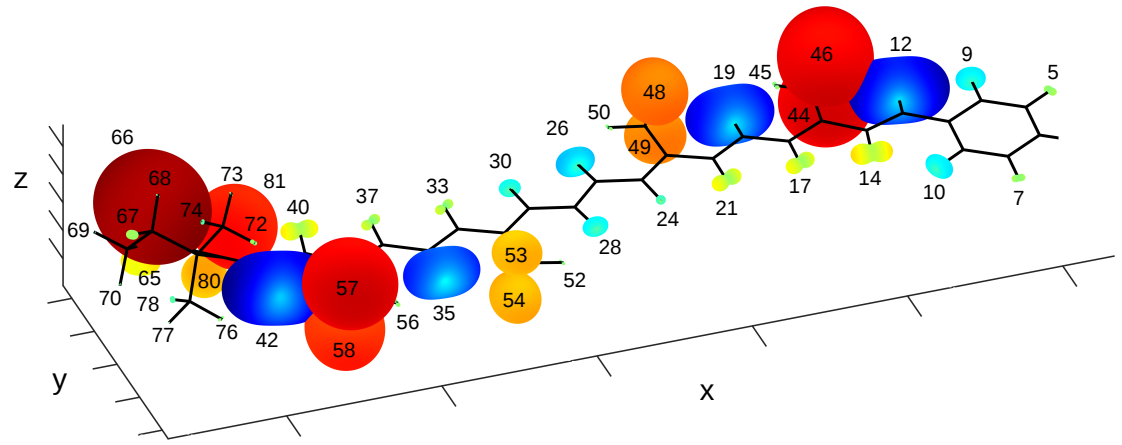

Figure 2.3: The hyperfine tensors of the CPF triad as calculated by density functional theory (DFT) with EPR-II basis set [12, 111]. The hyperfine surfaces were calculated with the equation $a(\hat{n}) = \hat{n}^T \boldsymbol{A}\, \hat{n}$, where $\hat{n}$ is a unit vector. Distance from the nucleus indicates magnitude, with red indicating a positive value, and blue a negative value. Anisotropy is visible by deviation from a spherical shape. The numerical values of each hyperfine tensor are listed in Appendix A.

currently available technology.

Identical Hyperfine Couplings Allow Simplification of Singlet Yield Calculation

Assuming negligible exchange and dipolar interactions, the Hamiltonian governing the coherent evolution of the radical pair has two contributions,

$$\hat{H} = \hat{H}_{\mathrm{HFI}} + \hat{H}_{\mathrm{ZEE}}\,, \tag{2.1}$$

where $\hat{H}_{\mathrm{HFI}}$ is the contribution from the hyperfine interaction, and $\hat{H}_{\mathrm{ZEE}}$ is the contribution from the Zeeman interaction.

If we consider a radical pair consisting of one electron coupled to two identical spin-half nuclei, and a second electron devoid of couplings, the hyperfine part of the Hamiltonian can be factorized:

$$\begin{aligned} \hat{H}_{\mathrm{HFI}} &= \vec{S}^{(A)} \cdot \boldsymbol{A} \cdot \vec{I}^{(1)} + \vec{S}^{(A)} \cdot \boldsymbol{A} \cdot \vec{I}^{(2)} \\ &= \vec{S}^{(A)} \cdot \boldsymbol{A} \cdot \left(\vec{I}^{(1)} + \vec{I}^{(2)} \right) \\ &= \vec{S}_A \cdot \boldsymbol{A} \cdot \vec{I}\,, \end{aligned} \tag{2.2}$$

where $\vec{S}^{(A)}$ is the vector of x, y and z spin operators of electron A, $\vec{I}^{(i)}$ is the vector of x, y and z spin operators of nucleus i, and $\boldsymbol{A}$ is the hyperfine interaction tensor.

The vector operator $\vec{I}$ is composed of the combined x, y and z spin operators of the two identical nuclei,

$$\begin{aligned}\vec{I} &= \begin{pmatrix} \hat{I}_{1,x} + \hat{I}_{2,x} \\ \hat{I}_{1,y} + \hat{I}_{2,y} \\ \hat{I}_{1,z} + \hat{I}_{2,z} \end{pmatrix} \\ &= \begin{pmatrix} \hat{I}_x \\ \hat{I}_y \\ \hat{I}_z \end{pmatrix} .\end{aligned} \tag{2.3}$$

We define a squared spin operator for the pair of identical nuclei,

$$\hat{I}^2 = \vec{I} \cdot \vec{I} , \tag{2.4}$$

which has commutation relations [151]

$$\begin{aligned}[\hat{I}^2, \hat{I}_x] &= 0 , \\ [\hat{I}^2, \hat{I}_y] &= 0 , \\ [\hat{I}^2, \hat{I}_z] &= 0 .\end{aligned} \tag{2.5}$$

The hyperfine component of the Hamiltonian, $\hat{H}_{\mathrm{HFI}}$ is a linear combination of terms

$$\hat{H}_{\mathrm{HFI}} = \sum_{p,q=x,y,z} \hat{S}_p^{(A)} \hat{I}_q . \tag{2.6}$$

The above Hamiltonian must commute with the squared spin operator of both nuclei, $\hat{I}^2$, due to **equation 2.5**. Since the nuclear Zeeman term has been neglected, $\hat{H}_{\mathrm{ZEE}}$ trivially commutes with $\hat{I}^2$. The total spin of the two particles is therefore a constant of motion, so we can block-diagonalize the Hamiltonian by choosing an appropriate basis. Such a basis would be $|S, m\rangle$, where S is the total nuclear spin quantum number, and m is the projection of the total nuclear spin on the chosen quantization axis.

The allowed values of S follow the familiar Clebsch-Gordan rules of adding angular momenta, which are integer-spaced values

$$|s_1 - s_2| \leq S \leq s_1 + s_2\,, \tag{2.7}$$

where s_1 and s_2 are the spin quantum numbers of nucleus 1 and nucleus 2, respectively.

A pair of spin-half nuclei with identical hyperfine couplings would therefore result in a block-diagonal Hamiltonian, with one block governing the coherent evolution of states with $S = 1$ (which has states $|1, +1\rangle$, $|1, 0\rangle$ and $|1, -1\rangle$) and the second block governing the state with $S = 0$ (which has the state $|0, 0\rangle$). This is equivalent to simulating two separate systems, one coupled to a spin-one particle, and the other coupled to a spin-zero particle. This reduces the size of the problem, as the original Hamiltonian would have had $16^2 = 256$ elements, while the two separate Hamiltonians have a total of $12^2 + 4^2 = 160$ elements.

This reduction of the problem's size generalizes to the case of more than two identical nuclei, and can be applied when there are multiple independent groups of identical nuclei. The total spin of each block, and the number of blocks, can be generated using the rules of adding angular momentum [151].

2.2 Simulations

All simulations assumed an initial singlet state of the biradical. Simulations were performed using the exponential model of radical pair decay, as outlined in **section 1.10.2** in the introductory chapter. This model assumes that the decay rate constant of the singlet state is identical to the decay rate constant of the triplet state, where the equation of motion of the density matrix is

$$\frac{d\hat{\rho}}{dt} = -i\left[\hat{H}, \hat{\rho}\right] - k\hat{\rho}\,. \tag{2.8}$$

In practice, the assumption of equal rate constants is unlikely to be correct; experiment gives $k_S \gg k_T$ at 110 K, and $k_S \ll k_T$ at 298 K in a solvent of 2-methyltetrahydrofuran [162, 115]. However, as the aim of the current work was to attempt a proof-of-concept spin dynamic simulation by symmetry reduction rather than the reproduction of experimental data, the correctness of the kinetic model is not of prime importance. The advantage of using the exponential model is that the singlet yield is simple to calculate by diagonalization of the spin Hamiltonian, and the simulation can be performed in Hilbert space rather than the higher dimension Liouville space.

Applied Field Direction was Parameterized on a Lebedev Grid

The direction of the applied magnetic field was chosen to be nodes of a Lebedev grid, as each node represents an equal area on the surface of a sphere [78]. This avoids the issue of a concentration of datapoints at the poles, which arises when using a grid of equally spaced Euler angles θ and ϕ. The spherical average of the singlet yield was found to converge with a 642 point grid (**figure 2.4**).

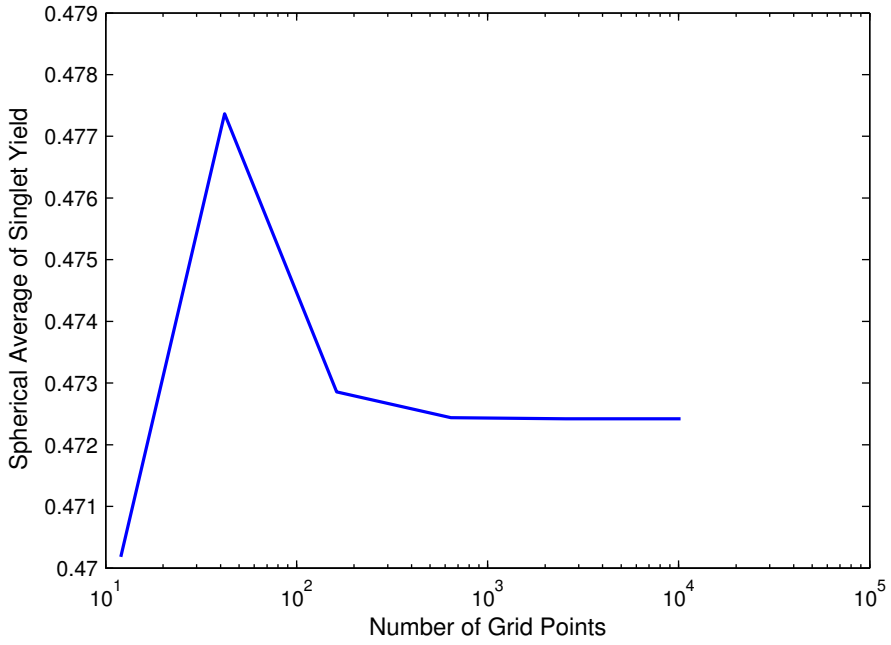

Figure 2.4: Spherical average of the singlet yield for a radical pair with a single hyperfine coupling to one of the electrons, as a function of Lebedev grid size. The hyperfine tensor was that of proton 19 from triad K, calculated by density functional theory. Simulation parameters: $k = 10^7\,\mathrm{s}^{-1}$, $B_0 = 2\,\mathrm{mT}$.

2.3 Error in Singlet Yield when Treating Similar Nuclei Identically

Singlet Yield Simulations were Performed using Subsets of the Carotenoid's Hyperfine Couplings

Visual inspection of the hyperfine tensors in **figure 2.3** suggested that certain nuclei had closely matching hyperfine tensors. Possible groupings are listed in **table 2.1**. In order to assess the feasibility of considering similar nuclei to be identical, two calculations of singlet recombination yield were performed with each grouping of hyperfine tensors:

1. With the unmodified hyperfine tensors calculated by DFT
2. With an identical hyperfine coupling for each similar proton, chosen to be the average of the tensors from the DFT calculation.

Table 2.1: Protons with similar hyperfine tensors in the carotenoid moiety of triad K. The numbers refer to the nuclei in figure 2.3.

Groupings of Similar Nuclei
5, 7
9, 28, 30
12, 42
14, 40
17, 21
17, 21, 33, 37
19, 35
24, 30
33, 37

The mean unsigned error in the second, approximate, calculation was then calculated to be

$$\% \text{ Error} = \frac{\sum_i \left|\Phi^A_{i,\text{DFT}} - \Phi^A_{i,\text{AVG}}\right|}{\sum_i \Phi^A_{i,\text{DFT}}} \times 100\,, \tag{2.9}$$

where Φ^A is the anisotropic component of the singlet yield (*i.e.* the singlet yield minus the spherical average), and i refers to a direction of the applied magnetic field on the Lebedev grid. The subscript DFT refers to the singlet yield from calculation

1, while AVG corresponds to the calculation 2. The spherical average was subtracted from each singlet yield as the yields were highly isotropic (anisotropy was typically of the order of 1 % of the spherical average), and the error in the isotropic component was very low. There was no need to weight singlet yields at different applied field directions when calculating the percentage error, as a Lebedev grid gives each point an equal weighting [78].

A Set of Similar Hyperfine Couplings could not Reliably be Represented by a Set of Identical Couplings

The use of average hyperfine tensors in place of individual hyperfine tensors was an acceptable approximation only at rate constants higher than $10^7\,\mathrm{s}^{-1}$ (**figure 2.5)**. Given that the hyperfine couplings in the carotenoid (calculated by DFT) were of the order 0.2 mT, which corresponds to an angular frequency of approximately $3.5 \times 10^7\,\mathrm{s}^{-1}$, we can surmise that the approximation worked at higher rate constants due to a reduction in the hyperfine-induced spin evolution over the lifetime of the radical pair, with the result that differences in hyperfine couplings were less consequential than with a lower rate constant.

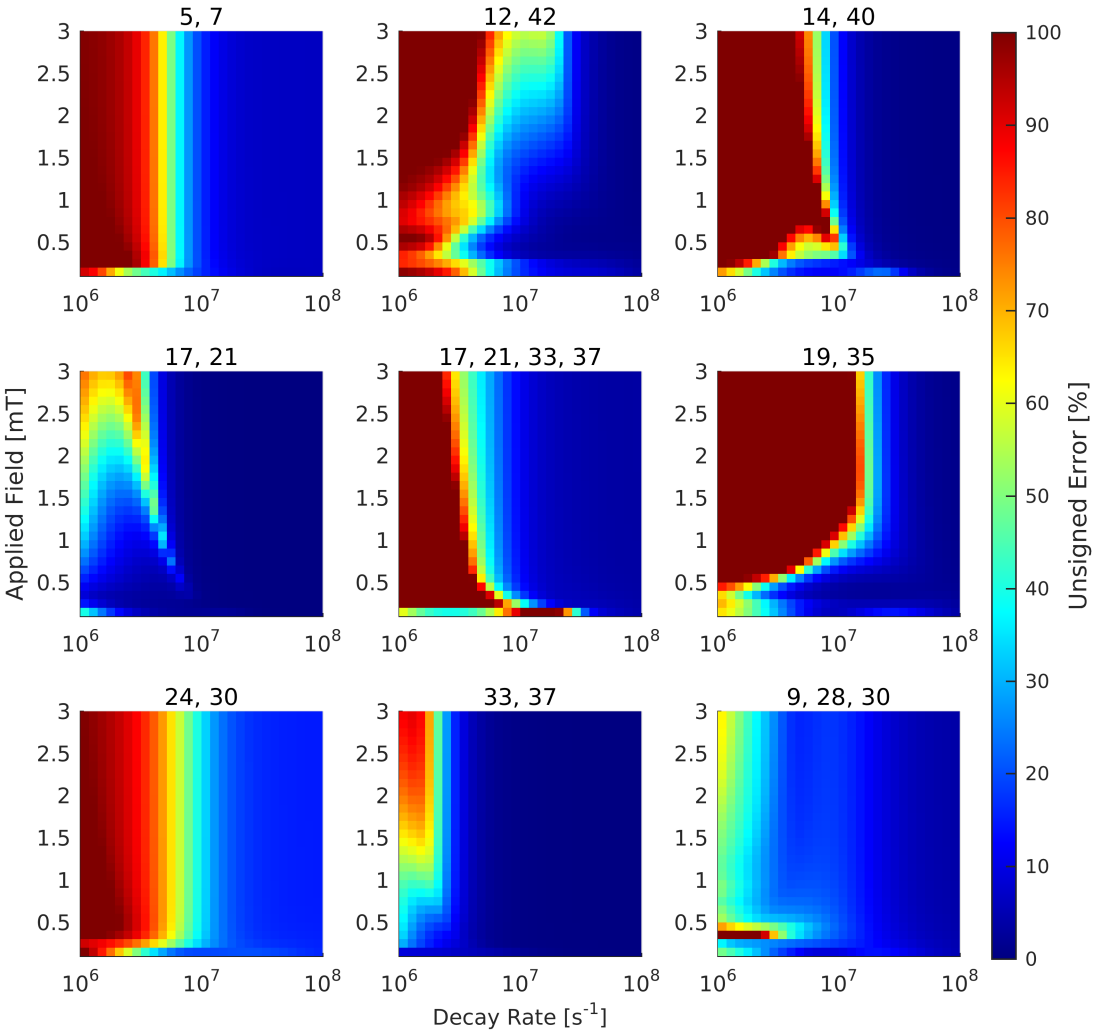

Figure 2.5: Mean unsigned error in the anisotropic component of the singlet yield, when calculated with identical, averaged, hyperfine tensors. The applied magnetic field directions for each calculation were on a 642 point Lebedev grid. Each plot refers to a calculation with one of the electrons in the radical pair coupled to the listed protons from the carotenoid moiety (figure 2.3).

2.4 Error Propagation in Singlet Yield Anisotropy

A Monte Carlo study was performed in order to survey the sensitivity of the singlet yield calculation to deviation in the orientation of hyperfine tensors that are identical in their individual eigenbases. This diagonalized form was chosen to be

$$\boldsymbol{A} = \begin{pmatrix} -1.25 & 0 & 0 \\ 0 & -1.25 & 0 \\ 0 & 0 & 1 \end{pmatrix} \mathrm{mT}\,, \tag{2.10}$$

as this tensor is similar to the anisotropic couplings calculated for the carotenoid cation radical (**appendix A**), but is cylindrically symmetric (*i.e.* lacks rhombicity). This tensor can therefore be rotated to any possible orientation in space with only two Euler angles, which simplifies Monte Carlo sampling of different orientations (**figure 2.6**).

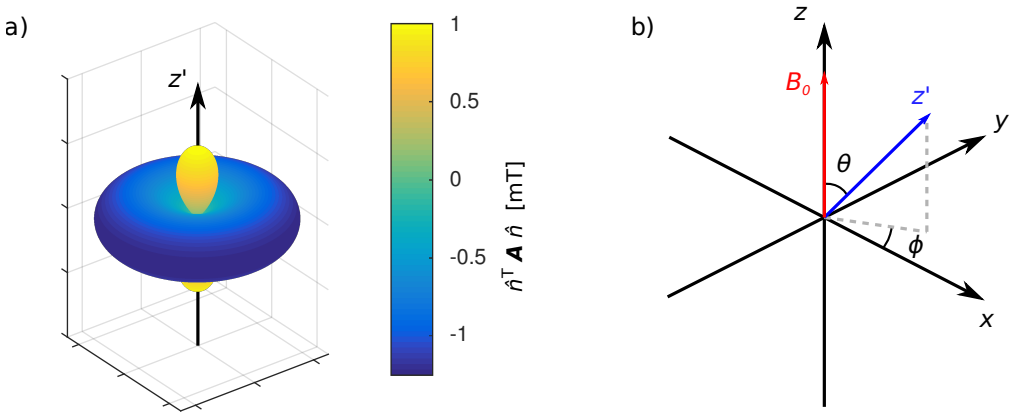

Figure 2.6: a) Representation of the hyperfine tensor from equation 2.10, with axis z', about which the tensor is cylindrically symmetrical. b) Axis system used in the Monte Carlo sampling. $\vec{B}_0$ was kept parallel to the z axis, while the direction of z' was sampled as a function of Euler angles θ and ϕ.

As a reference, the anisotropic component of the singlet yield[2] was calculated with z' of all hyperfine tensors aligned with the applied magnetic field vector ($\Phi^A_{\parallel}$). The anisotropic component of the singlet yield was then sampled as a function of two parameters for each nucleus in the Monte Carlo assay:

[2]That is, the singlet yield with $\vec{B}_0 \parallel z$, minus the spherical average of the singlet yield over all possible orientations of $\vec{B}_0$

- θ: inclination of each hyperfine tensor's z' axis, sampled from a normal distribution with zero mean and standard deviation σ_θ.
- ϕ: azimuth of each hyperfine tensor's z' axis, sampled from a uniform distribution

The resulting uncertainty in the anisotropic component of the singlet yield was then calculated as

$$\frac{\langle|\Phi_{\parallel}^{A} - \Phi_{\sigma}^{A}|\rangle}{\Phi_{\parallel}^{A}}, \tag{2.11}$$

where Φ_{σ}^{A} is a Monte Carlo sample of the anisotropic component of the singlet yield, with uncertainty, σ_θ, in inclination.

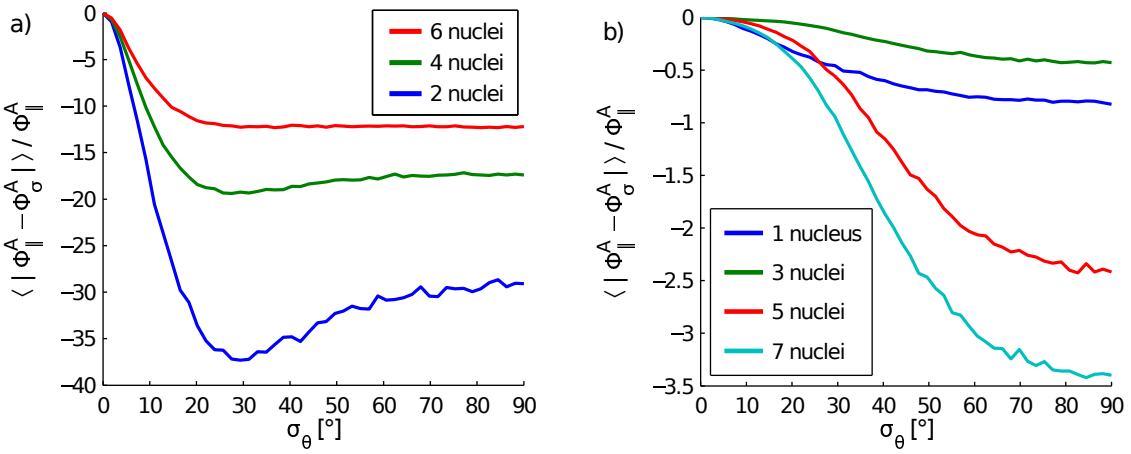

Figure 2.7: Mean relative deviation in the anisotropic component of the singlet yield, as a function of standard deviation in the inclination, θ, of the z' axis each hyperfine tensor. Each point was calculated from 2000 Monte Carlo samples. For each hyperfine tensor, θ was sampled separately from a normal distribution with standard deviation σ_θ and mean 0. The azimuth, ϕ, was sampled separately for each hyperfine tensor, from a uniform distribution $\mathcal{U}(0, 2\pi)$. $\Phi_{\parallel}^{A}$ is the anisotropic component of the singlet yield with all hyperfine tensors aligned with the applied magnetic field vector. Φ_{σ}^{A} is one of the Monte Carlo samples. Simulation parameters: $k = 5 \times 10^6\,\mathrm{s}^{-1}$, $B_0 = 1.5\,\mathrm{mT}$, $\vec{B}_0 \parallel z$.

Uncertainty in the Directionality of an Even Number of Similar Hyperfine Tensors Translated to a Large Uncertainty in Singlet Yield

The results of the Monte Carlo assay (**figure 2.7**) suggest that with an even number of nuclei with similar hyperfine tensors, the assumption of identical, aligned,

hyperfine tensors is a poor one. In all cases sampled with an even number of nuclei, the mean deviation from the fully aligned singlet yield reached its maximum with uncertainty in inclination (θ) of just 30°. The mean deviation was highest with two hyperfine couplings, and decreased with increasing number of such couplings. In contrast, with an odd number of nuclei, the anisotropic component of the singlet yield was fairly insensitive to uncertainty in orientation of the hyperfine tensors.

2.5 Theoretical Analysis of Error Propagation

The Eigenstates of an Electron with two Identical Hyperfine Couplings are Degenerate Pairs with Singlet or Triplet Nuclear Multiplicity

In the absence of an external magnetic field, the Hamiltonian of an electron coupled to a pair of spin-half nuclei with identical hyperfine tensors is

$$\hat{H}_{\mathrm{HFI}} = \vec{S} \cdot \boldsymbol{A} \cdot \left(\vec{I}_1 + \vec{I}_2\right) , \tag{2.12}$$

where the nuclei have been labeled 1 and 2. Following the proof in **section 2.1**, this Hamiltonian can be block-diagonalized into two parts:

1. The electron coupled to a singlet nuclear state (two states)
2. The electron coupled to the triplet nuclear state (six states)

Trivially, the two states with singlet nuclear character are degenerate, and have zero energy, as the magnetic moment of the singlet nuclear state is zero. With spin quantization axis, these eigenstates are most simply described as[3]

$$\begin{aligned} |\psi_1\rangle &= |\uparrow\rangle \left(|\alpha\beta\rangle - |\beta\alpha\rangle\right) \\ |\psi_{1'}\rangle &= |\downarrow\rangle \left(|\alpha\beta\rangle - |\beta\alpha\rangle\right) \\ \omega_1 &= \omega_{1'} = 0 \,, \end{aligned} \tag{2.13}$$

[3]No matter the chosen quantization axis, the singlet state is always $|\alpha\beta\rangle - |\beta\alpha\rangle$.

where ω_1 and $\omega_{1'}$ are the energies, the electronic state are described with $\uparrow$ and $\downarrow$, and the nuclear states are described with α and β for clarity.

The Hamiltonian with triplet nuclear state can be solved by diagonalizing

$$\hat{H} = \vec{S} \cdot \boldsymbol{A} \cdot \vec{I}^{(S=1)}\,, \tag{2.14}$$

where $\vec{I}^{(S=1)}$ is the vector of spin operators for a spin-one particle.

For an axial hyperfine coupling with an isotropic component, the degenerate pairs of eigenstates take the form

$$\begin{aligned} |\psi_2\rangle &= |\uparrow, +1\rangle \\ |\psi_{2'}\rangle &= |\downarrow, -1\rangle \end{aligned} \tag{2.15}$$

$$\begin{aligned} |\psi_3\rangle &= \frac{1}{\sqrt{|c|^2+1}} \left(c\,|\uparrow, 0\rangle + |\downarrow, +1\rangle\right) \\ |\psi_{3'}\rangle &= \frac{1}{\sqrt{|c|^2+1}} \left(c\,|\downarrow, 0\rangle + |\uparrow, -1\rangle\right) \end{aligned} \tag{2.16}$$

$$\begin{aligned} |\psi_4\rangle &= \frac{1}{\sqrt{|c|^2+1}} \left(|\uparrow, 0\rangle - c\,|\downarrow, +1\rangle\right) \\ |\psi_{4'}\rangle &= \frac{1}{\sqrt{|c|^2+1}} \left(|\downarrow, 0\rangle - c\,|\uparrow, -1\rangle\right)\,, \end{aligned} \tag{2.17}$$

where the quantization axis is parallel to the z' axis of the hyperfine tensor, and c depends on the isotropic hyperfine coupling constant and the axiality. The states are also doubly-degenarate if the hyperfine tensor is rhombic as well as axial, but are more complicated than those shown above.

In each degenerate pair of eigenstates, the two states are spin-polarized in different directions. The degeneracies are therefore split by the application of a magnetic field, under the Zeeman interaction. Given a small perturbative Zeeman interaction,

$$\hat{H}^{(1)}_{\mathrm{ZEE}} = \gamma_e \vec{B}_0 \cdot \vec{S}\,, \tag{2.18}$$

such that the full Hamiltonian is specified by

$$\hat{H} = \hat{H}^{(0)}_{\mathrm{HFI}} + \hat{H}^{(1)}_{\mathrm{ZEE}}\,, \tag{2.19}$$

the first order correction to the energy of the eigenstates of the Hamiltonian $\hat{H}^{(0)}_{\mathrm{HFI}}$ is [119]

$$E^{(1)}_n = \langle \psi^{(0)}_n | \hat{H}^{(1)}_{\mathrm{ZEE}} | \psi^{(0)}_n \rangle\ , \tag{2.20}$$

where $\psi^{(0)}_n$ is the n^{th} eigenstate of $\hat{H}^{(0)}_{\mathrm{HFI}}$. The perturbations with applied field both parallel and perpendicular to the hyperfine z axis are summarized in **table 2.2**.

Table 2.2: First order perturbation, by a magnetic field, to the energies of the eigenstates of the hyperfine Hamiltonian. $\omega_0 = \gamma_e B_0$ is the Larmor frequency of a free electron. $\alpha = \frac{1}{2\sqrt{|c|^2+1}}$; see equations 2.16 and 2.17.

Eigenstate	$\vec{B}_0 \parallel z$	$\vec{B}_0 \perp z$
$E^{(1)}_1$	$\omega_0/2$	0
$E^{(1)}_{1'}$	$-\omega_0/2$	0
$E^{(1)}_2$	$\omega_0/2$	0
$E^{(1)}_{2'}$	$-\omega_0/2$	0
$E^{(1)}_3$	$\alpha(c-1)$	0
$E^{(1)}_{3'}$	$-\alpha(c-1)$	0
$E^{(1)}_4$	$\alpha(c+1)$	0
$E^{(1)}_{4'}$	$-\alpha(c+1)$	0

A Radical Pair with an Even Number of Identical Hyperfine Couplings has a Degenerate Pair of Eigenstates Under a Weak Magnetic Field

If a second electron, devoid of hyperfine couplings, is added to the system, and a magnetic field is applied, the Hamiltonian becomes

$$\hat{H} = \vec{S}^{(A)} \cdot \boldsymbol{A} \cdot \left(\vec{I}^{(1)} + \vec{I}^{(2)}\right) + \left(\vec{S}^{(A)} + \vec{S}^{(B)}\right) \cdot \gamma_e \vec{B}_0\,, \tag{2.21}$$

where electrons have been given labels A and B. Since electron B has no couplings to electron A or either nucleus, the above Hamiltonian's eigenstates are a direct

product of those of the single electron system with two identical hyperfine couplings (**table 2.2**), and those of the electron without hyperfine couplings. The resulting energy levels are shown in **figure 2.8**.

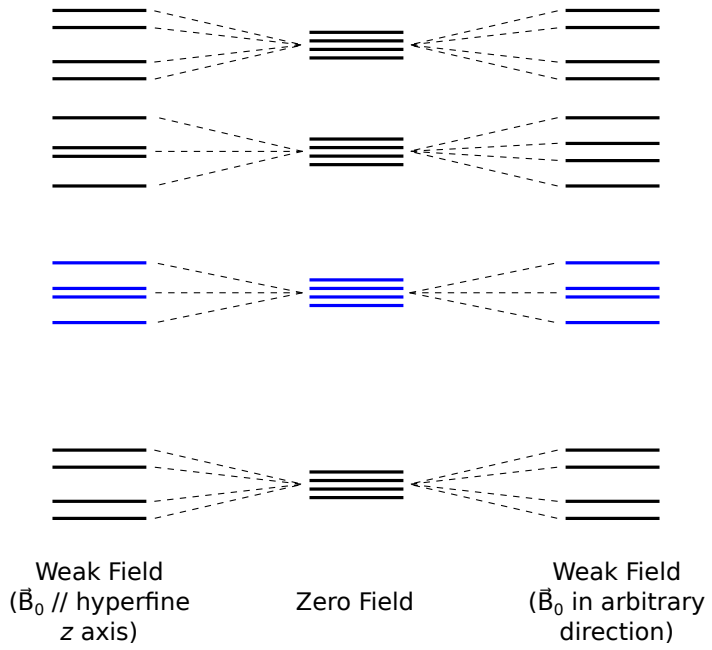

Figure 2.8: Energy levels of a radical pair with two identical, anisotropic, axial, hyperfine couplings to electron A, and no couplings to electron B. The diagram shows the effect of a weak applied magnetic field, far weaker than the strength of the hyperfine coupling. States with singlet nuclear character are shown in blue. Note that a pair of degenerate states with singlet nuclear character is maintained even with an applied magnetic field.

Two degenerate eigenstates with singlet nuclear state are preserved,

$$\begin{aligned} |\phi_1\rangle &= |\uparrow\downarrow\rangle \left(|\alpha\beta\rangle - |\beta\alpha\rangle\right) \\ |\phi_{1'}\rangle &= |\downarrow\uparrow\rangle \left(|\alpha\beta\rangle - |\beta\alpha\rangle\right) \\ \omega_1 &= \omega_{1'} = 0\,, \end{aligned} \tag{2.22}$$

where the chosen quantization axis is parallel to the applied magnetic field. Moreover, it is clear that this pair of states is degenerate at any applied field strength, as long as the difference in the g-factors of the two electrons is negligible. This result generalizes to a system with an even number of identical hyperfine couplings, as all such systems can be block-diagonalized, where one block has has zero total nuclear

spin (**equation 2.2**, p. 43).

If one of the hyperfine couplings is perturbed in the slightest, the symmetry is broken, so we can expect that the degeneracy will be lifted. Unfortunately, the number of variables needed to describe this non-symmetrical system makes proving this hypothesis analytically extremely difficult.

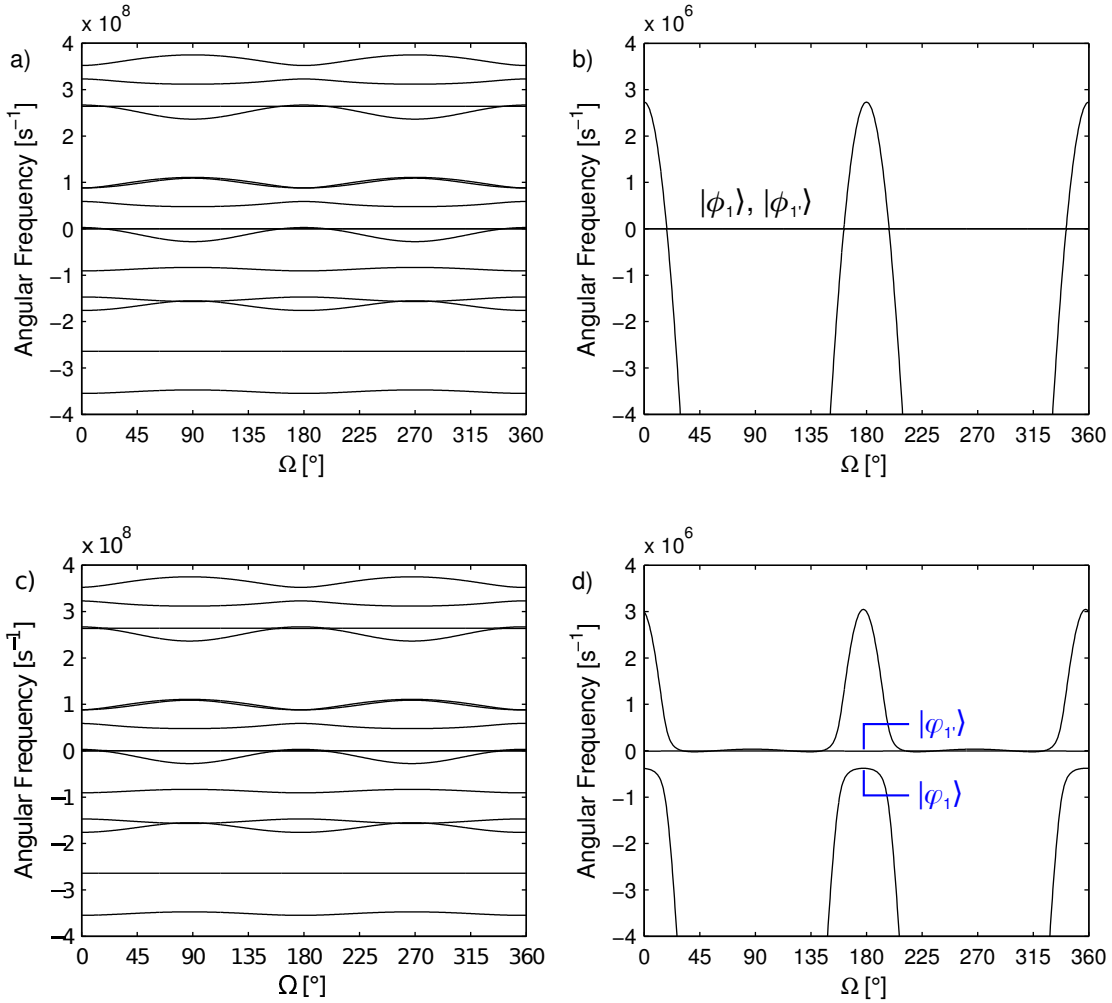

Figure 2.9: Eigenstate energies of a radical pair with two spin-half hyperfine couplings to electron A, and no hyperfine couplings to electron B, as a function of the direction of a 1.5 mT applied magnetic field. The angle Ω is the inclination of the magnetic field with respect to the reference axis z. a) Two identical axial hyperfine couplings, with their z' axes parallel to z. b) The same data with an expanded scale, showing the two degenerate states with singlet nuclear character. c) The same hyperfine tensors, but one with z' inclined 5° with respect to the z axis, and the other with z' parallel to z. d) The same data with an expanded scale, showing where degeneracy is lifted as a result of the non-equivalency of the two hyperfine couplings.

Non-alignment of Hyperfine Couplings Lifts Degeneracies in a Two-Nuclei Radical Pair

The energies of eigenstates of the Hamiltonian were calculated, as a function of the direction of the applied magnetic field, for the two-nuclei system previously studied by Monte-Carlo analysis (**section 2.4**). Both hyperfine tensors were, in their diagonal form, as shown in **equation 2.10**. If the z' axes of the two hyperfine tensors were aligned, there was a pair of degenerate eigenstates with zero energy, as expected from **equation 2.22**. If the two tensors were slightly out of alignment, the degeneracies were lifted (**figure 2.9**).

With a 5° difference in the direction of the z' axis of each tensor, the lifting of the degenaracies was of the order of $10^5\,\mathrm{s}^{-1}$. Furthermore, level crossings with a third eigenstate were eliminated (**figure 2.9**). The lifting of degeneracies was significant at magnetic field inclinations of around 0° and 180°, meaning that they would particularly influence the anisotropy in the singlet yield. Moreover, the effect would presumably be even greater if differences in the axiality, rhombicity, and isotropic component of each hyperfine tensor were introduced.

For the system with two aligned hyperfine couplings, the eigenstates $|\phi_1\rangle$ and $|\phi_{1'}\rangle$ in **figure 2.9.b** are those in **equation 2.22**. For the non-aligned system (**figure 2.9.d**), at $\theta = 180°$,

$$\begin{aligned} |\varphi_1\rangle &\approx |\phi_1\rangle \\ |\varphi_{1'}\rangle &\approx |\phi_{1'}\rangle \ , \end{aligned} \tag{2.23}$$

as evidenced by **table 2.3**.

Table 2.3: Inner product between eigenstates in figure 2.9.b and those in 2.9.d ($\theta = 180°$)

	$\lvert\phi_1\rangle$	$\lvert\phi_{1'}\rangle$
$\langle\varphi_1\rvert$	0.9563	0
$\langle\varphi_{1'}\rvert$	0	0.9956

Using the two degenerate eigenstates from the aligned system, we can define an

electronic singlet state,

$$|S\rangle\left(|\alpha\beta\rangle - |\beta\alpha\rangle\right) = \frac{|\phi_1\rangle - |\phi_{1'}\rangle}{\sqrt{2}} \approx \frac{|\varphi_1\rangle - |\varphi_{1'}\rangle}{\sqrt{2}}\,, \tag{2.24}$$

and an electronic triplet state,

$$|T_0\rangle\left(|\alpha\beta\rangle - |\beta\alpha\rangle\right) = \frac{|\phi_1\rangle + |\phi_{1'}\rangle}{\sqrt{2}} \approx \frac{|\varphi_1\rangle + |\varphi_{1'}\rangle}{\sqrt{2}}\,, \tag{2.25}$$

where there is no coherent interconversion due to their degeneracy. In the non-aligned system, corresponding states can be constructed from the two non-degenerate eigenstates, giving

$$\frac{|\varphi_1\rangle - |\varphi_{1'}\rangle}{\sqrt{2}} \approx |S\rangle\left(|\alpha\beta\rangle - |\beta\alpha\rangle\right)\,, \tag{2.26}$$

and

$$\frac{|\varphi_1\rangle + |\varphi_{1'}\rangle}{\sqrt{2}} \approx |T_0\rangle\left(|\alpha\beta\rangle - |\beta\alpha\rangle\right)\,. \tag{2.27}$$

Since $|\varphi_1\rangle$ and $|\varphi_{1'}\rangle$ have different energies, coherent evolution interconverts the states in **equations 2.26 and 2.27**, resulting in interconversion between singlet and triplet electronic states.

With an initial singlet electronic state, this interconversion reduces the average electronic singlet probability over the lifetime of the radical pair, compared to the system with aligned hyperfine tensors. This effect is very non-linear with respect to the direction of the applied magnetic field, as the lifting of the degeneracy is only significant at inclination angles close to $\Omega = 0°$ and $\Omega = 180°$.

As discussed previously, the non-degeneracies spaced by 180° will exist for any system with an even number of similar hyperfine couplings to one of the electrons. This is why the approximation of identical couplings fails. However, with more than two nuclei, the effect on the spin dynamics should be smaller - with a larger number of eigenstates involved, the lifting of a single degeneracy should have a smaller effect. This would explain the reduction in error propagation with a larger number of nuclei seen in **figure 2.7.a**.

A Radical Pair with an Odd Number of Identical Hyperfine Couplings is not Expected to have Degeneracies Under a Weak Magnetic Field

The existence of an isolated nuclear singlet subspace, in the case of identical, aligned, hyperfine tensors, was essential for the effect discussed in the previous section. This is due to the fact that the hyperfine coupling has no effect in the aforementioned subspace, thus allowing a pair of degenerate eigenstates under the Zeeman Hamiltonian, no matter the direction of the applied magnetic field.

With an odd number of identical, aligned, hyperfine couplings, the rules of addition of angular momentum preclude a spin-zero nuclear state [151], so there is, in general, no isolated subspace with inoperative hyperfine couplings. Therefore, a non-aligned system is not expected to have degeneracies lifted that result in the additional electronic singlet-triplet interconversion seen with an even number of couplings.

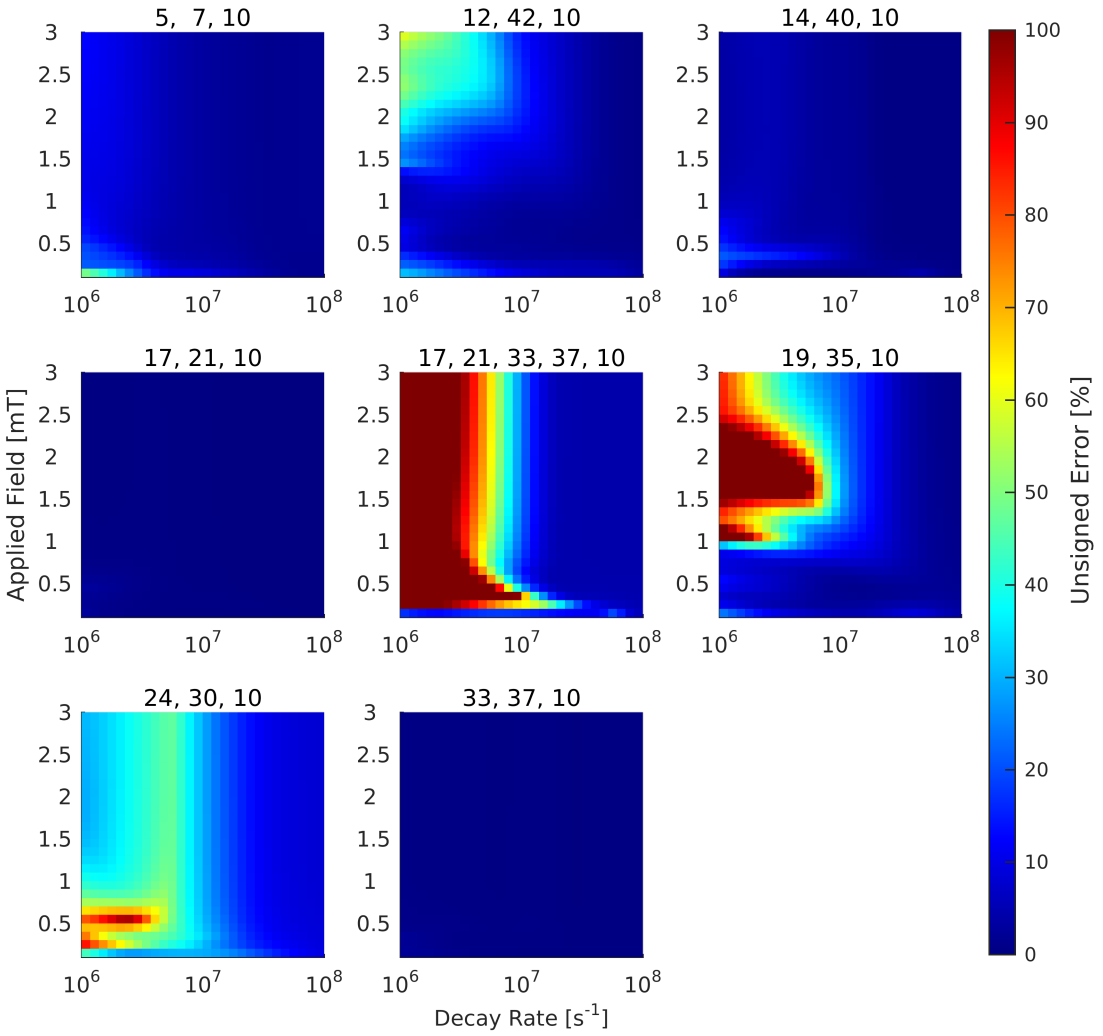

Figure 2.10: Mean unsigned error in the anisotropic component of the singlet yield, calculated with averaged hyperfine tensors, over applied magnetic field directions on a 642 point Lebedev grid. Nucleus 10 was included in all calculations, but was not averaged. Each plot refers to a calculation with one of the electrons in the radical pair coupled to the listed protons from the carotenoid moiety (figure 2.3).

2.6 A Possible Workaround

The difficulty in applying the symmetry reduction, with an even number of similar hyperfine tensors, was due to the existence of a degenerate pair of nuclear singlet states when all hyperfine tensors are identical, which is lifted when the tensors are nonidentical. In principle, if additional interactions were present, the degeneracy that exists in the identical case could be lifted.

To test this idea, the simulations presented in **figure 2.5** were repeated with hyperfine tensor 10 included in all calculations, but not averaged (**figure 2.10**). These calculations revealed four pairs of nuclei that could be considered to be identical. Additional calculations, with tensor 10 replaced with tensor 26 and with tensor 35, are presented in **Appendix B**, in order to convince the reader that the results in **figure 2.10** are not an artifact.

As a proof of concept, the anisotropy in the singlet yield from the biradical in triad K was calculated with with the hyperfine couplings listed in **table 2.4**. This was not meant to be an accurate simulation, but to demonstrate that the symmetry factorization could allow fifteen nuclei to be included.

Table 2.4: Protons included in the simulation of the carotenoid-fullerene radical pair. The numbers refer to atoms in figure 2.3. Couplings listed on the same row were considered identical, and were represented in the calculation by a set of identical, averaged, hyperfine tensors.

Groupings of Similar Nuclei
9, 28, 30
12, 42
14, 40
17, 21
33, 37
10
19
26
35

The calculated singlet yield, as a function of applied field strength, is shown for three perpendicular field directions in **figure 2.11**. The simulations showed a small low field effect, consistent with Timmel's argument that a large number of anisotropic hyperfine couplings should quench the low field effect [170]. This weak

low field effect also matched experimental results measured late in the lifetime of the radical pair [162]. However, measurements at earlier times showed a pronounced low field effect, which may be because some of the weaker hyperfine couplings require a longer time to have a significant effect on the spin state. The largest anisotropic hyperfine couplings calculated by DFT were of the order of 1 mT, corresponding to an oscillation period of $\sim$ 50 ns. However, typical couplings were of the order of 0.1 mT, or a period of $\sim$ 500 ns. Experimental curves were collected at 100 ns, 450 ns and 900 ns, which is consistent with the idea that the effect of certain hyperfine couplings should only be visible at later times. This observation could be exploited by removing some of the smaller couplings from the calculation, in order to simulate earlier times.

The width of the simulated magnetic field effect curves was consistent with experimental measurements, which suggests that the neglect of spin relaxation in the simulations was an acceptable assumption. However, one should not overinterpret the simulations, as the experimental data was collected at 120 K, where the assumption of equal k_S and k_T is a poor one.

The largest anisotropy calculated was at 3 mT, with this property decreasing in magnitude at weaker applied field strengths (**figures 2.12 and 2.13**). Again, this is similar to what Storey found experimentally. However, the experimental setup had the excitation and probe beams positioned at 90° to each other, and polarized perpendicularly to each other, so the measured anisotropy cannot be directly compared to the simulations without taking into account photoselection.

Surprisingly, the simulations predict a change in the shape of the anisotropy at extremely low field strengths. Unfortunately, to the knowledge of the author, there has been no convincing measurement of anisotropy at fields below 1 mT, so this result cannot be validated.

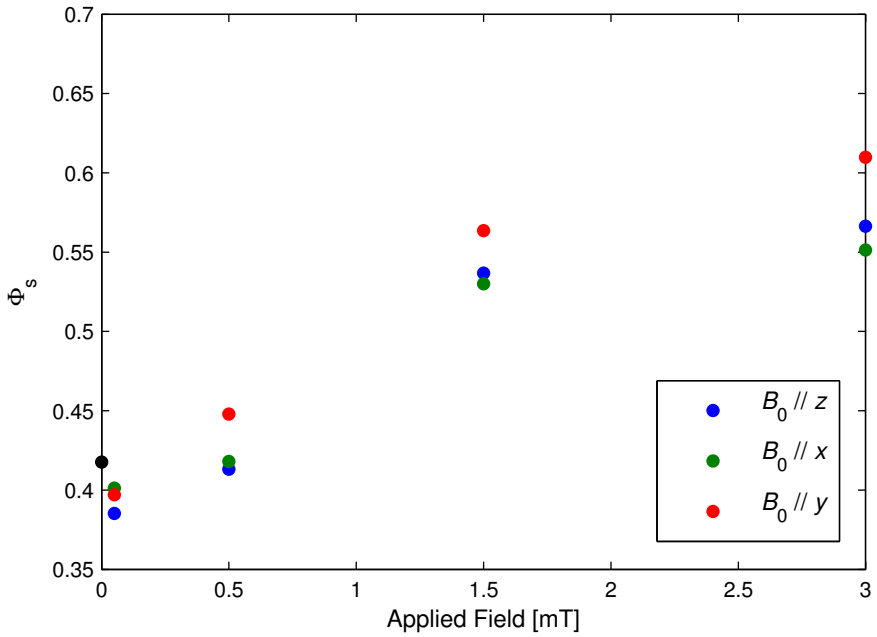

Figure 2.11: Calculated singlet yield in the CPF triad as a function of applied magnetic field strength. The zero field calculation is plotted in black. The axes are those in figure 2.3 (p. 43); x corresponds to the long axis of the molecule, and y corresponds to the perpendicular direction in the plane of the carotenoid moiety. A small low field effect is visible, and there is considerable anisotropy at fields of 0.5 mT and greater.

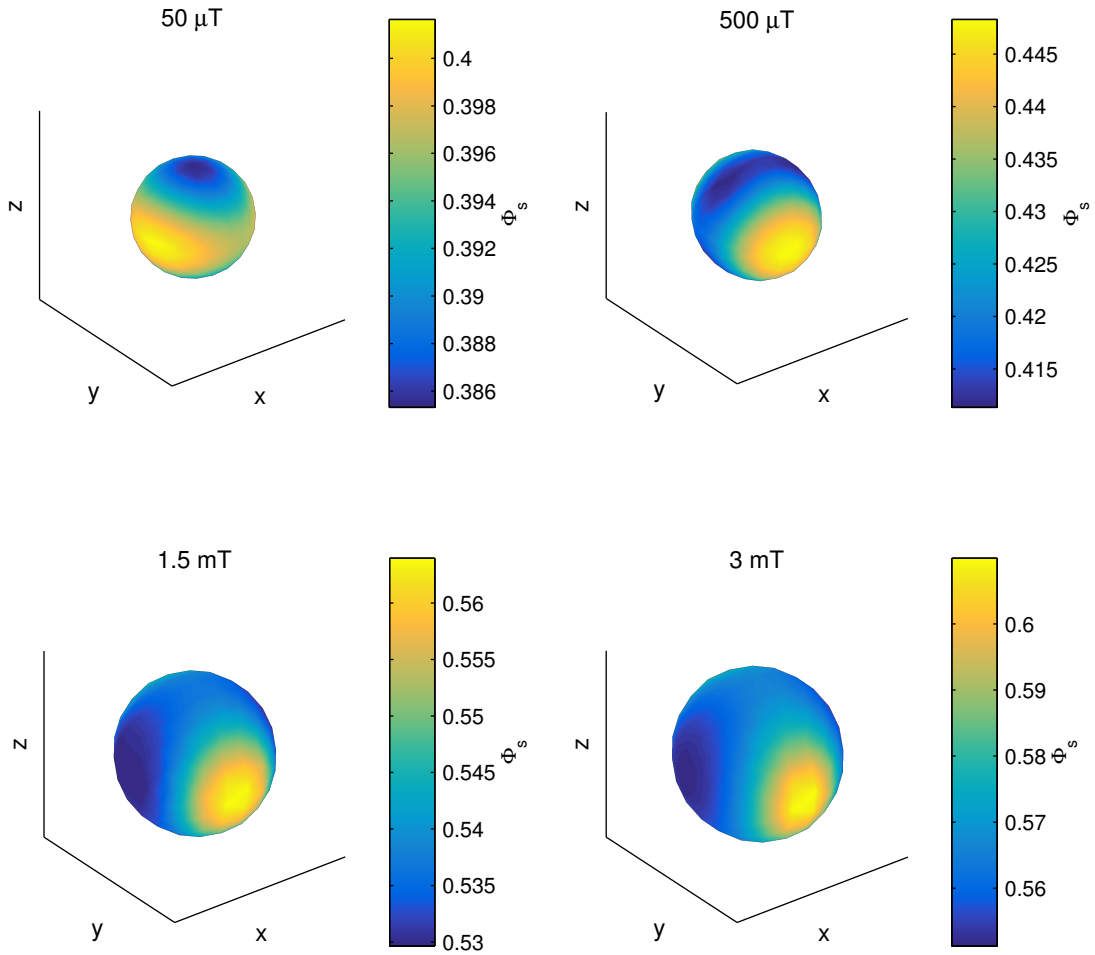

Figure 2.12: Simulation of the singlet recombination yield from the biradical in triad K, with the direction of the magnetic field on a 162 node Lebedev grid. Distance from origin in a particular direction represents singlet yield with the magnetic field along said direction. The singlet yield is also reflected by the color. At zero applied field, the singlet yield was 0.4177.

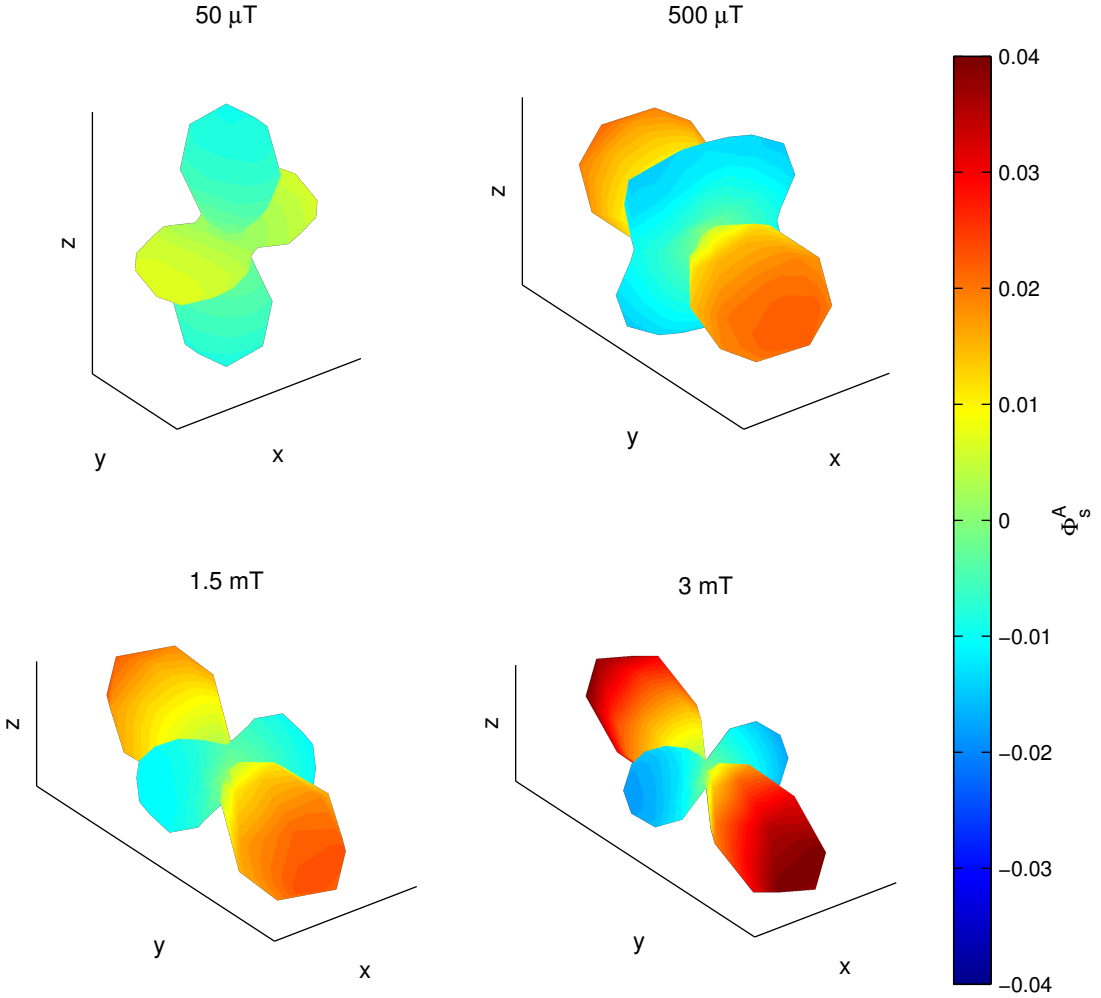

Figure 2.13: Anisotropic component of singlet yield from the biradical in triad K, calculated by subtracting the spherical average from each of the singlet yield plots in figure 2.12. Distance from origin in a particular direction represents deviation of singlet yield from spherical average with the magnetic field along said direction. Sign is represented by color, with red representing positive, and blue representing negative deviation. The axes are the those of the carotenoid fragment in figure 2.3.

2.7 Conclusions

This chapter has explored the viability of treating similar hyperfine tensors as identical, when calculating anisotropy in the singlet recombination yield of a radical pair. Equal hyperfine tensors mean that the size of the calculation can be reduced, allowing more nuclei to be included.

If the similar nuclei are the only ones present in the spin system, and there is an even number of them, the couplings must be extraordinarily similar in order to be treated as identical. Fortunately, few physical radical pairs have only near-identical hyperfine couplings. The difficulty in treating couplings as identical vanishes if additional anisotropic couplings are present in the spin system.

Accordingly, the singlet yield in triad K was calculated with 15 hyperfine couplings, using an exponential decay model of the biradical. This result should be validated experimentally before it can be fully trusted, as many other nuclei were omitted, spin relaxation was neglected, and the singlet and triplet decay rate constants are unlikely to be equal *in vitro*.

More nuclei could feasibly be included in the symmetry-reduced calculation - a further simulation was attempted, with an additional isotropic interaction representing the remaining couplings, according the averaging method of Schulten and Bittl [154]. The calculation failed, but only because the 32 GB of random-access memory on the computational node was insufficient.

A possible follow-up would be to simulate the radical pair by propagating the spin system and calculating the singlet yield by numerical integration, rather than diagonalization of the Hamiltonian. This would allow the usage of sparse linear algebra routines, significantly lowering the memory requirements for the computation. Such routines could not be used with the methodology of the current work, as MATLAB's eigenvalue solver function `eig()` accepts only dense matrices. The propagation and integration approach would also allow unequal singlet/triplet decay rate constants, and would allow calculation of the effect of the magnetic field at

specific points in time. This would better reflect the published experimental data, where magnetic field effects have typically been reported at 200 ns after excitation [162], before the biradical has fully decayed.

Manolopoulos *et al.* [116, 106] have developed a semi-classical approach to simulating radical pair reactions with many isotropic hyperfine couplings. This approach has reproduced the experimental findings on triad K, for an isotropic solution. Work is still in progress on extending the theory to anisotropic couplings. Therefore, at the time of writing, the present work is the most comprehensive effort toward simulating the effect of anisotropic interactions on the spin dynamics of the triad K.

Chapter 3

Effect of Spin Relaxation Caused by Singlet-Tripled Dephasing on Magnetic Field Effects on Cryptochrome-based Radical Pairs

Hogben has proposed that a light-induced radical pair in the protein cryptochrome experiences rapid singlet-triplet dephasing [79, 113], due to rapid modulation of the interelectron separation. The aim of the current chapter is to clarify whether this dephasing is the dominant spin relaxation mechanism in transient absorption studies of cryptochromes. The conclusions of this chapter may also be relevant *in vivo*, as the high viscosity of a biological cell may disfavor other relaxation mechanisms based on molecular motion.

3.1 Cryptochrome and Photolyase

The current, and the following chapter, deal with *in vitro* spin relaxation in four proteins:

- Cyclobutyl pyrimidine dimer (CPD) photolyase from the bacteria *Eschicheria*

coli (*Ec*PL, UniProt P00914)

- Cryptochrome DASH from the frog *Xenopus laevis* (*Xl*Cry, UniProt Q75WS4)
- Cryptochrome 1 from the plant *Arabidopsis thaliana* (*At*Cry, UniProt Q43125)
- Cryptochrome from the fruit fly *Drosophila melanogaster* (*Dm*Cry, Uniprot O77059).

Photolyases and Cryptochromes have Homologous Structures

Photolyases and cryptochromes are flavoproteins (*i.e.* they contain a bound flavin adenine dinucleotide molecule, henceforth called FAD) that have a wide range of functions *in vivo*. All known photolyases and cryptochromes (apart from protobacterial cryptochromes [62]) share a homology region containing the non-covalently bound FAD, with an adjacent a chain of three tryptophans leading away from the FAD (**figure 3.1**). This conserved chain acts as an electron transfer pathway to and from the FAD, which plays a part in many of the different biological rôles of cryptochromes and photolyases.

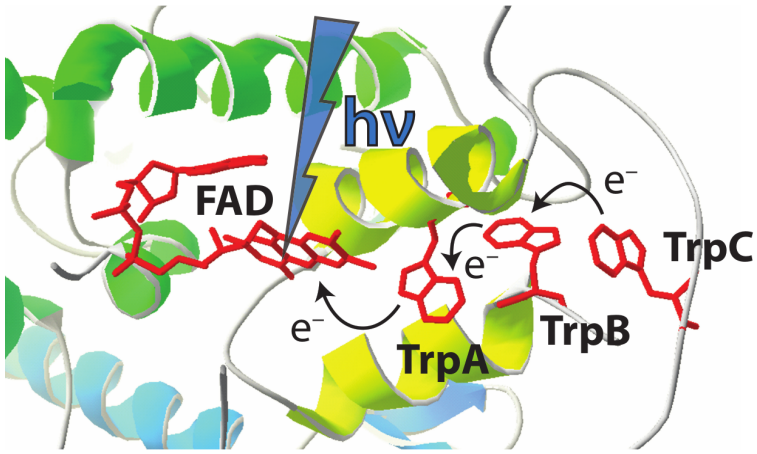

Figure 3.1: The tryptophan triad adjacent to the bound FAD molecule in *Xenopus laevis* cryptochrome DASH (UniProt Q75WS4). All of the cryptochromes and the photolyase discussed in the present work contain a similar tryptophan chain leading to the FAD binding pocket. *In vitro*, excitation of the bound FAD with blue light results in electron transfer from the tryptophan adjacent to the FAD, triggering a cascade transfer from the other two tryptophans in the triad.

CPD photolyases are understood to repair damage to deoxyribonucleic acid

(DNA) by catalyzing the monomerization of cyclobutyl pyrimidine dimers, which are formed between adjacent bases after exposure to ultraviolet light. This repair is initiated by blue light, which excites the flavin in its $FADH^-$ form, which then reduces the cyclobutyl pyrimidine dimer [24].

Some cryptochromes also effect a biological response to blue light, initiated by absorption of a photon by the FAD — for example, *Dm*Cry regulates the circadian feedback loop, due to the fact that scattered light from the sun has differing blue content different times of day [34]. In addition, many cryptochromes and photolyases contain a second ligand, 5,10-methenyltetrahydrofolate, in a separate binding pocket, which has a different excitation spectrum to FAD, and is suspected to transfer photoexcitation energy to the FAD. However, not all cryptochromes are light activated; mammalian cryptochrome, which is also a component of the central circadian clock located in the brain, is not exposed to light [67]. Instead, light is detected by the eye, and the information is sent to the central clock.

Light sensitive cryptochromes tend to accumulate in the cell nucleus, where they are activated by phosphorylation following photoexcitation [189]. They contain two domains, the photolyase homology region (PHR) containing the FAD, which is located at the N-terminus, and an unstructured C-terminus that appears to be crucial for *in vivo* function [189]. Following photoexcitation, the protein is thought to enter a signaling state by opening up and extending the C-terminus. Many of the published crystal structures of cryptochrome contain only the PHR.

*Ec*PL, *Xl*Cry, *At*Cry and *Dm*Cry have Different Functions *in Vivo*

*Ec*PL, in common with other photolyases, is known to repair damage to DNA caused by ultraviolet light. It does so by binding the photoproduct, a cyclobutane pyrimidine dimer, between adjacent nucleobases, and splitting the cyclobutane ring. This process is understood to involve blue-light initiated electron transfer involving the protein's flavin ligand [143].

Despite the structural similarity between cryptochromes and photolyases, the

primary function of the former does not appear to be DNA repair. As discussed above, cryptochromes are involved in the peripheral circadian clock in insects, and the central clock in mammals. Cryptochrome DASH is a poorly understood group, which is based on structural similarity, and is named after the first species in which it was found (*Drosophila*, *Arabidopsis*, *Synechocystis* and *Human*). Very little is known about the biological function of CryDASH; however, it is speculated to be a transcriptional regulator due to its non-specific DNA binding activity. Both *Xenopus* and *Synechocystis* cryptochrome DASH have shown weak DNA repair ability when expressed in *E. coli*, presumably due their structural similarity to photolyase [35].

*At*Cry is a blue-light photoreceptor that regulates a wide variety of biological processes, including circadian rhythms and tropic growth [189]. In addition, the conserved tryptophan triad appears to be play a part in the photoreduction of the FAD in the cell environment. However, the photoreduction also occurs if the triad is mutated to redox-inactive phenylalanine, albeit at a slower rate, possibly due to the presence of metabolites in the cell [41].

*Dm*Cry is a blue light receptor found in fruit files [40], and is responsible for the oscillation of peripheral circadian clocks. It is thought to do so by repressing the transcription of certain DNA sequences, in response to blue light [34]. The protein has been postulated to be essential for magnetoreception in flies [61], and work is ongoing to clarify the mechanism [47]. *Dm*Cry is distinct from the other three proteins in that it has a tetrad of tryptophans leading to its FAD binding pocket, rather than a triad [134]. The fourth tryptophan appears to be conserved in animal cryptochromes (except for the DASH type) [129].

Cryptochromes have also been proposed to play a rôle in magnetoreception

Evidence for this rôle has been observed in *D. Melanogaster*, where electromagnetic fields have been found to disrupt geotaxis, but not in mutants lacking cryptochrome [47]. Furthermore, four different types of cryptochrome has been found in the eye of

migratory birds. These species are well established to rely on the geomagnetic field for navigation, but can only do so when their eyes are uncovered [125]. Studies *in vitro* have found that a magnetic field can alter the singlet recombination yield of a photogenerated radical pair in *Ec*PL and *At*Cry [113], but as yet no evidence has been found for an anisotropic response at the geomagnetic field strength. No other protein found in the eye of birds has shown a magnetic field effect *in vitro*.

3.2 *In Vitro* Photochemistry of Cryptochromes

Much work has been done to elucidate the photochemistry of cryptochromes. It is well established that the FAD bound in cryptochromes, when in its fully oxidized state, can be excited by blue light, which triggers the formation of a spacially separated radical pair [63, 16, 21, 81, 134]. This occurs by electron transfer to FAD along the conserved chain of tryptophans (**figure 3.1**, p. 70) to create a $FAD^{\bullet-}$ $TrpH^{\bullet+}$ radical pair (RP1). This radical pair can either recombine to the ground state, or react to form a longer lived radical pair (RP2, **figure 3.2**).

In most cryptochromes investigated to date, RP2 represents $FAD^{\bullet-}$ $Trp^{\bullet}$, formed by deprotonation of $TrpH^{\bullet+}$. This is often assumed to be proton loss to the surrounding solvent, but it has also been suggested that $TrpH^{\bullet+}$ could be deprotonated by a neighboring histidine residue [81].

In *At*Cry, in addition to the deprotonation of of the tryptophan radical, $FAD^{\bullet-}$ reacts with an adjacent aspartic acid residue [101, 169]:

$$FAD^{\bullet-} + AspH \longrightarrow FADH^{\bullet} + Asp^{-}$$

This protonation of the flavin does not occur in the other three proteins studied in this thesis, due to the lack of an aspartic acid residue and other unclear structural differences [128]. Naturally, the tryptophan radical in *At*Cry also loses a proton to the solvent, leading to a long-lived $FADH^{\bullet}$ $Trp^{\bullet}$ radical pair (RP2). The faster of the two proton transfers depends on experimental conditions [113, 127]. From a spin-

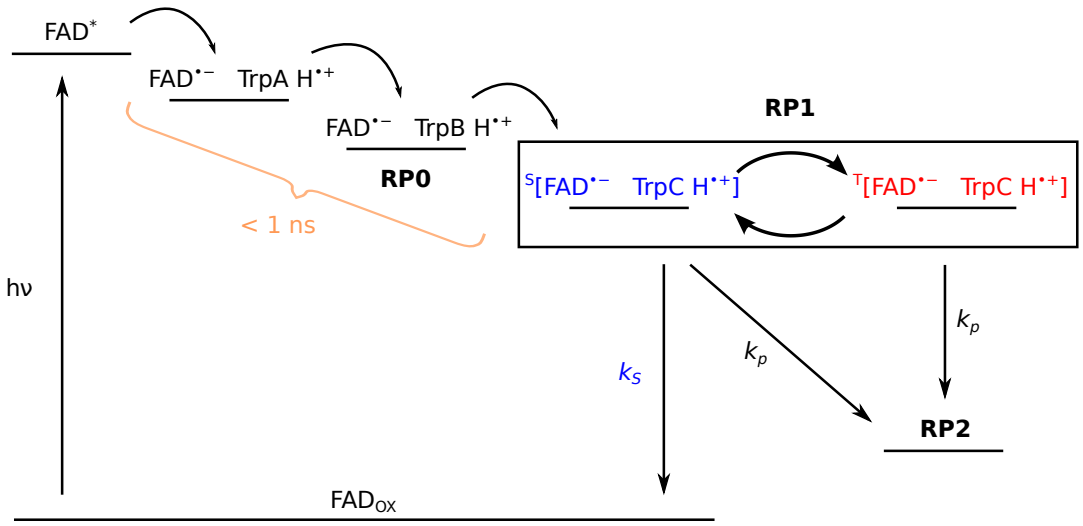

Figure 3.2: Reaction scheme for the radical pair found in cryptochromes and photolyases, following excitation of the fully oxidized FAD with blue light. RP1 indicates the starting radical pair for all simulations in this chapter, with a lifetime of $\sim 1\,\mu s$. RP2 is a much longer lived radical pair ($> 100\,\mu s$), formed by deprotonation of $TrpH^{\bullet+}$ and/or protonation of $FAD^{\bullet-}$ with rate constant k_p. The rate constant k_s represents recombination of the radical pair to the ground state, and is only possible when RP1 is in a singlet state. RP0 was included implicitly in simulations by means of singlet-triplet dephasing.

chemistry perspective, the nature of the proton transfer step is largely irrelevant, as both types represent a non-spin selective conversion to a secondary, long-lived, radical pair.

Experimental evidence suggests that the $FAD^{\bullet-}$ $TrpH^{\bullet+}$ radical pair has an initial singlet state in both *Xl*Cry and *Ec*PL [74, 16], indicating that electron transfer is much faster than intersystem crossing in the excited FAD^{*}. The assumption of an initial singlet state was applied to all cryptochrome radical pairs discussed in this thesis.

It is important to note that the *in vitro* photochemistry does not necessarily correspond to that found *in vivo*, due to the presence of additional biochemical molecules in the cell [41]. Therefore caution must be taken not to overinterpret the results presented in the current work.

3.3 Cryptochrome and Avian Magnetoreception

Cryptochrome has been postulated to be the part of a magnetoreception system, located in the eye of birds. According to this theory, the direction of the earth's magnetic field would affect the reaction products of a radical pair created by absorption of blue light [152]. Moreover, cryptochrome has been found in the retina of garden warblers [126], European robins, and chickens [133], however a signal transduction chain has yet to be discovered.

Spin-relaxation considerations suggest that $FAD^{\bullet-}$ $TrpH^{\bullet+}$ is not a good candidate for a biological magnetoreceptor, due to libration of the tryptophan's indole ring [91]. Alternative radical pairs have been proposed that are composed of $FAD^{\bullet-}$ and superoxide (as the latter has no hyperfine couplings), or of $FAD^{\bullet-}$ and an ascorbic acid radical (as the latter has weak hyperfine couplings) [104]. The viability of the former radical pair has been questioned, due to the large spin-orbit coupling in superoxide. This coupling is expected to rapidly change in directionality and magnitude, due to molecular motion of the superoxide, and therefore quickly induce spin-relaxation [79].

Recent studies have suggested that broadband radio frequencies, with nT amplitude, can disrupt the European robin's ability to use its magnetic compass [43, 155]. This does not appear to be a resonance effect, as two separate excitation bands (0 to 500 kHz, and 0.5 to 3 MHz) had the same disorienting effect. This broadband effect can be reconciled with the radical pair mechanism of magnetoreception as long as the lifetime of the radical pair exceeds 100 µs [59, 76].

An alternative theory of magnetoreception involves nanoparticles of magnetite. Experimental evidence supports the existence of a magnetite-based intensity sensor in night-migratory songbirds, possibly in addition to a radical-pair based compass sensor [152]. A ferromagnetic resonance theory exists that could arguably [96, 13] explain the broadband radio frequency effect discussed above; however, this theory does not include a detailed mechanism beyond heating of the nanoparticle, and has

limited experimental evidence [28].

3.4 The Spin System of the Radical Pair in Cryptochrome

All simulations started from the radical pair with one unpaired electron in FAD, and the second unpaired electron in the terminal tryptophan. The initial spin state was assumed to have 100 % singlet character. Exchange and dipolar interactions were assumed to be negligible at the separation of flavin and terminal tryptophan ($\sim 1.9\,\mathrm{nm}$), While there has been no direct measurement of these two parameters, fitting of EPR measurements on *Xl*Cry suggest $D = -0.36\,\mathrm{mT}$ and $J = 0.24\,\mathrm{mT}$ [16], such that they may cancel out [39]. These two interactions have been calculated to be negligible with configuration interaction singles theory [83]; however, the calculation omitted much of the protein surrounding the radical pair, so its accuracy is questionable. The only interaction included explicitly was the hyperfine interaction between each unpaired electron and its surrounding nuclei.

For the purposes of the current chapter, the spin system was assumed to be isotropic, as one would expect if anisotropic hyperfine couplings were effectively averaged by rotational tumbling. The isoalloxazine ring of the $\mathrm{FAD}^{\bullet-}$ radical has 13 nuclei with non-zero nuclear spin. The $\mathrm{TrpH}^{\bullet+}$ radical has 14 such nuclei. It is not possible to fully simulate such a large spin system with currently available technology, therefore a reduced set of hyperfine couplings was used.

For an isotropic system, a useful approximation is to combine several hyperfine couplings into an effective coupling [154, 88]. In a given radical, a set of N nuclear spins is commonly represented by a single nucleus with spin $\tilde{I}$ and hyperfine coupling

$$\tilde{a}^2 = \frac{1}{\tilde{I}(\tilde{I}+1)} \sum_{i=1}^{N} a_i^2 \, I_i(I_i+1)\,. \tag{3.1}$$

This formula was originally proposed by Schulten and Bittl [154], as it was found

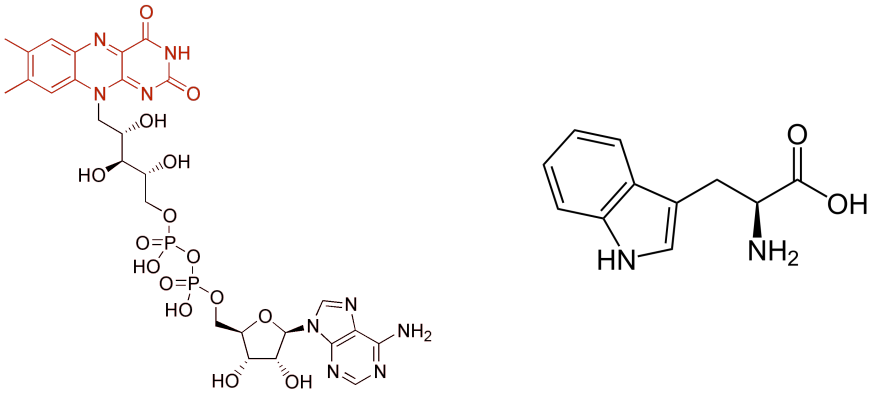

(a) (b)

Figure 3.3: a) The flavin adenine dinucleotide (FAD) that is bound inside the cryptochromes and photolyase discussed in the current work. The isoalloxazine ring, which is the host to the unpaired electron in $FAD^{\bullet-}$ [109], is shown in red. b) The amino acid tryptophan, which hosts the second unpaired electron in the radical pair investigated in the current chapter.

to reproduce the triplet probability of a full spin system at short and intermediate timescales. The approximation appears to work reasonably well for fitting experimental data [88], and does not entail the difficulties in approximating an anisotropic spin system discussed in **chapter 2**.

Hyperfine couplings were calculated by Ilya Kuprov [149] using the unrestricted B3LYP functional and the EPR-III basis set, after geometry optimization with the restricted open-shell B3LYP functional and a gaussian basis set. The $FAD^{\bullet-}$ was approximated by a flavin with a methyl group replacing the adenine dinucleotide moiety. The specific couplings used to simulate the $FAD^{\bullet-}$ $TrpH^{\bullet+}$ radical pair are shown in **table 3.1**.

3.5 The MARY Experiment

Magnetically Altered Reaction Yield (MARY) is an experiment, typically performed with absorption or fluorescence spectroscopy, where the signal in the presence of a magnetic field is compared to the signal in zero field. MARY curves, as a function of field strength, often have a Lorentzian shape [171, 88, 161] (if any low field effect is ignored). A MARY curve can be summarized by the saturation high field

Table 3.1: Hyperfine couplings used in all simulations in the current chapter. The couplings were calculated using density functional theory [149]. The largest individual hyperfine couplings in each radical were included, and the rest were included as an effective coupling constant $\tilde{a}$, one for each radical (equation 3.1). The effective coupling in $FAD^{\bullet-}$ was calculated over twelve nuclei, the effective coupling in $TrpH^{\bullet+}$ also over twelve nuclei, according to equation 3.1.

Radical	Nucleus	HFI [mT]	HFI [s^{-1}]
$FAD^{\bullet-}$	N	0.5233	9.215×10^7
	$\tilde{a}$ ($\tilde{I} = 1/2$)	1.1065	1.948×10^8
$TrpH^{\bullet+}$	H	1.6046	2.826×10^8
	H	−0.5983	-1.054×10^8
	$\tilde{a}$ ($\tilde{I} = 1/2$)	0.9157	1.612×10^8

effect (HFE_{max}), the linewidth at half saturation ($B_{1/2}$), and the maximum low field effect (LFE_{max}). An example MARY curve is shown in **figure 3.4**, with a visual description of these three parameters.

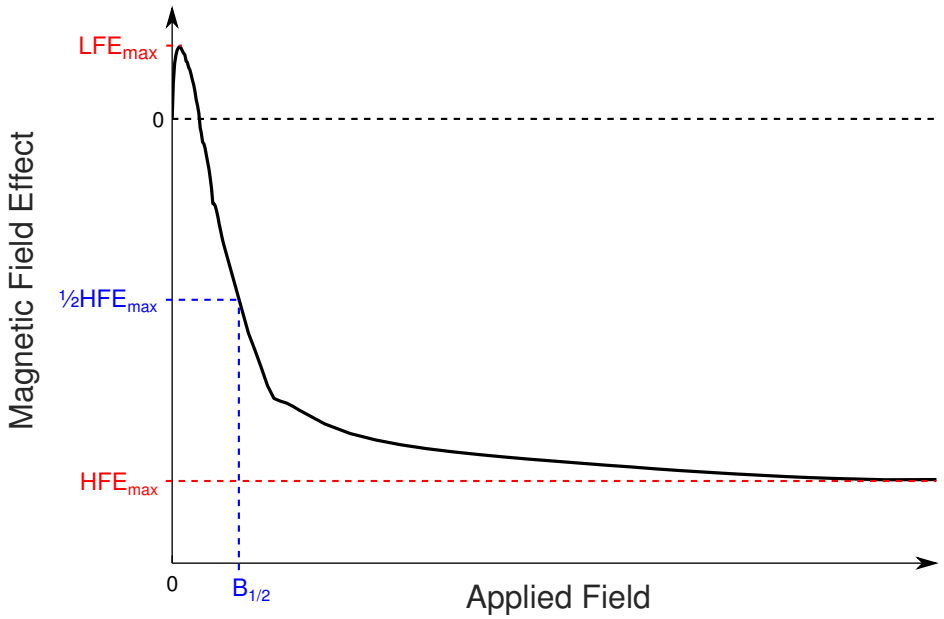

Figure 3.4: An example MARY curve calculated for a $FAD^{\bullet-}$ $TrpH^{\bullet+}$ radical pair, showing the maximum low field effect (LFE_{max}), the saturation high field effect (HFE_{max}), and the linewidth parameter $B_{1/2}$ (the applied field at which the magnetic field effect is $\frac{1}{2}\,HFE_{max}$).

The experimental MARY curves presented in the current work were measured by transient absorption, unless indicated otherwise. Data were collected by T. Biskup, K. Maeda, A. Robinson and K. Henbest. The fully oxidized flavin, FAD_{OX}, was excited with a 460 nm laser flash, and the probe wavelength was 510 nm, corresponding

to the transient signal from RP2. These magnetic field effects were measured after the complete decay of RP1, and were expressed as a percentage

$$\Gamma(B_0) = \frac{\Delta A(B_0) - \Delta A(0)}{\Delta A(0)} \times 100\,, \tag{3.2}$$

where $\Delta A(B_0)$ is the transient absorption signal at 510 nm, at magnetic field strength B_0.

Magnetic field effects were simulated by first calculating the fractional yield of RP2 (versus recombination to the ground state), Φ_2, and then calculating the percentage

$$\Gamma(B_0) = \frac{\Phi_2(B_0) - \Phi_2(0)}{\Phi_2(0)} \times 100\,. \tag{3.3}$$

3.6 Radical Pair Reactivity

As discussed in the introductory chapter, the time evolution of the density matrix in Liouville space follows

$$\frac{d\vec{\rho}}{dt} = -i\hat{\hat{H}}\vec{\rho} - \hat{\hat{K}}\vec{\rho} - \hat{\hat{R}}\vec{\rho} \tag{3.4}$$

where $\hat{\hat{H}}$, $\hat{\hat{K}}$ and $\hat{\hat{R}}$ are the Hamiltonian, reactivity and relaxation superoperators, respectively. The reactivity superoperator can be separated into two parts,

$$\hat{\hat{K}} = \hat{\hat{K}}_s + \hat{\hat{K}}_p\,, \tag{3.5}$$

where $\hat{\hat{K}}_s$ represents recombination to the ground state, and $\hat{\hat{K}}_p$ represents the formation of RP2. As the latter process is not spin-selective, $\hat{\hat{K}}_p$ was chosen to be proportional to the identity matrix,

$$\hat{\hat{K}}_p = k_p\,\hat{\hat{\mathbb{1}}}\,. \tag{3.6}$$

For singlet recombination, Haberkorn's kernel [71] was used, where

$$\hat{\hat{K}}_s = \frac{k_s}{2}\left(\hat{P}_S\hat{\rho} + \hat{\rho}\hat{P}_S\right) \tag{3.7}$$

in which $\hat{P}_S$ is the singlet projection operator. This has the effect of decaying the singlet population, $\langle S|\,\hat{\rho}\,|S\rangle$, with a rate constant of k_s, and off-diagonal elements ($\langle S|\,\hat{\rho}\,|T\rangle$ and $\langle T|\,\hat{\rho}\,|S\rangle$), corresponding to a coherent superposition of singlet and triplet states, with a rate constant of $\frac{k_s}{2}$. This decay of coherences is known as singlet-triplet dephasing, and can be thought of as individual spin systems in the ensemble "collapsing" into singlet or triplet states. This dephasing has the effect of changing the initial pure electronic state into a mixed state, where different components of the ensemble have different spin states.

Although other reactivity superoperators have been proposed that are based on quantum measurement theory [86], experiments suggest that Haberkorn's treatment is the most appropriate for the cryptochrome radical pair [112]. Furthermore, theoretical justification, both from an orthodox standpoint [82] and from a quantum information standpoint [29], exists in favor of Haberkorn's method.

Considering a stationary quantum state

$$|\psi\rangle = \begin{pmatrix} a \\ b \end{pmatrix},$$

where the amplitude of

$$|\alpha\rangle = \begin{pmatrix} 1 \\ 0 \end{pmatrix}$$

decays with a rate constant of k, the time dependence

$$|\psi(t)\rangle = \begin{pmatrix} ae^{-kt} \\ b \end{pmatrix}.$$

Converting the above state to a density matrix representation,

$$\begin{aligned}\hat{\rho}(t) &= |\psi(t)\rangle \langle\psi(t)| \\ &= \begin{pmatrix} ae^{-kt} \\ b \end{pmatrix} \begin{pmatrix} a^* e^{-kt} & b^* \end{pmatrix} \\ &= \begin{pmatrix} |a|^2 e^{-2kt} & ab^* e^{-kt} \\ a^* b e^{-kt} & |b|^2 \end{pmatrix} .\end{aligned}$$

The off-diagonal elements decay at half the rate of the diagonal elements, which is identical to Haberkorn's kernel.

3.7 Singlet-Triplet Dephasing due to Exchange Interaction

Shushin has demonstrated that a radical pair whose separation is modulated as a function of time experiences a dephasing effect [157]. His original formulation assumed two states with different separation between the unpaired electrons: a distant state, where the exchange interaction J_1 is negligible (here called RP1), and a contact state, where the exchange interaction J_0 is large (here called RP0). The radical pair therefore hops between states according to

$$\mathrm{RP0} \underset{k_{10}}{\overset{k_{01}}{\rightleftharpoons}} \mathrm{RP1} \tag{3.8}$$

Assuming that the exchange interaction in the contact state

$$|J_0| \gg k_{01} \gg k_{10} \,, \tag{3.9}$$

such that significant spin evolution occurs under the exchange interaction in the contact RP_0 state, then singlet-triplet dephasing occurs with rate

$$k_{\mathrm{STD}} = k_{10} \,.$$

The dephasing superoperator in Hilbert space is then

$$\hat{\hat{R}} = k_{\mathrm{STD}} \left(\hat{P}_S \hat{\rho} \hat{P}_T + \hat{P}_T \hat{\rho} \hat{P}_S \right) , \tag{3.10}$$

where $\hat{P}_T$ is the triplet projection operator.

Singlet-triplet dephasing may be the reason why there have been difficulties measuring low field effects in cryptochromes and photolyases. If sufficiently rapid, the dephasing greatly reduces the low field effect, as it destroys any coherence between the singlet and triplet states, ultimately preventing singlet-triplet interconversion. Simulations suggest that, for the $\mathrm{FAD}^{\bullet -}$ $\mathrm{TrpH}^{\bullet +}$ radical pair, dephasing rates up to $10^7\,\mathrm{s}^{-1}$ allow the initial coherent conversion from singlet to triplet state, but that further coherent oscillations are damped (**figure 3.5**).

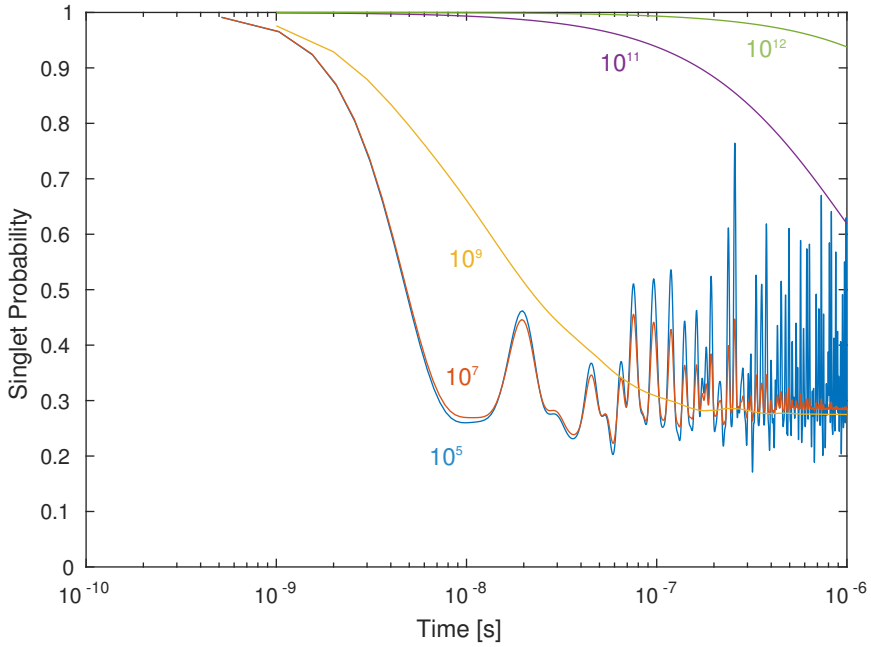

Figure 3.5: Effect of singlet-triplet dephasing on the singlet probability as a function of time in a simplified $\mathrm{FAD}^{\bullet -}$ $\mathrm{TrpH}^{\bullet +}$ radical pair. The dephasing rate constant, k_{STD}, is displayed next to the corresponding curve, with units of s^{-1}. Parameters: $B_0 = 0$, $k_s = k_p = 0$.

The Liouville-von Neumann equation (**equation 1.41**, p. 27) indicates that there is negligible direct population transfer between diagonal elements of the density matrix at a small enough timestep. Instead, population transfer relies on the development of off-diagonal coherences in the density matrix. Considering a den-

sity matrix in the singlet-triplet basis, the dephasing causes off-diagonal elements to decay, so there is competition between the latter and coherent population transfer. Even when $k_{\mathrm{STD}} < \tilde{a}$ (where $\tilde{a}$ is the average hyperfine coupling in RP1), the dephasing can halt singlet-triplet interconversion at long enough timescales (**figure 3.6**). Dephasing rates much larger than the magnitude of the hyperfine coupling ($\gg 10^8\,\mathrm{s}^{-1}$) effectively halt singlet to triplet population transfer, akin to the quantum Zeno effect [122].

In the absence of singlet-triplet dephasing, a weak magnetic field dampens the oscillations in the singlet-triplet probability (**figure3.6.a**). The net result is a reduction in the time-average of the singlet probability in the presence of the magnetic field. When dephasing is active, singlet-triplet interconversion is damped at any field strength, meaning that a weak field has a much smaller effect than in the absence of dephasing (**figure 3.6.b**).

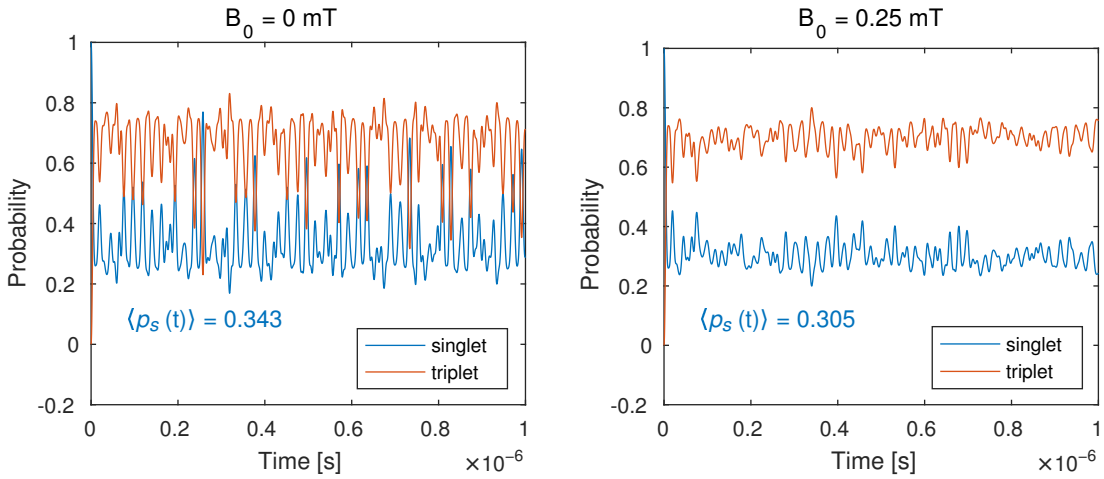

(a) $k_{\mathrm{STD}} = 0$

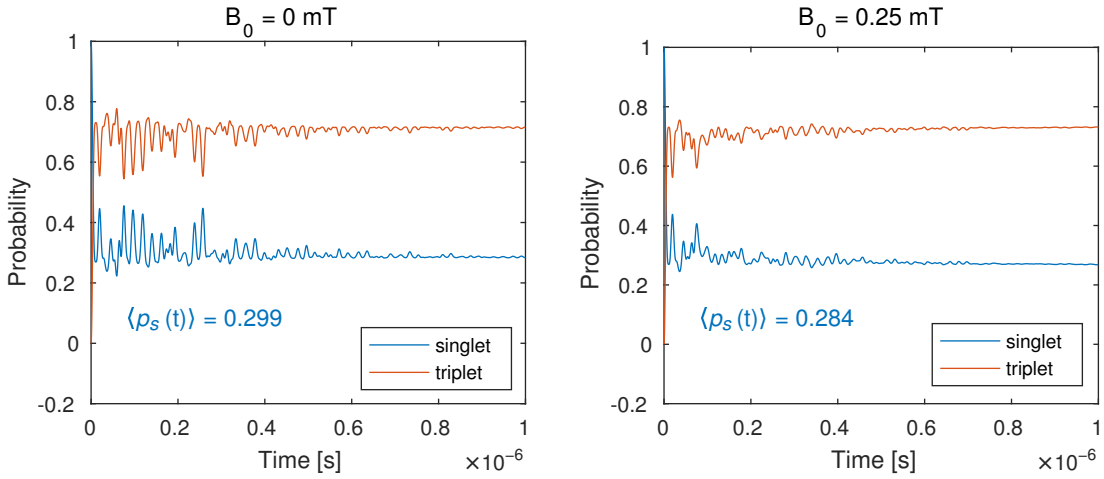

(b) $k_{\mathrm{STD}} = 10^7\,\mathrm{s}^{-1}$

Figure 3.6: Simulation of time evolution of electronic singlet and triplet probabilities for the simplified $\mathrm{FAD}^{\bullet-}$ $\mathrm{TrpH}^{\bullet+}$ radical pair described in table 3.1, showing the effect of singlet-triplet dephasing. The initial singlet probability was 1, and in all cases evolved to ~ 0.3 within $10^{-8}\,\mathrm{s}$. $k_s = k_p = 0$.

3.8 Effect of Rate Constants on MARY shape

As discussed by Hogben [78, 113], increasing the singlet-triplet dephasing rate increases the MARY linewidth, all other parameters being constant (**figure 3.7**). There is also an increase in $\mathrm{HFE}_{\mathrm{max}}$ with k_{STD}, however this effect is not particularly large at the dephasing rates discussed in the current chapter ($\sim 10^7\,\mathrm{s}^{-1}$).

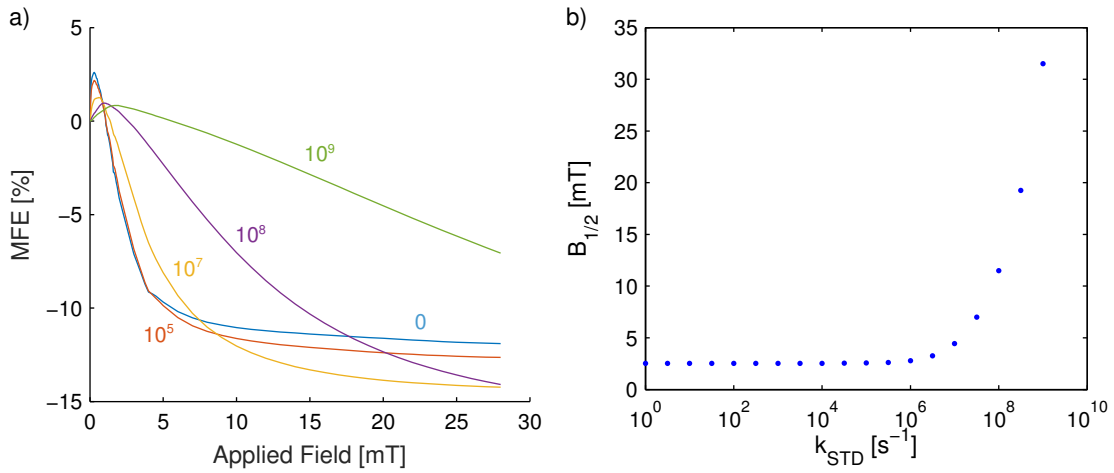

Figure 3.7: Effect of varying singlet-triplet dephasing rate, with k_s and k_p fixed, for the simplified $\mathrm{FAD}^{\bullet-}$ $\mathrm{TrpH}^{\bullet+}$ radical pair. a) Simulated MARY curves, with the corresponding k_{STD} indicated above the curve in s^{-1} units. b) MARY linewidth (in terms of $B_{1/2}$) as a function of k_{STD}. $B_{1/2}$ was determined by fitting the curves in (a) to a piecewise polynomial. Parameters: $k_s = k_p = 10^6\,\mathrm{s}^{-1}$.

The ratio $\frac{k_s}{k_p}$ also has a large effect on the shape of the MARY curve (**figure 3.8**). Increasing $\frac{k_s}{k_p}$ results in a larger MARY linewidth. This effect is presumably due to the same mechanism that increases linewidth with increasing k_{STD}, as singlet recombination inherently entails singlet-triplet dephasing.

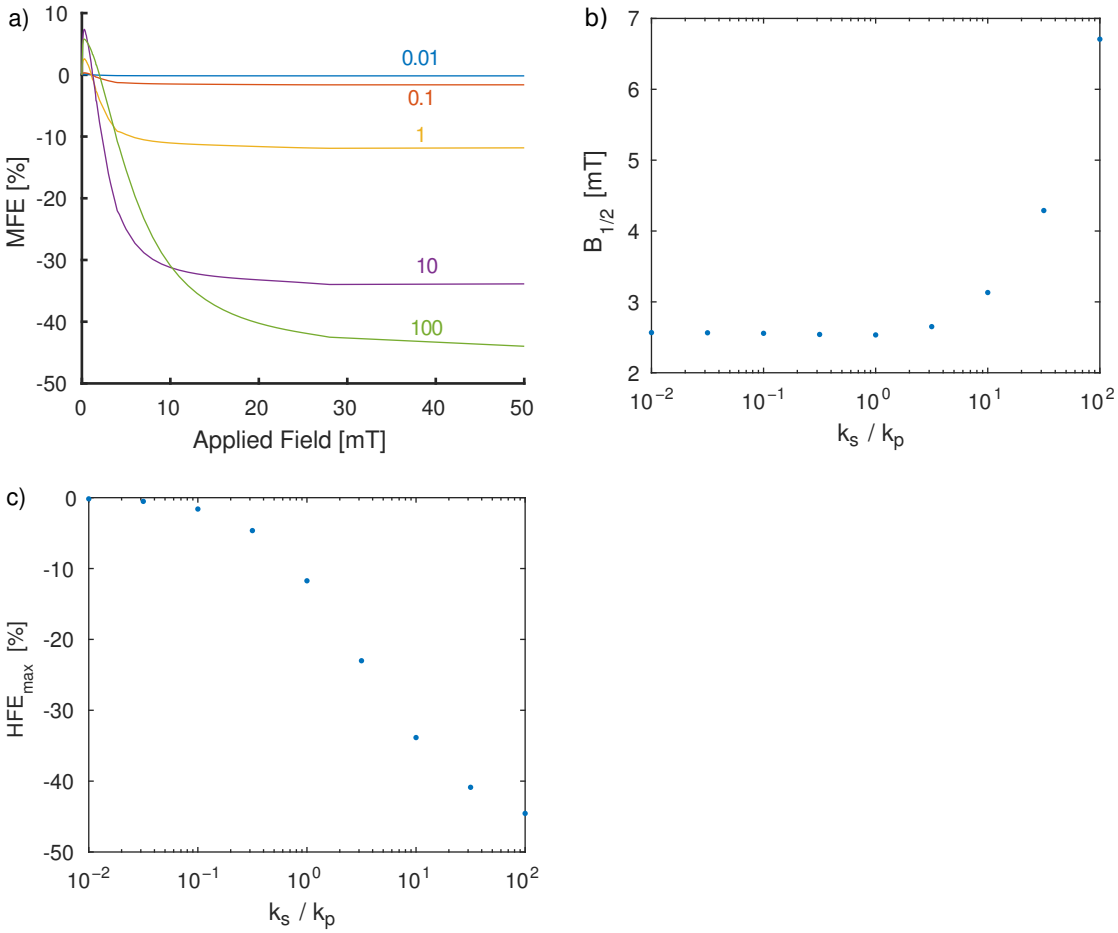

Figure 3.8: Effect of varying the ratio $\frac{k_s}{k_p}$, in the absence of singlet-triplet dephasing, for the simplified $FAD^{\bullet -}$ $TrpH^{\bullet +}$ radical pair. a) MARY curves; the ratio is displayed above the corresponding curve. b) Linewidth of MARY curves. c) Saturation high field effect. Parameters: $k_{\mathrm{STD}} = 0$, $k_s + k_p = 2 \times 10^6\,\mathrm{s}^{-1}$.

Furthermore the magnitude of $\mathrm{HFE}_{\mathrm{max}}$ increases sharply with $\frac{k_s}{k_p}$. This effect can be understood by considering a simplified system with constant singlet recombination rate constant κ_s, that does not depend on the quantum state of RP1. Considering a simple branched reaction scheme,

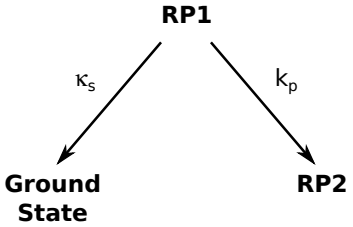

then the fractional yield of RP2,

$$\Phi_2 = \frac{k_p}{\kappa_s + k_p}\,. \tag{3.11}$$

If we now take κ_s to represent an average singlet recombination rate constant, as one would observe experimentally,

$$\kappa_s \approx k_s \left\langle p_s(t) \right\rangle_{\text{time}}, \tag{3.12}$$

where $p_s(t)$ is the singlet probability at time t.

At zero field, assuming efficient singlet-triplet interconversion (by coherent or incoherent evolution), one would expect

$$\kappa_s \approx 0.25\, k_s\,, \tag{3.13}$$

due to the similarity in energy of the singlet and triplet electronic states. This gives

$$\Phi_2(0) \approx \frac{k_p}{0.25\, k_s + k_p}\,. \tag{3.14}$$

Assuming that at high field, the $T_\pm$ states are energetically isolated from the S state, such that the only interconversion is $S \leftrightarrow T_0$,

$$\kappa_s \approx 0.5\, k_s\,, \tag{3.15}$$

giving, at high field saturation,

$$\Phi_2(\infty) \approx \frac{k_p}{0.5\, k_s + k_p}\,. \tag{3.16}$$

As the experimental results in this chapter represent

$$\Gamma(B_0) = \frac{\Phi_2(B_0) - \Phi_2(0)}{\Phi_2(0)} \times 100\,\%\,, \tag{3.17}$$

the approximate saturation high field effect

$$\mathrm{HFE}_{\max} = \Gamma(\infty) \approx -\frac{0.25\, k_s}{0.5\, k_s + k_p} \times 100\,\% \,. \tag{3.18}$$

This gives us two limiting cases,

$$\Gamma(\infty) = -\frac{k_s}{4\, k_p} \times 100\,\% \,, \quad k_p \gg k_s \,,$$

and

$$\Gamma(\infty) = -50\,\% \,, \quad k_s \gg k_p \,.$$

It is important to state that, although the largest percentage effect predicted by this formula and observed in simulations (**figure 3.8.c**) is when $k_s \gg k_p$, it would be very difficult to actually measure the effect under these conditions. This is because $\Phi_2 \approx 0$ (**equation 3.16**), so small changes in Φ_2 result in a large percentage effect, even though the absolute change is small.

3.9 Previous Fitting of Experimental Data

Hogben has fitted MARY curves measured for *Ec*PL (50 % glycerol, 260 K, pH 7.5) and *At*Cry (60 % glycerol, 270 K, pH 7.5) to the singlet-triplet dephasing model [78, 113]. Her results suggest a singlet-triplet dephasing rate of $k_{\mathrm{STD}} \approx 10^7\,\mathrm{s}^{-1}$ in both systems. This corresponds to a hopping process within the protein according to **figure 3.9**.

To the knowledge of the author, no published work has fully determined the electron transfer kinetics in *At*Cry. However, based on femtosecond spectroscopy measurements on several mutants of *Ec*PL, Liu has determined [109]

$$k_{01} \approx 6.6 \times 10^9\,\mathrm{s}^{-1}$$

$$k_{10} \approx 1 \times 10^7\,\mathrm{s}^{-1} \,.$$

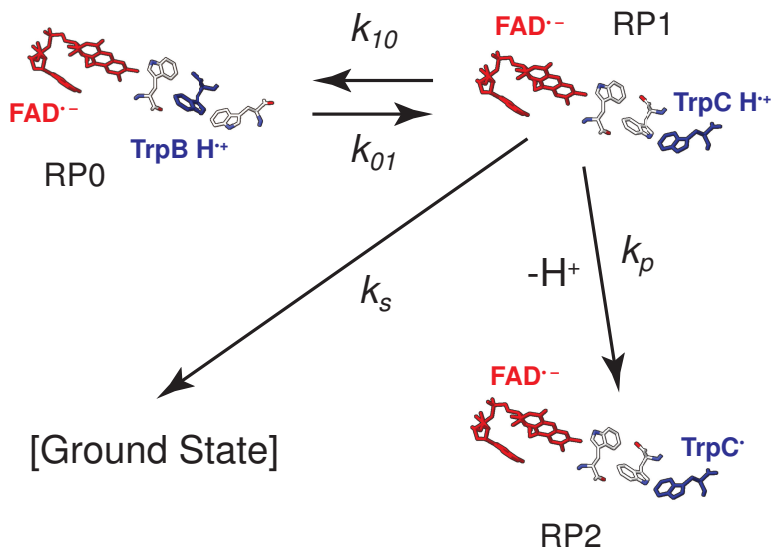

Figure 3.9: Possible electron hopping between TrpB and TrpC in the cryptochrome/photolyase radical pair. Experimental studies suggest that RP1 is far more stable than RP0, making $k_{01} \gg k_{10}$ [109, 16].

With these rate constants, Shushin's dephasing model holds, giving

$$k_{\mathrm{STD}} = k_{10} \approx 10^7\,\mathrm{s}^{-1}$$

as long as RP0 experiences an exchange interaction

$$|J| \gg k_{01}\,.$$

Unfortunately, there is no direct experimental evidence of the magnitude of the exchange interaction in RP0. Therefore, it is not currently possible to ascertain with great certainty that the electron hopping entails singlet-triplet dephasing, even though Liu's results suggest that significant electron back hopping does occur during the lifetime of RP1.

3.10 Fitting Experimental MARY Curves Using Bayesian Probability

Rate constants k_s, k_p and k_{STD} were estimated by fitting experimental MARY curves to the singlet-triplet dephasing model, using Bayes' approach to probability. Sivia argues that when dealing with properties that vary over a wide range of magnitudes, such as rate constants, a log-normal distribution is appropriate [158]. This is equivalent to treating the logarithm of the rate constant as being normally distributed. Therefore we define new parameters

$$\begin{aligned} \chi_s &= \log_{10} k_s \\ \chi_p &= \log_{10} k_p \\ \chi_{\mathrm{STD}} &= \log_{10} k_{\mathrm{STD}} \,, \end{aligned} \tag{3.19}$$

which we represent together vectorially with $\vec{\chi}$. The posterior probability distribution for $\vec{\chi}$, given the experimental data, follows the proportionality

$$p\left(\vec{\chi} \,|\, \{d_i\}, I\right) \propto p\left(\{d_i\} \,|\, \vec{\chi}, I\right) \times p\left(\vec{\chi} \,|\, I\right) \,, \tag{3.20}$$

where $\{d_i\}$ represents the set of experimentally collected data, I represents any background knowledge, and $p\left(\vec{\chi} \,|\, I\right)$ is the prior probability distribution of $\vec{\chi}$. No previous knowledge of $\vec{\chi}$ was assumed, so the prior probability was taken to be a constant. This is equivalent to assuming that χ_s, χ_p and χ_{STD} each have an initial uniform distribution. We therefore reduce **equation 3.20** to

$$p\left(\vec{\chi} \,|\, \{d_i\}, I\right) \propto p\left(\{d_i\} \,|\, \vec{\chi}, I\right) \,. \tag{3.21}$$

Taking the logarithm of the right hand side, we define the *logarithmic likelihood function*,

$$L = \ln\left[\, p\left(\{d_i\} \,|\, \vec{\chi}, I\right)\right] \,. \tag{3.22}$$

Assuming that each experimental datapoint d_i is sampled from a normal distribution, with experimentally determined uncertainty, σ_i, about the true value, $\mu_i(\vec{\chi})$, determined by the true rate constants, $\vec{\chi}$,

$$\begin{aligned} L &= \ln\left(\prod_i^n \frac{1}{\sigma_i\sqrt{2\pi}} \exp\left[-\frac{(d_i-\mu_i(\vec{\chi}))^2}{2\sigma_i^2}\right]\right) \\ &= C - \sum_i^n \frac{(d_i-\mu_i(\vec{\chi}))^2}{2\sigma_i^2} \end{aligned} \tag{3.23}$$

for a set of n experimental measurements. Although we do not know the true rate constants, $\vec{\chi}$, we can find their best estimates by maximizing the log-likelihood function.

The fitting was carried out with MATLAB's `lsqnonlin()` function, which uses a trust-region reflective algorithm based on Newton's method [32, 33] to minimize a non-analytic function. As with conventional least squares, the trust-region reflective algorithm solves problems of the type

$$\min_x ||f(x)||^2 = \min_x \left(f_1(x)^2 + f_2(x)^2 + \cdots + f_n(x)^2\right) , \tag{3.24}$$

for a set of n experimental datapoints and a fitting parameter, x. For the present purposes, we substitute

$$f_i(x)^2 \to f_i(\vec{\chi})^2 = \frac{(d_i-\mu_i(\vec{\chi}))^2}{2\sigma_i^2} , \tag{3.25}$$

and the minimum found by `lsqnonlin()` is the maximum of the likelihood function due to a sign change we have inserted in $f_i(\vec{\chi})$.

For this minimization, d_i was chosen to be the mean experimental magnetic field effect at the i^{th} applied field strength, expressed as a percentage. The uncertainty, σ_i, was chosen to be the standard error of the magnetic field effect, while $\mu_i(\vec{\chi})$ was the simulated magnetic field effect with rate constants $\vec{\chi}$.

In addition, the lifetime of the radical pair was constrained to the experimental decay rate. This was done by including $f_D(\vec{\chi})$ as a term to be minimized, with the

same form as **equation 3.25**, but with

$$d_D = k_{\text{exp}} \,,$$

the experimentally determined decay rate of RP1 at zero applied field, with a corresponding (experimentally determined) uncertainty, σ_D. The overall decay rate according to the theoretical model, $\mu_D(\vec{\chi})$, was simulated by propagating of the spin system, and fitting the decay of the trace of the density matrix to an exponential.

The maximum likelihood rate constants, $\vec{\chi}_0$, were thereby estimated using both experimental magnetic field effects and the decay kinetics.

3.11 Uncertainty of Fitted Rate Constants

The uncertainty in the fitted rates was determined assuming a multivariate Gaussian posterior,

$$p(\vec{\chi} \,|\, d_i, I) = |2\pi\mathbf{\Sigma}|^{-\frac{1}{2}} \exp\left[-\frac{1}{2}(\vec{\chi} - \vec{\chi}_0)^{\mathrm{T}}\mathbf{\Sigma}^{-1}(\vec{\chi} - \vec{\chi}_0)\right] . \tag{3.26}$$

Under this assumption, we can estimate the uncertainty in the fitted rate constants using the covariance matrix, $\mathbf{\Sigma}$. The Hessian matrix of second derivatives (with respect to $\vec{\chi}$), taken of the logarithm of the multivariate Gaussian, is related to the covariance matrix by

$$\mathbf{\Sigma} = -\left[\nabla\nabla \log\left(p(\vec{\chi} \,|\, d_i, I)\right)\right]^{-1} , \tag{3.27}$$

where $\nabla\nabla$ is the Hessian operator.

According to the proportionality in **equation 3.21**, the posterior probability is proportional to the likelihood function (**equation 3.23**), giving

$$\log\left(p(\vec{\chi} \,|\, d_i, I)\right) = C' - \sum_i^n \frac{(d_i - \mu_i(\vec{\chi}))^2}{2\sigma_i^2} \,, \tag{3.28}$$

where C' is some constant. We can therefore calculate the covariance matrix by

taking the Hessian of the log-likelihood function, as the constant disappears under differentiation:

$$\mathbf{\Sigma} = -\left[\nabla\nabla L\right]^{-1}. \tag{3.29}$$

Simplifying the Hessian of the log-likelihood function gives

$$\left[\nabla\nabla L\right]_{q,r} = -\sum_{i}^{n} \frac{1}{\sigma_i^2}\left[\frac{\partial\mu_i(\vec{\chi})}{\partial\chi_q}\,\frac{\partial\mu_i(\vec{\chi})}{\partial\chi_r} + (\mu_i(\vec{\chi}) - d_i)\frac{\partial^2\mu_i(\vec{\chi})}{\partial\chi_q\partial\chi_r}\right]\Bigg|_{\vec{\chi}=\vec{\chi}_0}, \tag{3.30}$$

where the logarithmic rate constants χ_s, χ_p and χ_{STD} have been indexed with q and r. This equation was solved numerically for each dataset, using MATLAB's *DERIVESTsuite*. The covariance matrix was then calculated using **equation 3.29**, and the the uncertainty of each χ_r calculated as

$$\sigma_r = \sqrt{\mathbf{\Sigma}_{rr}}\,. \tag{3.31}$$

3.12 Fitting Results for *Xl*Cry

MARY curves for *Xl*Cry were measured by Till Biskup by transient absorption, at a range of different conditions. All samples were in aqueous solutions containing 50 mM Tris−HCl, 250 mM NaCl, and differing concentrations of glycerol. All samples had concentrations of *Xl*Cry within experimental error of each other, as determined by UV-Vis spectroscopy.

The theoretically fitted MARY curves fit the experimental curves well. Although the theoretical curves predicted a low field effect, this was in each case within the scatter of the measurement (**figure 3.10**). No low field effect was apparent in the experimental results.

The fitted rate constants k_s, k_p and k_{STD}, with uncertainties, are shown in **figure 3.11**. The singlet recombination and proton transfer rates varied significantly with experimental conditions; however, the singlet-triplet dephasing rate did not.

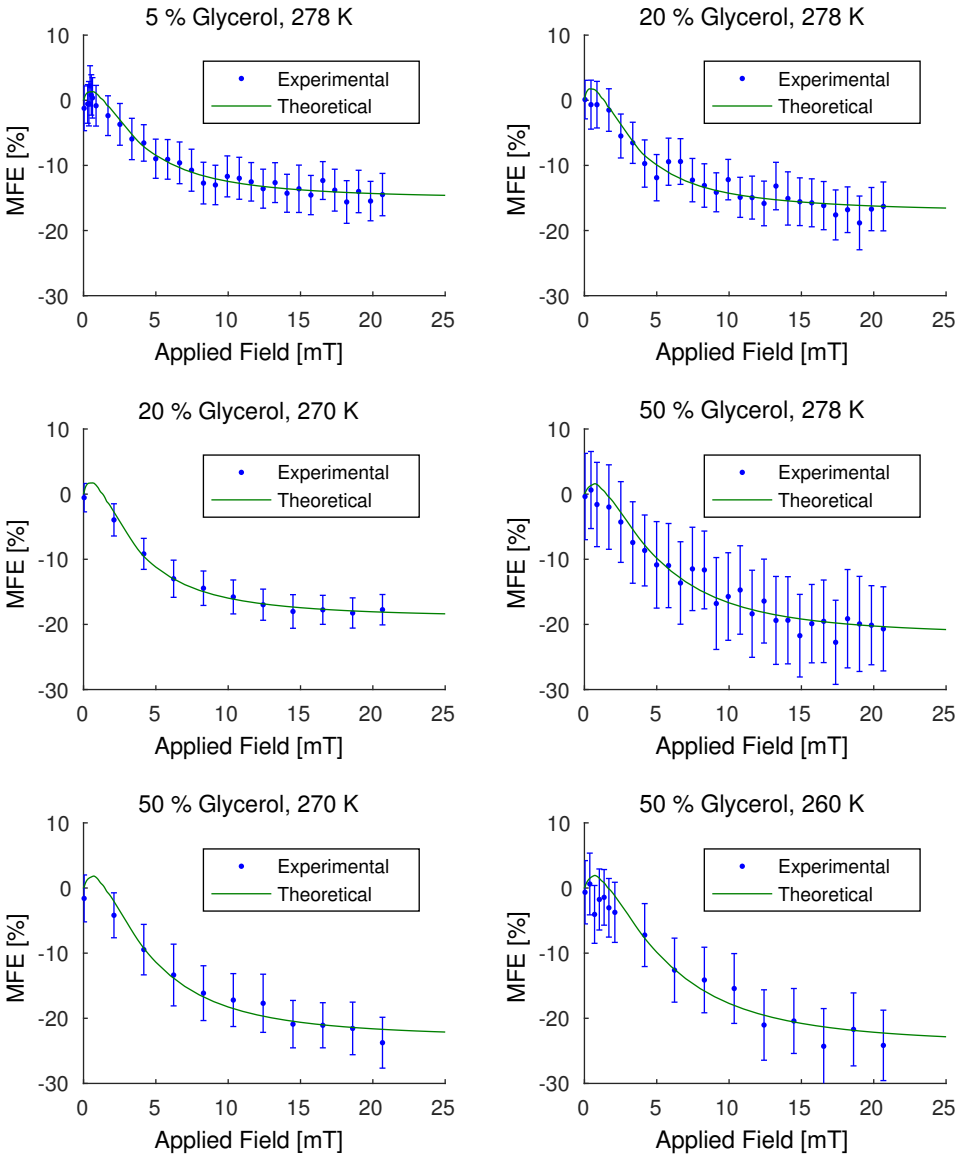

Figure 3.10: Experimental MARY curves collected by Till Biskup on *Xl*Cry, with the best fit to the simplified $FAD^{\bullet-}$ $TrpH^{\bullet+}$ model. Each datapoint was calculated from ten field on and field off traces, and represents a time average from 1 to 10 µs.

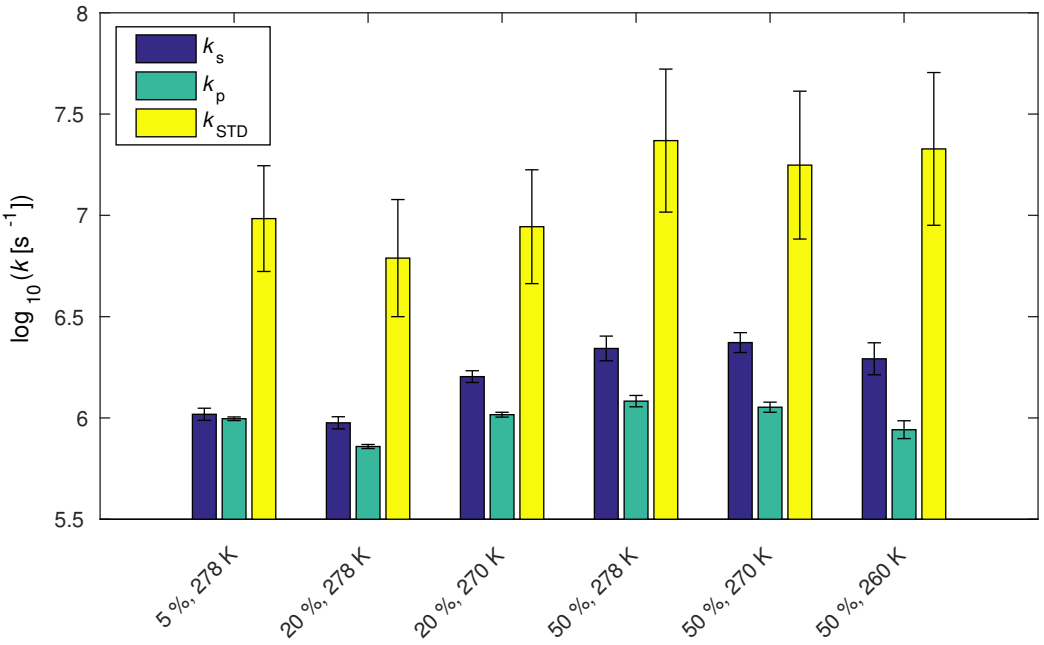

Figure 3.11: Fitted rate constants for *Xl*Cry, at different glycerol percentages and temperatures. Error bars represent standard deviations, estimated by Bayesian probability. The recombination rate constant, k_s, showed the greatest variation with experimental conditions. The deprotonation rate constant, k_p, was only weakly affected, while the dephasing rate constant, k_{STD}, did not change significantly.

3.13 Comparison with Experiment

No unequivocal trend was apparent in the fitted rate constants, k_s and k_p, when plotted against viscosity and temperature (**figure 3.12**). The singlet recombination rate appears to increase with viscosity to a plateau, while the proton transfer rate initially increases followed by a decrease. However, it is hard to ascertain these trends due to the large uncertainties in the fitted rates, and the scarcity of data.

The apparent increase in k_s with viscosity could due to internal structural change caused by solvation. It is well established that water molecules can penetrate the internal structure of a protein [58]. Furthermore, computer simulations suggest that these water molecules can play an important role in stabilizing the active site of a protein, particularly with regard to binding a ligand (such as FAD) in place [25, 53]. The same studies suggest that the nature of the solvent affects the conformation of residues on the surface of the protein, which in turn affects the dynamics of residues within the protein. This appears to depend not only on viscosity, but also the nature

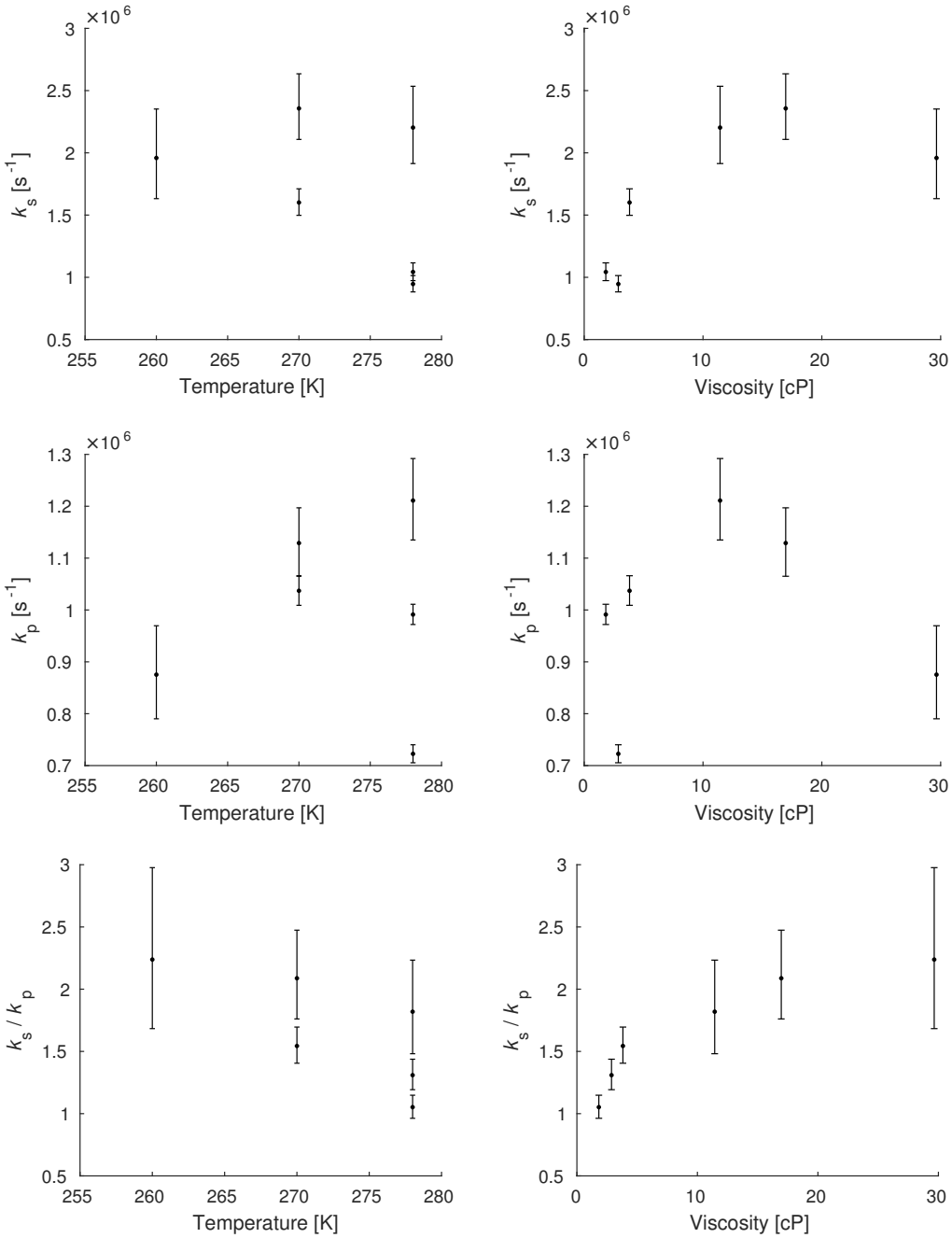

Figure 3.12: Fitted rate constants k_s and k_p for *Xl*Cry, as a function of temperature and viscosity. The error bars were calculated from the uncertainty, σ, in the Bayesian posterior distribution, with top and bottom error bars at points $10^{\chi \pm \sigma}$, where $\chi = \log_{10} k$.

of the solvent.

It is possible that, at lower viscosities (*i.e.* lower glycerol concentrations), a water molecule is more likely to diffuse into *Xl*Cry and stabilize the flavin and tryptophan chain, and thus discourage radical pair recombination. If this hypothesis is true, both viscosity and water content should contribute to the change in k_s. To test this idea, the glycerol could be replaced with a solvent with a different viscosity, to see if water content or viscosity is the more important factor.

Moreover, viscosity alone has been found to change the frequency of collective harmonic oscillations within a pancreatic trypsin inhibitor protein [73]. Molecular dynamics simulations suggest that higher viscosity could increase the frequency of these harmonics — if the same effect occurs in cryptochromes, the increase in internal motions could be responsible for the increase in k_s with viscosity.

While it is intuitive to expect that viscosity would also affect k_p, the homology structure of *Xl*Cry [15] suggests that the terminal tryptophan has a solvent accessibility of only 5 % relative to a tryptophan in an unfolded polypeptide chain. This could be why there was no apparent trend linking viscosity to k_p.

Experimentally, there was no evident correlation between temperature and the MARY linewidth parameter, $B_{1/2}$, in *Xl*Cry; however, the linewidth did increase linearly with viscosity (**figure 3.13**). This result supports the hypothesis that the internal dynamics of the protein are affected by viscosity, because in the singlet-triplet dephasing model, linewidth increases with k_s and k_{STD}, which both reflect electron hopping inside the protein.

Alternatively, singlet-triplet dephasing could simply be the wrong mechanism of spin-relaxation, such that the fitted rate constants are not accurate.

3.14 Data Fitting on *Dm*Cry

A MARY curve was measured for *Dm*Cry at 20 % glycerol and 278 K, by broadband cavity-enhanced absorption spectroscopy [107, 131]. and fitted to the singlet-triplet

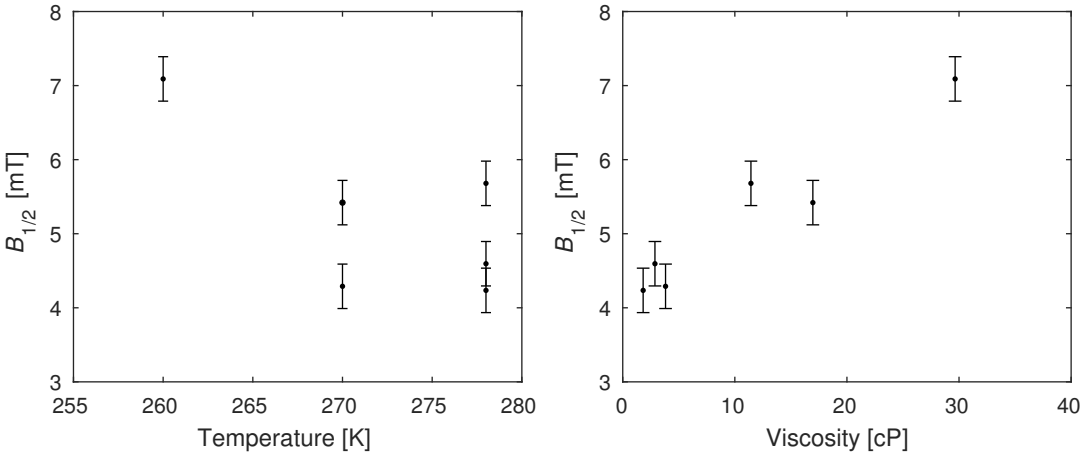

Figure 3.13: Experimentally determined linewidth ($B_{1/2}$) of the MARY curves from *Xl*Cry. There was a clear positive correlation between linedwidth and viscosity.

dephasing model (**figure 3.14**). The resulting rate constants are

$$k_s = 10^{4.8\pm0.2}\,\mathrm{s}^{-1}$$

$$k_p = 10^{5.5\pm0.0}\,\mathrm{s}^{-1}$$

$$k_{\mathrm{STD}} = 10^{7.0\pm0.8}\,\mathrm{s}^{-1}\,.$$

The resulting dephasing rate is the same magnitude as that fitted for *Xl*Cry, *At*Cry and *Ec*PL, consistent with the broad linewidth of the *Dm*Cry MARY curve. However, in contrast to the other three proteins, the singlet recombination rate is much smaller than the deprotonation rate in *Dm*Cry, with

$$k_s \approx \frac{k_p}{10}.$$

This ratio is consistent with the relatively weak magnetic field effect measured in *Dm*Cry. Fittings performed on *Xl*Cry, *Ec*PL and *At*Cry [113] predict, under all conditions tested, k_s of similar magnitude or larger than k_p.

This contrast makes sense if, as the crystal structure of *Dm*Cry suggests, there is a tetrad rather than a triad of tryptophan residues sequentially arranged next to the FAD ligand. If the terminal radical pair contains one unpaired electron on the flavin the flavin and the second on TrpD rather than on TrpC, the greater separation is expected to result in a much smaller singlet recombination rate than

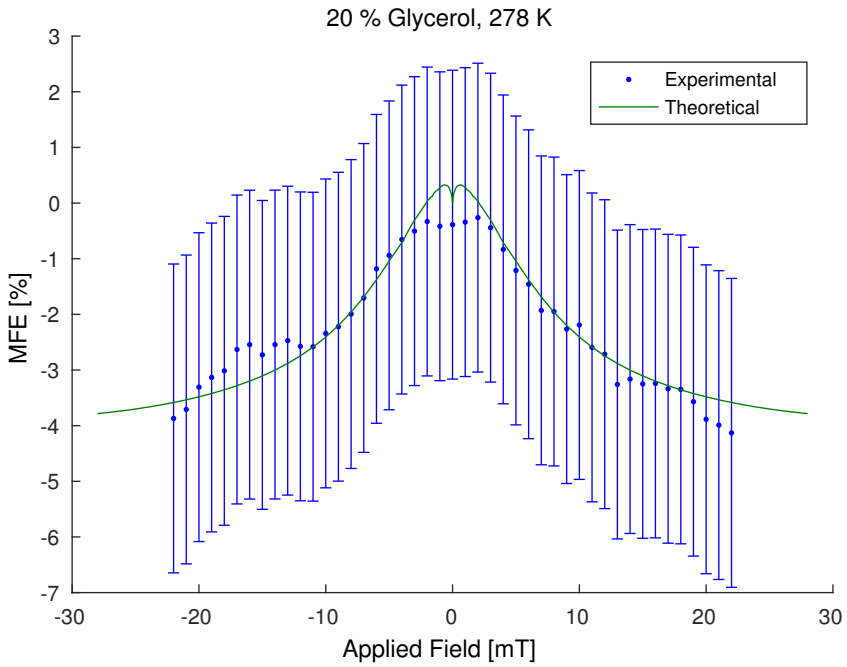

Figure 3.14: MARY curve for *Dm*Cry, measured at pH 7. The experimental curve shape was measured by broad-band cavity enhanced absorption spectroscopy by Dr Jing Li. The data were then scaled by the saturation magnetic field effect measured by transient absorption, by Dr Kevin Henbest. Error bars represent the standard deviation of 500 individual measurements. The theoretical curve was obtained by fitting the data to the singlet-triplet dephasing model, with the radical pair lifetime constrained to that measured by transient absorption at zero field.

in cryptochromes with just a triad of tryptophans.

3.15 Conclusions

Although the singlet-triplet dephasing model fit the experimental data in all cases, and the fitted k_{STD} is similar to the electron hopping rate found experimentally by Liu [109], the validity of the model is still uncertain. The weakness of the model is that there is as yet, no experimental evidence that the exchange interaction in RP0 is large. However, given the distance between the radicals in RP0, a large exchange interaction is physically plausible [39].

According to the crystal structure of *Dm*Cry, there is a fourth tryptophan, further from the $\mathrm{FAD}^{\bullet-}$ than the third tryptophan. Recent experimental results suggest that $\mathrm{TrpH}^{\bullet+}$ in RP1 is located on this fourth tryptophan, which suggests that if there is any electron hopping, it is between TrpC and TrpD, neither of which is expected to

have a large exchange interaction. Paradoxically, the simulations in the current work predict a significant singlet-triplet dephasing effect in *Dm*Cry – this may simply be a case of the dephasing mimicking the effect of some other relaxation mechanism, such as modulation of anisotropic hyperfine interactions by rotational tumbling of the protein, or libration of the $TrpH^{\cdot+}$ radical [91].

To test the importance of the singlet-triplet dephasing mechanism experimentally, two MARY experiments are proposed on the following proteins:

1. *Xl*Cry or *Ec*PL mutated to have a fourth tryptophan at the end of the triad
2. *Dm*Cry mutated to replace TrpD with a non redox active residue, such as phenylalanine

If the singlet-triplet dephasing model is correct, the first MARY curve would be expected to have a narrower linewidth than in the wildtype protein.

If the singlet-triplet dephasing is indeed an important relaxation mechanism, it should also be active in a cryptochrome magnetoreceptor *in vivo*. Such a cryptochrome would presumably be immobilized in a membrane, in an extremely viscous environment, such that internal protein dynamics would play the dominant rôle in spin relaxation. *In vitro*, protein tumbling can also contribute to spin relaxation, which will be discussed in the following chapter.

Chapter 4

Effect of Spin Relaxation Caused by Rotational Tumbling on Magnetic Field Effects on Cryptochrome-based Radical Pairs

4.1 Introduction

The work in this chapter was carried out in order to better understand spin relaxation processes relevant to *in vitro* studies on cryptochromes. As concluded in the previous chapter, singlet-triplet dephasing is unlikely to be a complete picture, so this chapter will discuss the effect of rotational tumbling of the cryptochrome in solution. The results of this chapter are unlikely to apply to a cryptochrome-based magnetosensor *in vivo*, as such a sensor would most likely be immobilized on a surface or in a membrane.

Rotational diffusion was modeled *via* the Stochastic Liouville Equation, with a second order approximation of the diffusion equation, on a 24×48 grid, as described previously in the literature [102, 103, 181].

Two radical pairs were simulated. The first included a single nitrogen hyperfine coupling of the form below.

$$\mathrm{e_1}^- - \mathrm{N} \qquad \mathrm{e_2}^-$$

This simulation was simplified using the separation scheme described in [102]. A second, more realistic, radical pair was simulated with two nitrogens, one coupled to each electron, as in the diagram below.

$$\mathrm{e_1}^- - \mathrm{N_1} \qquad \mathrm{e_2}^- - \mathrm{N_2}$$

For this second radical pair, the aforementioned separation was not possible due to the inclusion of the stochastic diffusion. Instead, the spin system was propagated according to the Stochastic Liouville Equation, and integrated to give the singlet yield.

4.1.1 The Spin Systems

The first radical pair, with a single nitrogen, was simulated with hyperfine parameters $a = 1\,\mathrm{mT}$ (isotropic component), $\Delta A = 3\,\mathrm{mT}$ (axiality) and $\delta A = 0\,\mathrm{mT}$ (rhombicity), as defined in **section 1.6.4** of the introductory chapter. This gave a hyperfine tensor of the form

$$A = \begin{pmatrix} 0.5 & 0 & 0 \\ 0 & 0.5 & 0 \\ 0 & 0 & 2 \end{pmatrix} \mathrm{mT} \tag{4.1}$$

The second radical pair system was chosen to mimic the flavin-tryptophan radical pair found in cryptochromes and photolyases. The hyperfine couplings were taken from density functional calculations at the UB3LYP/EPR-III level, on free $\mathrm{FAD}^{\bullet-}$ and $\mathrm{TrpH}^{\bullet+}$ molecules [149]. The most anisotropic hyperfine coupling from each molecule was chosen (**figure 4.1**) for inclusion in the calculation, as memory constraints meant that it was not possible to include all hyperfine couplings. As other hyperfine couplings were neglected, as were dipolar interactions between the

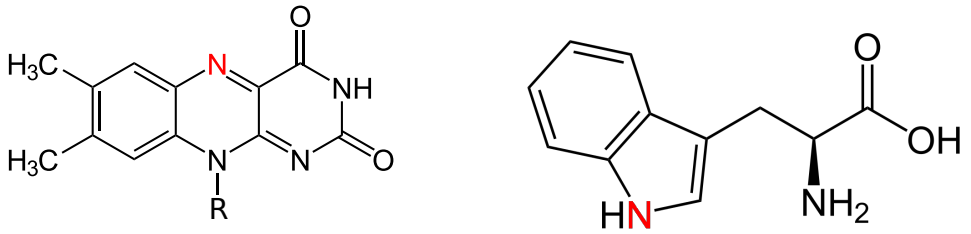

(a) (b)

Figure 4.1: The nuclei included in the simulation with two nitrogens, one coupled to each electron, highlighted in red. a) The isoalloxazine ring of FAD, and b) tryptophan.

two electrons, the extent of spin relaxation calculated in the current chapter is likely to be an underestimate.

The most anisotropic coupling calculated for $FAD^{\bullet-}$ was

$$A = \begin{pmatrix} -0.1001 & 0 & 0 \\ 0 & -0.0868 & 0 \\ 0 & 0 & 1.7569 \end{pmatrix} \mathrm{mT}\,, \tag{4.2}$$

($\Delta A = 3.70\,\mathrm{mT}$) where the tensor's z axis is perpendicular to the plane of the molecule. The most anisotropic coupling calculated for $TrpH^{\bullet+}$ was

$$A = \begin{pmatrix} -0.0530 & 0 & 0 \\ 0 & -0.0637 & 0 \\ 0 & 0 & 1.0812 \end{pmatrix} \mathrm{mT}\,, \tag{4.3}$$

($\Delta A = 2.28\,\mathrm{mT}$) where the tensor's z axis is perpendicular to the plane of the molecule.

For the purposes of the calculation, rhombicity was assumed to be zero. This is not a bad assumption, as $\delta A \approx 0.1\,\mathrm{mT}$ in the $FAD^{\bullet-}$ nitrogen, and $\delta A \approx 0.01\,\mathrm{mT}$ in the $Trp^{\bullet+}$ nitrogen. Furthermore, it was necessary to assume that both tensors shared an eigenbasis (*i.e.* both were diagonal in the same basis), in order to limit the diffusion calculation to two Euler angles (specifying the orientation of the radical pair with respect to the applied magnetic field). This assumption was less satisfactory, as it was equivalent to assuming that that the plane normals of $FAD^{\bullet-}$ and $Trp^{\bullet-}$ are parallel, which is not the case in known cryptochrome crystal structures. However, this assumption was necessary, as the calculation would have been too

computationally expensive with three Euler angles.

The hyperfine tensor for the $FAD^{\bullet-}$ radical used in the singlet yield calculations was therefore

$$A = \begin{pmatrix} -0.093 & 0 & 0 \\ 0 & -0.093 & 0 \\ 0 & 0 & 1.76 \end{pmatrix} \text{mT}\,, \tag{4.4}$$

while the hyperfine tensor for the $TrpH^{\bullet+}$ radical was

$$A = \begin{pmatrix} -0.058 & 0 & 0 \\ 0 & -0.058 & 0 \\ 0 & 0 & 1.08 \end{pmatrix} \text{mT}\,. \tag{4.5}$$

4.1.2 Axis System

Orientation of the Spin System was Parameterized with Two Euler Angles

As the spin systems had cylindrical symmetry, their orientation in space could be parameterized by two Euler angles, α and β (**figure 4.2**). Here, $0 \leq \alpha \leq 2\pi$ and $0 \leq \beta \leq \pi$.

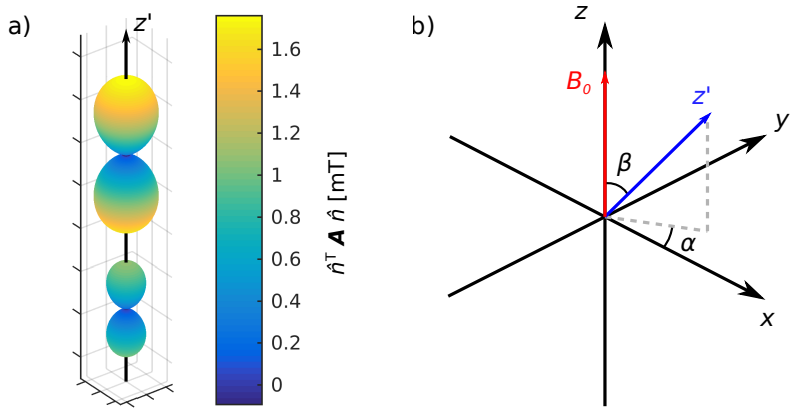

Figure 4.2: a) Representation of the hyperfine tensor for the nitrogen from $FAD^{\bullet-}$ (top), and the nitrogen from $TrpH^{\bullet+}$ (bottom), showing the z' axis, about which the couplings have cylindrical symmetry. b) Axis system for the rotationally diffusing system. The applied magnetic field, B_0, was always parallel to the z axis. The z' axis was parameterized with Euler angles α and β.

When discretized, the Euler angles form a grid on a unit sphere, where each node

represents an area on the surface of the sphere of approximately

$$S \approx \sin\beta\,\delta\alpha\,\delta\beta\,, \tag{4.6}$$

where $\delta\alpha$ and $\delta\beta$ are the grid spacings of α and β, respectively [119]. If α and β are spaced uniformly, the spacing of nodes decreases closer to the poles, meaning that these locations are over-represented. For the purpose of the current chapter, the substitution

$$q = -\cos\beta\,, \quad -1 \leq q \leq 1 \tag{4.7}$$

was used, such that each node would represent an identical area, to avoid bias from over-represenation of nodes close to the poles. This substitution gives

$$d\beta = \frac{dq}{\sin\beta}\,, \tag{4.8}$$

and together with **equation 4.6**, the approximate area represented by a node is

$$S \approx \delta\alpha\,\delta q\,, \tag{4.9}$$

such that all nodes represent an equal area when α and q are evenly spaced. Following Lau *et al.* [103], a 24×48 grid was used, giving

$$\begin{aligned} \delta\alpha &= \frac{2\pi}{24} \\ &= \frac{\pi}{12} \end{aligned} \tag{4.10}$$

and

$$\begin{aligned} \delta q &= \frac{2}{48} \\ &= \frac{1}{24}\,. \end{aligned} \tag{4.11}$$

The discretization was offset by $\frac{\delta q}{2}$ at the poles, to avoid singularities. The variables

α and q were therefore discretized to

$$\begin{aligned} \alpha_i &= (i-1)\,\delta\alpha\,, \quad i = 1, 2, \ldots, 24 \\ q_j &= -1 + \left(j - \frac{1}{2}\right)\,\delta q\,, \quad j = 1, 2, \ldots, 48 \end{aligned} \tag{4.12}$$

Initial Orientational Distribution Followed the Rules of Photoselection

In order to simulate excitation with a polarized laser, as occurs in the transient absorption experiment, simulations were performed with a photoselected initial distribution of radial pairs. The photoselection axis was chosen to be along z, making the initial orientation of z' follow a distribution

$$P(\alpha, \beta) \propto \cos^2 \beta\,, \tag{4.13}$$

or

$$P(\alpha, q) \propto q^2\,, \tag{4.14}$$

This distribution was discretized and stored in vector form as $\vec{P}(t)$, which at time $t = 0$ is,

$$\vec{P}(0) = \begin{pmatrix} P_{\alpha_1,q_1}(0) \\ P_{\alpha_1,q_2}(0) \\ P_{\alpha_1,q_3}(0) \\ \vdots \\ P_{\alpha_2,q_1}(0) \\ P_{\alpha_2,q_2}(0) \\ P_{\alpha_2,q_3}(0) \\ \vdots \\ P_{\alpha_M,q_N}(0) \end{pmatrix} = \left(M \sum_{j=1}^{N} q_j^2 \right)^{-1} \begin{pmatrix} q_1^2 \\ q_2^2 \\ q_3^2 \\ \vdots \\ q_1^2 \\ q_2^2 \\ q_3^2 \\ \vdots \\ q_N^2 \end{pmatrix}\,, \tag{4.15}$$

where the normalization factor ensures that the sum of all probabilities is equal to 1. There was no need to weight each element by the area on the unit sphere it represents, as each element represents an equal area.

4.1.3 Rotational Tumbling

Diffusion About a Single Axis

Tumbling about a single axis follows a differential equation analogous to Fick's second law of diffusion [156]:

$$\frac{dP(\alpha,t)}{dt} = -D\frac{d^2P(\alpha,t)}{d\alpha^2}\,, \tag{4.16}$$

where $P(\alpha,t)$ is the orientational probability density as a function of Euler angle α, and D is the rotational diffusion coefficient, with units $\mathrm{rad}^2\,\mathrm{s}^{-1}$. This coefficient is inversely proportional to the frictional drag, ζ:

$$D = \frac{k_\mathrm{B}T}{\zeta}\,, \tag{4.17}$$

where k_B is Boltzmann's constant, and T is the absolute temperature. Assuming that the protein containing the radical pair is a uniform sphere,

$$\zeta = 8\pi\eta R^3\,, \tag{4.18}$$

where η is the dynamic viscosity of the solvent, and R is the radius of the protein [100].

In practice, the above equation is incorrect, as cryptochrome is not a sphere, and the radical pair is not located at the geometric center of the protein. Furthermore, the radical anion form of the flavin is thought to cause an extension of the C-terminus of cryptochrome [141]. This would mean that the protein would rotate more quickly around the long axis of the molecule than around perpendicular axes. This could cause the relaxation calculated in this chapter to be an underestimate, or an overestimate, depending on the orientation of the anisotropic hyperfine couplings with respect to the long protein axis.

The rotational diffusion tensor can be estimated from the crystal structure, by

modelling the individual atoms in the protein as point sources of friction [99]. This would give a more accurate value for the rotational correlation time. Alternatively, this correlation time could be measured directly by dynamic light scattering of polarized light [153].

Diffusion About Two Axes

In general, the orientation of a three-dimensional object in space can be determined by three Euler angles, α, β and γ. There are many parameterization schemes, but for the purposes of this thesis, the angles represent, in succession,

1. rotation about molecular z axis by α,
2. rotation about molecular y axis by β,
3. a second rotation about molecular z axis by γ.

Generalizing the orientational probability density to $P(\Omega, t)$, where Ω represents the three Euler angles, α, β and γ, the tumbling must follow a differential equation of the form

$$\frac{d}{dt}P(\Omega, t) = \hat{D}P(\Omega, t)\,, \tag{4.19}$$

where $\hat{D}$ is the diffusion operator. For isotropic diffusion [57],

$$\hat{D} = -D\hat{J}^2\,, \tag{4.20}$$

where $\hat{J}$ is the total angular momentum operator for a classical particle. With a zyz convention for Euler angles [57],

$$-\hat{J}^2 = \frac{d^2}{d\beta^2} + \cot\beta\frac{d}{d\beta} + \frac{1}{\sin^2\beta}\left(\frac{d^2}{d\alpha^2} + \frac{d^2}{d\gamma^2} - 2\cos\beta\frac{d^2}{d\alpha d\gamma}\right)\,. \tag{4.21}$$

All spin systems studied in the current chapter had cylindrical symmetry, such that it was necessary to take into account only two degrees of rotational freedom. This was an approximation, as a realistic radical pair in a cryptochrome does not

have cylindrical symmetry. This approximation is another reason why the relaxation calculated in the current chapter is an underestimate.

The axis of cylindrical symmetry, z', could be parameterized with just two Euler angles (figure 4.2), as the third rotation in the zyz scheme would have no effect on the spin dynamics. This simplified the above equation to [176]

$$\begin{aligned} -\hat{J}^2 &= \nabla^2 \\ &= \frac{d^2}{d\beta^2} + \cot\beta\frac{d}{d\beta} + \frac{1}{\sin^2\beta}\frac{d^2}{d\alpha^2}\,, \end{aligned} \tag{4.22}$$

resulting in the diffusion operator

$$\hat{D} = D\left(\frac{d^2}{d\beta^2} + \cot\beta\frac{d}{d\beta} + \frac{1}{\sin^2\beta}\frac{d^2}{d\alpha^2}\right) \tag{4.23}$$

The Diffusion Equation was Discretized by Finite Difference

Changing variable from β to q using **equation 4.7**, the diffusion operator becomes

$$\hat{D} = D\left((1-q^2)\frac{d^2}{dq^2} - 2q\frac{d}{dq} + \frac{1}{1-q^2}\frac{d^2}{d\alpha^2}\right) \tag{4.24}$$

Infinitesimal changes in α and q were discretized by substitution with their grid spacings

$$\begin{aligned} d\alpha &\to \delta\alpha \\ dq &\to \delta q\,, \end{aligned}$$

while the differential operators were discretized using second order, centered, finite differences. For a discretized variable x,

$$\begin{aligned} \delta x_n &= \frac{x_{n+1} - x_{n-1}}{2} \\ \delta^2 x_n &= x_{n-1} - 2x_n + x_{n+1} \end{aligned} \tag{4.25}$$

Using these approximations, the diffusion operator $\hat{D}$ was converted into a matrix

operator $\hat{W}$ that acts on the vector of orientational probabilities $\vec{P}(t)$, as described by

$$\frac{d}{dt}\vec{P}_{ij}(t) = D\sum_{k,l}\hat{W}_{ij,kl}\vec{P}_{kl}(t)\,, \tag{4.26}$$

where the probability vector has been doubly indexed according to

$$\vec{P}_{ij} = P_{\alpha_i,q_j} \tag{4.27}$$

(see **equation 4.15**), as have the rows and columns of $\hat{W}$.

Following Wagner-Rundell and Lau, [181, 102], since there are three terms in $\hat{D}$ (**equation 4.24**), $\hat{W}$ can be split into three components:

$$\begin{aligned}
\hat{D} &\to D\left(\hat{W}^{(qq)} + \hat{W}^{(q)} + \hat{W}^{(\alpha\alpha)}\right) \\
(1-q^2)\frac{d^2}{dq^2} &\to \hat{W}^{(qq)} \\
-2q\frac{d}{dq} &\to \hat{W}^{(q)} \\
\frac{1}{1-q^2}\frac{d^2}{d\alpha^2} &\to \hat{W}^{(\alpha\alpha)}\,.
\end{aligned} \tag{4.28}$$

Following the centered finite difference scheme (**equation 4.25**), the diagonal elements of the diffusion matrices are

$$\begin{aligned}
\hat{W}^{(qq)}_{ij,ij} &= -\frac{2}{\delta q^2}\left(1-q_j^2\right) \\
\hat{W}^{(q)}_{ij,ij} &= 0 \\
\hat{W}^{(\alpha\alpha)}_{ij,ij} &= -\frac{2}{\delta\alpha^2}\frac{1}{1-q_j^2}\,.
\end{aligned} \tag{4.29}$$

Off-diagonal elements of $\hat{W}$ depend on whether they couple interior or edge elements of $\vec{P}$. For the coordinate α, with $j = 1$ to N and $i = 2$ to $M-1$,

$$\begin{aligned}
\hat{W}^{(\alpha\alpha)}_{ij;i+1,j} &= \frac{1}{1-q_j^2}\frac{1}{\delta\alpha^2} \\
\hat{W}^{(\alpha\alpha)}_{ij;i-1,j} &= \frac{1}{1-q_j^2}\frac{1}{\delta\alpha^2}
\end{aligned} \tag{4.30}$$

Periodic boundary conditions were applied at the edges, as directions α_1 and α_M correspond to adjacent nodes (for the same q_j). Therefore, for $j = 1$ to N,

$$\begin{aligned} \hat{W}^{(\alpha\alpha)}_{Mj;1j} &= \frac{1}{\delta\alpha^2}\frac{1}{1-q_j^2} \\ \hat{W}^{(\alpha\alpha)}_{Mj;M-1,j} &= \frac{1}{\delta\alpha^2}\frac{1}{1-q_j^2} \\ \hat{W}^{(\alpha\alpha)}_{1j;Mj} &= \frac{1}{\delta\alpha^2}\frac{1}{1-q_j^2} \\ \hat{W}^{(\alpha\alpha)}_{1j;2j} &= \frac{1}{\delta\alpha^2}\frac{1}{1-q_j^2} \end{aligned} \tag{4.31}$$

For the interior elements of coordinate q, with $j = 2$ to $N-1$ and $i = 1$ to M, the matrix elements corresponding to the second derivative are

$$\begin{aligned} \hat{W}^{(qq)}_{ij;i,j+1} &= \frac{1}{\delta q^2}\left(1-q_j^2\right) \\ \hat{W}^{(qq)}_{ij;i,j-1} &= \frac{1}{\delta q^2}\left(1-q_j^2\right)\,, \end{aligned} \tag{4.32}$$

while the elements corresponding to the first derivative are

$$\begin{aligned} \hat{W}^{(q)}_{ij;i,j+1} &= -\frac{q_j}{\delta q} \\ \hat{W}^{(q)}_{ij;i,j-1} &= \frac{q_j}{\delta q}\,. \end{aligned} \tag{4.33}$$

Exterior elements of coordinate q have neighboring nodes over the pole, which means that if M is even, nodes $(\alpha_i\,,\,q_1)$ and $(\alpha_{i+\frac{M}{2}}\,,\,q_1)$ are adjacent, as are $(\alpha_i\,,\,q_N)$ and $(\alpha_{i+\frac{M}{2}}\,,\,q_N)$, for $i = 1$ to $\frac{M}{2}$. This means that, if we define a new variable,

$$i' = \begin{cases} i + \frac{M}{2}, & \text{if } i \leq \frac{M}{2} \\ i - \frac{M}{2}, & \text{if } i > \frac{M}{2}\,, \end{cases}$$

at the north pole, for $i = 1$ to M,

$$\begin{aligned}
\hat{W}^{(qq)}_{i1;i2} &= \frac{1}{\delta q^2}\left(1 - q_1^2\right) \\
\hat{W}^{(qq)}_{i1;i',1} &= \frac{1}{\delta q^2}\left(1 - q_1^2\right) \\
\hat{W}^{(q)}_{i1;i2} &= -\frac{q_1}{\delta q} \\
\hat{W}^{(q)}_{i1;i',1} &= \frac{q_1}{\delta q}\,.
\end{aligned} \tag{4.34}$$

At the south pole, for $i = 1$ to M,

$$\begin{aligned}
\hat{W}^{(qq)}_{iN;i,N-1} &= \frac{1}{\delta q^2}\left(1 - q_N^2\right) \\
\hat{W}^{(qq)}_{iN;i',N} &= \frac{1}{\delta q^2}\left(1 - q_N^2\right) \\
\hat{W}^{(q)}_{iN;i,N-1} &= \frac{q_N}{\delta q} \\
\hat{W}^{(q)}_{iN;i',N} &= -\frac{q_N}{\delta q}\,.
\end{aligned} \tag{4.35}$$

All other matrix elements were set to zero, and the full diffusion matrix was constructed as

$$\hat{W} = \hat{W}^{(qq)} + \hat{W}^{(q)} + \hat{W}^{(\alpha\alpha)}\,, \tag{4.36}$$

giving the differential matrix equation for diffusion

$$\frac{d}{dt}\vec{P}(t) = D\hat{W}\vec{P}(t)\,. \tag{4.37}$$

4.1.4 Calculating the Singlet Recombination Yield

For spin systems including a single nitrogen hyperfine coupling, the singlet yield was calculated directly from the combined diffusion and spin propagator. The spin dynamics were calculated in Liouville space, and the initial density array spanning diffusion space was constructed as

$$\vec{\boldsymbol{\rho}}(\mathbf{0}) = \vec{P}(0) \otimes \frac{\vec{P}_S}{N_{\text{nuc}}}\,, \tag{4.38}$$

where $\vec{P}(0)$ is the array of initial probabilies of each molecular orientation (**equation 4.15**), $\vec{P}_S$ is the flattened singlet projection operator, N_{nuc} is the number of nuclear states, and $\boldsymbol{\vec{\rho}(t)}$ has been typeset in bold font to indicate that it spans spin and diffusion space. This resulted in a density array of the form

$$\boldsymbol{\vec{\rho}(t)} = \begin{pmatrix} \vec{\rho}^{(1,1)}(t) \\ \vec{\rho}^{(1,2)}(t) \\ \vec{\rho}^{(1,3)}(t) \\ \vdots \\ \vec{\rho}^{(2,1)}(t) \\ \vec{\rho}^{(2,2)}(t) \\ \vec{\rho}^{(2,3)}(t) \\ \vdots \\ \vec{\rho}^{(M,N)}(t) \end{pmatrix}, \tag{4.39}$$

where $\hat{\rho}^{(i,j)}$ refers to the individual density array for the node $(\alpha_i\,,\,q_j)$, weighted by the probability of finding a molecule with this orientation.

In a similar fashion, the Hamiltonian superoperator spanning the diffusion space was constructed as

$$\hat{\hat{\boldsymbol{H}}} = |ij\rangle\langle ij| \otimes \hat{\hat{H}}^{(i,j)}\,, \tag{4.40}$$

where $|ij\rangle$ is a basis vector in diffusion space, and $\hat{\hat{H}}^{(i,j)}$ is the Hamiltonian superoperator for a molecule with orientation $(\alpha_i\,,\,q_j)$. This gave a superoperator of the form

$$\hat{\hat{\boldsymbol{H}}} = \begin{pmatrix} \hat{\hat{H}}^{(1,1)} & 0 & 0 & 0 & 0 & 0 & 0 \\ 0 & \hat{\hat{H}}^{(1,2)} & 0 & 0 & 0 & 0 & 0 \\ 0 & 0 & \ddots & 0 & 0 & 0 & 0 \\ 0 & 0 & 0 & \hat{\hat{H}}^{(2,1)} & 0 & 0 & 0 \\ 0 & 0 & 0 & 0 & \hat{\hat{H}}^{(2,2)} & 0 & 0 \\ 0 & 0 & 0 & 0 & 0 & \ddots & 0 \\ 0 & 0 & 0 & 0 & 0 & 0 & \hat{\hat{H}}^{(M,N)} \end{pmatrix} \tag{4.41}$$

Finally, the diffusion superoperator spanning spin and diffusion space was constructed as

$$\hat{\hat{\boldsymbol{W}}} = \hat{W} \otimes \mathbb{1}_{\text{L}}\,, \tag{4.42}$$

where $\mathbb{1}_{\text{L}}$ is the identity matrix in Liouville spin space.

The differential equation governing the motion of the system was therefore

$$\frac{d}{dt}\vec{\boldsymbol{\rho}}(\boldsymbol{t}) = \left(-i\hat{\hat{\boldsymbol{H}}} + D\hat{\hat{\boldsymbol{W}}} - k\,\mathbb{1}\right)\vec{\boldsymbol{\rho}}(\boldsymbol{t})\,, \tag{4.43}$$

where $\mathbb{1}$ is the identity matrix in the combined spin and diffusion space, and k is the decay rate constant. For simplicity, the electronic singlet and triplet decay rate constants were assumed to be equal, as in the exponential model (**section 1.10.2**). In practice, this assumption is incorrect; because the proton transfer step discussed in **section 3.2** of **chapter 3** is non-spin selective (*i.e.* its decay operator is proportional to the identity matrix), the existence of a separate singlet-selective decay channel means that the overall singlet decay rate must be larger than the overall triplet decay rate.

Equation 4.43 is trivially solved to give

$$\begin{aligned}\vec{\boldsymbol{\rho}}(\boldsymbol{t}) &= e^{(-i\hat{\hat{\boldsymbol{H}}}+D\hat{\hat{\boldsymbol{W}}}-k\,\mathbb{1})t}\vec{\boldsymbol{\rho}}(\boldsymbol{0}) \\ &= e^{-kt}e^{(-i\hat{\hat{\boldsymbol{H}}}+D\hat{\hat{\boldsymbol{W}}})t}\vec{\boldsymbol{\rho}}(\boldsymbol{0})\,,\end{aligned} \tag{4.44}$$

which in turn can be solved for the singlet yield using **equation 1.50** from the introductory chapter (p. 36). This method was used for all calculations with a single nitrogen hyperfine coupling.

Unfortunately, due to the size of the matrices involved, this method was too computationally expensive for the spin system with two nitrogen nuclei. Instead, the spin-diffusion system was propagated through time using

$$\hat{U}(t) = e^{-kt}e^{(-i\hat{\hat{\boldsymbol{H}}}+D\hat{\hat{\boldsymbol{W}}})t}\,, \tag{4.45}$$

and numerically integrated to give the singlet yield with

$$\begin{aligned}\Phi_s &= k\int_0^\infty \vec{\boldsymbol{P}}_{\boldsymbol{S}}^{\mathrm{T}}\,\vec{\boldsymbol{\rho}}(t)\,dt \\ \Phi_s &= k\int_0^\infty \vec{\boldsymbol{P}}_{\boldsymbol{S}}^{\mathrm{T}}\,\hat{U}(t)\,\vec{\boldsymbol{\rho}}(0)\,dt\,.\end{aligned} \tag{4.46}$$

The propagator, as described above, is an extremely large, dense, matrix. Fortunately, Suzuki has proven that [164]

$$e^{x(\boldsymbol{A_1}+\boldsymbol{A_2}+\ldots+\boldsymbol{A_q})} = e^{\frac{x}{2}\boldsymbol{A_1}} \ldots e^{\frac{x}{2}\boldsymbol{A_{q-1}}} e^{x\boldsymbol{A_q}} e^{\frac{x}{2}\boldsymbol{A_{q-1}}} \ldots e^{\frac{x}{2}\boldsymbol{A_1}} + \mathcal{O}(x^3)\,. \tag{4.47}$$

Applying Suzuki's result to **equation 4.45**,

$$\hat{\hat{U}}(t) \approx e^{-kt} e^{-i\hat{\hat{\boldsymbol{H}}}\frac{t}{2}} e^{D\hat{\hat{\boldsymbol{W}}}t} e^{-i\hat{\hat{\boldsymbol{H}}}\frac{t}{2}}\,, \tag{4.48}$$

giving

$$\vec{\boldsymbol{\rho}}(\boldsymbol{t}+\boldsymbol{\Delta t}) \approx e^{-k\,\Delta t} e^{-i\hat{\hat{\boldsymbol{H}}}\frac{\Delta t}{2}} e^{D\hat{\hat{\boldsymbol{W}}}\,\Delta t} e^{-i\hat{\hat{\boldsymbol{H}}}\frac{\Delta t}{2}} \vec{\boldsymbol{\rho}}(\boldsymbol{t})\,, \tag{4.49}$$

for a sufficiently small timestep Δt. This is equivalent to performing the coherent spin evolution that would occur over half a timestep, followed by the stochastic diffusion over the full timestep, and finally the remaining spin evolution.

In practice, the exponential decay was omitted from the time propagation, as being a scalar, it could be applied post-hoc to the non-decaying singlet probability, $p_s(t)$, with no loss in accuracy. The spin dynamics and diffusion were therefore propagated according to

$$\vec{\boldsymbol{\rho}}(\boldsymbol{t}+\boldsymbol{\Delta t}) \approx e^{-i\hat{\hat{\boldsymbol{H}}}\frac{\Delta t}{2}} e^{D\hat{\hat{\boldsymbol{W}}}\,\Delta t} e^{-i\hat{\hat{\boldsymbol{H}}}\frac{\Delta t}{2}} \vec{\boldsymbol{\rho}}(\boldsymbol{t})\,. \tag{4.50}$$

The timestep was chosen to be

$$\Delta t = \frac{1}{2\left\|\hat{\hat{H}}\right\|_\infty}\,,$$

in accordance with Nyquist's condition for avoiding the aliasing of an oscillating signal.

Suzuki's approximation allowed a considerable reduction in the computational time and memory requirements, as the spin evolution at each point in diffusion space was performed on Hilbert-space density matrices rather than flattened arrays. For

these calculations, the combined diffusion-spin density array had the form

$$\tilde{\boldsymbol{\rho}}(\boldsymbol{t}) = \begin{pmatrix} \hat{\rho}^{(1,1)}(t) \\ \hat{\rho}^{(1,2)}(t) \\ \hat{\rho}^{(1,3)}(t) \\ \vdots \\ \hat{\rho}^{(2,1)}(t) \\ \hat{\rho}^{(2,2)}(t) \\ \hat{\rho}^{(2,3)}(t) \\ \vdots \\ \hat{\rho}^{(M,N)}(t) \end{pmatrix}, \tag{4.51}$$

where each $\hat{\rho}^{(i,j)}(t)$ is a non-flattened density matrix in Hilbert space, corresponding to a spin system with orientation $(\alpha_i\,,\,q_j)$.

The diffusion superoperator took the form

$$\hat{\tilde{\boldsymbol{W}}} = \hat{W} \otimes \mathbb{1}_{\mathrm{H}}\,, \tag{4.52}$$

where $\mathbb{1}_H$ is the identity matrix in Hilbert space. This meant that the dimension of the diffusion superoperator was greatly reduced compared to when using Liouville space. Furthermore, elements of the diffusion superoperator that were smaller than the electronic precision[1] of the smallest population (in diffusion space) were rounded to zero to reduce memory costs.

For each timestep, each density matrix in $\tilde{\boldsymbol{\rho}}(\boldsymbol{t})$ was first propagated using the familiar solution to the Liouville-von Neumann equation,

$$\hat{\rho}^{(i,j)}(t + \frac{\Delta t}{2}) = e^{-i\hat{H}^{(i,j)}\frac{\Delta t}{2}}\,\hat{\rho}^{(i,j)}(t)\,e^{i\hat{H}^{(i,j)}\frac{\Delta t}{2}}\,. \tag{4.53}$$

The diffusion step was then performed,

$$\tilde{\boldsymbol{\rho}}(\boldsymbol{t}+\boldsymbol{\Delta t}) = e^{D\hat{\tilde{\boldsymbol{W}}}\Delta t}\tilde{\boldsymbol{\rho}}(\boldsymbol{t})\,, \tag{4.54}$$

[1]Simulations were performed with double (64 bit) precision, where floating point numbers are encoded with a mantissa and an integer exponent. The mantissa is accurate to approximately $\pm 2 \times 10^{-16}$.

followed by a second coherent evolution step according to **equation 4.53**.

The singlet probability, as a function of time, was calculated by applying the exponential decay, and summing over all orientations in diffusion space:

$$p_s(t) = e^{-kt} \sum_i^M \sum_j^N \mathrm{Tr}\left[\hat{P}_S \hat{\rho}^{(i,j)}(t)\right] . \tag{4.55}$$

This gave a singlet yield of

$$\Phi_s = k \int_0^\infty e^{-kt} \sum_i^M \sum_j^N \mathrm{Tr}\left[\hat{P}_S \hat{\rho}^{(i,j)}(t)\right] dt \, . \tag{4.56}$$

This integral was evaluated numerically, with MATLAB's trapezoidal integration function `trapz()`.

4.1.5 Irreducible Spherical Tensors

To generate the Hamiltonian operator, $\hat{H}^{(i,j)}$, as a function of Euler angles α and β, the hyperfine couplings were parameterized in terms of irreducible spherical tensors. These tensors are an orthogonal set of matrices that can therefore be used to fully specify any matrix. The rank-2 tensors (**table 4.1**) are pertinent to the current work, as they can be used to parameterize the anisotropic component of the hyperfine interaction.

The usage of irreducible spherical tensors greatly aids the simulation of spin systems rotating in space, as these tensors are relatively simple to rotate, expanding into a linear combination of the basis tensors:

$$\hat{\hat{R}}(\alpha,\beta,\gamma)\hat{T}^{(l)}_m = \sum_{m'=-l}^{l} \hat{T}^{(l)}_{m'} \mathcal{D}^{(l)}_{m',m}(\alpha,\beta,\gamma) \, , \tag{4.57}$$

where $\mathcal{D}^{(l)}_{m',m}(\alpha,\beta,\gamma)$ are Wigner's (scalar) functions [151].

Table 4.1: The irreducible spherical tensors, and their coefficients for an anisotropic hyperfine tensor

m	$a_m^{(2)}$	$\hat{T}_m^{(2)}$
2	$+\frac{1}{2}(a_{xx} - a_{yy} - i(a_{xy} + a_{yx}))$	$+\frac{1}{2}\vec{S} \cdot \begin{pmatrix} 1 & i & 0 \\ i & -1 & 0 \\ 0 & 0 & 0 \end{pmatrix} \cdot \vec{I}$
1	$-\frac{1}{2}(a_{xz} + a_{zx} - i(a_{yz} + a_{zy}))$	$-\frac{1}{2}\vec{S} \cdot \begin{pmatrix} 0 & 0 & 1 \\ 0 & 0 & i \\ 1 & i & 0 \end{pmatrix} \cdot \vec{I}$
0	$+\frac{1}{\sqrt{6}}(2a_{zz} - (a_{xx} + a_{yy}))$	$+\frac{1}{\sqrt{6}}\vec{S} \cdot \begin{pmatrix} -1 & 0 & 0 \\ 0 & -1 & 0 \\ 0 & 0 & 2 \end{pmatrix} \cdot \vec{I}$
-1	$+\frac{1}{2}(a_{xz} + a_{zx} + i(a_{yz} + a_{zy}))$	$+\frac{1}{2}\vec{S} \cdot \begin{pmatrix} 0 & 0 & 1 \\ 0 & 0 & -i \\ 1 & -i & 0 \end{pmatrix} \cdot \vec{I}$
-2	$+\frac{1}{2}(a_{xx} - a_{yy} + i(a_{xy} + a_{yx}))$	$+\frac{1}{2}\vec{S} \cdot \begin{pmatrix} 1 & -i & 0 \\ -i & -1 & 0 \\ 0 & 0 & 0 \end{pmatrix} \cdot \vec{I}$

The hyperfine interaction can therefore be described as

$$\hat{H} = \vec{S} \cdot \boldsymbol{A} \cdot \vec{I} = \hat{H}_{\text{iso}} + \sum_{m=-2}^{2} a_m^{(2)} \hat{T}_m^{(2)} \,. \tag{4.58}$$

If we define a set of operators,

$$\hat{Q}_{km} = a_m^{(2)} \hat{T}_k^{(2)} \,, \tag{4.59}$$

the Hamiltonian, rotated in any spatial direction, is

$$\hat{H}(\alpha, \beta, \gamma) = \hat{H}_{\text{iso}} + \sum_{k,m=-2}^{2} \hat{Q}_{km} \mathcal{D}_{k,m}^{(2)}(\alpha, \beta, \gamma) \,. \tag{4.60}$$

This method of rotation, while conceptually more complex than using explicit rotation matrices, avoids the need for matrix multiplication, so is numerically more stable than the latter method.

4.1.6 Rotational Correlation Time

If an ensemble of linear molecules is initially perfectly aligned with some axis Z, and no force present to keep the molecules aligned, the order decays exponentially according to

$$\frac{\langle \cos\theta \rangle_t}{\langle \cos\theta \rangle_{t=0}} = e^{-\frac{t}{\tau_c}}\,, \tag{4.61}$$

where θ is the angle between the linear molecule and the Z axis, and τ_c is the rotational correlation time (also called the *rotational relaxation time*) [156]. This time constant can be thought of as the average time taken for a molecule to rotate through approximately one radian. As the rotational correlation time is more intuitively understandable than the diffusion coefficient, simulation results were presented in terms of the former property.

The rotational correlation time is related to the rotational diffusion coefficient, and the exact relation can be derived as follows. The eigenfunctions of the diffusion operator in **equation 4.23** (p. 109) are the spherical harmonics:

$$\hat{D}Y_l^m = -Dl(l+1)Y_l^m\,, \tag{4.62}$$

meaning that all eigenfunctions decay, apart from the Y_0^0 harmonic, which is in the nullspace of the diffusion operator. This makes perfect physical sense, as this non-decaying harmonic corresponds to a uniform distribution of orientations.

Taking the spherical harmonics as a basis for $P(\alpha, \beta, t)$,

$$\begin{aligned} P(\alpha,\beta,t) &= \sum_{l=0}^{\infty}\sum_{m=-l}^{l} C_{lm}Y_l^m(\alpha,\beta)e^{-tDl(l+1)} \\ &= \sum_{l=0}^{\infty}\sum_{m=-l}^{l} C_{lm}Y_l^m(\alpha,\beta)e^{-\frac{t}{\tau_l}} \end{aligned} \tag{4.63}$$

where C_l^m are the coefficients fitted to the initial distribution of orientations.

Rotational correlation times are typically measured by the decay in fluorescence polarization [75]. An incident beam polarized along $\vec{e}_i$ excites a distribution of

fluorophores

$$P(\Omega) = |\vec{\mu}_a(\Omega) \cdot \vec{e}_i|^2 \,, \tag{4.64}$$

where $\vec{\mu}_a(\Omega)$ is the transition dipole moment for absorption of a molecule with orientation Ω. This essentially gives an initial orientational distribution

$$P_\mu(\theta) = \cos^2\theta \,, \tag{4.65}$$

where θ is the angle between the transition dipole moment and $\vec{e}_i$.
Fitting this initial distribution to the spherical harmonics,

$$P(\Omega) = \int |\vec{\mu}_a(\Omega) \cdot \vec{e}_i|^2 \sum_{l,m} Y_l^m(\Omega)\, d\Omega \,, \tag{4.66}$$

the only terms that survive the integration are Y_0^0, and some linear combination of Y_2^m terms. Plugging the above result into **equation 4.63**, and assuming that fluorescent decay is much slower than rotational tumbling,

$$\begin{aligned} P(\alpha, \beta, t) &= C_{00} Y_0^0 + \sum_{m=-2}^{2} C_{2m} Y_2^m e^{-6Dt} \\ &= C_{00} Y_0^0 + \sum_{m=-2}^{2} C_{2m} Y_2^m e^{-\frac{t}{\tau_2}} \,. \end{aligned} \tag{4.67}$$

From the above equation, it is clear that the experimentally measured decay in fluorescence polarization, *i.e.* the rotational correlation time, is

$$\tau_c = \tau_2 = \frac{1}{6D} \,. \tag{4.68}$$

4.2 Validation of Suzuki Propagation

The singlet yield calculated by propagation with Suzuki's method was validated, using the spin system with a single nitrogen, against that calculated directly by solving the matrix inversion in **equation 1.50** from the introductory chapter (p.

36). The resulting error in the singlet yield was, in all cases, less than 0.05 % (**figure 4.3**).

The propagation of the spin system with Suzuki's method was curtailed once the cumulative trace of all density matrices in $\tilde{\boldsymbol{\rho}}(\boldsymbol{t})$ (*i.e.* the the radical pair population) dropped below a certain tolerance. This stopping tolerance was chosen to be 10^{-5}, as the singlet yield converged to plotting accuracy at this value (**figure 4.3**).

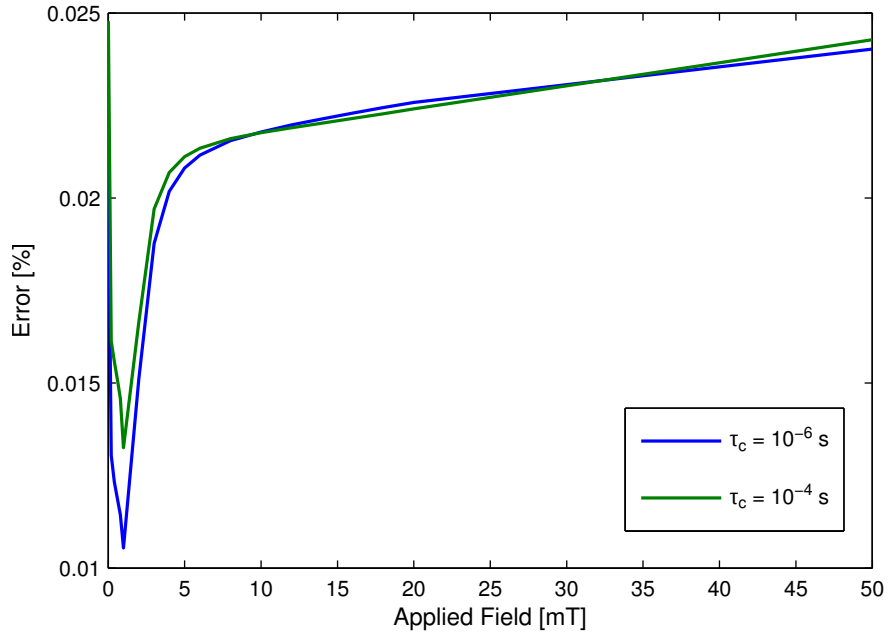

(a) Error with Suzuki propagation

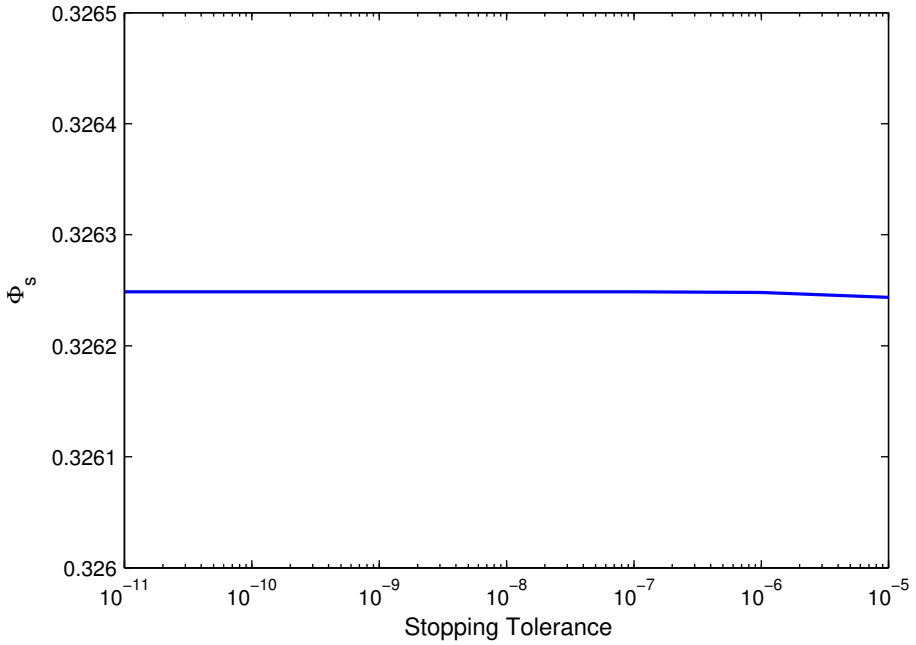

(b) Convergence of Suzuki propagation

Figure 4.3: Validation of the singlet yield calculated with Suzuki's method. a) Error in the singlet yield for a radical pair with a single nitrogen hyperfine coupling, comparing propagation with Suzuki's method to direct calculation by solving the inverse matrix multiplication. b) Singlet yield for a single proton radical pair, calculated with Suzuki's method, as a function of stopping tolerance, with $\tau_c = 10^{-6}\,\mathrm{s}^{-1}$. Parameters: $a = 1\,\mathrm{mT}$, $\Delta A = 3\,\mathrm{mT}$, $k = 10^6\,\mathrm{s}^{-1}$.

4.3 Simulation results

The simulations suggested that the effect of rotational tumbling on the singlet yield is not substantially different between a system with a single nitrogen hyperfine coupling and a system with two nitrogens, one coupled to each radical (**figure 4.4**). The largest difference was that with two nitrogens and slow rotational tumbling, the singlet yield curves reached saturation at 30 mT and took a Lorentzian shape, similar to experimental results reported in the literature for *E. coli* photolyase and *A. thaliana* cryptochrome [113].

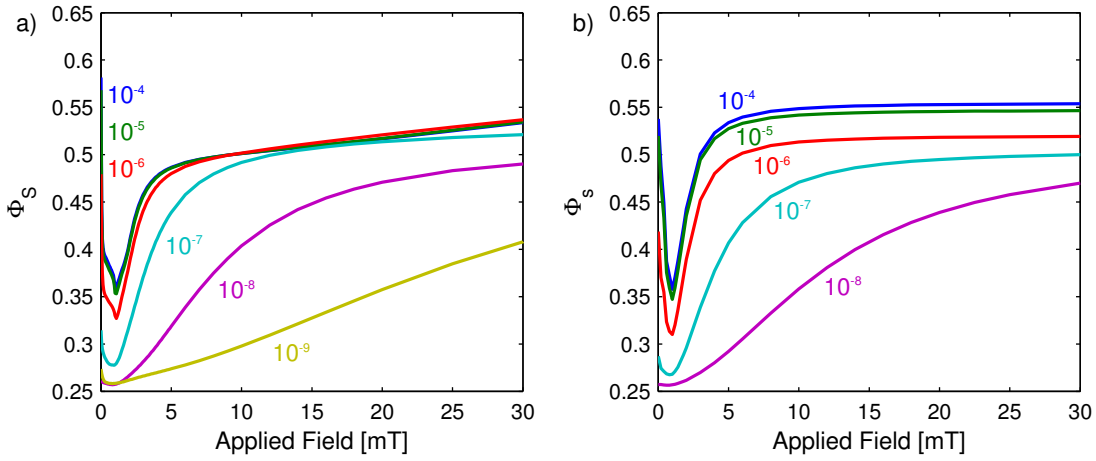

Figure 4.4: Singlet yield with isotropic molecular tumbling. The rotational correlation time, in seconds, is written next to the corresponding curve. a) Single nitrogen radical pair. Parameters: $a = 1\,\mathrm{mT}$, $\Delta A = 3\,\mathrm{mT}$, $k = 10^6\,\mathrm{s}^{-1}$. b) Two nitrogen radical pair. Nitrogen coupled to electron A: $a = 0.5\,\mathrm{mT}$, $\Delta A = 3.7\,\mathrm{mT}$. Nitrogen coupled to electron B: $a = 0.3\,\mathrm{mT}$, $\Delta A = 2.3\,\mathrm{mT}$, $k = 10^6\,\mathrm{s}^{-1}$.

The singlet recombination yield appears to be most sensitive to rotational correlation time when there is no applied magnetic field (**figure 4.5.a**). Therefore, the changes in the subtractive magnetic field effect

$$\Delta\Phi_s = \Phi_s(B_0) - \Phi_s(0)$$

mainly reflect changes in the singlet yield at zero field (**figure 4.5.b**). It is important to take this result into account for interpreting the effect of viscosity on experimental magnetic field effects, as these are commonly reported as subtraction data between

the field-on and field-off measurements [113, 46], or as the ratio between the two measurements [183].

The relative insensitivity of Φ_s at high field strengths can be explained by the energetic isolation of the electronic $T_{\pm1}$ states from the S-T_0 subspace. An applied field strength of 30 mT corresponds to a Zeeman splitting of $5.3 \times 10^9\,\mathrm{s}^{-1}$ (in angular frequency units). Drawing on a perturbative treatment, efficient spin relaxation between S-T_0 and $T_{\pm1}$ would require the rotational correlation time, and therefore the modulation of the anisotropic hyperfine couplings, to be of a similar order to the reciprocal of this Zeeman splitting ($\sim 10^{-10}\,\mathrm{s}$), which is much shorter than the times studied in the present work. Meanwhile, in the S-T_0 subspace, the hyperfine interaction causes quite efficient singlet-triplet interconversion, so relaxation effects are minimal.

The relative insensitivity of Φ_s at the low field minimum is due to the fact that at this field strength, the mixing between singlet and triplet states is at its most efficient, so the expected singlet probability over the lifetime of the radical pair is already close to the thermodynamic equilibrium value of 0.25.

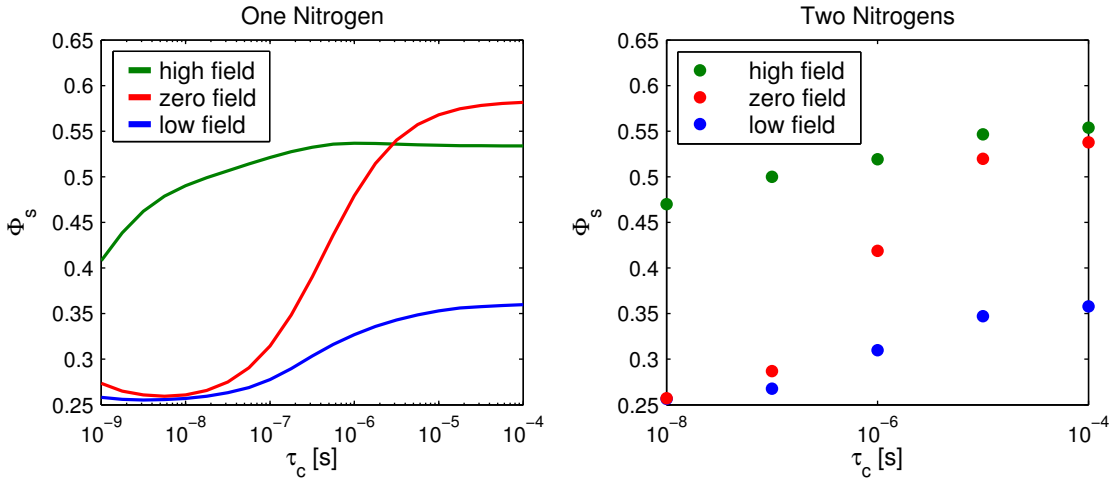

(a) Singlet recombination yield

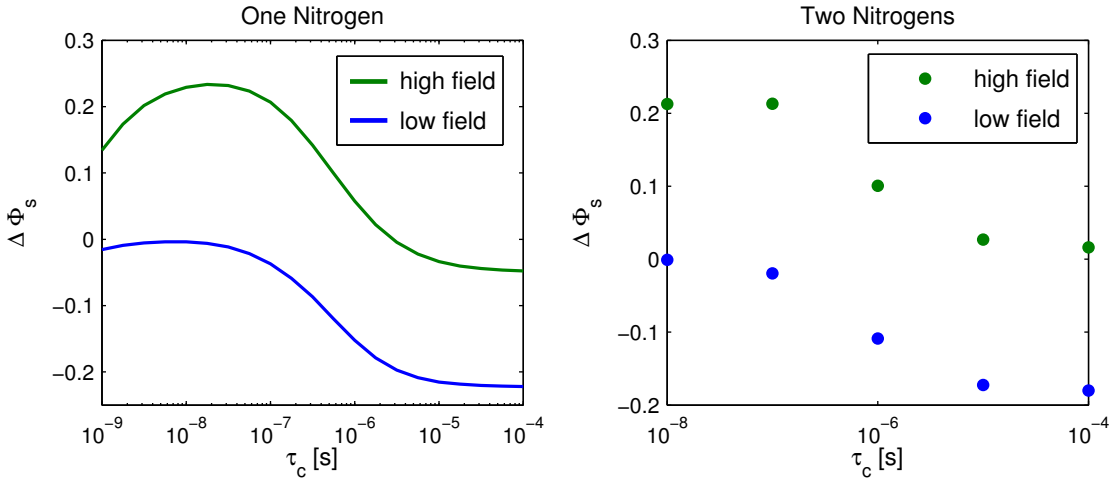

(b) Magnetic field effect $\Delta\Phi_s = \Phi_s(B_0) - \Phi_s(0)$

Figure 4.5: Simulation results at high, low, and zero field, as a function of the rotational correlation time, for a radical pair with a single nitrogen hyperfine coupling (left column), and a radical pair with two nitrogen hyperfine couplings, one in each radical (right column). The high field yield was simulated at $B_0 = 30\,\mathrm{mT}$. The low field yield was taken to be the lowest value in the curves shown in figure 4.4.

4.4 Comparison with Experiment

Assuming that cryptochrome and photolyase behave as uniform spheres in solution, their rotational diffusion constant is

$$D = \frac{k_B T}{8\pi\eta R^3}\,, \tag{4.69}$$

where η is the viscosity of the solvent, and R is the radius of the protein (see **section 4.1.3**). Erickson suggests that the typical specific volume of a protein is [44]

$$\nu = 7.3 \times 10^{-7}\,\mathrm{m}^3\ \mathrm{g}^{-1}\,, \tag{4.70}$$

such that one can estimate the equivalent spherical volume of the protein from its relative mass:

$$V = \frac{\nu M_R}{N_A} \tag{4.71}$$

where N_A is Avogadro's constant. This gives a radius of

$$R = \left(\frac{3\nu M_R}{4\pi N_A}\right)^{\frac{1}{3}}\,, \tag{4.72}$$

and a diffusion constant of

$$\begin{aligned} D &= \frac{k_B T}{6\eta V} \\ &= \frac{k_B T N_A}{6\eta\nu M_R} \end{aligned} \tag{4.73}$$

The rotational correlation time was therefore calculated as

$$\begin{aligned} \tau_c &= \frac{1}{6D} \\ &= \frac{\eta\nu M_R}{k_B T N_A} \end{aligned} \tag{4.74}$$

Magnetic field effects measured by transient absorption are reported here as a

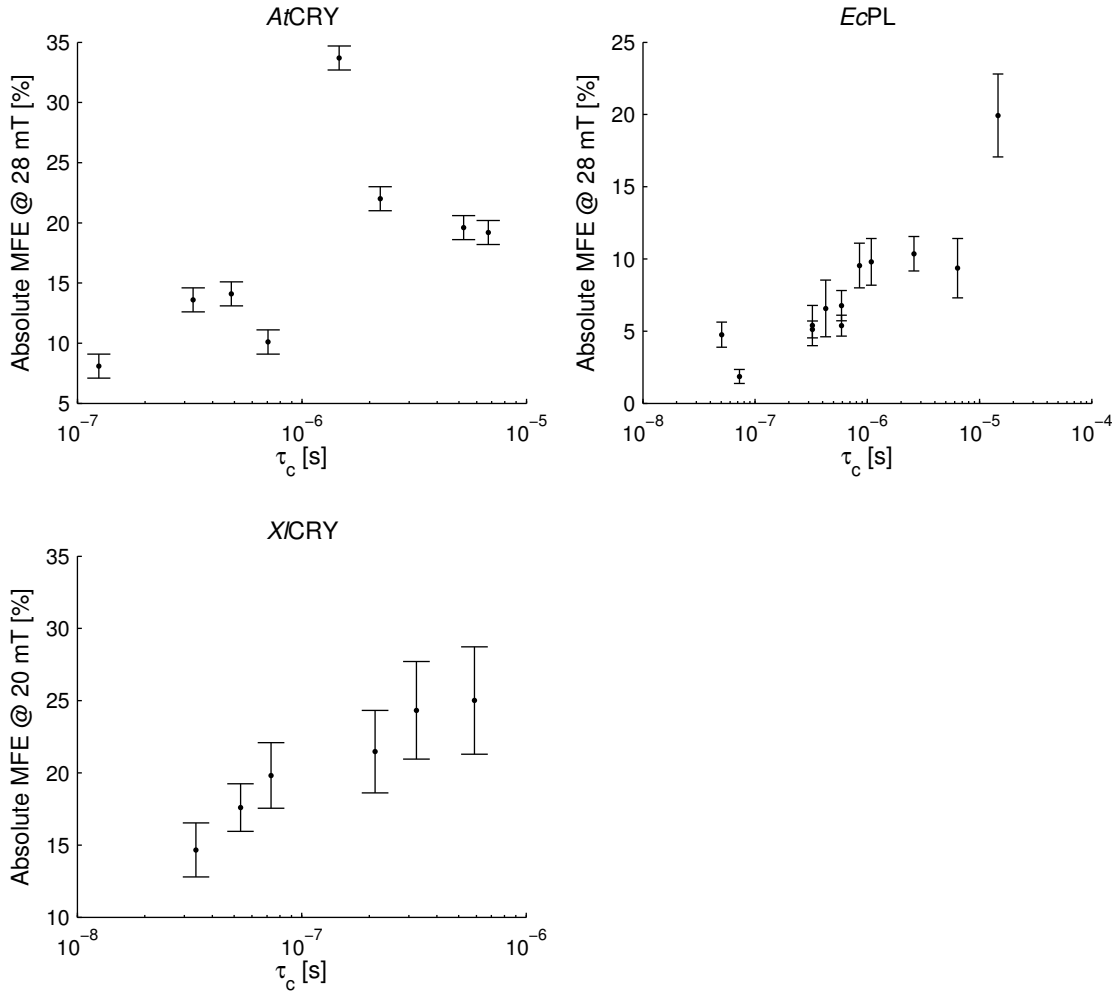

Figure 4.6: The rotational correlation times were estimated from the mass of each protein and the viscosity of the solution using equation 4.74. The viscosity was estimated from the temperature and glycerol percentage using published look-up tables [1]. The *At*Cry and *Ec*PL data were collected jointly by Robinson [148] and Maeda [113]. The *Xl*Cry data was collected by Till Biskup (unpublished).

percentage,

$$\text{MFE } [\%] = \frac{\Delta A(0) - \Delta A(B_0)}{\Delta A(0)}\,, \tag{4.75}$$

where B_0 is the applied magnetic field strength, and ΔA is the transient absorbance at 510 nm, after an excitation at 460 nm [113], and recorded after the primary radical pair had decayed. It must be noted that this absorption band corresponds to the deprotonated $\text{Trp}^{\bullet}$ of the secondary radical pair, rather than the singlet ground state, so the measured magnetic field effects had opposite sign to the simulated results presented in the current chapter.

The experimental magnetic field effects did not show the same trend as the simulated effects. Experimentally, the effect increased in magnitude with τ_c at high field (**figure 4.6**), whereas the simulations predicted the opposite trend (**figure 4.5**). However, if we note that few of the experimental data showed a low field effect [148, 14] (presumably due to some other type of spin relaxation), the increase in magnetic field effect with τ_c is similar to the increase in high field Φ_s predicted by simulation (**figure 4.5**). The experimental result is therefore what one would expect if rotational tumbling had negligible effect at weak applied fields, but had a significant effect at stronger magnetic field strengths.

In addition, MARY linewidth ($B_{1/2}$) was found to increase with τ_c in experiments carried out on *Xl*Cry (**figure 4.7**). This is the opposite trend to the one found in the rotational tumbling simulations (**figure 4.4**). This increase is likely due to a change in the rate constant k_s with glycerol concentration, which alters the rate of singlet-triplet dephasing (as discussed in the previous chapter).

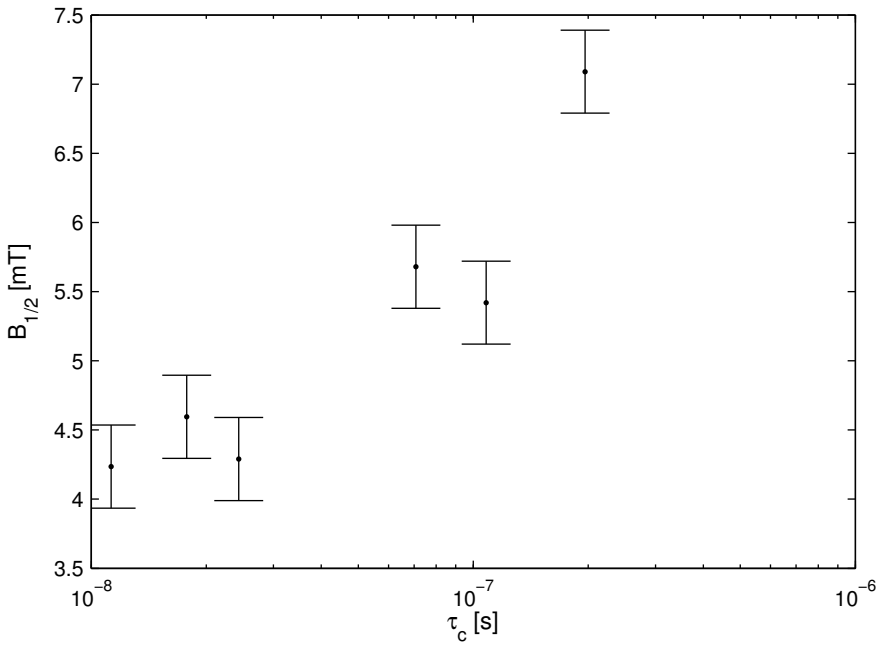

Figure 4.7: Linewidth of experimental MARY curves measured on *Xl*Cry, as a function of rotational correlation time. The rotational correlation time was estimated from the temperature and glycerol composition of the solution.

4.5 Conclusions

The extent of spin relaxation arising from rotational tumbling calculated in the present chapter is likely to be an underestimate. The hyperfine couplings in the flavin were approximated by a single nitrogen with an axiality of 3.70 mT, while those in the tryptophan radical were approximated by a single nitrogen with an axiality of 2.28 mT. The total absolute hyperfine axiality, calculated using

$$\sum_i |\Delta A_i| \,,$$

is 7.70 mT for $FAD^{\bullet-}$, and 9.54 mT for $TrpH^{\bullet+}$, using hyperfine couplings calculated by DFT [149]. Taking into account the fact that only two Euler angles were taken into account in the simulations, the extent of spin relaxation could have been underestimated by a factor of up to five. This would means that the singlet yield curves in **figure 4.5** should be slightly broadened. However, as the rotational correlation time varied over eight orders of magnitude, an underestimation in the hyperfine anisotropy of half an order of magnitude does not significantly affect the conclusions of the present chapter.

The fact that that a low field effect was not evident in the transient absorption experiments carried out on *Xl*Cry under any conditions [14], and could only intermittently be measured on *Ec*PL and *At*Cry at specific conditions [148], suggests that modulation of anisotropic hyperfine couplings by rotational tumbling was not the principal relaxation mechanism. This is because the simulations on the model system predict a substantial low field effect under experimental conditions where none was observable. Furthermore, the experimental linewidths were not consistent with those from the simulations; indeed the two had opposite trends. Therefore rotational tumbling does not have a dominant effect on the spin dynamics in the transient absorption experiment.

The relaxation mechanism responsible for the lack of a low field effect could be the

singlet-triplet dephasing discussed in the previous chapter, or libration of the $TrpH^{\cdot+}$ radical simulated by Kattnig *et al.* [91]. Nevertheless, assuming that one of these relaxation mechanisms eliminated the low field effect *in vitro*, the general increase in the magnitude of the high field effect as a function of rotational correlation time is consistent with the effect found by simulation in the current chapter. However, the same trend is expected from a modification of the ratio $\frac{k_s}{k_p}$, as discussed in the previous chapter.

A shortcoming of the simulations was that a maximum of two hyperfine couplings could be included. It is possible that the lack of an experimental low field effect was in part due to the many hyperfine couplings in the $FAD^{\cdot-}$ $TrpH^{\cdot+}$ radical pair. It is worth noting that radical pair composed of flavin mononucleotide (FMN) and tryptophan showed no experimental low field effect, while a FMN ascorbic acid radical pair, with far fewer hyperfine couplings, showed a significant low field effect [123, 90].

Rotational tumbling is unlikely to be a significant source of spin relaxiation *in vivo*, as cryptochrome is likely to be fixed in a membrane, or in a cell far more viscous than the solutions considered in the current chapter. In a living cell, singlet-triplet dephasing (discussed in the previous chapter) and libration of the residues containing the radicals will have a far more significant contribution to spin relaxation than tumbling.

Chapter 5

Detection of Anisotropy in Spin-Chemical Reactions with AMELIA

The work in this chapter was carried out in order to evaluate the AMELIA (Angle Modulated Experiment for Lock-In Detection of Anisotropy) experiment, which measures anisotropy in spin-chemical reactions. Here, anisotropy refers to differing singlet recombination yield as a function of the direction of the applied magnetic field. This can occur due to anisotropic spin interactions in an aligned system, such as the hyperfine interaction in a radical pair aligned in a liquid crystal solvent [111].

Storey has convincingly measured magnetic field effect anisotropy with applied fields as low as 0.8 mT, using a transient absorption experiment [162]. AMELIA is also designed to measure anisotropy at weak magnetic fields (< 10 mT), but is based on steady-state fluorescence spectroscopy, using a rotating magnetic field with lock-in detection to improve sensitivity.

The current chapter will consider not reactions between radical pairs, but triplet exciton annihilation in polyacene crystals, which are known to exhibit anisotropic magnetic field effects. The anisotropy is not due to a hyperfine interaction, but due to zero-field splitting within each exciton. Such crystals are far easier to prepare than

aligned or otherwise immobilized radical pairs. Anthracene and tetracene crystals were chosen as evaluation samples, as these crystals are relatively well understood on both a theoretical and experimental level. Both anthracene [84, 31, 92, 165] and tetracene crystals [60, 89] have shown anisotropic magnetic field effects on fluorescence, at relatively large magnetic fields (40 mT to 500 mT). However, experimental results [84, 10] suggested that anisotropy could exist at lower applied fields ($<$ 10 mT).

Polyacene Crystals have a Wide Range of Potential Applications

Polyacene crystals and films have gained much scientific attention in recent years. These materials have been proposed as novel sensitizing dyes for solar cells, as excitation with visible or UV light can produce two energy carriers (two triplet excitons) per photon absorbed. The polyacene molecules could be layered upon a material with a more positive reduction potential than the triplet exciton state, and therefore inject electrons into the substrate. The electrons would then be free to traverse an external circuit and power an external load [142]. The solar cell could then be placed in a magnetic field of an appropriate strength to minimize triplet-triplet annihilation.

Functionalized polyacenes, including anthracene and tetracene, have been used to improve the efficiency of organic light-emitting devices (OLEDs). These compounds have been used both as light-emitting layers and hole transport layers [137]. These work by placing a voltage across the polyacene, and therefore injecting electrons and holes. The electrons and holes meet to form a singlet or triplet exciton. The singlet state fluoresces directly, while the triplet state phosphoresces much more slowly. Typically, to improve efficiency, the emitting layer is functionalized to promote intersystem crossing from triplet to singlet [184]. An alternative method could be to promote emission due to triplet exciton annihilation, by applying a suitable magnetic field.

Furthermore, a MASER (microwave amplification by the stimulated emission

of radiation) has been constructed by photoexciting pentacene with a laser in a resonnant cavity [140]. This maser relies on an isolated pentacene molecule in a crystal matrix, where intersystem crossing converts the excited singlet state to a triplet subspace with a population inversion.

5.1 Magnetic Field Effects on Polyacene Crystals

Photoexcitation Produces Mobile Triplet Excitons

The idea that light absorbed by an organic crystal can migrate as an exciton was first proposed in the 1950s [110, 37]. Evidence for the process appeared in the form of delayed fluorescence after ultraviolet excitation of naphthalene and phenanthrene crystals [159, 17], which was later explained by singlet exciton fission to form a pair of triplet excitons, together with diffusion and mutual annihilation of triplet excitons (**figure 5.1**) [77, 132]. Jortner published a theory of triplet exciton hopping between molecules, arguing that the migration is caused by weak exchange interactions together with lattice phonons [87]. This theory was improved by Swenberg [165] to account for anisotropy in the diffusion tensor, and then by Suna to incorporate magnetic field effects and spin relaxation [163].

Singlet excitons have also been shown to be mobile in polyacene crystals [179], although unlike triplet excitons, they are thought to have delocalized character due to charge transfer [186]. However, there is no evidence that the dynamics of singlet excitons can be affected by a magnetic field, so they have little relevance to the this thesis.

Triplet Exciton Fusion is Spin Selective

A triplet exciton is a pair of electrons in an excited triplet state. The principal interaction between the electrons, zero-field splitting, does not interconvert singlet and triplet states, so the singlet state can be ignored and the pair of electrons treated as a single, spin-one, particle.

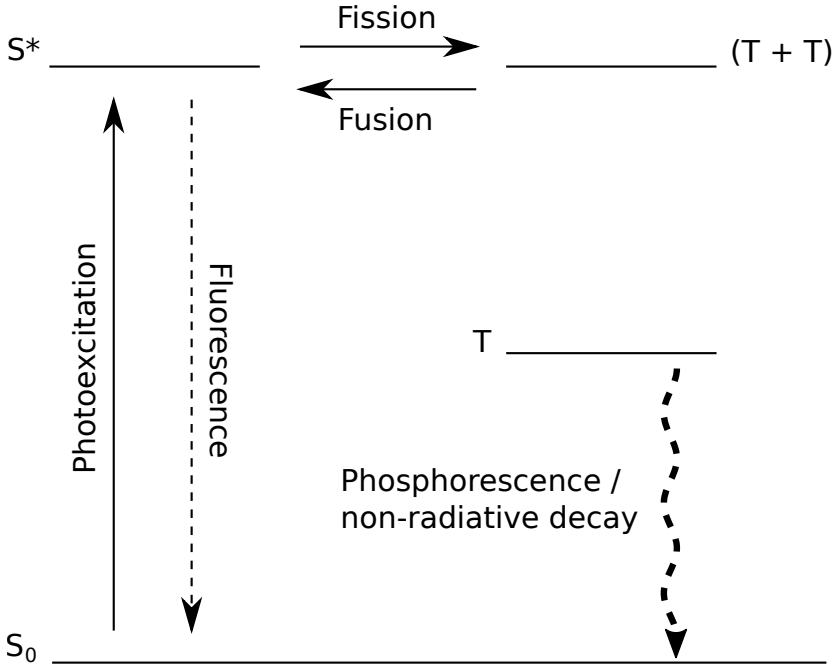

Figure 5.1: Singlet exciton fission to produce two triplet excitons, whose overall energy is similar to that of the excited singlet state. Triplet excitons can also be created directly from the S_0 state with a strong red excitation.

When a pair of triplet excitons come in contact, the spin state of the pair must follow the Clebsch-Gordon rules of adding spin, where the combined spin quantum number S has allowed values [151]

$$S = |S_1 - S_2|\,,\ |S_1 - S_2| + 1\,, \cdots\,, S_1 + S_2\,. \tag{5.1}$$

For a pair of triplet excitons, the allowed states are therefore

$$\begin{aligned} S &= 0 \quad \text{(singlet)} \\ S &= 1 \quad \text{(triplet)} \\ S &= 2 \quad \text{(quintet)}\,. \end{aligned} \tag{5.2}$$

When a molecule in its ground S_0 state absorbs a photon, the excited S^* state maintains singlet character. The excited molecule can react with a neighboring molecule in its ground state to form a pair of triplet excitons whose combined spin

state is singlet:

$$S_0 + S^* \longrightarrow (T + T)^{S=0} \tag{5.3}$$

Conversely, a pair of triplet excitons can react to form a pair of molecules in the singlet state, as long as the exciton pair has an overall singlet state:

$$T + T \xrightarrow{\text{spin selective}} S_0 + S^* \longrightarrow S_0 + S_0 + h\nu \tag{5.4}$$

Although a pair of triplet excitons created according to **equation 5.3** has an initial singlet state, the pair quickly gains quintet character due to coherent spin evolution, which is caused by the zero field splitting within each exciton. Instead of fusing, a pair of triplet excitons can diffuse apart. This creates a reaction scheme very similar to the radical pair mechanism, where the singlet recombination yield can be altered by an external magnetic field (**figure 5.2**).

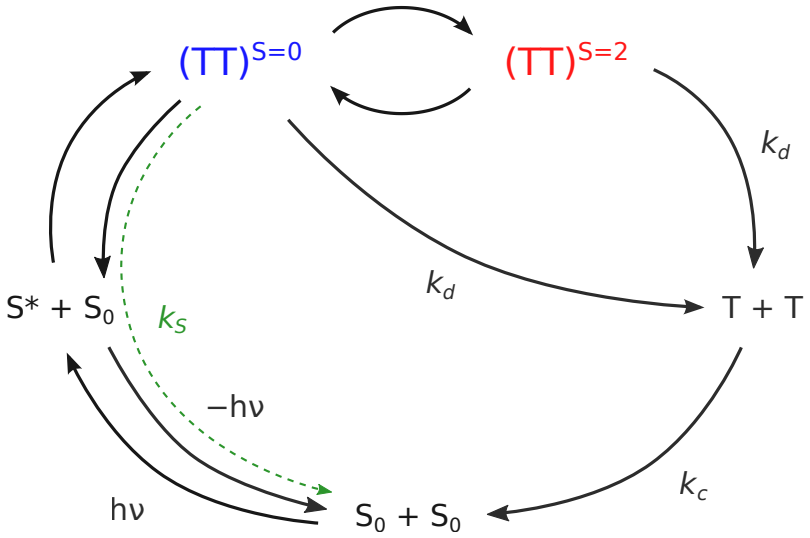

Figure 5.2: Reaction scheme for a pair of triplet excitons generated from an excited singlet state. The contact exciton pair (TT) has an initial singlet state, which is coherently interconverted with a quintet state, due to zero field splitting within each exciton. The rate of interconversion can be modefied by the direction and strength of an applied magnetic field. The triplet exciton pair can either spin-selectively recombine to the ground singlet state at rate k_s, resulting in delayed fluorescence, or diffuse apart at rate k_d. The rate k_c represents return of an individual triplet exciton to the ground state, by phosphorescence or non-radiative means.

This effect has been well studied in crystalline anthracene – an applied magnetic

field can alter the rate of triplet exciton annihilation, and therefore alter the delayed fluorescence intensity from the reaction in **equation 5.4**. [121, 10]. Moreover, this effect depends not only on the strength of the applied magnetic field, but also on the field's direction, due to the anisotropy of the zero field splitting interaction [84].

In addition to singlet exciton fusion, the S_1 state leads to photodimerization in anthracene, and presumably in higher acenes too [167]. The photoexcitation beam power must therefore be minimized to avoid degradation of the crystal.

Hyperfine and Interexciton Dipolar Interactions are Negligible

In principle, dipolar effects between excitons, and hyperfine coupling between an exciton and its surrounding nuclei, could contribute to this anisotropy. However, there is no evidence of hyperfine coupling in the EPR spectrum of triplet excitons in tetracene or anthracene, which this is thought to be due to rapid exciton hopping between host molecules [187, 10]. Suna [163] estimates that the dipolar interaction between excitons is

a) negligible for interexciton distances greater than two lattice spaces,

b) an order of magnitude smaller (in frequency units) than the exciton hopping rate,

and can therefore be neglected. Furthermore, Burdett's study of quantum beats in the transient fluorescence from crystalline tetracene showed no evidence of a dipolar interaction between excitons [26].

Triplet Excitons Diffuse in the *ab* Plane

Triplet excitons in anthracene and tetracene are believed to be mobile in two dimensions only, otherwise their re-encounter probability would be too low to explain the magnetic field effects observed [165]. This diffusion anisotropy has been experimentally observed in both anthracene [45] and tetracene [4], with the diffusion restricted to the crystallographic *ab* plane in both cases. The measured diffusion coefficient

in anthracene was of the order of $10^{-4}\,\mathrm{cm}^2\,\mathrm{s}^{-1}$, while that of tetracene has been measured to be of the order of $10^{-3}\,\mathrm{cm}^2\,\mathrm{s}^{-1}$.

Delocalization Splits the Excited Electronic States

On absorption of a photon, the excited singlet state (*i.e.* a singlet exciton) is delocalized across several lattice positions. This effect is responsible for the Davydov splitting in the energy of the absorption and emission bands in the electronic spectra of polyacene crystals [144]. To a first approximation, this is due to electric dipolar effects between adjacent molecules of differing orientation (**figure 5.3**) [186]. The transition dipole moment is spread over several neighboring molecules, and is the vector addition of the unimolecular transition dipole moments. In the case of two inequivalent sites, each dipole moment can be pointing one of two ways, giving two possible perpendicular transition dipole moments in the crystal.

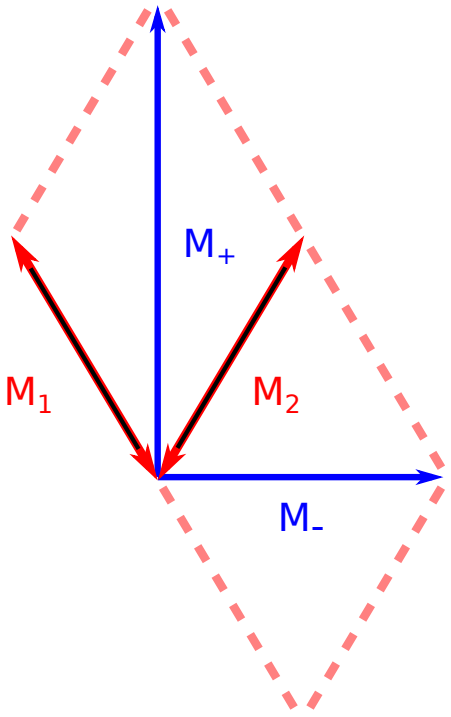

Figure 5.3: Davydov splitting of an excited electronic state in a crystal. M_1 and M_2 are molecular transition dipole moments of orientationally inequivalent molecules. M_+ and M_- are the resulting Davydov transition dipole moments that would be observed in the crystal.

The practical effect on emission spectroscopy from triplet-triplet annihilation is that

due to Davydov splitting, there is less emission anisotropy than there would have been given a single transition dipole moment.

Crystal Quality is Paramount

Triplet excitons can become trapped at defect sites in the crystal lattice, such as substitutions or grain boundaries [165], where alternative annihilation mechanisms are active [121, 26]. Therefore the raw material used for the crystallization must be extensively purified, for example by zone refining or repeated sublimation in an inert gas - raw polyacenes from mainstream chemical manufacturers, even at scintillation grade, are not pure enough [139]. The crystal quality can be verified by observing the crystal between crossed polarizers. A poor quality crystal shows clear grain boundaries when rotated, and displays a mosaic pattern at maximum extinction [108].

5.1.1 Anthracene

The first conclusive evidence of triplet exciton annihilation in anthracene was presented by Kepler [92], where the annihilation was postulated to be responsible for delayed fluorescence. A magnetic field effect on this fluorescence was subsequently measured by Johnson [85], and a spin-chemical mechanism was presented by Johnson and Merrifield [84]. These authors found a 5 % increase in the triplet exciton annihilation rate at 35 mT, and at saturation a 15 % decrease in the annihilation rate at 500 mT. Furthermore, they found that the magnitude of the magnetic field effect depended on the orientation of the applied magnetic field, which they explained, at high field, to be caused by level crossings in energy levels of the spin Hamiltonian. Although they observed anisotropy at weaker magnetic fields too, they did not provide a theoretical justification for this, and the weakest field studied was 10 mT. For comprehensive reviews, see Merrifield [121] and Avakian [10].

In the work by Merrifield and Johnson, triplet excitons were generated by direct excitation with intense red light; however, Klein demonstrated that triplet excitons

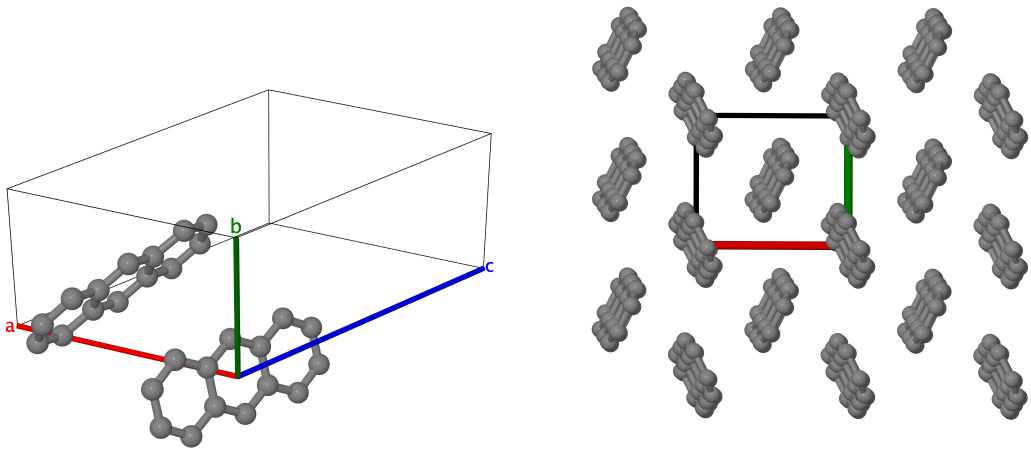

Figure 5.4: Left: unit cell of anthracene. a and b axes are orthogonal, as are b and c, while the angle $\widehat{ac}$ (also known as β) is 124.7°. Right: herringbone pattern viewed along the c axis.

could also be generated by fission of an excited singlet state, following excitation with UV light [97]. Singlet exciton fission is believed to be rather endothermic ($\sim 50\,\mathrm{kJ\,mol^{-1}}$) in anthracene [11], and as such triplet exciton generation this way is very inefficient ($\sim 0.2\,\%$) [60].

The presence of triplet excitons has been confirmed by electron paramagnetic resonance [70, 68], which gives zero field splitting parameters of

$$\begin{aligned} D &= -5.6 \pm 1.0\mathrm{mT} \\ E &= 35 \pm 3.0\mathrm{mT}\,, \end{aligned} \tag{5.5}$$

and gives indirect support to the exciton hopping mechanism due to the lack of hyperfine splitting.

Crystalline anthracene has a monoclinic unit cell ($a = 8.56\,\text{Å}$, $b = 6.04\,\text{Å}$, $c = 11.16\,\text{Å}$, $\beta = 124.7°$, **figure 5.4**), with two molecules related by a symmetry transformation (space group $P2_1/a$) [146, 27]. The long axis of both molecules is approximately aligned with the c crystallographic axis (**figure 5.5**). The symmetry of this unit cell means that the b axis is one of the principal axes of anisotropic phenomena, while the other two axes lie in the ac plane, intermediate to the non-orthogonal a and b axes.

Anthracene crystals can be oriented using their optical properties. Nakada [130] has experimentally measured the principal optical axes[1] and principal refractive indices of crystalline anthracene. The principal axes can be identified as directions of maximal extinction when viewed through a polarizing microscope with polarizer and analyzer oriented at 90° to each other. [108].

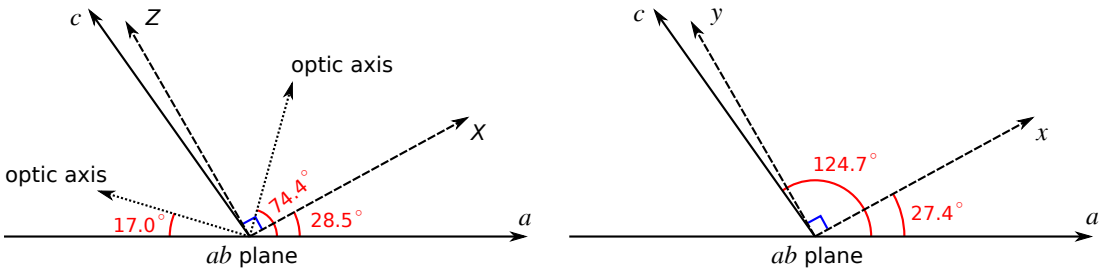

(a) Optical Axes

(b) Zero field splitting axes

Figure 5.5: Principal optical axes (X, Y and Z) of the refractive index tensor [130], and of the zero field splitting tensor (x, y and z) [84], in relation to the crystallographic axes. The b, Y and z axes are parallel, and go into the page. Note that the principal optical axes and zero field splitting axes are within experimental error of each other.

Suna has estimated the spin-relaxation rate constant for a pair of triplet excitons in anthracene to be $8.2 \times 10^7\,\mathrm{s}^{-1}$ [163]. He assumed stochastic modulation of the principal axes of the zero field splitting tensor, due to hopping between lattice cites in the *ab* plane, but neglected the effect of modulation of the interexciton dipolar interaction. The inclusion of the latter interaction would not greatly affect the estimate of the relaxation rate, as it is generally much weaker than the zero field splitting, and would be modulated by the same hopping rate.

5.1.2 Tetracene

Anisotropic magnetic field effects have been reported in tetracene, and have been confirmed by three different research groups [60, 120, 89, 69]. As with anthracene, anisotropy at high magnetic field ($\sim 300\,\mathrm{mT}$) has been explained in terms of level-crossings in the energies of the spin Hamiltonian, but little attention has been paid

[1] One must not confuse principal optical axes, which are eigenvectors of the refractive index tensor, with the optic axis, which is the axis along which no birefringence is visible.

to anisotropy at lower magnetic fields. The magnetic field effect has been demonstrated on triplet excitons generated by singlet exciton fission, by the fission of charge transfer excitons created by electrochemical means, and by direct excitation with intense red light.

The presence of triplet excitons has been confirmed by electron paramagnetic resonance [187], which gives zero field splitting parameters of

$$\begin{aligned} D &= -6.63\,\mathrm{mT} \\ E &= 26.53\,\mathrm{mT}\,. \end{aligned} \tag{5.6}$$

Singlet exciton fission to form a pair of triplet excitons is believed to be slightly endothermic ($\sim 20\,\mathrm{kJ\,mol^{-1}}$) in tetracene [69, 167], however, much less so than in anthracene. This makes the fission process much more energetically favorable in tetracene than in anthracene - the former has a measured fission efficiency of close to 100 % [187, 69]. The fission is thought to occur through nonadiabatic coupling mediated by intermolecular motion [191].

Magnetic field effects on steady state fluorescence from tetracene have opposite phase, depending on whether the triplet excitons were created by fission of the S_1 state or directly by excitation with red light [69]. This is because the initial spin state of the pair in the former case is singlet, while in the latter case excitons encounter randomly, so are far more likely to be in a quintet state when they collide.

Recent studies suggest that **figure 5.1** (p. 134) is not entirely accurate for tetracene. Tayebjee's time-resolved studies suggest that the S_1 state decays, on a picosecond timescale, to a state with multiexciton character, which fluoresces back to the ground state in nanoseconds [167]. This multiexciton state is believed to thermally fission into a pair of triplet excitons. For the purposes of this thesis, the existence of the multiexciton state is irrelevant, as it does not alter the hypothesis of the creation of a pair of excitons in overall spin singlet state.

Tetracene has a similar crystal structure to anthracene, except that its unit cell is triclinic ($a = 7.90\,\text{Å}$, $b = 6.03\,\text{Å}$, $c = 13.53\,\text{Å}$, $\alpha = 100.3°$ $\beta = 113.2°$, $\gamma = 86.3°$)

[27], meaning that the two molecules in the unit cell are unrelated by a symmetry transform. In practice, this means that the principal axes of macroscopic properties derived from average molecular properties (refractive index, zero field splitting...) are not aligned with any of the crystallographic axes.

Burdett estimates the population relaxation and dephasing times of a triplet exciton pair to be of the order of 1 ns [26]; however, he ignored the well established effect of exciton diffusion, which would better explain the damping in the quantum beats he observed. According to Suna's theory of relaxation due to hopping between molecules of different orientation, the spin relaxation time constant should be of the order 10^6 to $10^7\,\mathrm{s}^{-1}$ [163], based on a diffusion constant in the *ab* plane of $\sim 10^{-3}\,\mathrm{cm}^2\,\mathrm{s}^{-1}$ [6, 4].

5.1.3 Pentacene

Pentacene also exhibits singlet exciton fission, which is believed to be energetically downhill [168, 191], so much so that there is no evidence of fluorescence from crystalline pentacene in the scientific literature. This also suggests that the energetics prevent triplet exciton annihilation to reform the excited singlet state. Magnetic field effects on fluorescence are therefore unlikely; however, the triplet excitons could well take part in other spin-selective reactions.

5.2 The AMELIA Experiment

Magnetic field effects can be measured by applying an oscillating magnetic field to a sample and measuring the corresponding oscillation in fluorescence intensity [135, 182, 88, 178]. This method is particularly useful when the magnetically dependent fluorescence wavelength is superimposed on a much stronger bulk fluorescence.

Essentially, AMELIA measures the anisotropy in the steady-state fluorescence from a sample under continuous excitation (**figure 5.6**). An anisotropic sample is placed in a slowly rotating magnetic field of constant magnitude, and excited with a

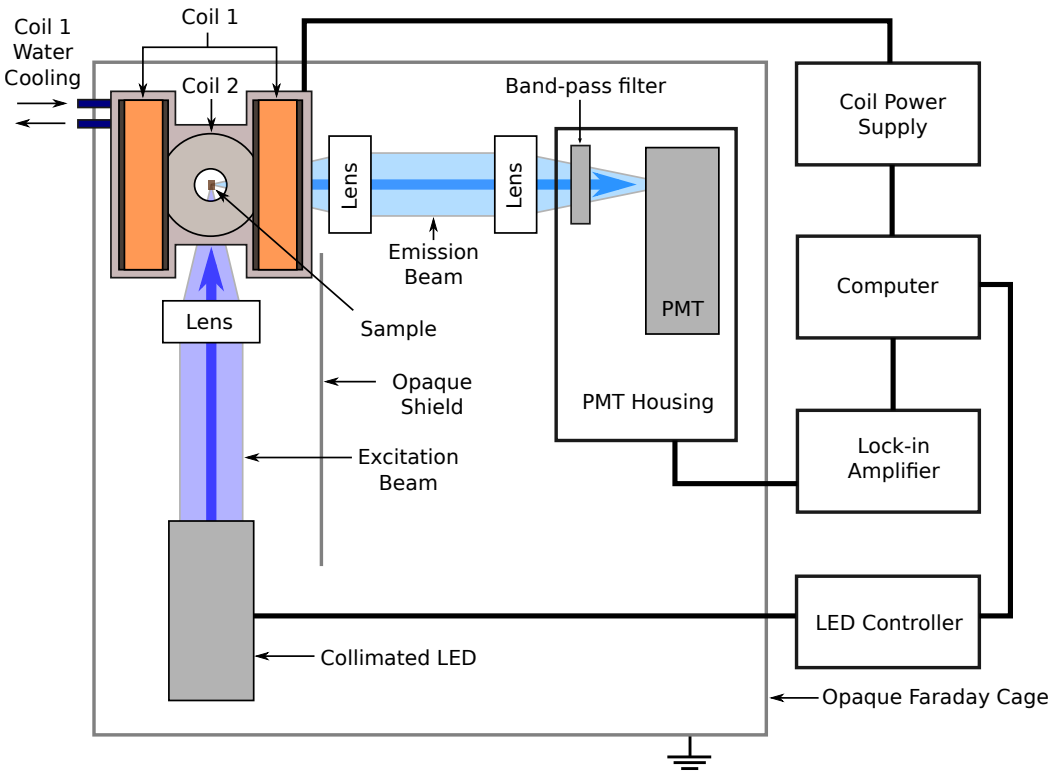

Figure 5.6: Bird's eye view of the AMELIA experiment. A rotating magnetic field was created by two pairs of Helmholtz coils, one horizontal (coil 1) and the second vertical (coil 2). An oriented sample was placed in the center of the coils, such that the field rotated in a specific crystal plane. Fluorescent emission from the sample was collected, and modulation in intensity, indicating anisotropy, was measured with a lock-in amplifier. The instrument was fully automated using a computer.

light-emitting diode (LED). Any modulation of the resultant fluorescence intensity is detected with a lock-in amplifier, which outputs a positive voltage R, whose magnitude is indicative of the anisotropy in the magnetic field effect. It is important to stress that this is **not a resonance effect**; rather the applied field rotates far more slowly than the timescale of the reaction dynamics, so that the fluorescence intensity at a given point in time is essentially the steady-state fluorescence expected for the given applied field strength and orientation. The AMELIA technique has been briefly described before [48, 162], but has been improved and fully validated in the current work.

Rotating Magnetic Field was Generated by a Pair of Helmholtz Coils

The larger coil (coil 1) was arranged horizontally, and the smaller coil (coil 2) vertically, with a sample inlet on top. Four port-holes 90° apart provided a path for light to reach and leave the sample. Small coil diameters (coil 1: 10 cm, coil 2: 5 cm) were chosen to minimize the inductance of the coils, and thereby facilitate the generation of low frequency (< 100 Hz) oscillating magnetic fields. The outer coil was cooled with distilled water supplied from a bucket using a small pump, while the inner coil did not require cooling as it did not heat noticeably. The coils and their housing were painted matt black, to avoid stray light reflecting onto the photomultiplier tube. The coil assembly was not shielded from the Earth's magnetic field.

The coils were calibrated (see **Appendix C**) to create a rotating magnetic field by generating in each coil a sinusoidal magnetic field of equal amplitude, but with a phase difference of 90°. The coils were able to provide a field strength of up to 10 mT when rotating at a frequency of 83 Hz, and a field strength of up to 17 mT when rotating at 31 Hz. These low frequencies were chosen such that the applied field would be approximately static on the timescale of the reaction dynamics. The sinusoidal voltage for each coil was generated in parallel using a computer-controlled signal generator card (Adlink DAQ-2501), and amplified using a custom-built power supply before being sent to the coils.

Table 5.1: Magnetic field stability parameters measured with a SENIS C-H3B-2m-E3D Hall probe connected to a TDS 220 oscilloscope *via* an in-house built amplifier.

Property	Coil 1	Coil 2
Amplitude Instability [%] (over 60 s period)	< 1	< 0.5
Frequency Drift [%]	< 0.1	< 0.05
Residual Magnetization [mT]	< 0.02	< 0.02
Inhomogeneity [%] (over 5 mm × 5 mm × 5 mm volume)	< 1	< 1
Orthogonality [°]	$\pm$ 0.5	$\pm$ 0.5

The coil stability was evaluated with a SENIS C-H3B-2m-E3D time-resolved three-dimensional Hall probe connected to a Tektronix TDS-220 oscilloscope (**table 5.1**). The coil assembly showed negligible residual magnetization; however, the

power supply had a DC offset that had to be calibrated. Coil 1 was less stable than coil 2, the former even becoming warm to the touch after a few minutes' continuous operation. This was most likely due to the larger size of coil 1; a longer coil length resulting in a greater electrical resistance, and a larger current required to generate the same magnetic field as coil 2.

Crystals were Mounted and Fixed to a Goniometer

Single crystal samples were glued to a circular float glass window using methyl 2-cyanoacrylate (Loctite Gel). This glue was chosen as it was found to produce negligible fluorescence at the excitation wavelengths of anthracene and tetracene. The glass window was then attached to a custom-built goniometer that suspended the sample between the coils. Liquid samples were held vertically between the coils in a fluorescence cuvette, using a custom-built holding rod.

The sample was excited using a collimated LED focused onto the sample with a lens, controlled by a Thorlabs DC2100 power supply attached to a computer. The fluorescence from the sample was collected by a lens along the axis perpendicular to the direction of the excitation beam (**figure 5.6**). A second lens focused the fluorescence beam onto the photomultiplier tube, passing through a band-pass filter of appropriate wavelength.

The experiment was surrounded on all sides by a grounded, opaque, Faraday cage, made of black anodized aluminium, in order to avoid electromagnetic interference and light contamination. The floor of the Faraday cage was made of a sheet of aluminium foil covered in black electrical tape. A black anodized aluminium shield prevented divergent light from the LED from reaching the photomultiplier tube (PMT). The PMT (Hamamatsu R928) and its transimpedance amplifier (Hamamatsu C6271) were encased in a magnetically shielded box, which was placed 37 cm from the magnetic coils, where the stray field from the coils was negligible. In addition, the photomultiplier tube was the side-on type, rated by the manufacturer to be less sensitive to stray magnetic fields than the head-on type [2].

Fluorescence Modulation was Measured by a Lock-in Amplifier

The signal from the photomultiplier tube was collected by a lock-in amplifier (Stanford Research Systems SR830) using a doubly-shielded cable (differential signal collection was not possible due to the design of the transimpedance amplifier). The PMT signal was sent to input A (for detection of the oscillating signal) and to auxiliary input 1 (to measure the raw PMT voltage). The shielding at the lock-in amplifier inputs was set to float, so that the PMT would only sense one ground and thus avoid noisy ground-loop currents. The gain of the PMT's transimpedance amplifier was set by a voltage signal from the lock-in amplifier's (LIA) auxiliary output. This was adjusted to give a (direct current) PMT voltage of approximately 10 V for every experiment. The shielding of the transimpedance amplifier's gain input was isolated from the rest of the PMT assembly's shielding, again to avoid a ground loop [160].

The signal at the lock-in amplifier's input A was AC-coupled to remove the direct current component, and harmonics of the reference frequency were removed using the device's SYNC filter. The reference frequency was chosen to be either twice or four times the magnetic field rotation frequency, as antiparallel applied field directions are equivalent – therefore any magnetically induced oscillation in the fluorescence must be at least twice the rotation frequency. To avoid slight differences between the lock-in amplifier's reference frequency and that of the rotation of the applied magnetic field, the LIA's internal oscillator was driven in parallel by a square wave from the same signal generator card (Adlink DAQ-2501) that was driving the magnetic coils.

High dynamic reserve (essentially the ratio of the LIA's output gain to its input gain) was used for all measurements, as the signal from the PMT tended to be noisy and overload the LIA at higher input gains. All measurements were recorded with a filter slope of 24 dB per octave. The sensitivity (essentially the highest voltage measurable by the LIA, and inversely proportional to gain) was chosen for each sample and orientation by performing two pre-measurements at high sensitivity, at

the maximum field strength, and half of that value. Quadrature detection was used to avoid the need of phasing the LIA to the input signal.

After setting the magnetic field strength, the LED illuminated the sample for a time period of 10× the time-constant, after which the LIA measured the average and standard deviation of the anisotropy R. The coils and LED were turned off for a period of 15× the time-constant before measuring the next point. This was to allow the sample to recover, and to avoid overheating the coils. Measurements were taken at random magnetic field order, to avoid a systematic error from sample degradation. The experiment was controlled by a C++ program co-written with Dr. Jonathan Storey. The calibration procedure is detailed in **Appendix C.**

5.3 Mathematical Description

A lock-in amplifier receives an input signal, compares it to in internal reference sine wave at a chosen frequency, and filters out all other frequencies. The device then measures the root mean square (RMS) voltage R at the chosen frequency; essentially measuring the Fourier component of the input signal at the reference frequency.

Naturally, the filtering is imperfect, as a LIA cannot fully filter out frequencies close to the one chosen. The filter bandwidth depends on the instrument's time constant (τ_c), with a larger time constant giving a sharper filter, at the expense of requiring a longer measurement time [160].

A modern LIA analyzes the input signal in quadrature (*i.e.* with both a sine and a cosine reference) in order to ensure correct phasing, giving RMS voltages X and Y corresponding to the two components 90° out of phase. These two components are combined to give

$$R = \sqrt{X^2 + Y^2}\,, \tag{5.7}$$

the RMS voltage of the oscillating input signal. In order to compute X (or Y), the LIA's phase-sensitive detector (PSD) compares the input voltage (V_{in}) to a voltage oscillating at the chosen reference frequency (V_{ref}). The signal computed by the LIA

(under a continuous time approximation) is

$$\begin{aligned} X(t) &= \frac{\sqrt{2}}{\tau_c} \int_{t-\tau_c}^{t} V_{\text{in}}(t') V_{\text{ref}}(t')\, dt' \\ &= \frac{\sqrt{2}}{\tau_c} \int_{t-\tau_c}^{t} V_{\text{PSD}}(t')\, dt' \end{aligned} \tag{5.8}$$

where the constant before the integration sign means that a correctly phased sinusoidal input signal with $V_{\text{rms}} = 1\,\text{V}$ results in a reading $X = 1\,\text{V}$ (once the value has stabilized). The time constant τ_c is chosen by the user, with a larger value giving a sharper frequency filter, but naturally requiring a longer duration before the reading stabilizes.

In the AMELIA experiment, V_{in} is AC-coupled to remove any direct-current signal. V_{ref} was chosen to be the second (or fourth) harmonic of the rotation frequency ω_{rot} of the applied magnetic field. This is because antiparallel directions of the applied field are equivalent for spin-chemical reactions, so the modulation in fluorescence must have a period of half that of the rotation of the magnetic field. Higher harmonic components are also expected, given that the high-field anisotropy measured by Johnson and Merrifield did not have a sinusoidal profile [84].

Assuming that the experimental signal is composed of an oscillation at $2\omega_{\text{rot}}$, plus additional noise frequencies ω_n,

$$V_{\text{in}}(t) = a \sin(2\omega_{\text{rot}} t) + b \cos(2\omega_{\text{rot}} t) + \sum_n \left[c_n \sin(\omega_n t) + d_n \cos(\omega_n t) \right]. \tag{5.9}$$

At second harmonic detection, for the X channel,

$$V_{\text{ref}}(t) = \sin(2\omega_{\text{rot}} t)\,, \tag{5.10}$$

giving

$$V_{\mathrm{PSD}}(t) = a\sin^2(2\omega_{\mathrm{rot}}t) + b\cos(2\omega_{\mathrm{rot}}t)\sin(2\omega_{\mathrm{rot}}t) + \sum_n \left[c_n \sin(\omega_n t)\sin(2\omega_{\mathrm{rot}}t) + d_n \cos(\omega_n t)\sin(2\omega_{\mathrm{rot}}t)\right]. \quad (5.11)$$

With an infinitely long time-constant, the only term that contributes to the integral in **equation 5.8** is $a\sin^2(2\omega_{\mathrm{rot}}t)$, as this term contains a constant according to the mathematical identity

$$\sin^2(\omega t) = \frac{1-\cos(2\omega t)}{2}. \quad (5.12)$$

The other terms are purely oscillatory, as evidenced by the trigonometric identities

$$\sin(\omega_1 t)\sin(\omega_2 t) = \frac{\cos[(\omega_1-\omega_2)t] - \cos[(\omega_1+\omega_2)t]}{2} \quad (5.13)$$

and

$$\cos(\omega_1 t)\sin(\omega_2 t) = \frac{\sin[(\omega_1+\omega_2)t] - \sin[(\omega_1-\omega_2)t]}{2}. \quad (5.14)$$

However, if some noise frequency ω_n is close to $2\omega_{\mathrm{rot}}$, the resulting $\cos[(\omega_n - 2\omega_{\mathrm{rot}})t]$ and $\sin[(\omega_n - 2\omega_{\mathrm{rot}})t]$ terms will oscillate slowly, and may be incompletely averaged out under the integral in **equation 5.8**, resulting in noise in the output X. In principle this can be solved by increasing the time constant, but there is a trade-off in terms of increased sample degradation under the continuous excitation with the LED. Noise frequencies are efficiently filtered out for

$$\tau_c \gg \frac{1}{|\omega_n - 2\omega_{\mathrm{rot}}|}. \quad (5.15)$$

The same signal processing occurs in the Y channel of the LIA, except with

$$V_{\mathrm{ref}}(t) = \cos(2\omega_{\mathrm{rot}}t). \quad (5.16)$$

The resulting X and Y signals, collected after a set period of time (once the signals have stabilized), are combined according to **equation 5.7** to give R, a measure

of the anisotropy in the magnetic field effect. A phase,

$$\theta = \arctan\left(\frac{Y}{X}\right) , \tag{5.17}$$

is also calculated, whose stability is a measure how well the LIA has discriminated the oscillating fluorescence over the background noise. The signal processing of an idealized fluorescence signal by the lock-in amplifier is demonstrated in **figure 5.7**.

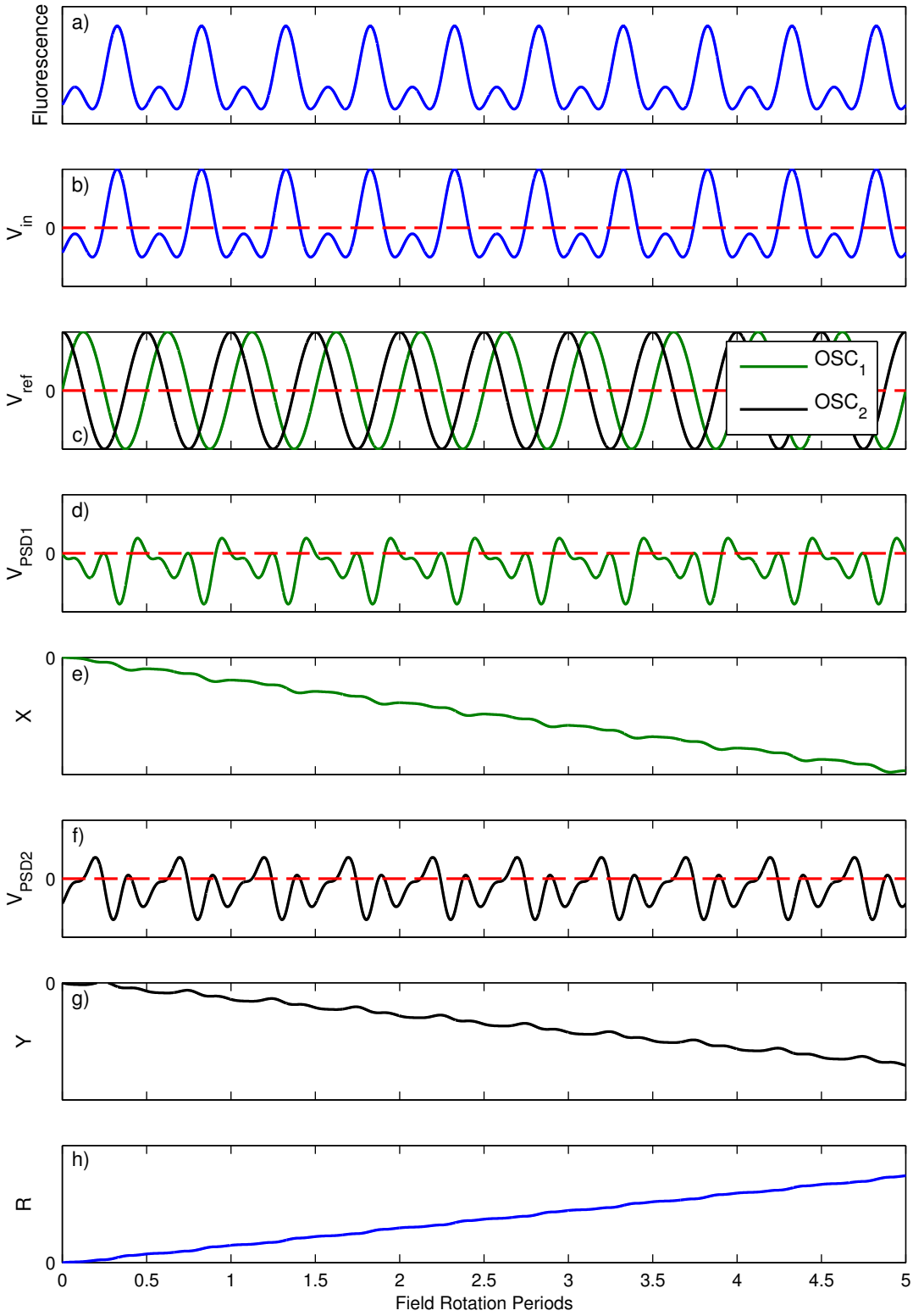

Figure 5.7: Signal processing in AMELIA experiment for an arbitrary field rotation frequency ($\tau_c \gg \omega_{\text{rot}}^{-1}$). a) Idealized fluorescence signal measured at the photomultiplier tube (note two periods per field rotation). b) AC coupled signal at lock-in amplifier input. c) Internal reference signals in the lock-in amplifier at twice the field rotation frequency, with 90° phase difference. d) V_{in} multiplied by OSC_1. e) LIA output X f) V_{in} multiplied by OSC_2. g) LIA output Y. h) LIA output R, which stabilizes after several τ_c have elapsed.

5.4 Validation with Pyrene/1,3-dicyanobenzene Solution

The magnetic field calibration was validated with an isotropic liquid sample, of pyrene and 1,3-dicyanobenzene (DCB) in 9:1 cyclohexanol-acetonitrile solution. Pyrene and DCB are known to form an excited complex (**figure 5.8**) by electron transfer, whose fluorescence to the ground state can be greatly altered by an applied magnetic field [135, 182, 48].

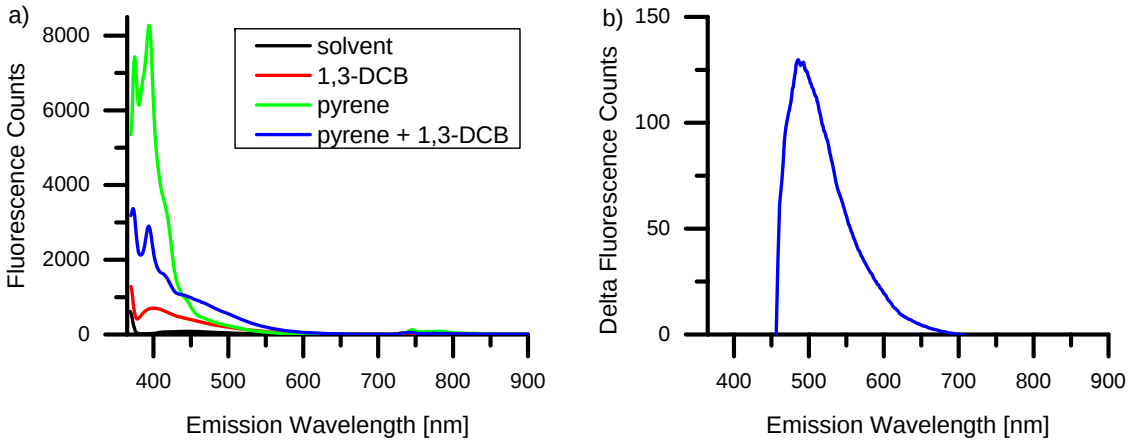

Figure 5.8: a) The steady state fluorescence spectrum of pyrene and 1,3-dicyanobenzene solution was not a linear combination of the spectra of individual pyrene and DCB solutions, indicating the formation of an excited complex. b) The spectrum of the excited complex, constructed by subtracting the individual pyrene and DCB spectra from the spectrum of the pyrene/DCB solution. Excitation wavelength: 365 nm, solvent: 9:1 cyclohexanol/acetonitrile, concentrations: 0.4 mM (pyrene) and 40 mM (DCB), Excitation slit: 5 nm, emission slit: 5 nm, PMT voltage: 700 V.

The pyrene-DCB solution was placed between the magnetic coils of the AMELIA aparatus in a 10×2 mm microcuvette, with the larger dimension facing the LED, such that the illuminated portion of the solution was as close as possible to the center of the coils. Three experiments were performed,

- Oscillating field in coil 1 only, with 2^{nd} harmonic detection
- Oscillating field in coil 2 only, with 2^{nd} harmonic detection

- Rotating field of constant magnitude supplied by both coils, with 2nd harmonic detection (*i.e.* the usual AMELIA experiment)

The rationale between the single-coil experiments was to create an oscillating fluorescence signal in the isotropic solution, due to the magnetic field sinusoidally oscillating about zero (**figure 5.9**). The oscillation in the fluorescence has a period half that of the oscillation in the magnetic field, so a second harmonic component in the oscillating fluorescence is expected.

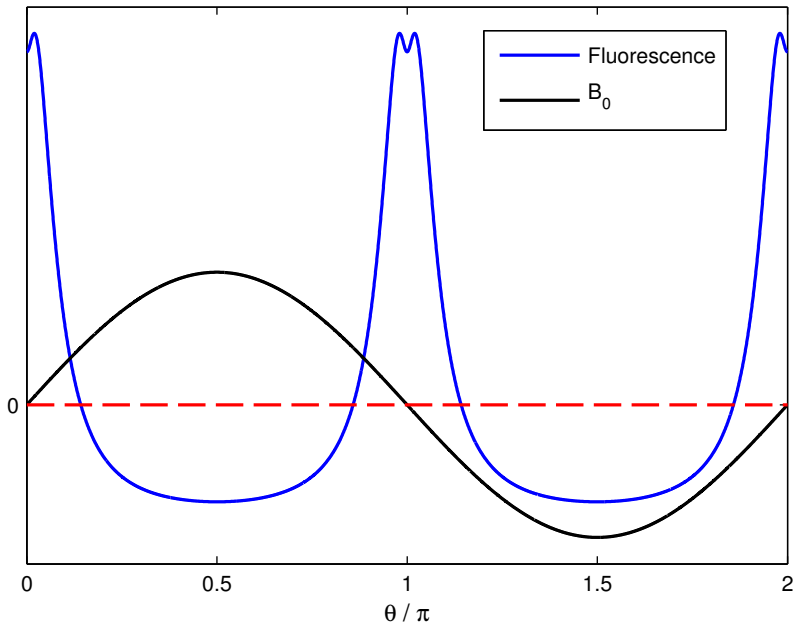

Figure 5.9: Idealized, AC coupled (zero mean), steady state fluorescence signal of an isotropic sample, with applied magnetic field $B_0 \propto \sin\theta$.

With second harmonic detection, the lock-in amplifier essentially measures the Fourier component of the oscillating fluorescence at twice the oscillation frequency of the magnetic field. Due to Dirichlet's conditions [20], there must be a second harmonic Fourier component in the fluorescence signal of the type shown in **figure 5.9**, as the signal

- is absolutely integratable over a period,
- has a finite number of extrema per period,
- has no discontinuities,

meaning that the signal's Fourier series must converge. Furthermore, the magnetic field effect curve could be reconstructed by measuring higher Fourier components.

The the pyrene-DCB sample was excited with a 365 nm LED (Thorlabs M365L2) with a power of 51.4 mW (100 mA LED current). A 495 ± 20 nm bandpass filter was placed before the photomultiplier tube, to pass the fluorescence from the excited pyrene/DCB complex and interdict that of the pyrene monomer (**figure 5.8**) [135, 182, 48]. The fluorescence component at the second harmonic of the magnetic field oscillation was detected with a time-constant of 300 ms, a wait-time of 3 s before collecting a datapoint, and a dead-time (of both magnetic coils and LED) of 4.5 s between datapoints, in a random order of magnetic field strengths. The lock-in amplifier's sensitivity was set to 100 mV.

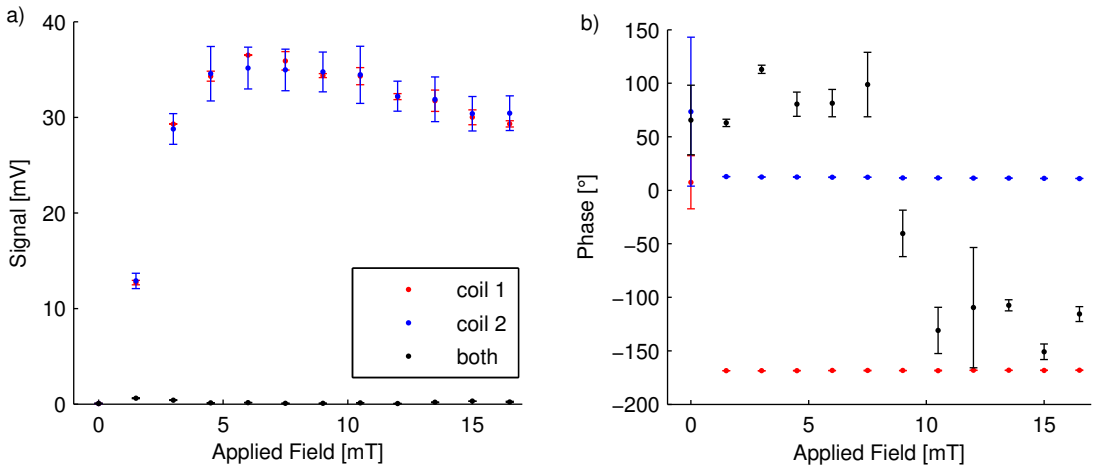

Figure 5.10: Validation of the experiment with an isotropic solution of 1 mM pyrene with 10 mM 1,3-dicyanobenzene in 9:1 cyclohexanol/acetonitrile at 31 Hz magnetic field rotation frequency. a) Lock-in amplifier reading at the 2nd harmonic of the field rotation frequency, measured with individual coils active and with both coils active. b) The corresponding phases.

The fluorescence cuvette was initially cleaned by soaking overnight in concentrated nitric acid, then rinsed with distilled water. A fresh pyrene-DCB sample was prepared for each of the three experiments. The cuvette was rinsed between samples with a five-solvent wash, namely, in succession, tetrahydrofuran, ethyl alcohol, dilute hydrochloric acid, distilled water and finally acetone. The cuvette was left to drip-dry or dried with a nitrogen stream before use with another sample. This careful washing procedure was necessary to remove residual pyrene and dicyanoben-

zene from the walls of the cuvette; otherwise these contaminants were visible in fluorescence assays on the empty cuvette.

In single coil mode, the lock-in amplifier's signals from coils 1 and 2 were within experimental error of each other (**figure 5.10**). The corresponding signal with both coils active (*i.e.* a rotating magnetic field of constant magnitude) was negligible, as expected from an isotropic solution. The difference between the measured phases from coil 1 and coil 2 was approximately 180°, consistent with the 90° phase difference in the fundamental frequency sent to each coil. The phase was constant as a function of applied field in single-coil mode, but showed no pattern with both coils active.

5.5 Anthracene Crystals

5.5.1 Experimental

Crystals were Grown by Solvent Evaporation

Zone-refined anthracene was obtained in sealed silica tubes from K. J. Tan and Mark Oxborrow (Imperial College, London). The lower and upper 10 cm of each tube was discarded (to remove heavier and lighter contaminants, respectively), and the remaining anthracene was used for crystallization from solvent (**table 5.2**) without further purification. It must be stressed that purification was **essential** in order to produce quality crystals. Purification by double recrystallization from dichloromethane [185] or acetone and benzene [117, 130] has also been reported, although this must be carried out in dark-room conditions, in order to avoid photo-oxidation to anthraquinone [31] or photodimerization [66].

Table 5.2: Result of crystallization attempts. The mass of zone-refined anthracene indicated was dissolved in 15 mL of solvent. A table of solubilities is given in Appendix D.

Solvent	Mass [g]	Result
acetone	0.113	✗
acetic acid	0.1	✗
dichloromethane	0.432	✓
1:1 dichloromethane-ether	0.2535	✗
N,N-dimethylformamide	0.27	✗
tetrahydrofuran	0.6	✓
diethyl ether	0.075	✗
ethyl acetate	0.17	✓
methanol	0.213	✗
toluene	0.195	✗

The glassware used for the crystallizations was purchased new, and washed with water and detergent, distilled water, ethanol and finally acetone, then dried upside-down in a special-purpose oven. Volumetric glassware was left to drip dry in a box covered and lined with filter paper, to avoid nullifying the calibration and to avoid contamination with dust. The same washing protocol was used after each crystallization, and the dry glassware was sealed with parafilm and stored in an

air-tight box to avoid contamination. Glass was chosen over disposable plastic due to the latter's limited solvent compatibility.

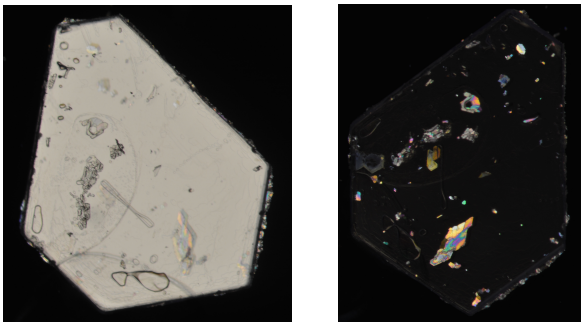

(a) crystal A

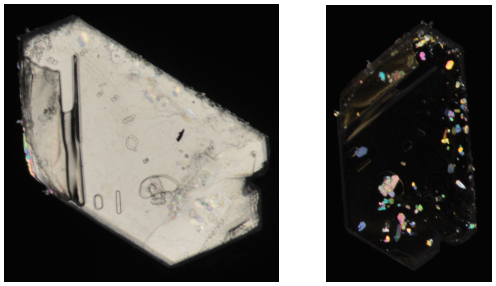

(b) crystal B

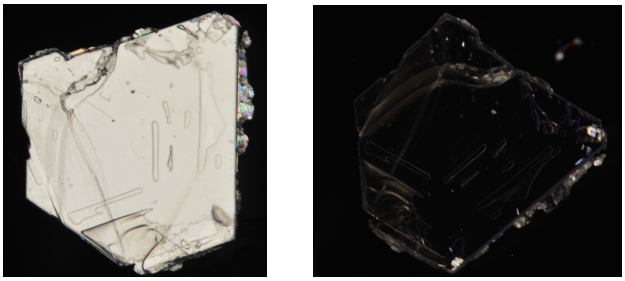

(c) crystal C

Figure 5.11: Good quality anthracene crystals grown from solution in dichloromethane, and imaged through a polarizing microscope. The crystals were platelets of approximately 2 mm in their longest dimension. The images in the left hand column were captured at maximum transmittance, the right hand at maximum extinction. The polarizer was oriented in the east-west direction, and the analyzer in the north-south direction. The areas of complete extinction indicate a uniform crystal domain, but note the slight imperfections in the form of microscopic crystallites.

The crystallization solvents were reagent grade (acetic acid, $> 99\,\%$ pure) and chromatography grade (all others, $> 99.8\,\%$ pure), and were used as purchased without further purification. The zone-refined anthracene was dissolved in 15 mL of solvent by sonication in a conical flask, under dark-room conditions (using a

red lamp as the sole lighting source). The solution was then filtered by gravity, and separated into two portions, one of 5 mL and a second of 10 mL, and each was stored in a clean glass phial. Phials were sealed with parafilm, with a small hole punctured with a needle. The solutions were then kept under an opaque but breathable cover in an infrequented fume hood, and checked on a weekly basis for crystals.

Of the solutions tested, only dichloromethane, tetrahydrofuran and ethyl acetate produced good quality crystals - platelets with face dimensions up to 2 mm by 5 mm. The highest quality were those from dichloromethane, where the anthracene crystallized at the liquid-air boundary and could be easily collected from the surface. Both the 5 mL and 10 mL fractions produced crystals of comparable quality, but in the latter the crystals took approximately double the time to grow.

Spectroscopy and Microscopy Indicated that Crystals were of Acceptable Quality

Infrared reflectance spectroscopy (Shimadzu IRAffinity 1s) showed no evidence of solvent inclusion in the crystals. Fluorescence spectroscopy (Hitachi F-4500 FL) confirmed that the crystals had the same emission bands as the raw zone-refined anthracene, and that the cyanoacrylate glue used to mount the crystals showed negligible emission (**figure 5.12**).

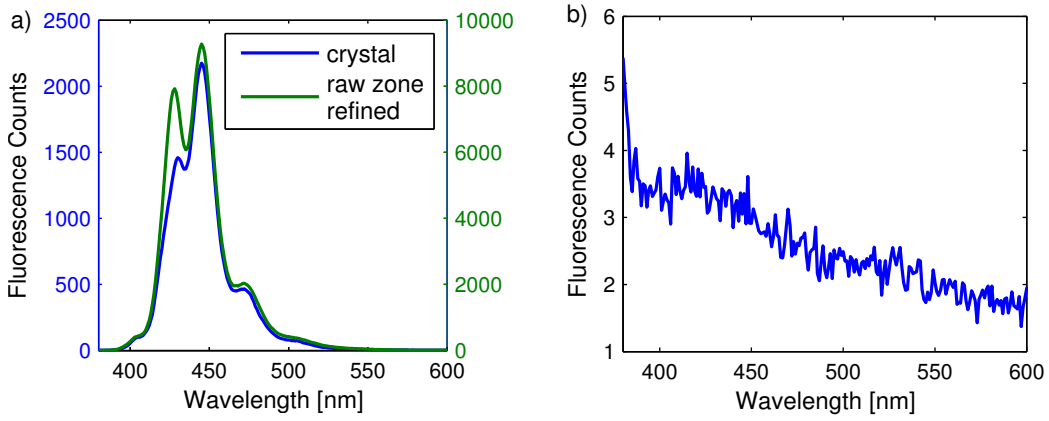

Figure 5.12: Emission from 365 nm excitation. a) Unmounted anthracene crystal grown from dichloromethane and purified precursor. Excitation slit: 5 nm, emission slit: 1 nm. b) Dry methyl 2-cyanoacrylate on glass window. Excitation slit: 10 nm, emission slit: 1 nm.

X-ray diffraction performed on an early crystallite indicated that the large face was the crystallographic *ab* plane, consistent with previous reports [108, 190, 185]. The morphology of the crystallite matched that of the larger crystals (**figure 5.13**), so Occam's principle suggested that the face of the larger platelets also lay in the *ab* plane. This also allowed the assignment of the *a* and *b* axes in the platelets, but not the *c* axis (see below).

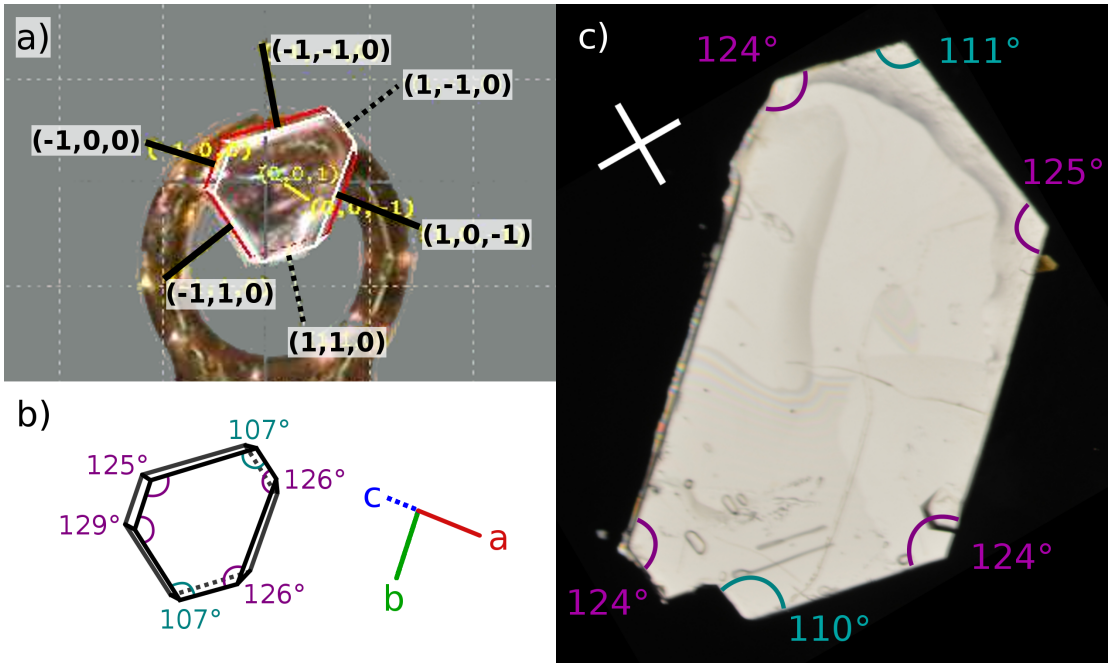

Figure 5.13: Anthracene crystal morphology. a) Surface normals of sub-millimeter crystallite as determined by X-ray diffraction, with associated Miller indices. b) Crystallographic axes and angles in the *ab* plane deduced from the X-ray diffraction data. c) Morphology of a 3 mm single crystal platelet grown from dichloromethane, imaged with a polarizing microscope at maximum transmittance. The crosshair indicates the orientation of the polarizers.

Crystal quality was evaluated using a polarizing microscope, using a crossed polarizer configuration. High quality crystals were identified as those with complete extinction when the microscope's polarizer and analyzer were aligned with the crystal's principal optical axes [108, 130] (**figure 5.11**, p. 157).

The principal axes of the refractive index tensor in the crystals' face coincided with the *a* and *b* directions assigned previously, consistent with Nakada's findings (**figure 5.5**, p. 140) [130].

Crystallographic c Axis was Determined using a Universal Stage Polarizing Microscope

Due to crystalline anthracene's monoclinicity, knowledge of the a and b axes does not fully determine the direction of c, instead limiting the direction to two possibilities. In principle, it is possible to determine the c direction from the slope of the thin crystal edges; unfortunately the platelets grown in the present work were too thin to make this possible. Therefore the c direction was determined in relation to the optic axis (**figure 5.5**, p. 140), which was found using a five-axis universal stage polarizing microscope (Leitz Wetzlar), using the procedure described in Emmons [42].

Magnetic Field Anisotropy Depended on Crystal Orientation

AMELIA was carried out on the three anthracene crystals shown in **figure 5.11** (p. 157), with the magnetic field rotating in the ab, ac and bc planes. The field rotation frequency was 83 Hz. The sample was excited with a 365 nm LED (Thorlabs M365L2) with a power of 5.1 mW (10 mA LED current), focused to a 7 mm diameter point. A 450 ± 20 nm bandpass filter was placed before the photomultiplier tube, to pass anthracene's strongest emission band (**figure 5.12**, p. 158). The oscillating component of the fluorescence (in both 2^{nd} and 4^{th} harmonic modes) was detected with a time-constant of 3 s, a wait-time of 30 s before collecting a datapoint, and a dead-time (of both magnetic coils and LED) of 45 s between datapoints, in a random order of magnetic field strengths. All measurements were carried out at high dynamic reserve, and with the LIA's SYNC filter active.

For the ac and ab measurements, the crystals were excited with face illumination, in order to create excitons as close to the center of the magnetic coils as possible. The emitted fluorescent light was therefore collected from the thin edge of the crystal. With the bc plane, the crystals had to be rotated such that the excitation beam was not perpendicular to the crystal face.

Although the measured anisotropy was weak, it was clearly distinguishable in

both 2^{nd} (**figure 5.14**, p. 162) and 4^{th} (**figure 5.15**, p. 163) harmonic detection modes. The 2^{nd} harmonic signal was an order of magnitude larger than the 4^{th} harmonic signal, apart from in the *ac* plane measurements. Furthermore, the anisotropy profile in the *ac* plane was markedly different to the profile in the *ab* and *bc* planes. It is also important to remark that, although 2^{nd} harmonic result with the magnetic field in the *ac* plane goes to zero at 8 mT, this does not mean that there is no anisotropy; the anisotropy is simply constrained to higher harmonic modes, as can be seen in **figure 5.15.b**.

The experiments was simulated according to the theory laid out in **section 5.5.2**. The magnetic and kinetic parameters for the simulations were taken from Johnson and Merrifield [84], (zero field splitting parameters $E = 35\,\mathrm{mT}$ and $D = -6.2\,\mathrm{mT}$; $k_s = 1.1 \times 10^9\,\mathrm{s}^{-1}$, $k_d = 2.8 \times 10^9\,\mathrm{s}^{-1}$). The simulations qualitatively reproduced the shapes of the experimental curves, and the magnitude trend between 2^{nd} and 4^{th} harmonic measurements. However, the position of the minimum in the *ac* plane measurement in 2^{nd} harmonic mode differed between experiment and theory. No unexplained fine structure appeared in the experiments, which supports the theoretical assumption of negligible hyperfine interactions within excitons and dipolar interactions between excitons.

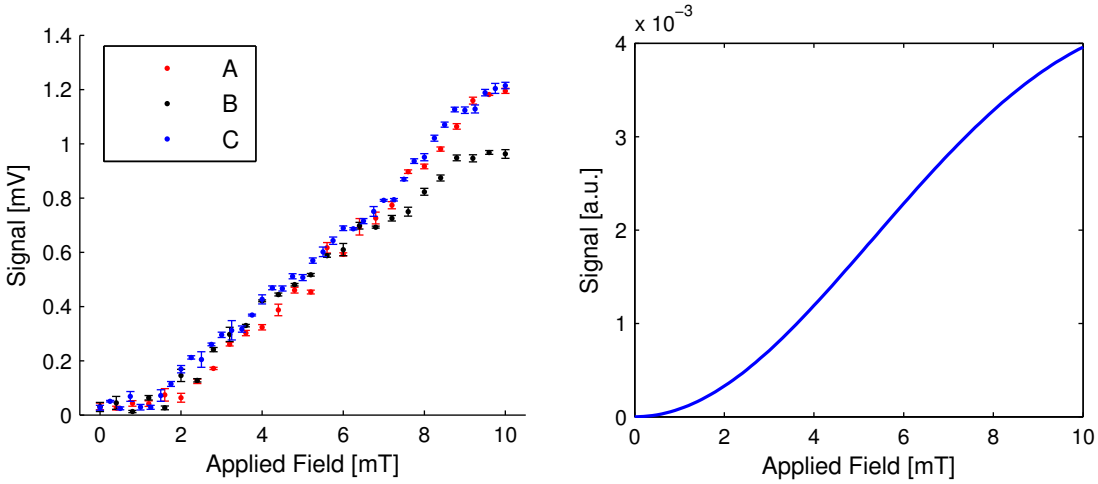

(a) *ab* plane

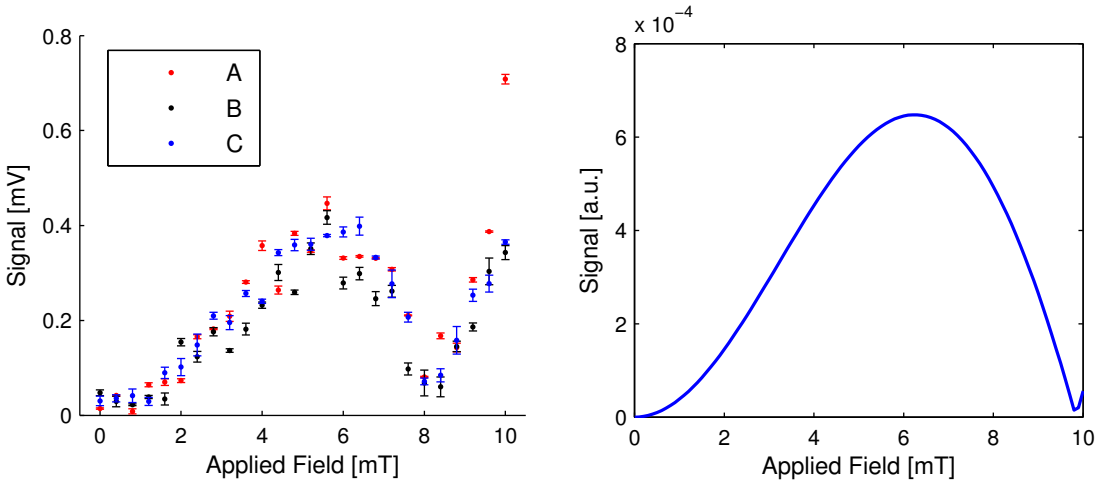

(b) *ac* plane

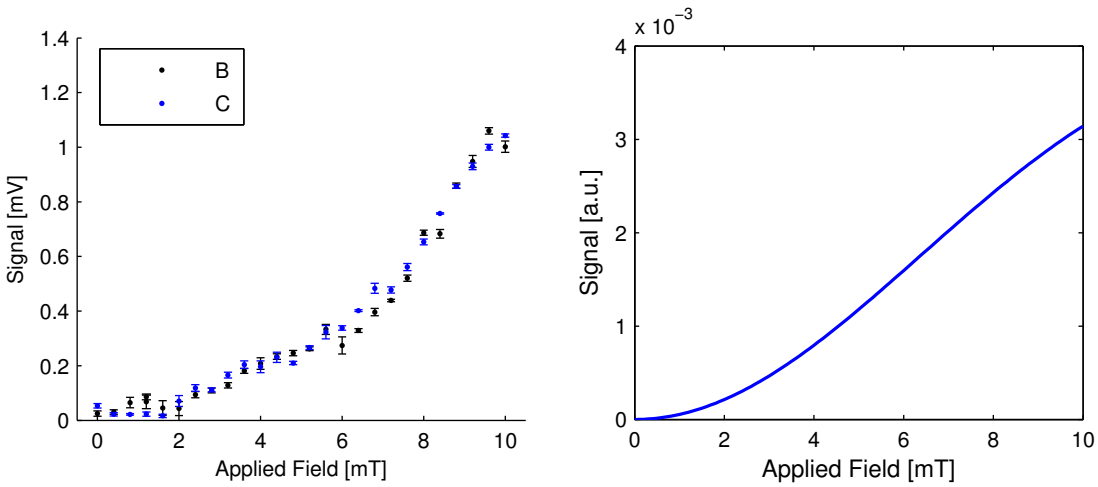

(c) *bc* plane

Figure 5.14: Experimental results (left column) and simulations (right column) of AMELIA on anthracene crystals A, B, and C, in 2$^{\text{nd}}$ harmonic detection mode.

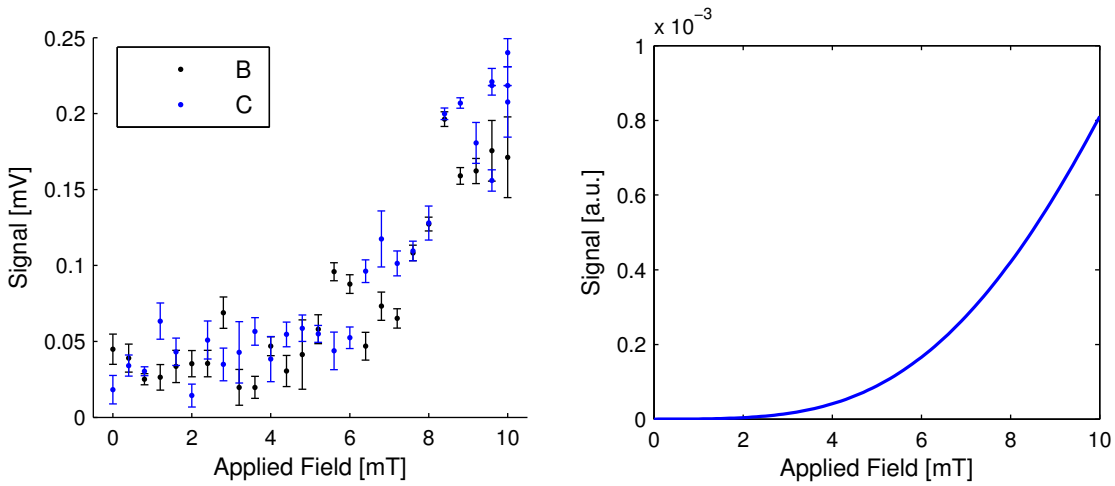

(a) *ab* plane

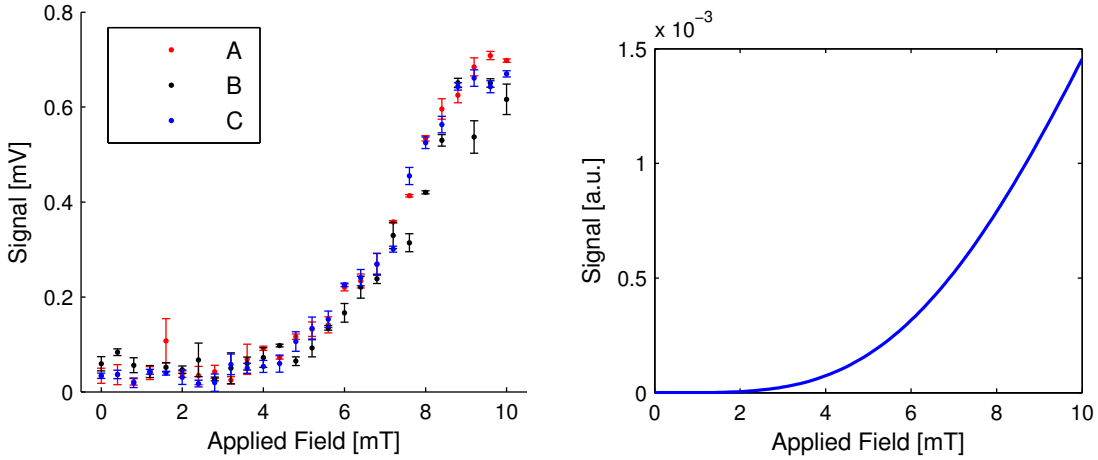

(b) *ac* plane

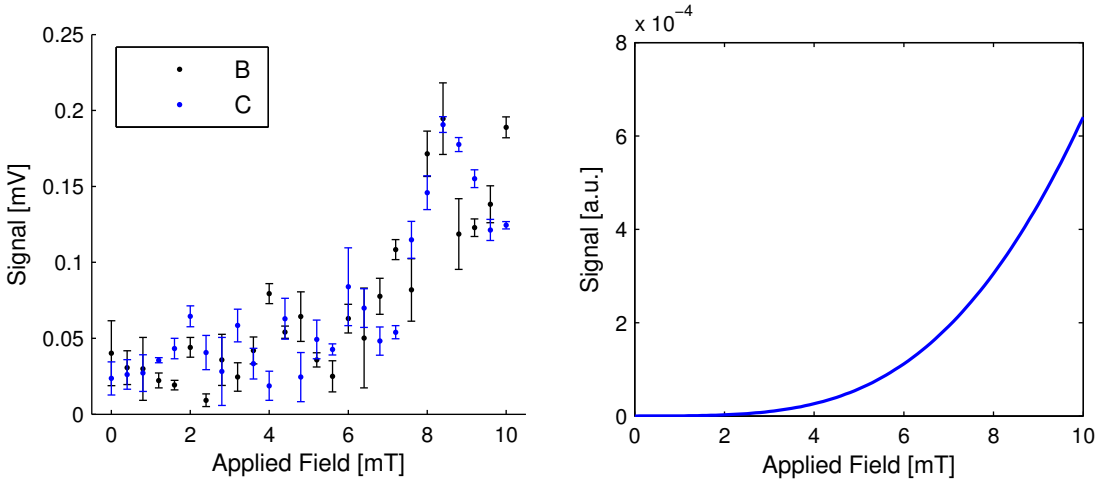

(c) *bc* plane

Figure 5.15: Experimental results (left column) and simulations (right column) of AMELIA on anthracene crystals A, B, and C, in 4^{th} harmonic detection mode. No measurements in the *ab* and *bc* planes of crystal A were collected as the crystal had degraded.

5.5.2 Theoretical Analysis

Simulations assumed as starting state a contact triplet exciton pair in a singlet spin state, created from a photoexcited singlet precursor according to

$$\mathrm{S_0 + S_0 \xrightarrow{h\nu} S_0 + S^* \longrightarrow (TT)\,.} \tag{5.18}$$

Exciton diffusion was modeled by assuming that the contact triplet exciton pair could recombine to the singlet precursor, or could diffuse apart[2] to form a free exciton pair that would decay along other pathways (not treated explicitly).

$$\mathrm{2\,S_0 \xleftarrow{h\nu} S_0 + S^* \xleftarrow{k_s} (TT) \xrightarrow{k_d} T + T\,,} \tag{5.19}$$

where k_s is the spin-selective singlet recombination rate, and k_d is the non-spin-selective rate of creation of a free exciton pair. Encounters between triplet excitons to reform a contact state were assumed to be insignificant, as fluorescence from such encounters has been reported to be negligible at room temperature [69]. The singlet yield was calculated as a function of applied magnetic field strength and direction, and the harmonic content analyzed to give the AMELIA signal at each field strength.

The assumption of a contact state follows Johnson and Merrifield's original analysis [84], where it gave an excellent agreement with experimental results. Suna later brought this assumption into question, arguing that the appearance of a contact state arose due to the large probability of reencounter with the constrained two-dimensional diffusion of excitons [163]. Unfortunately, both theories fit the experimental data equally well; however, Yong has recently argued that the bound (TT) state is the more accurate description [188].

[2] To be precise, this is not physical diffusion, but hopping of the exciton between molecules in the crystal lattice

Steady State Recombinant Fluorescence Intensity was Assumed to be Proportional to the Singlet Recombination Yield of a Transient Exciton Pair

For a transient contact exciton pair, we can assume an average singlet recombination rate,

$$\kappa_s = k_s \left\langle p_s(t) \right\rangle_{\text{time}} \tag{5.20}$$

weighted by the average singlet probability over the lifetime of the contact exciton pair. The singlet recombination yield is then

$$\Phi_s = \frac{\kappa_s}{\kappa_s + k_d} \,. \tag{5.21}$$

Under continuous illumination, we can assume an average singlet recombination rate

$$\kappa_s' = k_s \left\langle p_s(t) \right\rangle_{\text{ens}} \tag{5.22}$$

where the rate has been weighted by the average singlet probability over the ensemble of triplet exciton pairs. However, the ensemble average is identical to the time average, so

$$\kappa_s' = \kappa_s \tag{5.23}$$

The concentration of contact triplet triplet excitons thereby has a time-dependence according to

$$\frac{d[\text{TT}]}{dt} = -(\kappa_s + k_p)[\text{TT}] + k_{\text{ex}}[\text{S}_0] \,, \tag{5.24}$$

where k_{ex} is the excitation rate. Therefore, under steady-state conditions,

$$[\text{TT}] = \frac{k_{\text{ex}}[\text{S}_0]}{\kappa_s + k_p} \,. \tag{5.25}$$

The fluorescence intensity

$$\begin{aligned} F &\propto \kappa_s \left[\mathrm{TT}\right] \\ &\propto \frac{\kappa_s}{\kappa_s + k_d} k_{\mathrm{ex}} \left[\mathrm{S}_0\right] . \end{aligned} \tag{5.26}$$

Assuming that the ground state concentration $[\mathrm{S}_0]$ is affected negligibly by changes in κ_s, which is reasonable under the weak incident light intensity used in AMELIA,

$$F \propto \frac{\kappa_s}{\kappa_s + k_d} \tag{5.27}$$

results in, according to **equation 5.21**,

$$F \propto \Phi_s . \tag{5.28}$$

Singlet Yield was Calculated in Liouville Space

Following Johnson and Merrifield [84], coherent dynamics were described by the spin Hamiltonian

$$\hat{H} = \gamma_e \vec{B}_0 \cdot \left(\vec{S}_1 + \vec{S}_2\right) + \vec{S}_1 \cdot \boldsymbol{D} \cdot \vec{S}_1 + \vec{S}_2 \cdot \boldsymbol{D} \cdot \vec{S}_2 , \tag{5.29}$$

where $\vec{S}_n$ is the vector of x, y and z spin matrices of exciton n. A triplet exciton can be treated as a spin-one particle, so

$$\begin{aligned} \hat{S}_x &= \frac{1}{\sqrt{2}} \begin{pmatrix} 0 & 1 & 0 \\ 1 & 0 & 1 \\ 0 & 1 & 0 \end{pmatrix} , \\ \hat{S}_y &= \frac{i}{\sqrt{2}} \begin{pmatrix} 0 & -1 & 0 \\ 1 & 0 & -1 \\ 0 & 1 & 0 \end{pmatrix} , \\ \hat{S}_x &= \begin{pmatrix} 1 & 0 & 0 \\ 0 & 0 & 0 \\ 0 & 0 & -1 \end{pmatrix} . \end{aligned} \tag{5.30}$$

$\boldsymbol{D}$ is the zero-field splitting tensor of the triplet exciton, averaged over molecular sites ($E = 35\,\mathrm{mT}$, $D = -6.2\,\mathrm{mT}$) [84]. Other interactions were assumed to be

negligible, due to the rapid hopping of excitons. Recombination and separation processes were calculated by adding Haberkorn's singlet recombination kernel to the Liouville-von Neumann equation, giving

$$\frac{d\hat{\rho}}{dt} = -i\big[\hat{H}, \hat{\rho}\big] - \frac{k_s}{2}\left(\hat{P}_S\hat{\rho} + \hat{\rho}\hat{P}_S\right) - k_d\hat{\rho}\,, \tag{5.31}$$

where $\hat{\rho}$ is the density matrix describing the spin state of the exciton pair and $\hat{P}_S$ is the singlet projection operator. The spin state of the triplet exciton pair was described in the Zeeman basis, where the singlet state

$$|S\rangle = \frac{1}{\sqrt{3}}\left(|+1,-1\rangle + |-1,+1\rangle - |0,0\rangle\right)\,, \tag{5.32}$$

and

$$\hat{P}_S = |S\rangle\langle S|\,. \tag{5.33}$$

In Liouville space,

$$\vec{\rho}(t) = e^{-\hat{\hat{L}}t}\,\vec{\rho}(0) \tag{5.34}$$

where $\vec{\rho}$ is the density matrix reshaped row-wise into a vector, and the Liouvillian

$$\hat{\hat{L}} = i\hat{\hat{H}} + k_s\hat{\hat{K}}_s + k_d\hat{\hat{\mathbb{1}}}\,. \tag{5.35}$$

The Hamiltonian superoperator, $\hat{\hat{H}}$, was formed according to **equation 1.47** in the introductory chapter (p. 31), while the kinetics superoperator

$$\hat{\hat{K}}_s = \frac{1}{2}\left(\hat{P}_S \otimes \hat{\mathbb{1}} + \hat{\mathbb{1}} \otimes \hat{P}_s^{\,\mathrm{T}}\right)\,, \tag{5.36}$$

following **equation 1.46** (p. 30). Solving for the singlet recombination yield by means of **equation 1.50** (p. 36) gives

$$\Phi_s = k_s\,\vec{P}_S^{\dagger}\,\hat{\hat{L}}^{-1}\vec{\rho}(0)\,, \tag{5.37}$$

where $\vec{P}_S$ is the singlet projection operator flattened row-wise into a vector.

AMELIA was Simulated by Calculating Singlet Yield as a Function of Magnetic Field Direction

At a given applied magnetic field strength, **equation 5.37** was solved numerically (with Matlab's \ function) as a function of magnetic field angle within the crystallographic *ab*, *ac*, and *bc* planes. The angular spacing of the magnetic field within a plane was $\frac{\pi}{200}$. The magnetic field was assumed to be static at each field direction, as the experimental field rotation frequency (83 Hz) was negligible compared to the timescale of the reaction dynamics ($k_s = 1.1 \times 10^9\,\mathrm{s}^{-1}$, $k_d = 2.8 \times 10^9\,\mathrm{s}^{-1}$ [84]).

The simulated singlet yield varied markedly with field direction, and clearly showed components with periods π and $\frac{\pi}{2}$ corresponding to 2nd and 4th harmonics of the rotation frequency, respectively (**figure 5.16**). In particular, the *ac* plane simulation shows that at 10 mT, the oscillation in singlet yield is mainly at the 4th harmonic of the field rotation frequency, explaining the minimum in **figure 5.14.b** (p. 162).

In order to simulate the AMELIA experiment, the singlet yield was AC coupled by subtracting the average singlet yield over a field rotation period.

$$\Phi_s^{\mathrm{AC}}[i] = \Phi_s[i] - \frac{1}{N}\sum_{n=1}^{N}\Phi_s[n] \tag{5.38}$$

The AMELIA signal at the magnetic field strength in question was then calculated with

$$\begin{aligned} X &= \frac{1}{N}\sum_{n=1}^{N}\sin\big(h\theta[n]\big) \times \Phi_s^{\mathrm{AC}}[n] \\ Y &= \frac{1}{N}\sum_{n=1}^{N}\cos\big(h\theta[n]\big) \times \Phi_s^{\mathrm{AC}}[n] \\ R &= \sqrt{X^2 + Y^2}\,, \end{aligned} \tag{5.39}$$

where h is the detection harmonic.

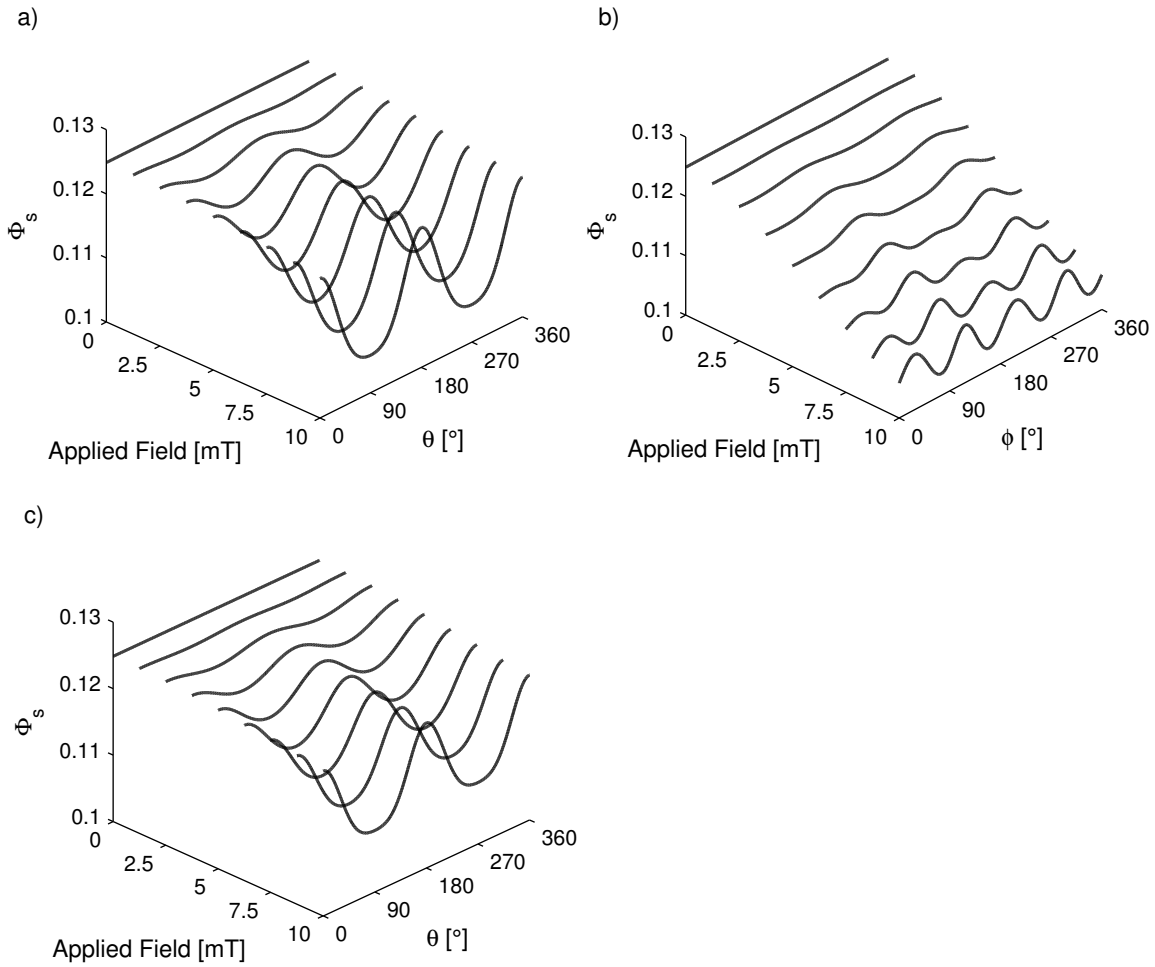

Figure 5.16: Simulations of the singlet recombination yield as a function of field strength and angle in a) *ab* plane, b), *ac* plane, c) *bc* plane. The 2^{nd} harmonic component is clearly visibile in the *ab* and *bc* simulations, while the progression from 2^{nd} harmonic to 4^{th} harmonic is visible in the *ac* plane simulation. θ: inclination angle with respect to *b*; ϕ: angle in *ac* plane with respect to *a*.

Singlet Yield was Modulated by Number of Eigenstates with Singlet Component

Unlike the high field case [84], calculations indicated that there were no level crossings of the Hamiltonian's eigenstates modulated by the direction of the applied magnetic field (**figure 5.17.a**). Furthermore, energy differences were of the order of $10^9\,\mathrm{s}^{-1}$ or greater, similar to the decay rate of the contact triplet exciton pair, so the anisotropy cannot be explained by modulation of energy differences. Instead, the singlet probability of each eigenstate of the Hamiltonian was found to change significantly by the direction of the applied field, reminiscent of the magnetically-induced mixing of sublevels (MIMS) described by van Dijk [178].

It was instructive to examine the singlet probability of each eigenstate of the spin Hamiltonian, ignoring reactivity and spin relaxation. Expanding the singlet state in terms of eigenstates,

$$|S\rangle = \sum_{n=1}^{6} s_n \,|n\rangle \ , \tag{5.40}$$

where the summation stops as six, as three eigenstates are guaranteed to have full triplet character due to the rule of conservation of parity. Taking the singlet state as the starting state, the wavefunction time evolution would follow

$$|\psi(t)\rangle = \sum_{n=1}^{6} s_n e^{-i\omega_n t} \,|n\rangle \ , \tag{5.41}$$

where ω_n is the n^{th} eigenvalue of the Hamiltonian. The singlet probability as a function of time is then

$$\begin{aligned} |\,\langle S\,|\,\psi(t)\rangle\,|^2 &= \left|\sum_{n=1}^{6} |s_n|^2 e^{-i\omega_n t}\right|^2 \\ |\,\langle S\,|\,\psi(t)\rangle\,|^2 &= \sum_{n,m}^{6} |s_n|^2 |s_m|^2 e^{-i(\omega_n-\omega_m)t} \,. \end{aligned} \tag{5.42}$$

Substituting $\omega_n - \omega_m = \omega_{nm}$ and taking a time average,

$$\begin{aligned} |\langle S \,|\, \psi(t) \rangle|^2 &= \sum_n^6 |s_n|^4 + \sum_{n,m,n\neq m}^6 |s_n|^2 |s_m|^2 e^{-i\omega_{nm}t} \\ \left\langle |\langle S \,|\, \psi(t) \rangle|^2 \right\rangle_{\text{time}} &= \sum_n^6 |s_n|^4 \,, \end{aligned} \tag{5.43}$$

where the second summation disappears as there are no degenerate eigenstates at low field, so the term oscillates about zero.

Trivially, the average singlet probability is maximized if the singlet state is one of the eigenstates of the Hamiltonian. The singlet probability would be minimized if each eigenstate had equal singlet probability,

$$|S\rangle = \frac{1}{\sqrt{6}} \sum_{n=1}^6 e^{-i\theta_n} |n\rangle \;, \tag{5.44}$$

where the time average singlet probability

$$\left\langle |\langle S \,|\, \psi(t) \rangle|^2 \right\rangle_{\text{time}} = \frac{1}{6} \,. \tag{5.45}$$

The direction of the applied magnetic field alters the singlet amplitude of each of the Hamiltonian's eigenstates, and therefore alters the singlet recombination yield. **Figures 5.17**, **5.18** and **5.19** reveal significant modulation in the singlet component of each eigenstate as a function of applied field direction. The average singlet probability, calculated with **equation 5.43**, indicates that this modulation was responsible for the change in singlet recombination yield with field direction.

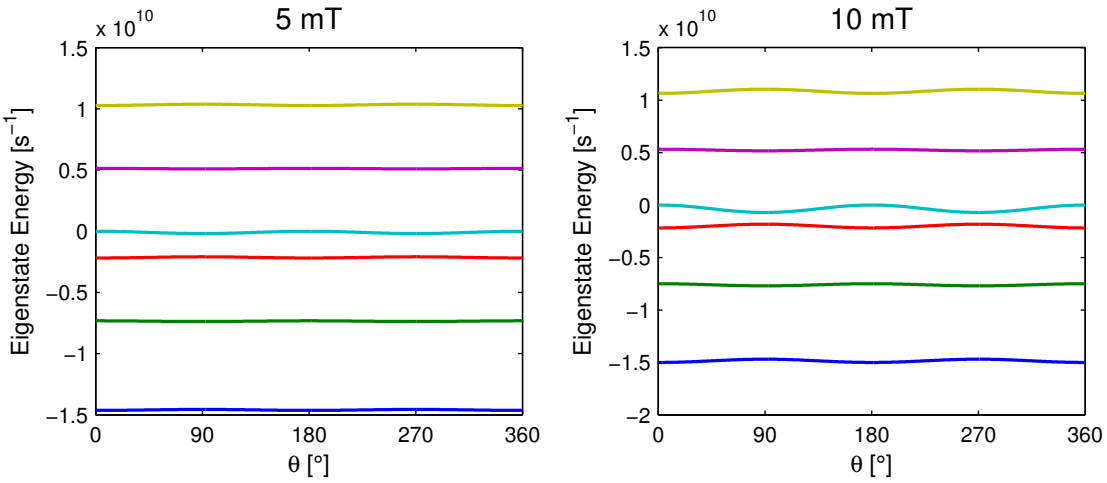

(a) Energy of the Hamiltonian's eigenstates

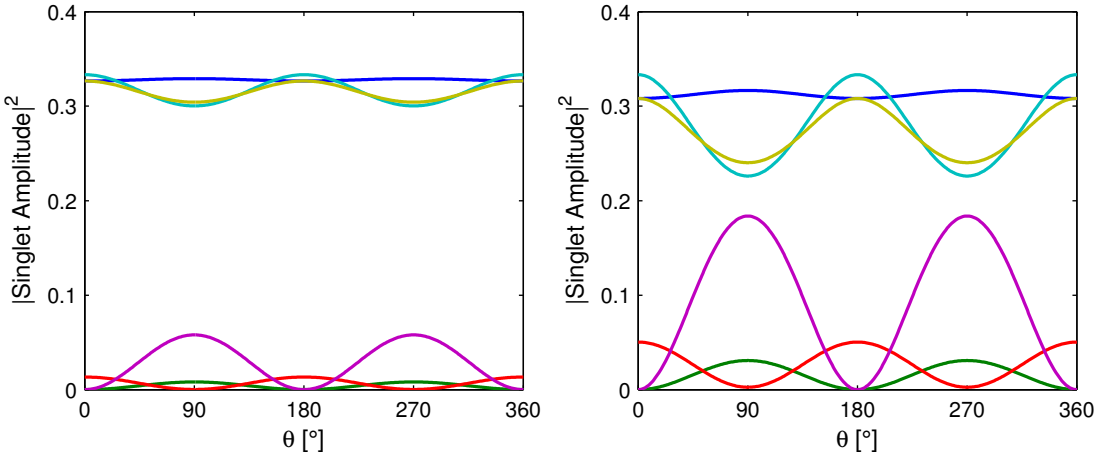

(b) Singlet component of the Hamiltonian's eigenstates

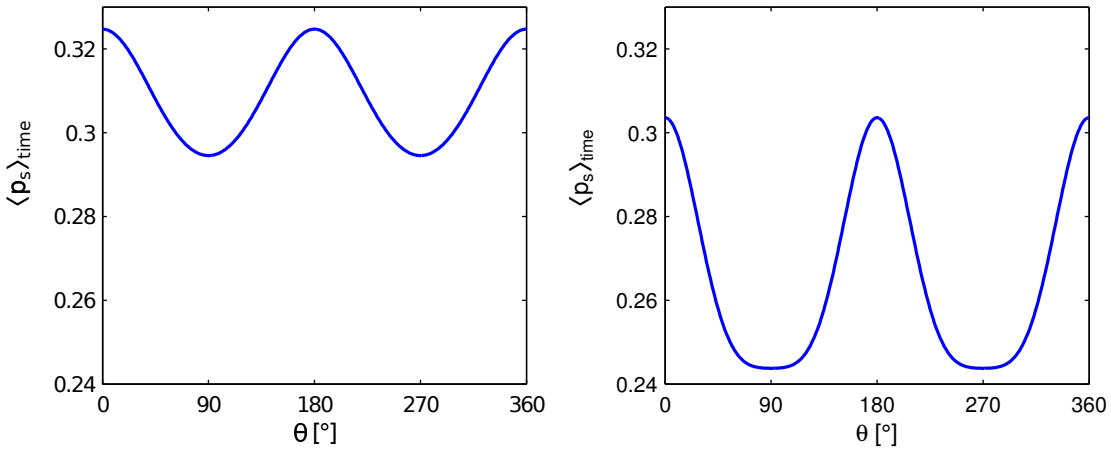

(c) Average singlet probability (ignoring relaxation and reactivity)

Figure 5.17: Calculation of eigenstate energies, their singlet amplitudes and the average singlet probability for an infinitely long lived exciton pair, with an applied magnetic field in the ***ab* plane**. The angle θ is with respect to the b axis, which coincides with the z axis of the zero field splitting tensor. First column is at 5 mT applied field, and second column at 10 mT.

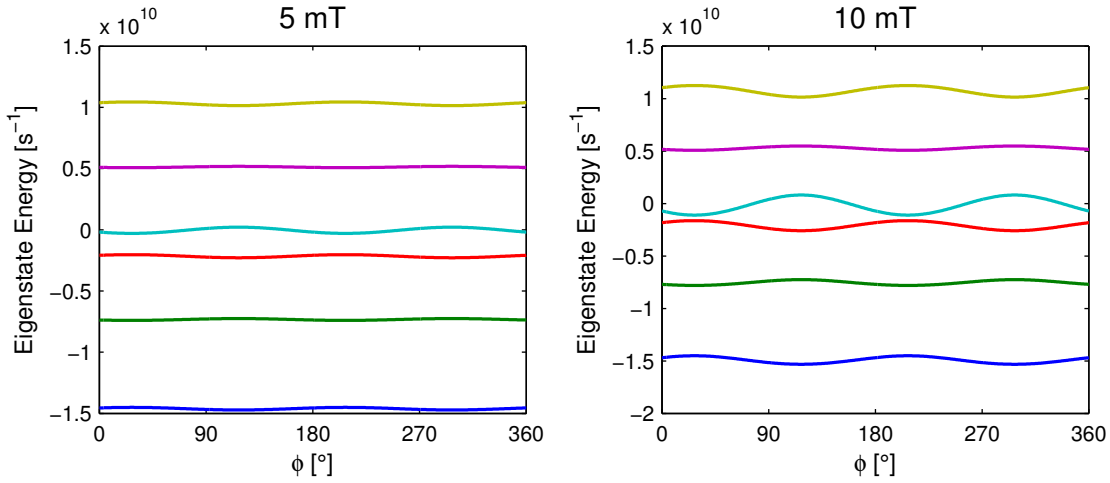

(a) Energy of the Hamiltonian's eigenstates

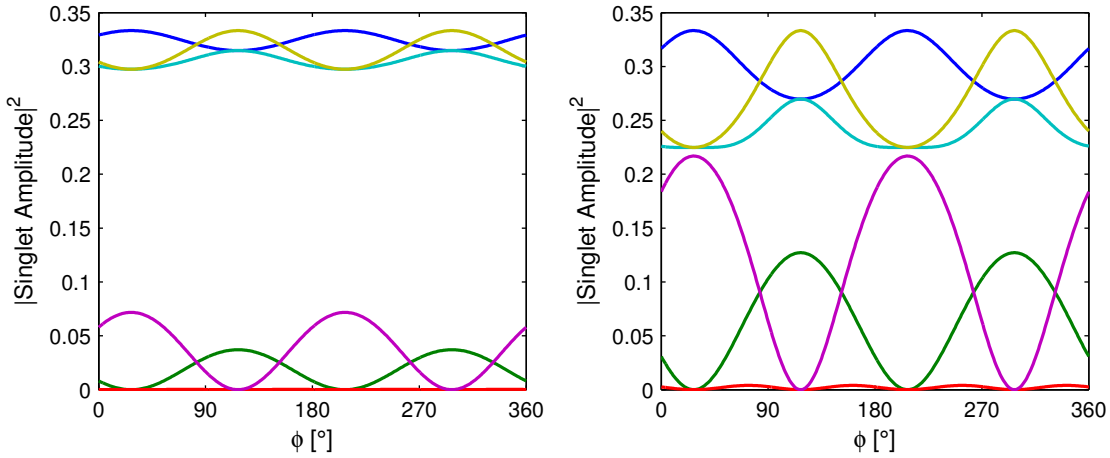

(b) Singlet component of the Hamiltonian's eigenstates

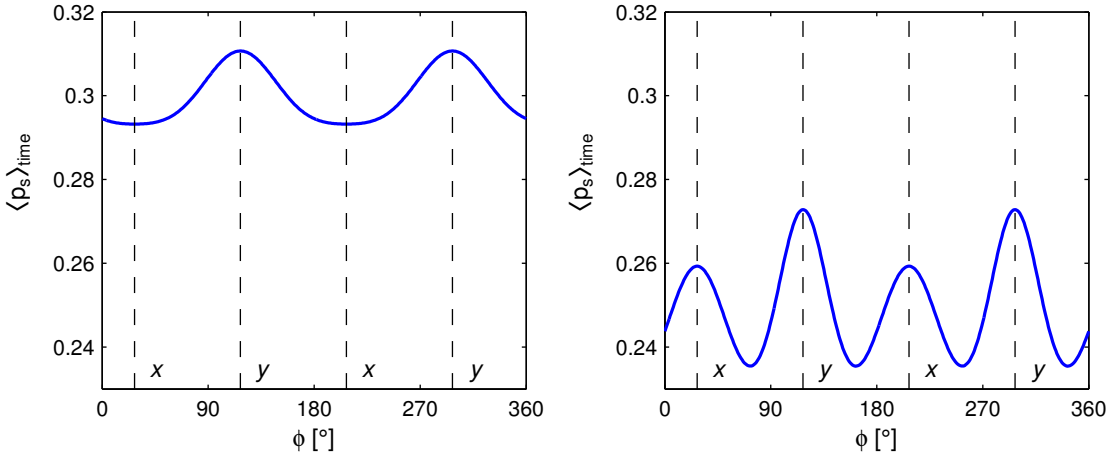

(c) Average singlet probability (ignoring relaxation and reactivity)

Figure 5.18: Calculation of eigenstate energies, their singlet amplitudes and the average singlet probability for an infinitely long lived exciton pair, with an applied magnetic field in the ***ac* plane**. The angle ϕ is with respect to the a axis. The dashed lines are the x and z axes of the zero field splitting tensor. First column is at 5 mT applied field, and second column at 10 mT.

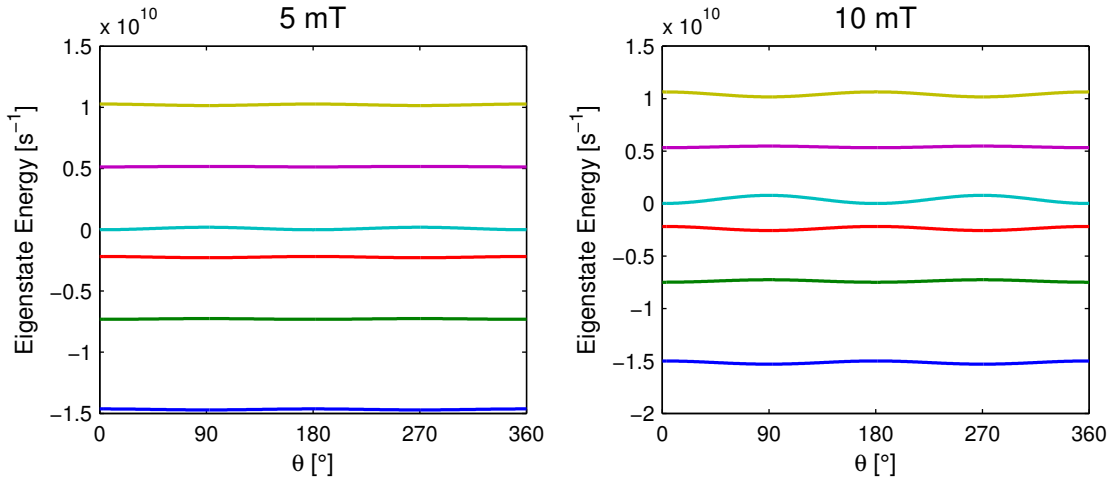

(a) Energy of the Hamiltonian's eigenstates

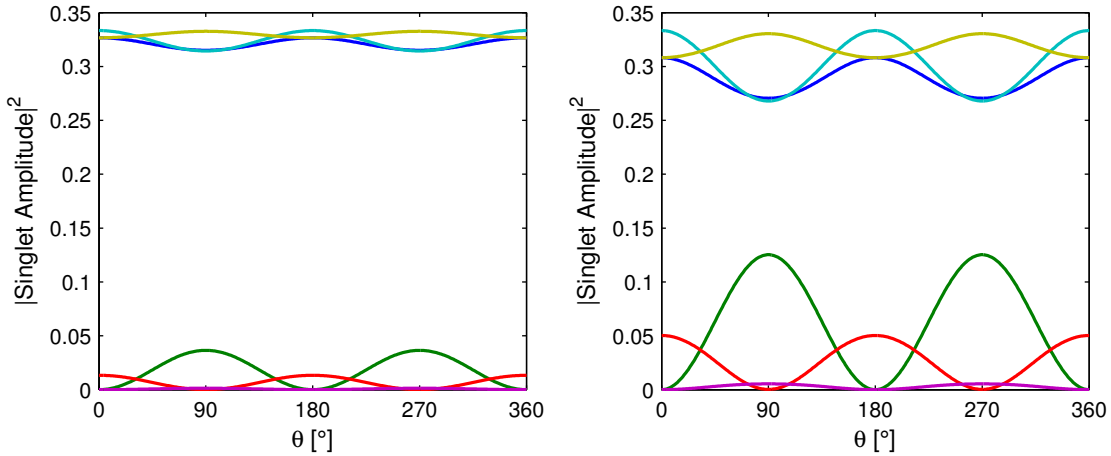

(b) Singlet component of the Hamiltonian's eigenstates

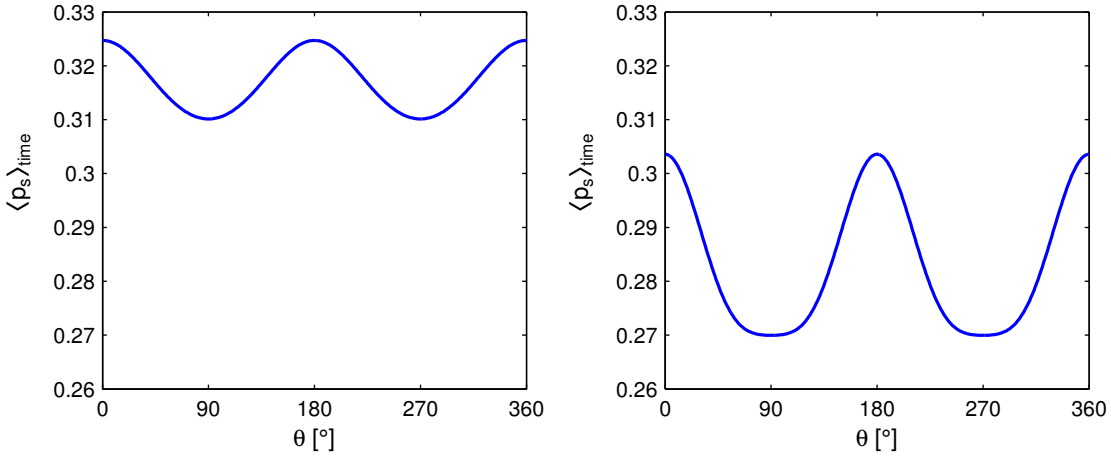

(c) Average singlet probability (ignoring relaxation and reactivity)

Figure 5.19: Calculation of eigenstate energies, their singlet amplitudes and the average singlet probability for an infinitely long lived exciton pair, with an applied magnetic field in the ***bc* plane**. The angle θ is with respect to the b axis, which coincides with the z axis of the zero field splitting tensor. First column is at 5 mT applied field, and second column at 10 mT.

5.6 Tetracene Crystals

5.6.1 Experimental

Tetracene crystals were supplied by K. J. Tan (Imperial College, London). The crystals were grown by sublimation and deposition in a temperature gradient, in a flow of inert gas. The raw tetracene was initially purified by repeated sublimation and deposition passes.

Crystals were Evaluated and Oriented with Polarizing Microscopy

Good quality sublimation flakes were selected that contained negligible inclusions, and showed full extinction with the polarizer or analyzer aligned with a principal optical axis (**figure 5.20**).

The tetracene crystals took the form of platelets, similar in morphology and size to anthracene crystals grown from solution. The face of the sublimation platelets was assumed to be the crystallographic ab plane, in line with previous studies [23, 147, 187]. The crystallographic b axis was assigned as parallel to the principal optical axis pointing towards the 105° vertices [23, 166], similar to the b axis in the anthracene crystals (**figures 5.13 and 5.21**, pp. 159 and 177).

Since tetracene crystals are triclinic, the crystallographic axes are an inconvenient basis. Therefore experiments were carried out with respect to an orthogonal axis system (a', b, c'), with a' perpendicular to b within the ab plane, and c' the surface normal of the ab plane.

Emission was Characterized by Fluorescence Spectroscopy

Fluorescence was measured with a Hitachi F-4500 FL spectrometer, by illuminating the face of the mounted crystals, and collecting light emitted from the side (**figure 5.22**). The crystals were positioned with the axis intermediate to a' and b pointing vertically; however, the bands in the excitation spectrum were too broad to show the Davydov splitting that has been widely reported in the literature [23, 144, 166, 186].

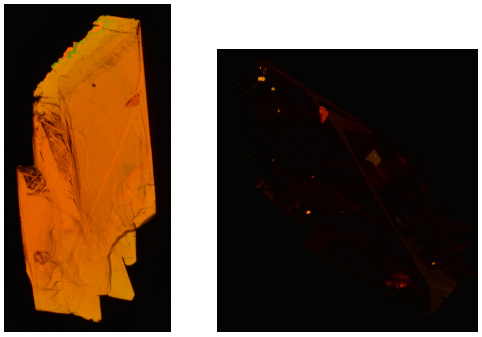

(a) tetracene A

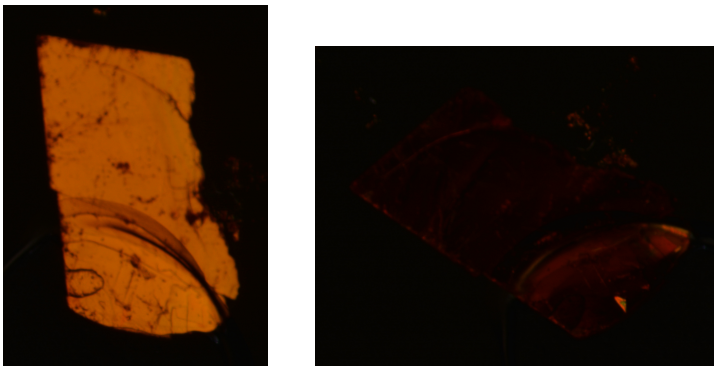

(b) tetracene B

Figure 5.20: Good quality tetracene crystals grown by sublimation The crystals were platelets, of approximately 3 mm in their longest dimension. The images in the left hand column were captured at maximum transmittance, the right hand at maximum extinction. The polarizer was oriented in the east-west direction, and the analyzer in the north-south direction.

The excitation spectrum of crystal A had maxima at 445 nm, 480 nm and 515 nm, consistent with the values reported by Bree and by Tayebjee [22, 167] from absorption spectroscopy. The emission spectrum of crystal A had maxima at 536 nm and 565 nm, consistent with the values reported by Tomkiewicz and by Tayebjee [173, 167].

However, in crystal B, the 536 nm band was reduced to a shoulder. According to Tayebjee's ultrafast studies, the 536 nm band corresponds to the emission from the S_1 state, while the 565 nm band corresponds to a slowly emitting state with mixed S_1 and multi-exciton character [167]. The two states are believed to be adiabatically coupled, with the latter energetically downhill. The dominance of the 565 nm band in crystal B therefore suggests frustration in the backward coupling from the slowly emitting state to the S_1 state, perhaps by some crystal defect. Noting that crystal

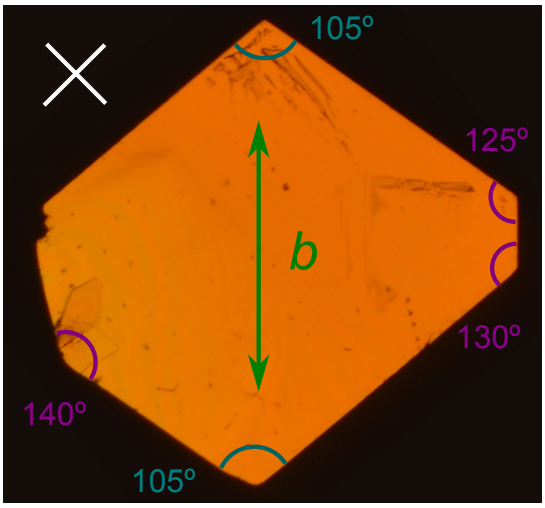

Figure 5.21: Tetracene crystal imaged with a polarizing microscope at maximum transmittance, showing the b crystallographic axis. The crosshairs indicate the orientation of the polarizers.

B was likely with defects, it was nevertheless studied by AMELIA due to its high degree of alignment (**figure 5.20**).

Tetracene Exhibited Strongly Anisotropic Magnetic Field Effects

AMELIA was carried out on the two tetracene crystals shown in **figure 5.20**, with the magnetic field rotating in the $a'b$ (could also be called ab), $a'c'$ and bc' planes. The field rotation frequency was 31 Hz. This was smaller than the 83 Hz used for anthracene, as the lower frequency allowed the coils to reach a higher field strength. Both frequencies were first tested on anthracene, and yielded identical results. The sample was excited with a 455 nm LED (Thorlabs M455L2) with a power of 0.26 mW (1 mA LED current), focused to a 7 mm diameter point. A 550 ± 30 nm bandpass filter was placed before the photomultiplier tube. The oscillating component of the fluorescence (in both 2^{nd} and 4^{th} harmonic modes) was detected with a time-constant of 3 s, a wait-time of 30 s before collecting a datapoint, and a dead-time (of both magnetic coils and LED) of 45 s between datapoints, in a random order of magnetic field strengths. All measurements were taken at high dynamic reserve.

The crystals were excited with face illumination, in order to create excitons as close to the center of the magnetic coils as possible. The emitted fluorescent light

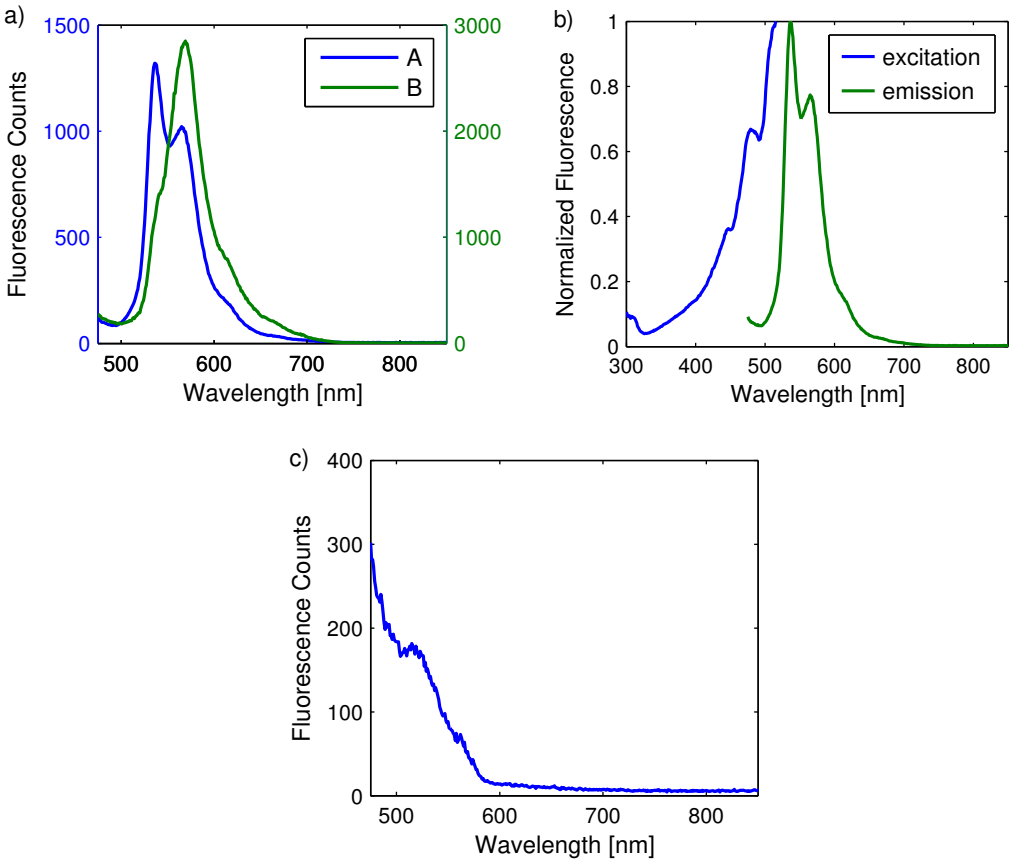

Figure 5.22: a) Fluorescence from mounted tetracene crystals A and B. Excitation wavelength: 455 nm, excitation slit: 10 nm, emission slit: 5 nm. b) Excitation spectrum (emission wavelength: 536 nm, excitation slit: 2.5 nm, emission slit: 10 nm) and emission spectrum (same parameters as in a)) of crystal A. c) Fluorescence from methyl 2-cyanoacrylate used to mount the crystals. Excitation wavelength: 455 nm, excitation slit: 10 nm, emission slit: 5 nm.

was therefore collected from the thin edge of the crystal.

The anisotropy plots differed markedly from those measured on anthracene crystals, no doubt because of large differences in the principal axes of the zero field splitting tensors. The signal amplitude with crystal B was lower than with crystal A. Since both crystals were measured with fluorescence amplified at the photomultiplier tube to the same (direct current) value, this means that a lower proportion of fluorescence followed the magnetically dependent pathway in crystal B than in crystal A. This is consistent with the hypothesis of frustrated repopulation of the S_1 state in crystal B.

The simulations matched the experimental results remarkably well. The mag-

netic parameters ($E = 26.5\,\mathrm{mT}$, $D = -6.6\,\mathrm{mT}$) were taken from Yarmus' EPR experiments [187], while the kinetics ($k_s = 2.0 \times 10^9\,\mathrm{s}^{-1}$, $k_d = 3.2 \times 10^8\,\mathrm{s}^{-1}$) were estimated from zero and high field fluorescence measurements (see below) [60, 89].

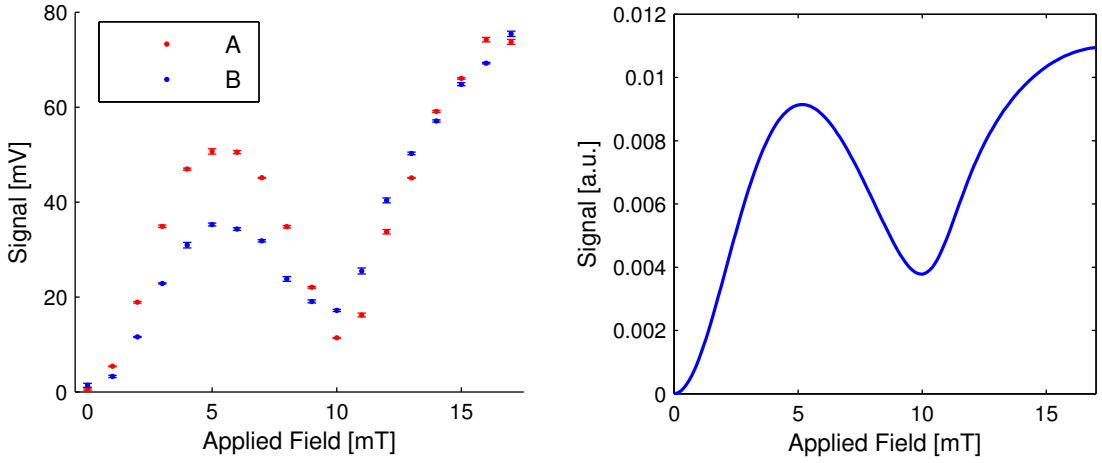

(a) $a'b$ plane

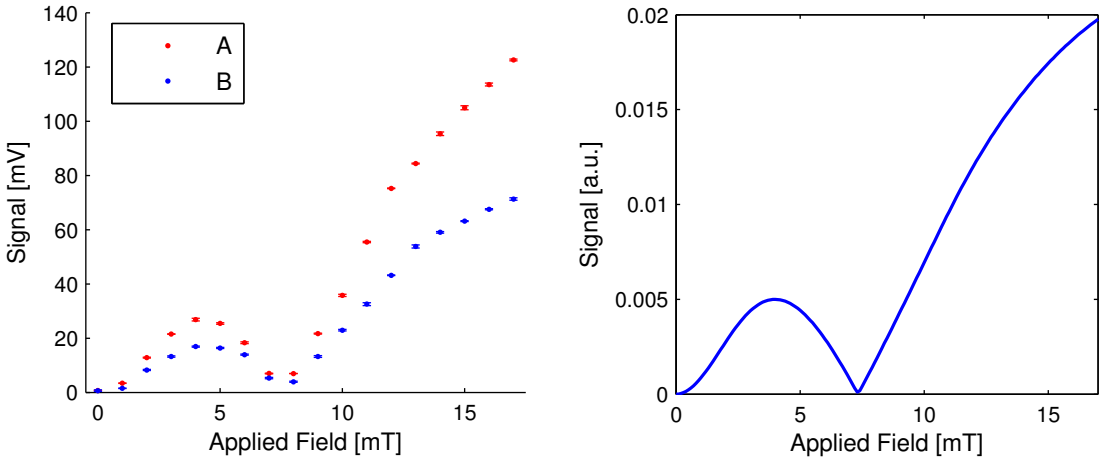

(b) $a'c'$ plane

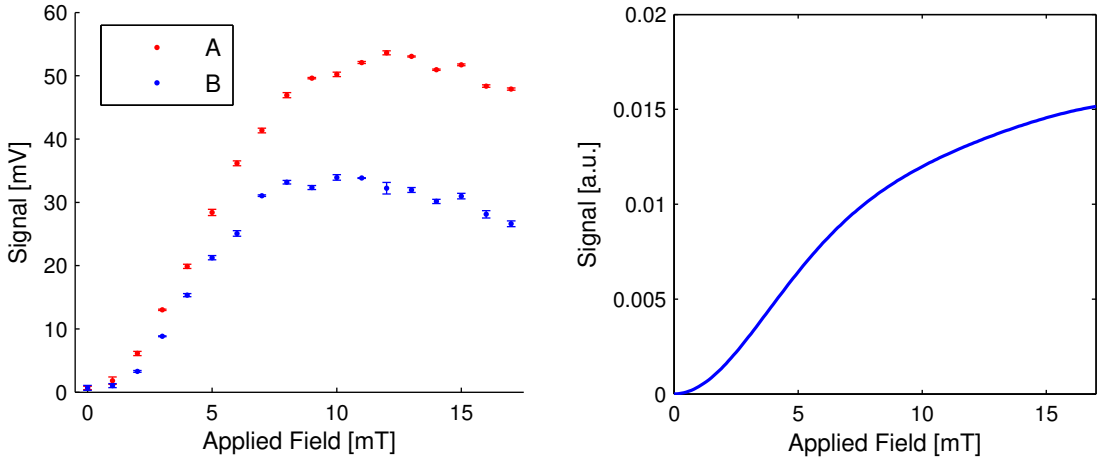

(c) bc' plane

Figure 5.23: Experimental results (left column) and simulations (right column) of AMELIA on tetracene crystals A and B, in 2$^{\text{nd}}$ harmonic detection mode.

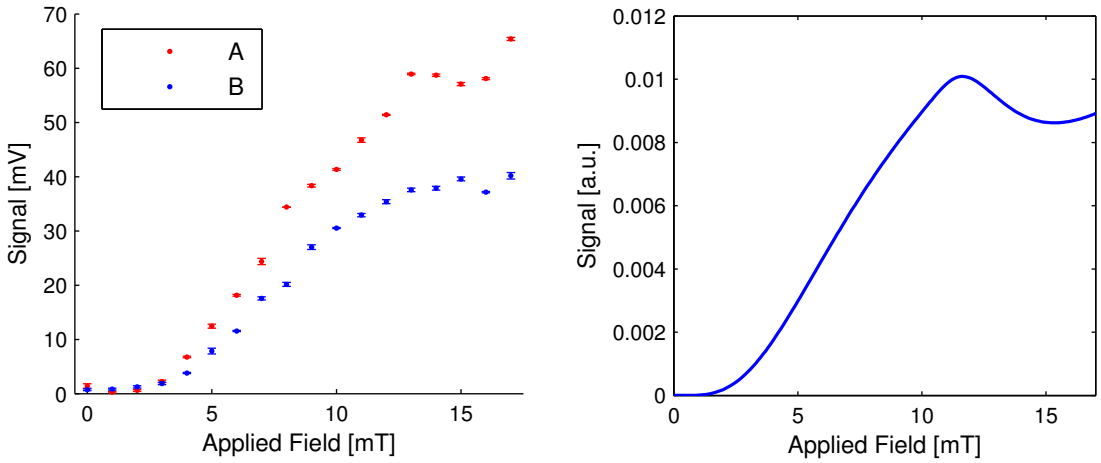

(a) $a'b$ plane

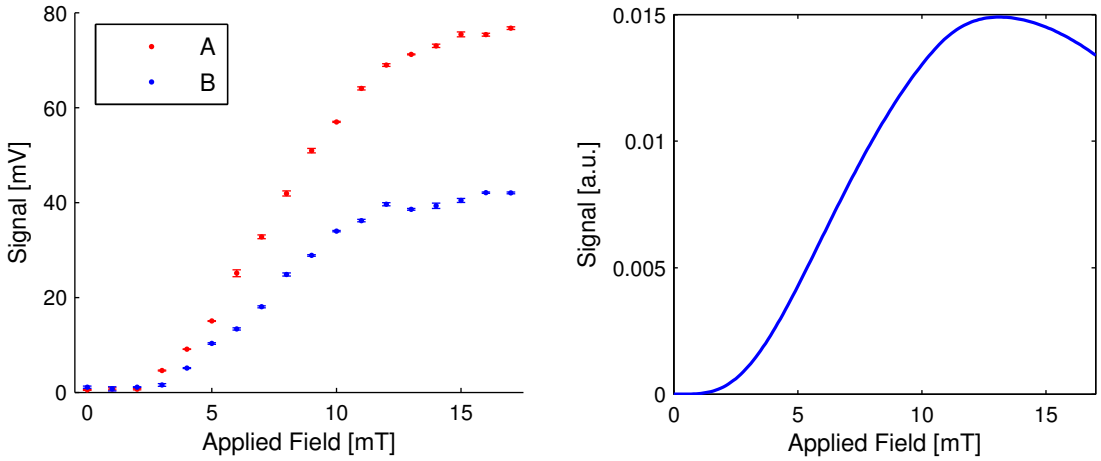

(b) $a'c'$ plane

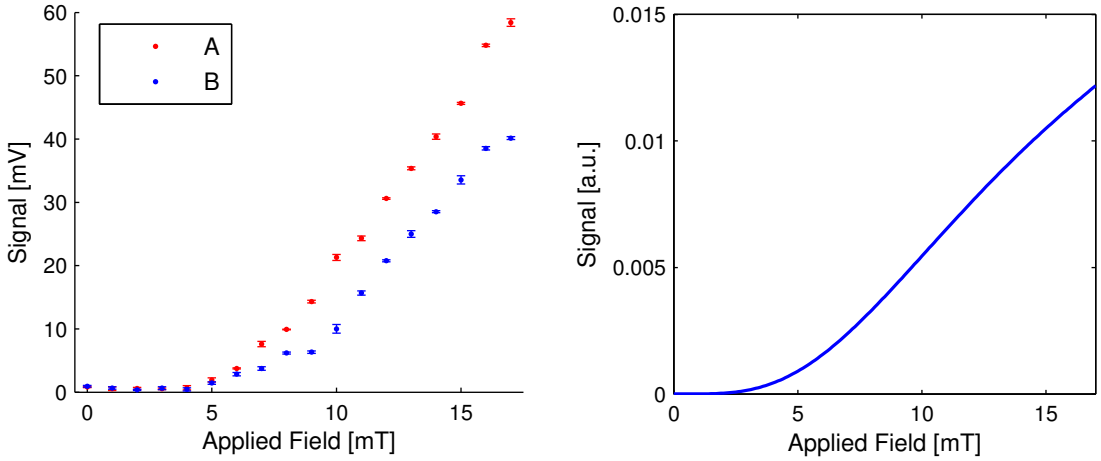

(c) bc' plane

Figure 5.24: Experimental results (left column) and simulations (right column) of AMELIA on tetracene crystals A and B, in 4^{th} harmonic detection mode.

5.6.2 Theoretical Analysis

The singlet yield in tetracene was simulated in the same way as the singlet yield in anthracene. A notable difference from anthracene is that tetracene's zero-field splitting tensor is not aligned with the crystallographic b axis and the ac plane [187], and neither is it aligned with the a', b and c' axes defined earlier (**figure 5.25**). However, the x and z axes of the zero field splitting tensor lie more or less in the $a'c'$ and bc' planes, respectively.

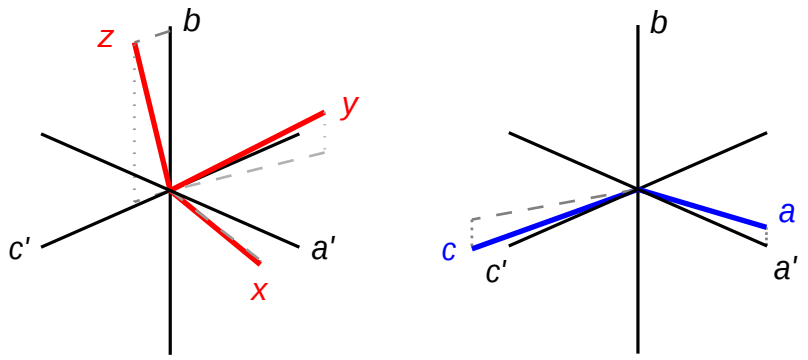

Figure 5.25: Zero field splitting (left) and crystallographic (right) axes of tetracene. The b component is shown with dots, and the $a'c'$ planar component with dashes.

Using the axes,

$$Q = \begin{array}{c} \\ a' \\ b \\ c' \end{array} \begin{array}{c} \begin{array}{ccc} x & y & z \end{array} \\ \begin{pmatrix} 0.9634 & 0.2634 & -0.0372 \\ -0.0269 & 0.2463 & 0.9714 \\ 0.2663 & -0.9330 & 0.2390 \end{pmatrix} \end{array}, \tag{5.46}$$

and zero field splitting parameters ($E = 26.5\,\mathrm{mT}$, $D = -6.6\,\mathrm{mT}$) measured by Yarmus [187], the zero field splitting tensor in the basis defined by a', b and c' is[3]

$$\boldsymbol{D} = Q \begin{pmatrix} 26.5\,\mathrm{mT} & 0 & 0 \\ 0 & -26.5\,\mathrm{mT} & 0 \\ 0 & 0 & -6.6\,\mathrm{mT} \end{pmatrix} Q^{\mathrm{T}} = \begin{pmatrix} 22.75 & -2.17 & 13.37 \\ -2.17 & -7.82 & 4.37 \\ 13.37 & 4.37 & -21.57 \end{pmatrix} \mathrm{mT}\,.$$

[3] A component of $\frac{D}{3}\mathbb{1}$ has been added to the usual form of the tensor. This simply shifts the energy of the triplet states by a constant, so has no effect on the spin dynamics

This tensor was used in all simulations of the spin dynamics of tetracene.

Unlike for anthracene, there is no literature estimate of the rates k_s or k_d for tetracene. These parameters were estimated using experimental fluorescence intensities at zero and high field, as will be explained in the following sections.

Limiting Zero-Field Singlet Yield

Two spin-one particles form a spin space of dimension 9, comprising a singlet, triplet, and quintet. In terms of each particle's spin state in the Zeeman basis, the singlet state is

$$|S\rangle = \frac{1}{\sqrt{3}} \left(|1,-1\rangle + |-1,1\rangle - |0,0\rangle \right) . \tag{5.47}$$

Under the zero field Hamiltonian, $|S\rangle$ is a linear combination of three eigenstates:

$$|S\rangle = \frac{1}{\sqrt{3}} \left(|v_1\rangle + |v_2\rangle - |v_3\rangle \right) . \tag{5.48}$$

Where

$$\begin{aligned} |v_1\rangle &= \frac{1}{2} \left(|1,-1\rangle + |-1,1\rangle - |1,1\rangle - |-1,-1\rangle \right) \\ |v_2\rangle &= \frac{1}{2} \left(|1,-1\rangle + |-1,1\rangle + |1,1\rangle + |-1,-1\rangle \right) \\ |v_3\rangle &= |0,0\rangle \ , \end{aligned}$$

with energies expressed as angular frequencies

$$\begin{aligned} \omega_1 &= 2D - 2E \\ \omega_2 &= 2D + 2E \\ \omega_3 &= 0 \, . \end{aligned}$$

As these three states are not degenerate in tetracene, coherent spin evolution causes oscillation away from the initial singlet state. Ignoring reactivity and spin-relaxation, the average singlet probability is $\frac{1}{3}$ according to **equation 5.43** (p. 171). We can

therefore define an average singlet recombination rate

$$\kappa_s = \frac{k_s}{3} \tag{5.49}$$

Using the same branching ratio argument as in **section 5.5.2**, the approximate limiting singlet yield (where reactivity is much slower than coherent interconversion rate ω_{min}) at zero field is

$$\Phi_s(0) = \frac{k_s/3}{k_s/3 + k_d}\,. \tag{5.50}$$

The approximate singlet yield from the above equation was validated against the singlet yield calculated quantum mechanically for anthracene (**section 5.5.2**), and the two yields yields matched almost perfectly (**figure 5.26**).

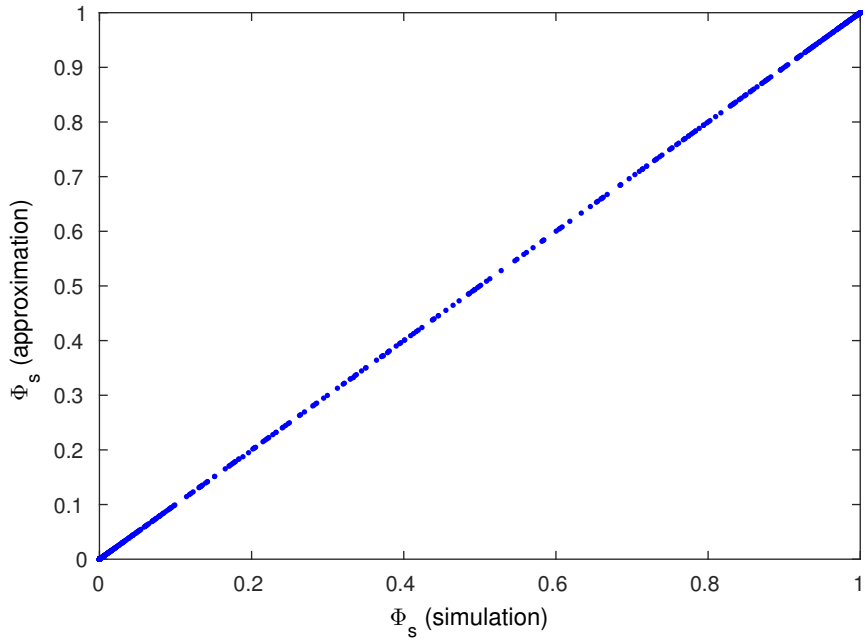

Figure 5.26: Approximate singlet yield at zero field, from equation 5.50, plotted against the singlet yield calculated quantum mechanically. The yield was calculated for 1000 samples of k_s and k_d, between 10^0 and $10^9\,\text{s}^{-1}$, with the exponent sampled from a uniform distribution. Parameters: $B_0 = 0\,\text{mT}$, $E = 35\,\text{mT}$, $D = -6.2\,\text{mT}$.

Limiting High-Field Singlet Yield

At high field, $|S\rangle$ is a linear combination of two eigenstates of the Hamiltonian

$$|S\rangle = \sqrt{\frac{2}{3}}\,|v_1\rangle - \sqrt{\frac{1}{3}}\,|v_2\rangle\ , \tag{5.51}$$

where

$$|v_1\rangle = \frac{1}{\sqrt{2}}\left(|1,-1\rangle + |-1,1\rangle\right)$$
$$|v_2\rangle = |0,0\rangle \ ,$$

with angular frequencies [121]

$$\omega_1 = D\left(1+\cos^2\gamma\right) + E\left(\cos^2\alpha - \cos^2\beta\right)$$
$$\omega_2 = 2\left(D-E\right)\cos^2\alpha + 2\left(D+E\right)\cos^2\beta\,,$$

where D and E are components of the zero field splitting tensor, and α, β and γ are the angles made by B_0 with the x, y and z axes of said tensor, respectively.

When $|v_1\rangle$ and $|v_2\rangle$ are energetically isolated, ignoring reactivity and spin relaxation, the furthest the spin state can evolve from the singlet state is

$$|\psi\rangle = \sqrt{\frac{2}{3}}\,|v_1\rangle + \sqrt{\frac{1}{3}}\,|v_2\rangle \ ,$$

which has singlet probability

$$|\,\langle S|\psi\rangle\,|^2 = \frac{1}{9}\,.$$

Therefore the singlet probability oscillates between $\frac{1}{9}$ and 1, giving an average singlet probability of $\frac{5}{9}$. Far from a level crossing, the limiting singlet yield ($k_s, k_d \ll \Delta\omega_{\min}$) at high field is then

$$\Phi_s^{\mathrm{OFF}}(\infty) = \frac{5k_s/9}{5k_s/9 + k_d}\,. \tag{5.52}$$

The approximate singlet yield from the above equation was validated against the singlet yield calculated quantum mechanically for anthracene. The singlet yields calculated with the two methods matched almost perfectly (**figure 5.27**).

Determination of k_s/k_d from Fluorescence Intensity

Assuming that fluorescence intensity is wholly from triplet exciton fusion (not unreasonable, as singlet to triplet conversion efficiency is believed to be close to 100 %

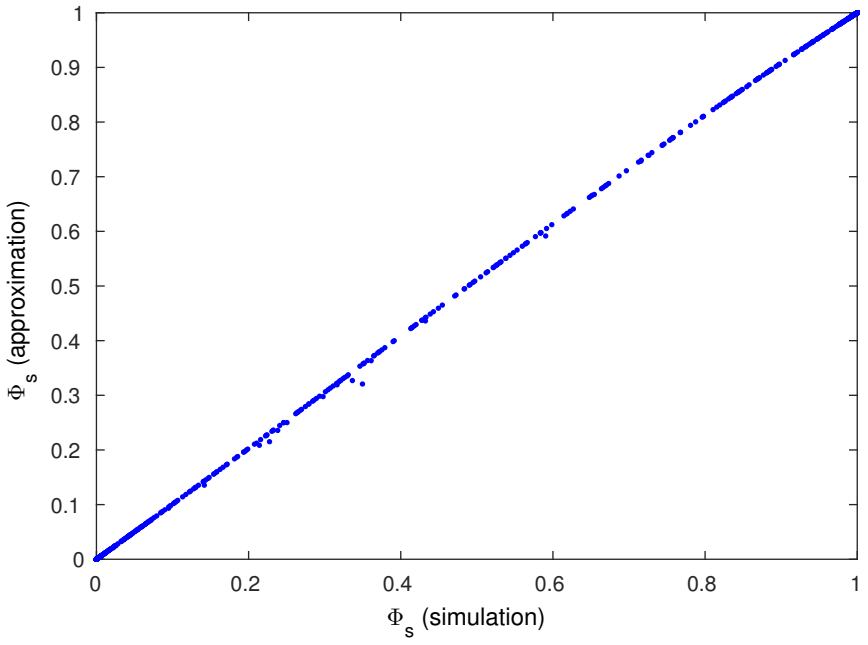

Figure 5.27: Approximate singlet yield at high field, from equation 5.52, plotted against the singlet yield calculated quantum mechanically. The yield was calculated for 1000 samples of k_s and k_d, between 10^0 and $10^9\,\mathrm{s}^{-1}$, with the exponent sampled from a uniform distribution. Parameters: $B_0 = 10\,\mathrm{T}$, $E = 35\,\mathrm{mT}$, $D = -6.2\,\mathrm{mT}$. The applied magnetic field was parallel to the z axis of the zero field splitting tensor, which is far from a level crossing [84].

[187, 10]), zero field and off resonance high field fluorescence intensities are proportional to **equations 5.50 and 5.52**, respectively. If we define R to be the fluorescence intensity at high field relative to low field,

$$R = \frac{F^{\mathrm{OFF}}(\infty)}{F(0)} = \frac{\Phi_s^{\mathrm{OFF}}(\infty)}{\Phi_s(0)}$$

substituting 5.50 and 5.52 into the right hand side, and rearranging, determines the ratio

$$\frac{k_s}{k_d} = \frac{5/3 - R}{5/9(R-1)}\,.$$

Literature values of R are 1.15 ± 0.01 [60] and 1.08 [89]. Geacintov [60] notes that a lower value indicates a poorer quality crystal, so using $R = 1.15 \pm 0.01$ results in the ratio:

$$\frac{k_s}{k_d} = 6.2 \pm 0.8\,. \tag{5.53}$$

Determination of k_s and k_d

The absolute values of the rate constants were estimated by simulating the AMELIA experiment on tetracene at the ratio determined above (equation 5.53), and manually varying the magnitude to get a satisfactory fit to the experimental data.

$$k_s = 10^{9.3\pm0.3}\,\mathrm{s}^{-1} \approx 2.0 \times 10^{9}\,\mathrm{s}^{-1}$$

$$k_d = 10^{8.5\pm0.3}\,\mathrm{s}^{-1} \approx 3.2 \times 10^{8}\,\mathrm{s}^{-1}$$

These rates are unlikely to be wholly accurate, as the zero-field splitting frequency is of the order $10^9\,\mathrm{s}^{-1}$, so the condition $k_s, k_d \ll \Delta\omega_{\mathrm{min}}$ is not well fulfilled.

Anisotropy in Eigenstate Energies and Singlet Amplitudes

As with anthracene, tetracene showed large anisotropy in eigenstate singlet amplitudes (**figures 5.28 to 5.30**). Furthermore, principal axes of the zero field splitting tensor were associated with extrema in the average singlet probability in both crystals. However, in the case of tetracene, eigenstates started to become degenerate at a much weaker applied magnetic field, since the zero field splitting parameter E is smaller in tetracene than in anthracene.

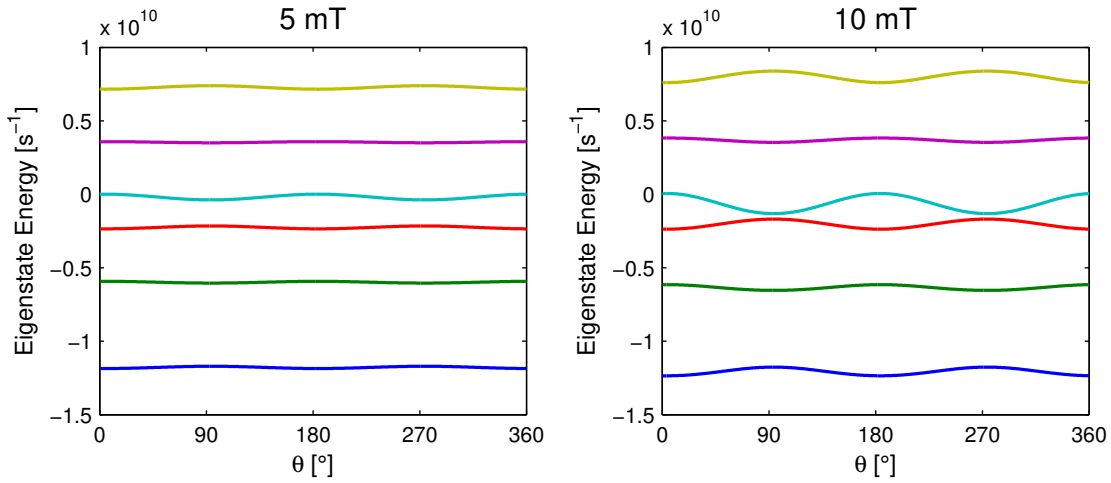

(a) Energy of Hamiltonian's eigenstates

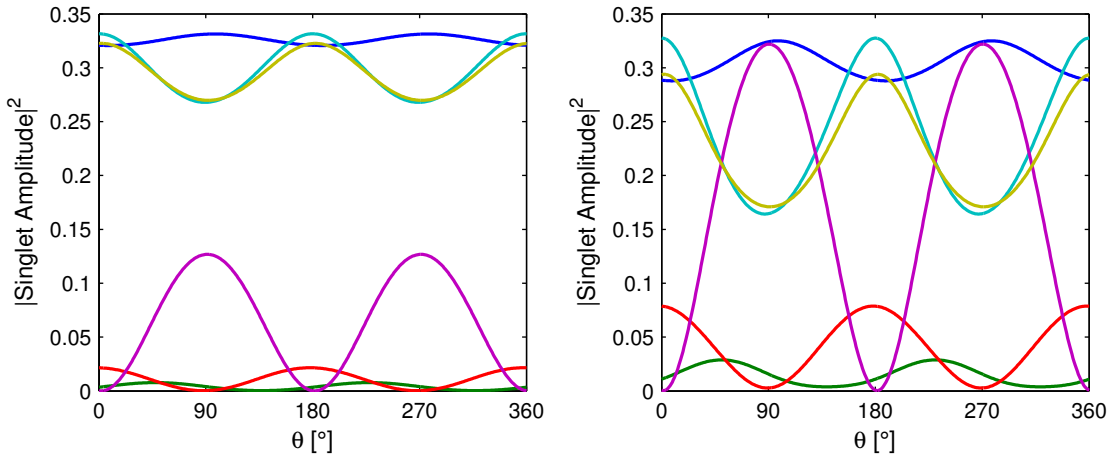

(b) Singlet component of Hamiltonian's eigenstates

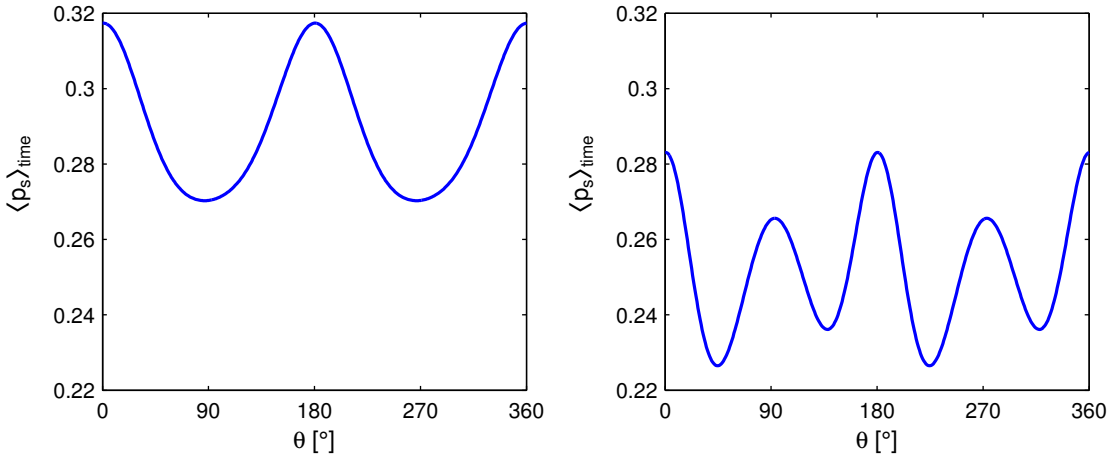

(c) Average singlet probability (ignoring relaxation and reactivity)

Figure 5.28: Calculation of eigenstate energies, their singlet amplitudes and average singlet probability for an infinitely long lived exciton pair, with an applied magnetic field in the ***a'b* plane**. The angle θ is the field direction with respect to the b axis. First column is at 5 mT applied field, and second column at 10 mT.

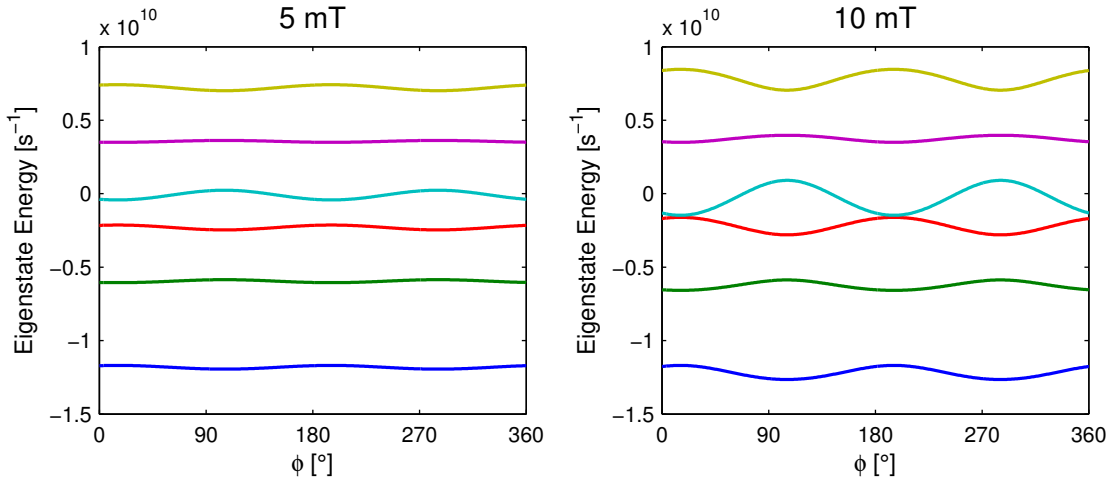

(a) Energy of Hamiltonian's eigenstates

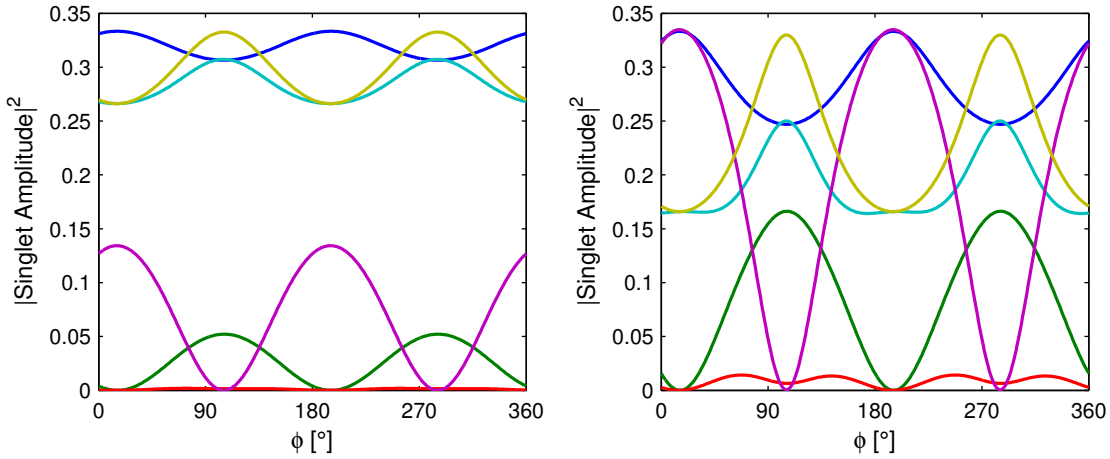

(b) Singlet component of Hamiltonian's eigenstates

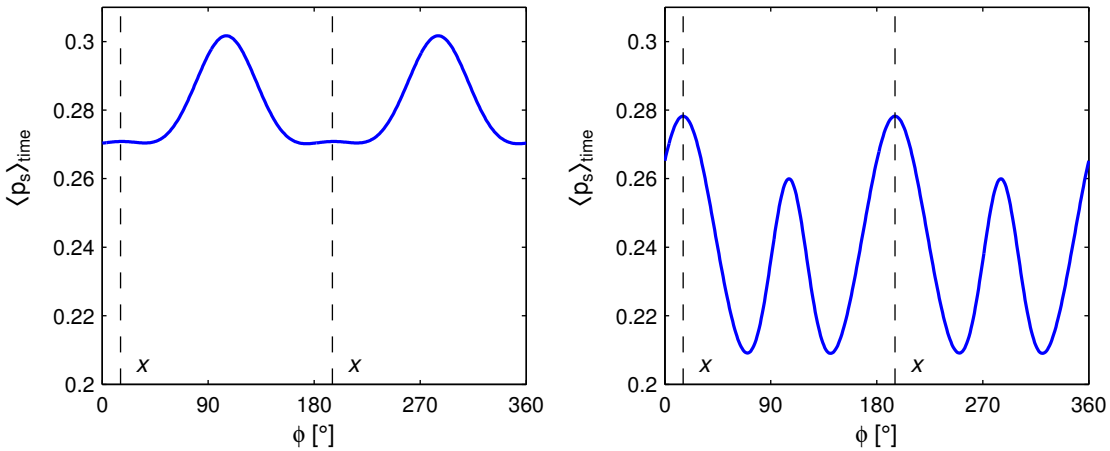

(c) Average singlet probability (ignoring relaxation and reactivity)

Figure 5.29: Calculation of eigenstate energies, their singlet amplitudes and average singlet probability for an infinitely long lived exciton pair, with an applied magnetic field in the ***a′c′* plane**. The angle ϕ is the field direction with respect to the a' axis. The dashed lines are the x axes of the zero field splitting tensor. First column is at 5 mT applied field, and second column at 10 mT.

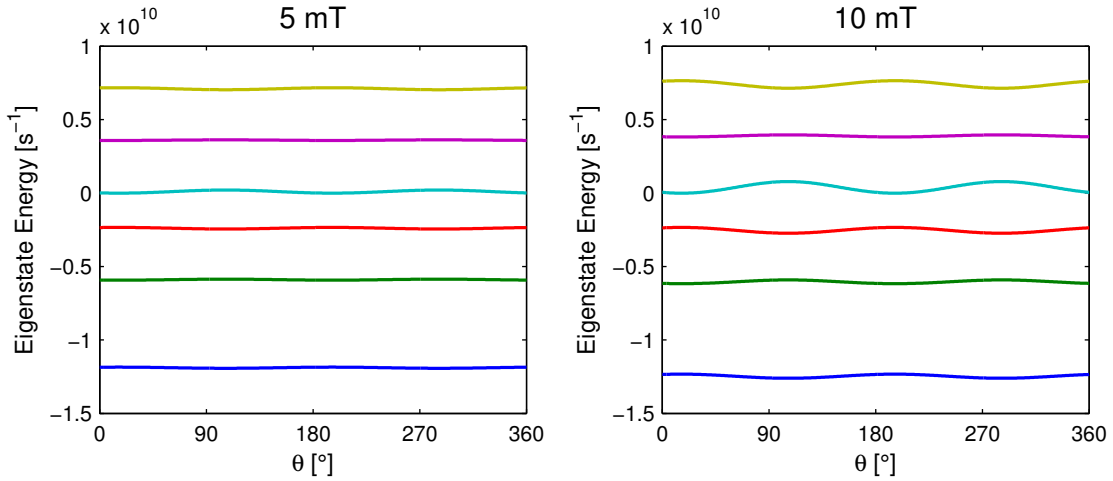

(a) Energy of Hamiltonian's eigenstates

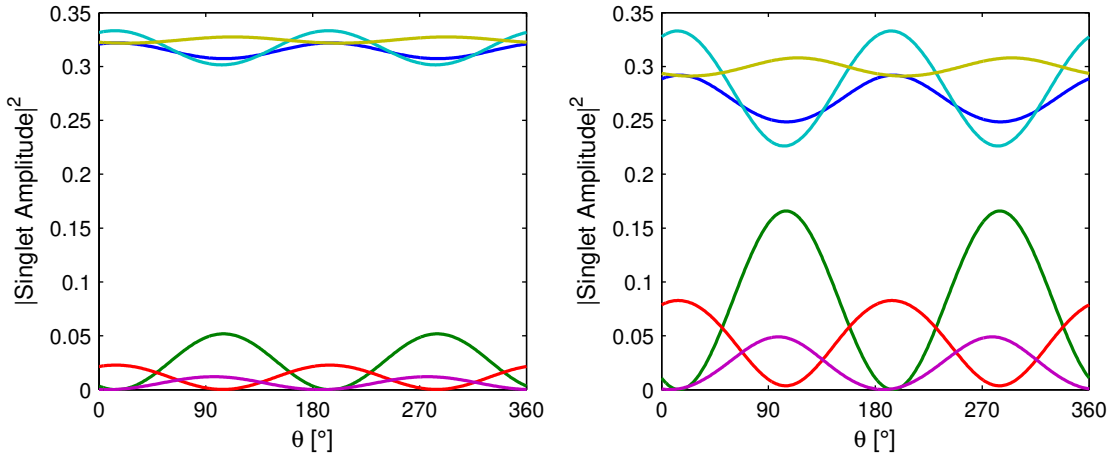

(b) Singlet component of Hamiltonian's eigenstates

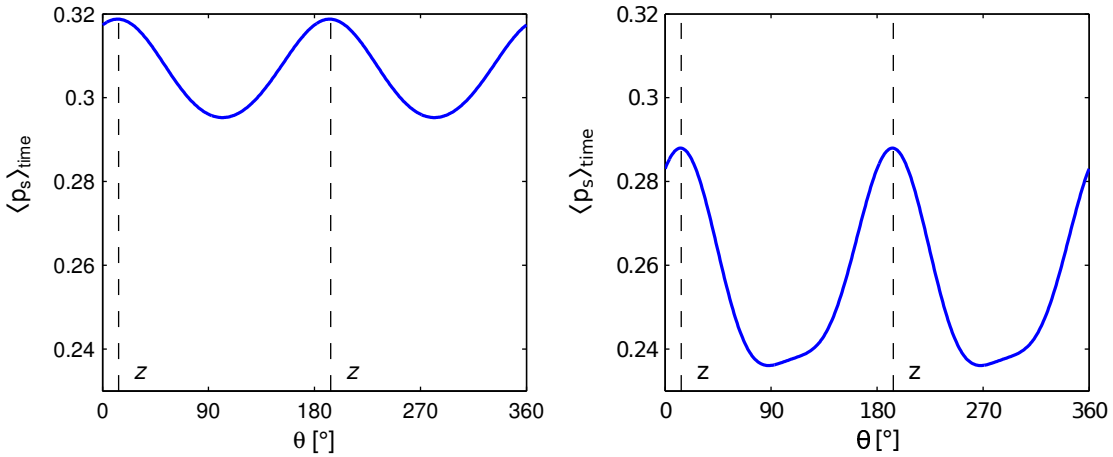

(c) Average singlet probability (ignoring relaxation and reactivity)

Figure 5.30: Calculation of eigenstate energies, their singlet amplitudes and average singlet probability for an infinitely long lived exciton pair, with an applied magnetic field in the ***bc′* plane**. The angle θ is the field direction with respect to the b axis. The dashed lines are the z axes of the zero field splitting tensor. First column is at 5 mT applied field, and second column at 10 mT.

5.7 Conclusions

Johnson and Merrifield's theory [84] of triplet exciton annihilation fit the experimental data adequately. There was no evidence of fine structure in the experimental results unaccounted for by the simulations, and therefore no evidence of interactions weaker than the zero-field splitting assumed to be present in each triplet exciton. This is in line with the established theory that excitons are so mobile as to average out any hyperfine or dipolar interactions [10, 187].

At weak magnetic field strengths ($< 10\,\mathrm{mT}$), anisotropy in tetracene and anthracene is caused by differences in eigenstate singlet amplitude, and not by eigenstate level crossings. To the author's knowledge, this mechanism has not been described in polyacene crystals before. The weakest field that Johnson and Merrifield [84] discussed was 40 mT, at which eigenstate level crossings indeed exist. There are therefore three distinct regions of magnetic field effect:

- Low field ($B_0 < D, E$): alteration of eigenstate singlet amplitudes
- Medium field ($B_0 \approx D, E$): level crossings aligned with principal axes of zero field splitting tensor
- High field ($B_0 \gg D, E$): level crossings at locations determined by ratio $\frac{D}{E}$

The fitted rate constants suggest that triplet excitons are less mobile in tetracene than in anthracene by an order of magnitude, but that singlet recombination kinetics are similar in the two materials. Given the established diffusion constant in anthracene ($\sim 10^{-4}\,\mathrm{cm^2\,s^{-1}}$) [11], the result in this thesis is consistent with the value for tetracene reported by Vaubel ($1.6 \times 10^{-5}\,\mathrm{cm^2\,s^{-1}}$) [180], but not with the values reported by Aladekomo and by Akselrod ($\sim 10^{-3}\,\mathrm{cm^2\,s^{-1}}$) [6, 4]. Since the literature consensus is for a higher diffusion rate in tetracene than in anthracene, the opposite trend found in the current work could be an artifact due to the neglect of spin relaxation.

Overall, the AMELIA experiment has been shown to be sensitive to anisotropic magnetic field effects in applied magnetic fields as low as 1 mT. The setup could now be used to study flavin mononucleotide-lysozyme crystals, or viscous solutions of molecules suspected to display anisotropic magnetic field effects (cryptochrome, carotenoid-porphyrin-fullerene triads...).

The experiment could be improved by adding a liquid nitrogen cryostat, which would allow the immobilization of samples in a solvent glass. The magnetic field stability could be improved by permanently installing a Hall probe in the magnetic coils, and setting the magnetic field using a feedback loop. Magnetic field effects at a sub-millitesla level could be probed with a new set of coils shielded from the Earth's magnetic field with mu-metal.

Appendix A

Magnetic Interactions in Carotenoid Radical Cation

Magnetic interactions in the carotenoid radical cation were calculated with the Gaussian software package by Ilya Kuprov using the ub3lyp functional with the EPR-II basis set [111, 12, 55].

A.1 Fermi Contact Coupling

	Fermi Contact Coupling			
Atom	$[E_h]$	[MHz]	[G]	$[10^{-4}\,cm^{-1}]$
1 C(13)	0.00443	4.98338	1.77819	1.66228
2 C(13)	-0.00382	-4.2934	-1.53199	-1.43212
3 C(13)	-0.00374	-4.20006	-1.49869	-1.40099
4 C(13)	0.00392	4.40314	1.57115	1.46873
5 H(1)	0.00031	1.36733	0.4879	0.45609
6 C(13)	0.00388	4.36505	1.55756	1.45603
7 H(1)	0.00029	1.29835	0.46328	0.43308
8 C(13)	-0.00735	-8.26553	-2.94934	-2.75708
9 H(1)	-0.00072	-3.22562	-1.15098	-1.07595
10 H(1)	-0.0007	-3.11966	-1.11317	-1.04061
11 C(13)	0.01177	13.23349	4.72204	4.41422
12 H(1)	-0.00226	-10.12413	-3.61254	-3.37705
13 C(13)	-0.01156	-12.99335	-4.63635	-4.33411
14 H(1)	0.00082	3.64551	1.30081	1.21601
15 C(13)	0.01349	15.16278	5.41046	5.05776

Atom	[E_h]	[MHz]	[G]	[10^{-4} cm^{-1}]
16 C(13)	-0.01044	-11.73332	-4.18674	-3.91381
17 H(1)	0.0006	2.65964	0.94903	0.88716
18 C(13)	0.01053	11.83856	4.22429	3.94892
19 H(1)	-0.00199	-8.88142	-3.16911	-2.96252
20 C(13)	-0.00895	-10.05915	-3.58935	-3.35537
21 H(1)	0.00059	2.6533	0.94676	0.88505
22 C(13)	0.00804	9.03289	3.22316	3.01305
23 C(13)	-0.0039	-4.38106	-1.56327	-1.46136
24 H(1)	-0.00014	-0.61143	-0.21817	-0.20395
25 C(13)	0.00255	2.87117	1.0245	0.95772
26 H(1)	-0.00088	-3.94012	-1.40593	-1.31428
27 C(13)	-5e-05	-0.05283	-0.01885	-0.01762
28 H(1)	-0.00055	-2.46517	-0.87963	-0.82229
29 C(13)	-0.00134	-1.5035	-0.53649	-0.50151
30 H(1)	-0.00045	-2.00255	-0.71456	-0.66798
31 C(13)	0.00546	6.13491	2.18909	2.04639
32 C(13)	-0.00668	-7.51503	-2.68155	-2.50675
33 H(1)	0.00032	1.41752	0.50581	0.47283
34 C(13)	0.00847	9.52456	3.3986	3.17705
35 H(1)	-0.00173	-7.7129	-2.75215	-2.57274
36 C(13)	-0.0086	-9.66724	-3.44951	-3.22464
37 H(1)	0.00035	1.58196	0.56448	0.52769
38 C(13)	0.012	13.49408	4.81502	4.50114
39 C(13)	-0.01077	-12.10739	-4.32022	-4.03859
40 H(1)	0.0007	3.13646	1.11917	1.04621
41 C(13)	0.01154	12.97505	4.62982	4.32801
42 H(1)	-0.00242	-10.80539	-3.85563	-3.60429
43 C(13)	-0.00466	-5.24043	-1.86992	-1.74802
44 H(1)	0.00301	13.46578	4.80492	4.4917
45 H(1)	0.0001	0.44005	0.15702	0.14679
46 H(1)	0.00308	13.75591	4.90845	4.58848
47 C(13)	-0.0032	-3.59426	-1.28252	-1.19892
48 H(1)	0.00208	9.31397	3.32346	3.10681
49 H(1)	0.00192	8.5941	3.06659	2.86668
50 H(1)	7e-05	0.33229	0.11857	0.11084
51 C(13)	-0.00258	-2.89588	-1.03332	-0.96596
52 H(1)	5e-05	0.23471	0.08375	0.07829
53 H(1)	0.00155	6.90822	2.46503	2.30433
54 H(1)	0.00161	7.20255	2.57005	2.40251
55 C(13)	-0.00436	-4.89713	-1.74742	-1.63351
56 H(1)	0.0001	0.4402	0.15707	0.14683
57 H(1)	0.00308	13.77456	4.9151	4.5947
58 H(1)	0.00256	11.42693	4.07741	3.81161
59 C(13)	-0.00858	-9.64344	-3.44102	-3.2167
60 C(13)	0.00993	11.16819	3.98509	3.72531
61 C(13)	0.00203	2.27828	0.81295	0.75995
62 C(13)	-0.00305	-3.42539	-1.22226	-1.14259
63 C(13)	-6e-05	-0.06255	-0.02232	-0.02086
64 C(13)	0.00061	0.68308	0.24374	0.22785

Atom	[E_h]	[MHz]	[G]	[10^{-4} cm^{-1}]
65 H(1)	0.00109	4.86765	1.7369	1.62367
66 H(1)	0.00363	16.23071	5.79152	5.41398
67 H(1)	0.00036	1.60642	0.57321	0.53584
68 H(1)	4e-05	0.17265	0.06161	0.05759
69 H(1)	-3e-05	-0.1429	-0.05099	-0.04767
70 H(1)	-2e-05	-0.09167	-0.03271	-0.03058
71 C(13)	-0.00123	-1.3855	-0.49438	-0.46215
72 H(1)	0.00012	0.51686	0.18443	0.17241
73 H(1)	1e-05	0.04381	0.01563	0.01461
74 H(1)	-0.00011	-0.49703	-0.17735	-0.16579
75 C(13)	-0.00146	-1.64485	-0.58692	-0.54866
76 H(1)	9e-05	0.4004	0.14287	0.13356
77 H(1)	-0.00018	-0.7935	-0.28314	-0.26468
78 H(1)	2e-05	0.08921	0.03183	0.02976
79 C(13)	-0.00308	-3.46521	-1.23647	-1.15587
80 H(1)	0.00155	6.92054	2.46942	2.30844
81 H(1)	0.00277	12.3884	4.42049	4.13232
82 H(1)	0.00017	0.77035	0.27488	0.25696
83 H(1)	-0.00085	-3.81115	-1.35991	-1.27126

A.2 Electron-Nucleus Dipolar Coupling

Eigenvalues (B_{aa}, B_{bb} and B_{cc}) are ordered from most negative to most positive, and the corresponding axis is displayed in row vector form.

		Fermi Contact Coupling						
Atom	Eigenvalue	[E_h]	[MHz]	[G]	[10^{-4} cm^{-1}]	Axis		
	B_{aa}	-0.0316	-4.235	-1.511	-1.413	0.5285	0.8403	0.1207
1 C(13)	B_{bb}	-0.0286	-3.844	-1.372	-1.282	0.8482	-0.5287	-0.0329
	B_{cc}	0.0602	8.079	2.883	2.695	-0.0362	-0.1198	0.9921
	B_{aa}	-0.0230	-3.088	-1.102	-1.030	-0.0363	-0.1198	0.9921
2 C(13)	B_{bb}	0.0103	1.380	0.492	0.460	0.8047	0.5852	0.1001
	B_{cc}	0.0127	1.708	0.609	0.570	-0.5925	0.8020	0.0752
	B_{aa}	-0.0220	-2.946	-1.051	-0.983	-0.0361	-0.1198	0.9921
3 C(13)	B_{bb}	0.0097	1.303	0.465	0.435	0.1877	0.9743	0.1244
	B_{cc}	0.0122	1.643	0.586	0.548	0.9816	-0.1907	0.0127
	B_{aa}	-0.0256	-3.440	-1.227	-1.147	-0.1717	0.9787	0.1121
4 C(13)	B_{bb}	-0.0253	-3.394	-1.211	-1.132	0.9845	0.1665	0.0549
	B_{cc}	0.0509	6.834	2.438	2.279	-0.0350	-0.1198	0.9922
	B_{aa}	-0.0009	-0.475	-0.169	-0.158	-0.0348	-0.1190	0.9923
5 H(1)	B_{bb}	-0.0004	-0.219	-0.078	-0.073	0.8632	0.4969	0.0898
	B_{cc}	0.0013	0.694	0.248	0.231	-0.5037	0.8596	0.0854
	B_{aa}	-0.0250	-3.355	-1.197	-1.119	0.9095	-0.4155	-0.0163
6 C(13)	B_{bb}	-0.0247	-3.316	-1.183	-1.106	0.4142	0.9018	0.1234

Atom	Eigenvalue	[E_h]	[MHz]	[G]	[10^{-4} cm^{-1}]	Axis		
	B_{cc}	0.0497	6.672	2.381	2.225	-0.0366	-0.1190	0.9922
	B_{aa}	-0.0009	-0.476	-0.170	-0.159	-0.0357	-0.1204	0.9921
7 H(1)	B_{bb}	-0.0004	-0.215	-0.077	-0.072	0.0643	0.9904	0.1225
	B_{cc}	0.0013	0.691	0.247	0.231	0.9973	-0.0682	0.0276
	B_{aa}	-0.0226	-3.038	-1.084	-1.013	-0.0353	-0.1198	0.9922
8 C(13)	B_{bb}	0.0093	1.244	0.444	0.415	0.6194	0.7765	0.1158
	B_{cc}	0.0134	1.794	0.640	0.598	0.7843	-0.6186	-0.0468
	B_{aa}	-0.0020	-1.069	-0.381	-0.357	0.9742	-0.2257	0.0078
9 H(1)	B_{bb}	-0.0011	-0.596	-0.213	-0.199	-0.0359	-0.1211	0.9920
	B_{cc}	0.0031	1.665	0.594	0.555	0.2230	0.9666	0.1261
	B_{aa}	-0.0023	-1.202	-0.429	-0.401	-0.5896	0.8044	0.0729
10 H(1)	B_{bb}	-0.0011	-0.561	-0.200	-0.187	-0.0385	-0.1182	0.9922
	B_{cc}	0.0033	1.763	0.629	0.588	0.8068	0.5822	0.1007
	B_{aa}	-0.0864	-11.595	-4.137	-3.868	0.9586	0.2757	0.0710
11 C(13)	B_{bb}	-0.0839	-11.261	-4.018	-3.756	-0.2821	0.9534	0.1070
	B_{cc}	0.1703	22.856	8.156	7.624	-0.0382	-0.1226	0.9917
	B_{aa}	-0.0092	-4.908	-1.751	-1.637	0.9745	-0.2240	0.0101
12 H(1)	B_{bb}	-0.0013	-0.689	-0.246	-0.230	-0.0381	-0.1212	0.9919
	B_{cc}	0.0105	5.597	1.997	1.867	0.2210	0.9670	0.1267
	B_{aa}	-0.0607	-8.150	-2.908	-2.719	-0.0372	-0.1241	0.9916
13 C(13)	B_{bb}	0.0241	3.237	1.155	1.080	0.0313	0.9916	0.1253
	B_{cc}	0.0366	4.913	1.753	1.639	0.9988	-0.0357	0.0330
	B_{aa}	-0.0026	-1.389	-0.496	-0.463	-0.0364	-0.1244	0.9916
14 H(1)	B_{bb}	-0.0020	-1.041	-0.372	-0.347	0.1116	0.9855	0.1277
	B_{cc}	0.0046	2.430	0.867	0.811	0.9931	-0.1153	0.0220
	B_{aa}	-0.0922	-12.371	-4.414	-4.126	-0.2029	0.9727	0.1127
15 C(13)	B_{bb}	-0.0891	-11.955	-4.266	-3.988	0.9786	0.1974	0.0579
	B_{cc}	0.1813	24.326	8.680	8.114	-0.0341	-0.1220	0.9919
	B_{aa}	-0.0451	-6.051	-2.159	-2.018	-0.0313	-0.1253	0.9916
16 C(13)	B_{bb}	0.0163	2.186	0.780	0.729	-0.1412	0.9827	0.1198
	B_{cc}	0.0288	3.865	1.379	1.289	0.9895	0.1363	0.0484
	B_{aa}	-0.0023	-1.206	-0.430	-0.402	-0.0186	-0.1603	0.9869
17 H(1)	B_{bb}	-0.0016	-0.863	-0.308	-0.288	-0.3570	0.9231	0.1432
	B_{cc}	0.0039	2.070	0.738	0.690	0.9339	0.3497	0.0744
	B_{aa}	-0.0763	-10.235	-3.652	-3.414	-0.6043	0.7923	0.0837
18 C(13)	B_{bb}	-0.0736	-9.882	-3.526	-3.296	0.7962	0.5967	0.0999
	B_{cc}	0.1499	20.118	7.178	6.711	-0.0293	-0.1270	0.9915
	B_{aa}	-0.0075	-4.015	-1.433	-1.339	0.9977	-0.0645	0.0200
19 H(1)	B_{bb}	-0.0013	-0.719	-0.257	-0.240	-0.0278	-0.1223	0.9921
	B_{cc}	0.0089	4.734	1.689	1.579	0.0615	0.9904	0.1238
	B_{aa}	-0.0443	-5.949	-2.123	-1.984	-0.0265	-0.1287	0.9913
20 C(13)	B_{bb}	0.0164	2.205	0.787	0.736	-0.2827	0.9522	0.1161
	B_{cc}	0.0279	3.744	1.336	1.249	0.9588	0.2772	0.0616
	B_{aa}	-0.0022	-1.181	-0.421	-0.394	0.0211	-0.2519	0.9675
21 H(1)	B_{bb}	-0.0020	-1.044	-0.372	-0.348	-0.3622	0.9001	0.2422
	B_{cc}	0.0042	2.225	0.794	0.742	0.9319	0.3555	0.0722
	B_{aa}	-0.0635	-8.526	-3.042	-2.844	-0.5932	0.7998	0.0920
22 C(13)	B_{bb}	-0.0575	-7.718	-2.754	-2.574	0.8047	0.5860	0.0951

Atom	Eigenvalue	[E_h]	[MHz]	[G]	[10^{-4} cm^{-1}]	Axis		
	B_{cc}	0.1210	16.243	5.796	5.418	-0.0221	-0.1304	0.9912
	B_{aa}	-0.0105	-1.409	-0.503	-0.470	-0.4906	0.8614	0.1316
23 C(13)	B_{bb}	-0.0012	-0.163	-0.058	-0.054	0.8714	0.4856	0.0698
	B_{cc}	0.0117	1.572	0.561	0.524	0.0038	-0.1489	0.9888
	B_{aa}	-0.0019	-1.034	-0.369	-0.345	0.0645	-0.1816	0.9813
24 H(1)	B_{bb}	-0.0015	-0.799	-0.285	-0.266	0.9180	-0.3747	-0.1297
	B_{cc}	0.0034	1.833	0.654	0.611	0.3912	0.9092	0.1425
	B_{aa}	-0.0372	-4.993	-1.782	-1.666	-0.6368	0.7644	0.1008
25 C(13)	B_{bb}	-0.0310	-4.160	-1.484	-1.388	0.7710	0.6295	0.0964
	B_{cc}	0.0682	9.153	3.266	3.053	-0.0103	-0.1391	0.9902
	B_{aa}	-0.0034	-1.821	-0.650	-0.607	0.9998	0.0174	0.0033
26 H(1)	B_{bb}	-0.0017	-0.897	-0.320	-0.299	-0.0010	-0.1319	0.9913
	B_{cc}	0.0051	2.719	0.970	0.907	-0.0177	0.9911	0.1319
	B_{aa}	-0.0250	-3.354	-1.197	-1.119	-0.5921	0.7976	0.1151
27 C(13)	B_{bb}	-0.0180	-2.416	-0.862	-0.806	0.8058	0.5846	0.0942
	B_{cc}	0.0430	5.770	2.059	1.925	-0.0078	-0.1485	0.9889
	B_{aa}	-0.0023	-1.252	-0.447	-0.418	0.9960	-0.0871	0.0189
28 H(1)	B_{bb}	-0.0017	-0.926	-0.330	-0.309	-0.0315	-0.1453	0.9889
	B_{cc}	0.0041	2.178	0.777	0.726	0.0834	0.9855	0.1475
	B_{aa}	-0.0220	-2.950	-1.053	-0.984	-0.5390	0.8341	0.1170
29 C(13)	B_{bb}	-0.0138	-1.845	-0.658	-0.616	0.8423	0.5328	0.0816
	B_{cc}	0.0357	4.796	1.711	1.600	-0.0057	-0.1425	0.9898
	B_{aa}	-0.0021	-1.139	-0.407	-0.380	0.9731	-0.1976	-0.1182
30 H(1)	B_{bb}	-0.0019	-1.013	-0.362	-0.338	0.0868	-0.1607	0.9832
	B_{cc}	0.0040	2.153	0.768	0.718	0.2132	0.9670	0.1392
	B_{aa}	-0.0513	-6.883	-2.456	-2.296	-0.5819	0.8042	0.1207
31 C(13)	B_{bb}	-0.0448	-6.009	-2.144	-2.004	0.8132	0.5748	0.0911
	B_{cc}	0.0961	12.892	4.600	4.300	-0.0039	-0.1511	0.9885
	B_{aa}	-0.0228	-3.057	-1.091	-1.020	-0.0029	-0.1611	0.9869
32 C(13)	B_{bb}	0.0061	0.817	0.291	0.272	-0.3231	0.9341	0.1515
	B_{cc}	0.0167	2.240	0.799	0.747	0.9463	0.3185	0.0548
	B_{aa}	-0.0022	-1.173	-0.419	-0.391	-0.0253	-0.1100	0.9936
33 H(1)	B_{bb}	-0.0014	-0.726	-0.259	-0.242	-0.5112	0.8555	0.0817
	B_{cc}	0.0036	1.900	0.678	0.634	0.8591	0.5059	0.0779
	B_{aa}	-0.0669	-8.974	-3.202	-2.993	-0.5252	0.8396	0.1388
34 C(13)	B_{bb}	-0.0635	-8.515	-3.038	-2.840	0.8510	0.5189	0.0815
	B_{cc}	0.1303	17.489	6.241	5.834	0.0036	-0.1609	0.9870
	B_{aa}	-0.0065	-3.478	-1.241	-1.160	0.9974	-0.0701	-0.0173
35 H(1)	B_{bb}	-0.0014	-0.771	-0.275	-0.257	0.0053	-0.1673	0.9859
	B_{cc}	0.0080	4.249	1.516	1.417	0.0720	0.9834	0.1665
	B_{aa}	-0.0263	-3.532	-1.260	-1.178	0.0093	-0.1525	0.9883
36 C(13)	B_{bb}	0.0073	0.978	0.349	0.326	-0.1817	0.9716	0.1516
	B_{cc}	0.0190	2.554	0.911	0.852	0.9833	0.1809	0.0187
	B_{aa}	-0.0023	-1.219	-0.435	-0.407	0.0009	-0.1513	0.9885
37 H(1)	B_{bb}	-0.0012	-0.635	-0.227	-0.212	-0.5212	0.8435	0.1296
	B_{cc}	0.0035	1.854	0.662	0.619	0.8534	0.5153	0.0781
	B_{aa}	-0.0859	-11.520	-4.111	-3.843	-0.2653	0.9517	0.1547
38 C(13)	B_{bb}	-0.0821	-11.013	-3.930	-3.673	0.9641	0.2640	0.0294

Atom	Eigenvalue	$[E_h]$	[MHz]	[G]	$[10^{-4}\,cm^{-1}]$	Axis		
	B_{cc}	0.1679	22.533	8.040	7.516	0.0129	-0.1569	0.9875
	B_{aa}	-0.0498	-6.683	-2.385	-2.229	0.0550	-0.1434	0.9881
39 C(13)	B_{bb}	0.0189	2.538	0.905	0.846	0.0053	0.9897	0.1434
	B_{cc}	0.0309	4.145	1.479	1.383	0.9985	0.0027	-0.0552
	B_{aa}	-0.0027	-1.465	-0.523	-0.489	0.0000	-0.0131	0.9999
40 H(1)	B_{bb}	-0.0016	-0.860	-0.307	-0.287	0.0595	0.9981	0.0131
	B_{cc}	0.0044	2.325	0.830	0.776	0.9982	-0.0595	-0.0008
	B_{aa}	-0.0840	-11.277	-4.024	-3.762	0.9674	0.2469	-0.0570
41 C(13)	B_{bb}	-0.0805	-10.796	-3.852	-3.601	-0.2426	0.9673	0.0738
	B_{cc}	0.1645	22.073	7.876	7.363	0.0733	-0.0576	0.9956
	B_{aa}	-0.0095	-5.085	-1.815	-1.696	0.9794	-0.1822	-0.0866
42 H(1)	B_{bb}	-0.0011	-0.607	-0.217	-0.203	0.0886	0.0025	0.9961
	B_{cc}	0.0107	5.692	2.031	1.899	0.1813	0.9833	-0.0186
	B_{aa}	-0.0007	-0.094	-0.034	-0.031	0.9847	-0.1718	-0.0297
43 C(13)	B_{bb}	-0.0006	-0.077	-0.027	-0.026	0.0058	-0.1375	0.9905
	B_{cc}	0.0013	0.171	0.061	0.057	0.1743	0.9755	0.1344
	B_{aa}	-0.0020	-1.069	-0.381	-0.357	0.0537	0.1916	0.9800
44 H(1)	B_{bb}	-0.0001	-0.046	-0.016	-0.015	0.9632	-0.2687	-0.0002
	B_{cc}	0.0021	1.115	0.398	0.372	0.2633	0.9440	-0.1990
	B_{aa}	-0.0017	-0.916	-0.327	-0.306	-0.0268	-0.1168	0.9928
45 H(1)	B_{bb}	-0.0003	-0.172	-0.061	-0.057	0.9911	0.1263	0.0416
	B_{cc}	0.0020	1.088	0.388	0.363	-0.1303	0.9851	0.1124
	B_{aa}	-0.0020	-1.062	-0.379	-0.354	-0.1228	-0.4237	0.8975
46 H(1)	B_{bb}	-0.0001	-0.052	-0.019	-0.017	0.9636	-0.2673	0.0056
	B_{cc}	0.0021	1.114	0.398	0.372	0.2375	0.8655	0.4411
	B_{aa}	-0.0013	-0.174	-0.062	-0.058	-0.0802	-0.1419	0.9866
47 C(13)	B_{bb}	-0.0001	-0.008	-0.003	-0.003	0.9787	-0.1988	0.0510
	B_{cc}	0.0014	0.181	0.065	0.060	0.1889	0.9697	0.1548
	B_{aa}	-0.0016	-0.869	-0.310	-0.290	0.0186	-0.4362	0.8997
48 H(1)	B_{bb}	0.0002	0.092	0.033	0.031	0.9951	0.0957	0.0258
	B_{cc}	0.0015	0.777	0.277	0.259	-0.0973	0.8948	0.4358
	B_{aa}	-0.0017	-0.887	-0.317	-0.296	-0.0658	0.1746	0.9824
49 H(1)	B_{bb}	0.0002	0.120	0.043	0.040	0.9936	0.1016	0.0485
	B_{cc}	0.0014	0.767	0.274	0.256	-0.0913	0.9794	-0.1802
	B_{aa}	-0.0014	-0.766	-0.273	-0.255	-0.0088	-0.1126	0.9936
50 H(1)	B_{bb}	-0.0004	-0.218	-0.078	-0.073	0.9273	0.3710	0.0503
	B_{cc}	0.0018	0.984	0.351	0.328	-0.3743	0.9218	0.1011
	B_{aa}	-0.0015	-0.202	-0.072	-0.067	-0.0295	-0.1481	0.9885
51 C(13)	B_{bb}	0.0001	0.008	0.003	0.003	0.9758	-0.2184	-0.0036
	B_{cc}	0.0014	0.194	0.069	0.065	0.2165	0.9646	0.1509
	B_{aa}	-0.0014	-0.724	-0.258	-0.241	-0.0002	-0.1418	0.9899
52 H(1)	B_{bb}	-0.0004	-0.233	-0.083	-0.078	0.9302	0.3633	0.0522
	B_{cc}	0.0018	0.957	0.341	0.319	-0.3670	0.9208	0.1319
	B_{aa}	-0.0016	-0.828	-0.295	-0.276	-0.0569	0.1440	0.9879
53 H(1)	B_{bb}	0.0002	0.112	0.040	0.037	0.9829	0.1816	0.0301
	B_{cc}	0.0013	0.716	0.256	0.239	-0.1750	0.9728	-0.1518
	B_{aa}	-0.0015	-0.815	-0.291	-0.272	0.0564	-0.4428	0.8949
54 H(1)	B_{bb}	0.0002	0.092	0.033	0.031	0.9873	0.1580	0.0159

Atom	Eigenvalue	[E_h]	[MHz]	[G]	[10^{-4} cm^{-1}]	Axis		
	B_{cc}	0.0014	0.723	0.258	0.241	-0.1484	0.8826	0.4461
	B_{aa}	-0.0009	-0.127	-0.045	-0.042	0.5173	-0.1590	0.8409
55 C(13)	B_{bb}	-0.0005	-0.068	-0.024	-0.023	0.8347	-0.1230	-0.5368
	B_{cc}	0.0015	0.195	0.070	0.065	0.1887	0.9796	0.0691
	B_{aa}	-0.0017	-0.905	-0.323	-0.302	0.0032	-0.1695	0.9855
56 H(1)	B_{bb}	-0.0004	-0.222	-0.079	-0.074	0.9893	0.1442	0.0215
	B_{cc}	0.0021	1.127	0.402	0.376	-0.1458	0.9749	0.1681
	B_{aa}	-0.0019	-0.998	-0.356	-0.333	0.1101	0.1618	0.9807
57 H(1)	B_{bb}	-0.0002	-0.125	-0.045	-0.042	0.9714	-0.2264	-0.0717
	B_{cc}	0.0021	1.123	0.401	0.375	0.2104	0.9605	-0.1821
	B_{aa}	-0.0020	-1.077	-0.384	-0.359	-0.0488	-0.4445	0.8945
58 H(1)	B_{bb}	0.0000	-0.021	-0.008	-0.007	0.9788	-0.1998	-0.0458
	B_{cc}	0.0021	1.098	0.392	0.366	0.1991	0.8732	0.4448
	B_{aa}	-0.0302	-4.055	-1.447	-1.353	0.4514	0.4507	0.7701
59 C(13)	B_{bb}	0.0122	1.634	0.583	0.545	0.8013	0.1751	-0.5721
	B_{cc}	0.0180	2.421	0.864	0.808	-0.3927	0.8754	-0.2821
	B_{aa}	-0.0602	-8.072	-2.880	-2.692	0.4603	0.6437	-0.6114
60 C(13)	B_{bb}	-0.0577	-7.737	-2.761	-2.581	0.8140	-0.5809	0.0012
	B_{cc}	0.1178	15.808	5.641	5.273	0.3544	0.4982	0.7913
	B_{aa}	-0.0035	-0.470	-0.168	-0.157	0.4050	0.3582	0.8412
61 C(13)	B_{bb}	-0.0020	-0.271	-0.097	-0.091	-0.3769	0.9037	-0.2033
	B_{cc}	0.0055	0.742	0.265	0.247	0.8330	0.2347	-0.5010
	B_{aa}	-0.0023	-0.304	-0.108	-0.101	-0.2470	-0.5774	0.7782
62 C(13)	B_{bb}	0.0004	0.051	0.018	0.017	0.9619	-0.2433	0.1248
	B_{cc}	0.0019	0.253	0.090	0.085	0.1173	0.7793	0.6156
	B_{aa}	-0.0011	-0.154	-0.055	-0.051	0.3444	0.6272	0.6986
63 C(13)	B_{bb}	-0.0007	-0.095	-0.034	-0.032	-0.2117	0.7768	-0.5931
	B_{cc}	0.0019	0.249	0.089	0.083	0.9146	-0.0564	-0.4003
	B_{aa}	-0.0015	-0.207	-0.074	-0.069	0.2944	0.3680	0.8820
64 C(13)	B_{bb}	-0.0008	-0.106	-0.038	-0.035	-0.3897	0.8889	-0.2408
	B_{cc}	0.0023	0.313	0.112	0.105	0.8726	0.2728	-0.4051
	B_{aa}	-0.0012	-0.620	-0.221	-0.207	0.1615	0.4962	0.8530
65 H(1)	B_{bb}	-0.0009	-0.456	-0.163	-0.152	0.7018	0.5500	-0.4528
	B_{cc}	0.0020	1.075	0.384	0.359	0.6938	-0.6718	0.2594
	B_{aa}	-0.0013	-0.700	-0.250	-0.233	-0.2707	-0.5844	0.7649
66 H(1)	B_{bb}	-0.0006	-0.338	-0.121	-0.113	0.7799	0.3327	0.5302
	B_{cc}	0.0019	1.038	0.370	0.346	-0.5644	0.7401	0.3657
	B_{aa}	-0.0004	-0.236	-0.084	-0.079	0.3615	0.3584	0.8608
67 H(1)	B_{bb}	-0.0002	-0.132	-0.047	-0.044	-0.3906	0.8965	-0.2092
	B_{cc}	0.0007	0.367	0.131	0.123	0.8466	0.2606	-0.4640
	B_{aa}	-0.0006	-0.329	-0.117	-0.110	0.7097	0.3648	0.6027
68 H(1)	B_{bb}	-0.0004	-0.212	-0.076	-0.071	-0.2443	0.9298	-0.2752
	B_{cc}	0.0010	0.541	0.193	0.180	-0.6608	0.0480	0.7490
	B_{aa}	-0.0005	-0.264	-0.094	-0.088	0.2515	-0.1298	0.9591
69 H(1)	B_{bb}	-0.0004	-0.210	-0.075	-0.070	0.2325	0.9701	0.0703
	B_{cc}	0.0009	0.473	0.169	0.158	0.9395	-0.2053	-0.2742
	B_{aa}	-0.0007	-0.365	-0.130	-0.122	0.0199	-0.3802	0.9247
70 H(1)	B_{bb}	-0.0006	-0.306	-0.109	-0.102	-0.1034	0.9191	0.3801

Atom	Eigenvalue	[E_h]	[MHz]	[G]	[10^{-4} cm^{-1}]	Axis		
	B_{cc}	0.0013	0.670	0.239	0.224	0.9944	0.1032	0.0210
	B_{aa}	-0.0014	-0.186	-0.066	-0.062	0.3746	0.4911	0.7864
71 C(13)	B_{bb}	-0.0006	-0.076	-0.027	-0.025	0.0715	0.8304	-0.5526
	B_{cc}	0.0020	0.262	0.094	0.087	0.9244	-0.2632	-0.2760
	B_{aa}	-0.0014	-0.721	-0.257	-0.240	0.5164	0.4151	0.7490
72 H(1)	B_{bb}	-0.0008	-0.450	-0.161	-0.150	-0.6385	0.7695	0.0137
	B_{cc}	0.0022	1.171	0.418	0.391	-0.5707	-0.4853	0.6624
	B_{aa}	-0.0009	-0.469	-0.167	-0.157	0.6895	0.5939	0.4147
73 H(1)	B_{bb}	-0.0005	-0.253	-0.090	-0.084	-0.5055	0.8045	-0.3119
	B_{cc}	0.0014	0.722	0.258	0.241	-0.5188	0.0054	0.8549
	B_{aa}	-0.0006	-0.298	-0.106	-0.099	0.3706	0.6102	0.7002
74 H(1)	B_{bb}	-0.0002	-0.132	-0.047	-0.044	-0.6569	0.7051	-0.2669
	B_{cc}	0.0008	0.430	0.153	0.143	-0.6566	-0.3611	0.6622
	B_{aa}	-0.0013	-0.173	-0.062	-0.058	0.3592	0.6130	0.7037
75 C(13)	B_{bb}	0.0003	0.047	0.017	0.016	-0.1090	0.7765	-0.6207
	B_{cc}	0.0009	0.126	0.045	0.042	0.9269	-0.1462	-0.3458
	B_{aa}	-0.0009	-0.463	-0.165	-0.154	-0.3289	0.4264	0.8426
76 H(1)	B_{bb}	-0.0006	-0.336	-0.120	-0.112	-0.4842	0.6899	-0.5381
	B_{cc}	0.0015	0.799	0.285	0.267	0.8108	0.5850	0.0205
	B_{aa}	-0.0004	-0.235	-0.084	-0.078	0.0299	0.1762	0.9839
77 H(1)	B_{bb}	-0.0002	-0.105	-0.038	-0.035	-0.5072	0.8509	-0.1370
	B_{cc}	0.0006	0.341	0.122	0.114	0.8613	0.4949	-0.1148
	B_{aa}	-0.0007	-0.381	-0.136	-0.127	-0.0475	-0.0610	0.9970
78 H(1)	B_{bb}	-0.0003	-0.164	-0.058	-0.055	-0.5185	0.8546	0.0276
	B_{cc}	0.0010	0.545	0.194	0.182	0.8537	0.5157	0.0722
	B_{aa}	-0.0021	-0.280	-0.100	-0.093	-0.2879	0.6218	0.7284
79 C(13)	B_{bb}	0.0004	0.055	0.020	0.018	-0.2079	0.7019	-0.6813
	B_{cc}	0.0017	0.225	0.080	0.075	0.9348	0.3476	0.0728
	B_{aa}	-0.0012	-0.638	-0.227	-0.213	0.5432	0.5318	0.6497
80 H(1)	B_{bb}	-0.0007	-0.391	-0.140	-0.130	0.8250	-0.4818	-0.2955
	B_{cc}	0.0019	1.029	0.367	0.343	-0.1559	-0.6965	0.7004
	B_{aa}	-0.0012	-0.652	-0.233	-0.217	0.4534	-0.1295	0.8818
81 H(1)	B_{bb}	-0.0004	-0.227	-0.081	-0.076	0.7219	-0.5269	-0.4486
	B_{cc}	0.0016	0.879	0.313	0.293	0.5227	0.8400	-0.1454
	B_{aa}	-0.0017	-0.894	-0.319	-0.298	0.4654	0.4013	0.7889
82 H(1)	B_{bb}	-0.0001	-0.075	-0.027	-0.025	0.7531	-0.6478	-0.1148
	B_{cc}	0.0018	0.969	0.346	0.323	0.4650	0.6476	-0.6037
	B_{aa}	-0.0042	-2.229	-0.795	-0.744	0.5375	0.8346	0.1203
83 H(1)	B_{bb}	-0.0003	-0.143	-0.051	-0.048	-0.0362	-0.1197	0.9922
	B_{cc}	0.0044	2.372	0.846	0.791	0.8425	-0.5376	-0.0342

Appendix B

Error Plots including a Non-Averaged Nucleus

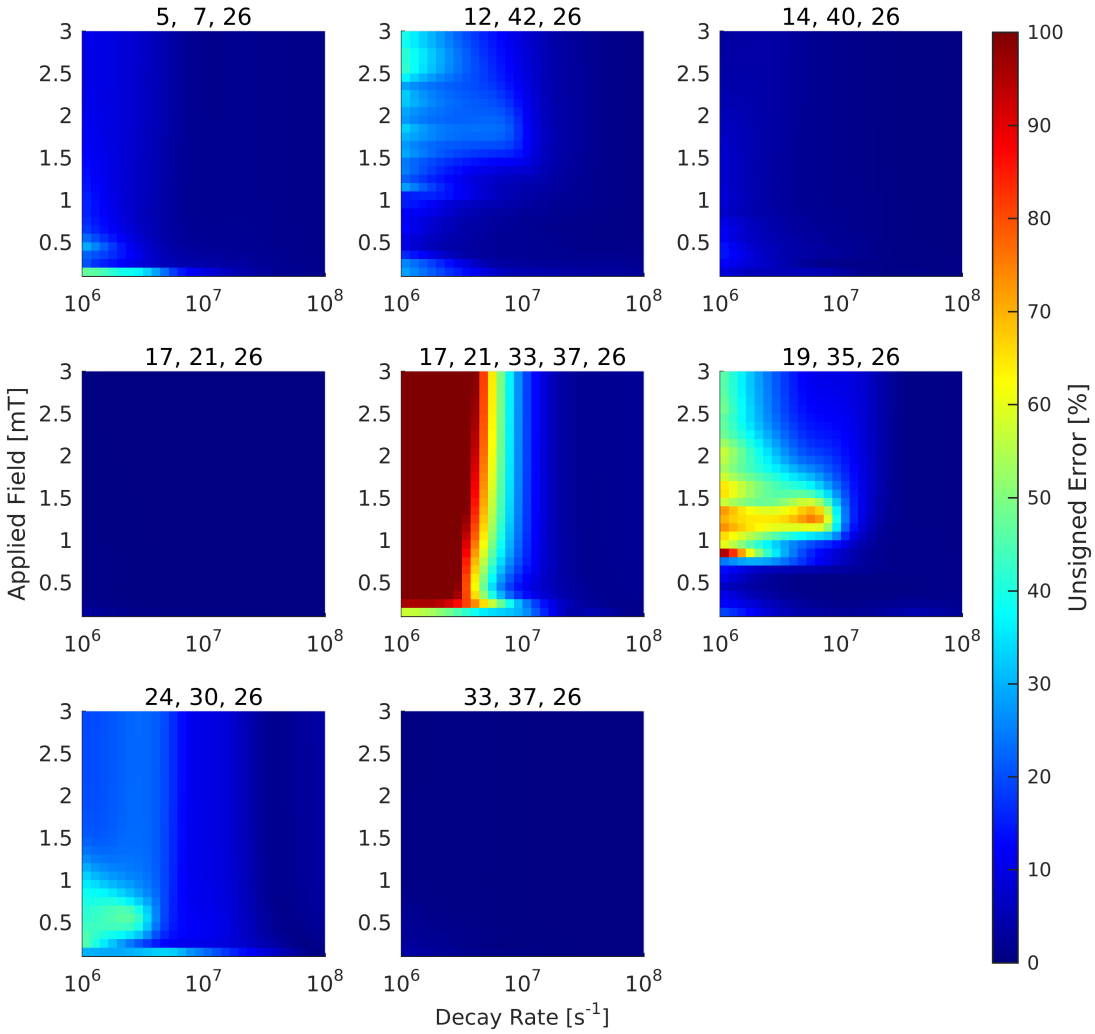

Figure B.1: Mean unsigned error in the anisotropic component of the singlet yield, calculated with averaged hyperfine tensors, over applied magnetic field directions on a 642 point Lebedev grid. Nucleus 26 was included in all calculations, but was not averaged. Each plot refers to a calculation with one of the electrons in the radical pair coupled to the listed protons from the carotenoid moiety (figure 2.3).

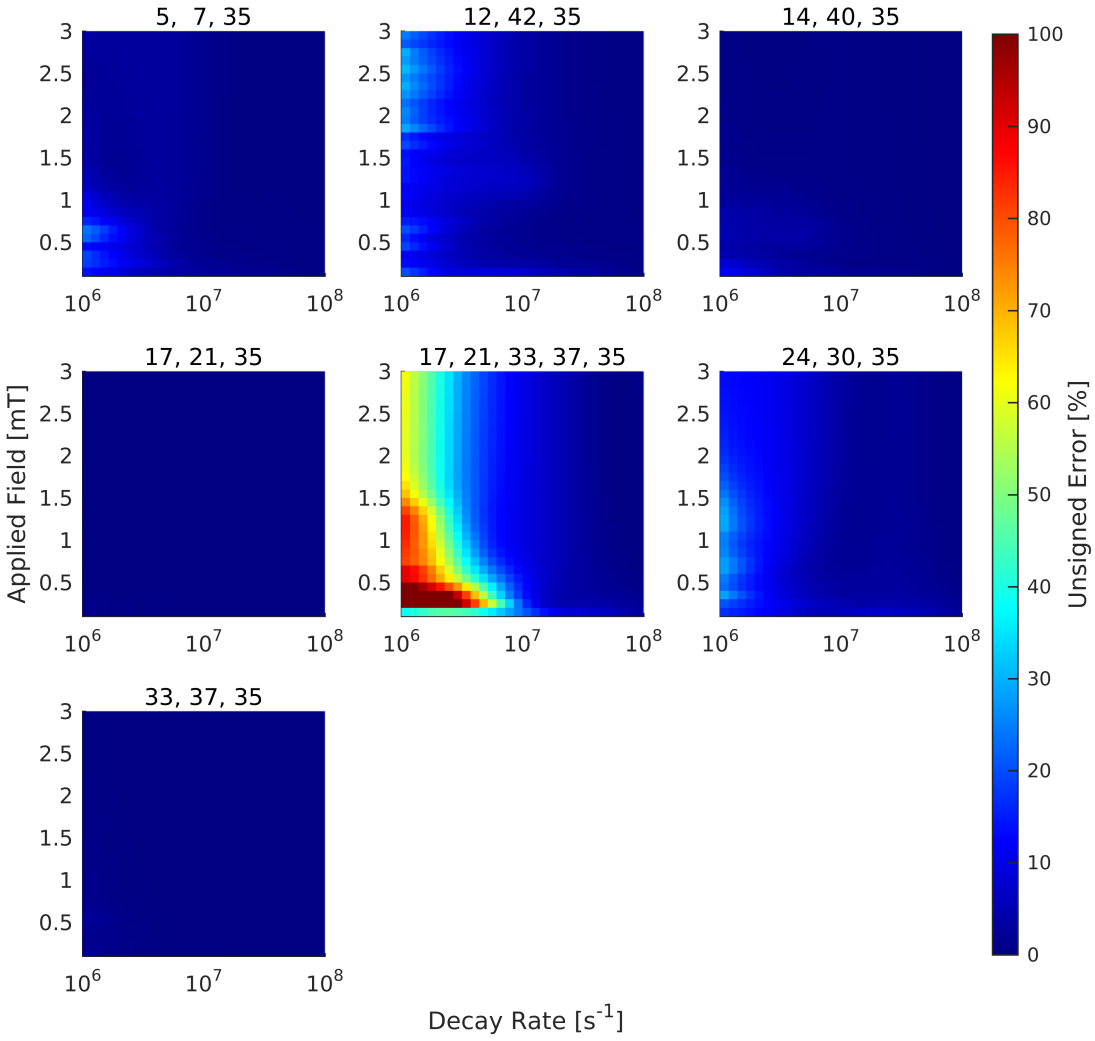

Figure B.2: Mean unsigned error in the anisotropic component of the singlet yield, calculated with averaged hyperfine tensors, over applied magnetic field directions on a 642 point Lebedev grid. Nucleus 35 was included in all calculations, but was not averaged. Each plot refers to a calculation with one of the electrons in the radical pair coupled to the listed protons from the carotenoid moiety (figure 2.3).

Appendix C

AMELIA Calibration and Alignment

The magnitude calibration was found to be very stable, changing no more than 0.8 % over a period of six months. The phase calibration also changed negligibly within this time period. However, the offset drifted significantly, and had to be calibrated at least every three months.

C.1 Magnitude Calibration

The magnitude of the oscillating field produced by each coil was calibrated from 0 to 9.5 V, with an interval of 0.5 V or 0.25 V. A separate calibration was necessary for each frequency, as the coil reactance increased significantly with frequency.

The magnitude of the oscillating field generated by each coil was measured using a SENIS C-H3B-2m-E3D three-dimensional Hall probe coupled to an amplifier built in-house. The magnitude was read using a Tektronix TDS-220 oscilloscope, which was calibrated before use (after a 20 minute warm-up period). Measurements were taken with the oscilloscope trace at zero vertical offset in order to ensure maximum accuracy. The SENIS was validated against a newer Lakeshore gaussmeter, and the slope of the measured magnetic field as a function of coil voltage was found to differ by no more than 2 %.

The exact calibration protocol is as follows:

1. Turn on the oscilloscope, coil power supply and water cooling and leave for 20 minutes to warm up.

2. Disconnect all leads from the oscilloscope, and perform a self-calibration.

3. Connect the AO2 output from the signal generator card to the external trigger port of the oscilloscope, and set the oscilloscope to external trigger mode.

4. Connect the X and Y outputs of the gaussmeter to inputs 1 and 2.

5. Ensure that the casing of the house-built amplifier for the SENIS gaussmeter is adequately grounded.

6. Using the custom-built Hall probe holder, insert the probe between the coils. Ensure that the cross on the Hall probe is centered vertically.

7. Using the calibration tab of the AMELIA 2.0 software, send an oscillating signal to coil 1.

8. Rotate the Hall probe around the vertical axis until the magnetic field is fully aligned with the X channel of the probe (the X is preferred to the Y as the former has lower rated output noise).

9. Use the oscilloscope to measure the peak-to-peak magnetic field measured on the X channel as a function of peak-to-peak applied voltage.

10. Calibrate coil 2 in the same way, but using the Z channel of the gaussmeter.

11. Record the applied voltages (in V) in the file `Ch1Amp.csv`, and the measured fields (in G) in `Ch1FieldStr.csv`, both located in the AMELIA software directory. The values saved in these files must be half the peak-to-peak value.

C.2 Offset Calibration

The SENIS gaussmeter drifted considerably, so was zeroed by placing the probe in a mu-metal box, and reading the magnetic field with a Tektronix TDS-220 oscillo-

Channel	Offset [G]	Standard Deviation [G]
X	-1.68	0.03
Y	-0.42	< 0.01
Z	-0.56	0.01

Table C.1: SENIS DC offset measured in a mu-metal box with a TDS 220 oscilloscope, using the 128 averages acquisition mode.

scope, or an ISO-TECH IDM67 multimeter. The most recently measured offsets are recorded in table C.1.

1. Place the Hall probe in a mu-metal box, and use the averaging mode of the oscilloscope to record the DC offset.

2. Align the Hall-probe with coil 1.

3. For each voltage calibrated in section C.1, adjust the offset in the calibration tab of the AMELIA 2.0 software until the sinusoidal trace on the oscilloscope is centered (taking into account the DC offset of the Hall probe).

4. Repeat for coil 2.

5. Record the calibrated offsets (in V) in `Ch1Ofst.csv` and `Ch2Ofst.csv`

C.3 Phase Calibration

The phase between the coils was measured once each coil's magnitude and offset had been calibrated. The phase was found to vary negligibly with field amplitude, but significantly with frequency.

C.3.1 Theory

If an oscillating magnetic field of equal magnitude but indeterminate phase is generated by each coil simultaneously, and the field from each coil is measured and input to the lock-in amplifier in subtraction mode, the voltage entering the amplifier has

following form:

$$\begin{aligned} V_{\text{in}} &= V_0 \left[\sin(\omega t + \phi_1) - \sin(\omega t + \phi_2 - \psi)\right] \\ &= 2V_0 \sin\left[\frac{2\omega t + \phi_1 + \phi_2 - \psi}{2}\right] \cos\left[\frac{\phi_1 - (\phi_2 - \psi)}{2}\right] \end{aligned} \tag{C.1}$$

Where V_0 is the amplitude of the signal recorded by the gaussmeter, ω is the rotation frequency of the magnetic field, ϕ_1 and ϕ_2 are phases due reactance of coils 1 and 2 respectively, and ψ is the user-input phase of coil 2.

The lock-in amplifier then multiplies the signal by the reference frequency, and removes the oscillating components with a long-pass filter to give a reading R. With user input coil 2 phase ψ':

$$R_0 \propto \cos\left[\frac{\phi_1 - (\phi_2 - \psi')}{2}\right] \tag{C.2}$$

If a second measurement is taken with $\psi = \psi' - \pi$, we obtain the following result:

$$\begin{aligned} R_{-\pi} &\propto \cos\left[\frac{\phi_1 - (\phi_2 - \psi' + \pi)}{2}\right] \\ R_{-\pi} &\propto \cos\left[\frac{\phi_1 - (\phi_2 - \psi')}{2} - \frac{\pi}{2}\right] \\ R_{-\pi} &\propto \sin\left[\frac{\phi_1 - (\phi_2 - \psi')}{2}\right] \end{aligned} \tag{C.3}$$

Since both proportionality constants are equal:

$$\begin{aligned} \frac{R_{-\pi}}{R_0} &= \frac{\sin\left[\frac{\phi_1 - (\phi_2 - \psi')}{2}\right]}{\cos\left[\frac{\phi_1 - (\phi_2 - \psi')}{2}\right]} \\ \frac{R_{-\pi}}{R_0} &= \tan\left[\frac{\phi_1 - (\phi_2 - \psi')}{2}\right] \\ \arctan\left[\frac{R_{-\pi}}{R_0}\right] &= \frac{\phi_1 - (\phi_2 - \psi')}{2} \\ 2\arctan\left[\frac{R_{-\pi}}{R_0}\right] - \psi' &= \phi_1 - \phi_2 \end{aligned} \tag{C.4}$$

Now the intrinsic phase difference is known, the calibrated phase for coil 2, ψ_{cal}, can be easily determined, as the phase difference between the two coils must be 90° for

a rotating magnetic field of constant magnitude:

$$\begin{aligned} \phi_1 - (\phi_2 - \psi_{\text{cal}}) &= \frac{\pi}{2} \\ \psi_{\text{cal}} &= \frac{\pi}{2} - (\phi_1 - \phi_2) \\ \psi_{\text{cal}} &= \frac{\pi}{2} - 2\arctan\left[\frac{R_{-\pi}}{R_0}\right] + \psi' \end{aligned} \tag{C.5}$$

Where ψ' is the user-input phase for measurement R_0.

C.3.2 Practice

The phase difference between coils was calibrated with a SENIS C-H3B-2m-E3D time-resolved gaussmeter connected to a house-built amplifier, in turn connected to a Stanford Research Systems SR830 lock-in amplifier.

1. Align X-channel of gaussmeter with coil 1, and Z-channel with coil 2.
2. Connect X-channel to input A, and Z-channel to input B of lock-in amplifier.
3. Put the lock-in amplifier in $A - B$ mode with first harmonic detection, and a time-constant much greater than the reciprocal field rotation frequency.
4. Connect the AO2 (TODO: double check this) output from the signal generator card to the external reference port of the lock-in amplifier.
5. In the calibration tab of the AMELIA 2.0 software, set each coil to produce a field of identical magnitude (using the earlier calibration from section C.1) at the desired frequency.
6. Take two measurements of R from the lock-in amplifier, one with a phase difference of 0°, and a second with a difference of 180°.
7. The calibrated phase difference for coil 2 is then:

$$\psi_{\text{cal}} = \frac{\pi}{2} - 2\arctan\left[\frac{R_{\pi}}{R_0}\right] \tag{C.6}$$

Where R_π is the lock-in amplifier reading with a programmed phase difference of 180°, and R_0 is the reading with a programmed phase difference of 0°.

8. For each applied voltage in `ChXAmp.csv`, set coil 1 phase to zero in the file `Ch1Phase.csv`, and record the calibrated phase in `Ch2Phase.csv`. The phase varies negligibly with applied voltage, so the same phase can be used for all calibration points.

Alternatively, the phase difference can be calculated from the phase of each coil with respect to the lock-in amplifier's internal oscillator. This is done by connecting the X and Z channels to the A input of the lock-in amplifier separately, and measuring θ for each coil.

C.4 Sample Calibration Files

The following are the latest calibration files for 83 Hz. Each line in the `Ch1XXX.csv` corresponds to a calibration point for coil 1, and as does each line in `Ch2XXX.csv` for coil 2. Note that the frequency must be listed for each point, common to both coils, in *both* `ChFreq.csv` and `FieldFreq.csv`. Additional frequencies can be appended.

`Ch1Amp.csv`

```
0
0.5
1
1.5
2
2.5
3
3.5
4
4.5
5
5.5
```

```
6
6.5
7
7.5
8
8.5
9
9.5
```

Ch1FieldStr.csv

```
0
5.86
11.75
17.6
23.2
29.4
35.2
41.2
47
53
58.8
64.4
70.4
76
81.6
87.2
93.6
98.4
103
107
```

Ch1Ofst.csv

```
-0.014
-0.012
-0.009
-0.013
-0.013
-0.013
-0.013
-0.005
-0.003
0.000
0.000
0.000
0.000
0.000
0.000
0.000
0.000
0.000
0.030
0.050
```

Ch1Phase.csv

```
0
0
0
0
0
0
0
0
0
0
0
0
0
```

```
0
0
0
0
0
0
0
0
```

Ch2Amp.csv

```
0
0.5
1
1.5
2
2.5
3
3.5
4
4.5
5
5.5
6
6.5
7
7.5
8
8.5
9
9.5
```

Ch2FieldStr.csv

```
0
8.32
16.6
24.9
32.8
41.2
48.8
57.6
65.2
73.2
82.4
90.4
99.2
108
117
125
131
140
149
155
```

Ch2Ofst.csv

```
-0.002
-0.002
-0.004
-0.005
-0.005
-0.010
-0.010
-0.010
-0.015
-0.015
0.000
0.020
```

```
0.025
0.035
0.020
0.020
0.015
0.020
0.030
0.060
```

Ch2Phase.csv

```
-65.10
-65.10
-65.10
-65.10
-65.10
-65.10
-65.10
-65.10
-65.10
-65.10
-65.10
-65.10
-65.10
-65.10
-65.10
-65.10
-65.10
-65.10
-65.10
-65.10
-65.10
```

ChFreq.csv

83
83
83
83
83
83
83
83
83
83
83
83
83
83
83
83
83
83
83
83

FieldFreq.csv

83
83
83
83
83
83
83
83
83
83
83
83
83

83

83

83

83

83

83

83

83

C.5 LED Alignment

UV blocking goggles must be worn when aligning LEDs with significant output in the UV spectrum. The LED must point away from the user to avoid direct irradiation. Always use the lowest LED power available.

1. Remove the magnetic coils and place a detector card at the sample position.
2. Adjust the LED and its lens longitudinally to focus the beam to a point at the sample location.
3. Replace the coils, and place a sliver of white printer paper over the inlet hole facing the LED (printer paper contains fluorescent optical brighteners).
4. Adjust the LED and its lens vertically and laterally to center the beam on the inlet hole.
5. Place a thin fluorescence cuvette between the coils, with a sliver of white paper inside. The paper's thin edge must be facing the photomultiplier tube (PMT).
6. Place a detector card in front of the PMT, and illuminate the paper's face.
7. Adjust the collimating and focusing lenses between the sample and the PMT to focus the scattered light to a point of the same height as the PMT's window.

8. Optionally, place a cylindrical lens directly in front of the PMT's window, to spread the beam laterally over the entirety of the detector (both 2.0 mm and 1.6 mm diameter lenses work).

Appendix D

Solubility of Anthracene

Solvent	Solubility [$\mathrm{g\,ml^{-1}}$]
acetone	0.0075 [72]
acetonitrile	0.00283 [72]
dichloromethane	0.0288 [3]
trichloromethane	0.024 [3]
N,N-dimethylformamide	0.0183 [72]
tetrahydrofuran	0.04 [174]
diethylether	0.0032 [3]
carbon disulfide	0.032 [138]
ethanol	0.0149 [138]
methanol	0.0142 [138]
methyl ethanoate	0.0081 [3]
heptane	0.0016 [5]
toluene	0.012 [5]

Table D.1: Solubility of anthracene in various solvents at room temperature.

Bibliography

[1] *Physical Properties of Glycerine and Its Solutions*. Glycerine Producers' Association, 1963.

[2] *Photomultiplier Tubes*, 3rd ed. Hamamatsu, 2007.

[3] Acree, Jr., W. E. Iupac-nist solubility data series. 98. solubility of polycyclic aromatic hydrocarbons in pure and organic solvent mixtures—revised and updated. part 3. neat organic solvents. *Journal of Physical and Chemical Reference Data 42* (2013), 1–223.

[4] Akselrod, G. M., Deotare, P. B., Thompson, N. J., Lee, J., Tisdale, W. A., Baldo, M. A., and Bulović, V. M. M. V. Visualization of exciton transport in ordered and disordered molecular solids. *Nature Communications 5* (2014).

[5] Al-Sharrah, G. K., Ali, S. H., and Fahim, M. A. Solubility of anthracene in two binary solvents containing toluene. *Fluid Phase Equilibria 193*, 1–2 (2002), 191 – 201.

[6] Aladekomo, J. B., Arnold, S., and Pope, M. Triplet exciton diffusion and double photon absorption in tetracene. *Physica Status Solidi B 80*, 1 (1977), 333–340.

[7] Alvarez, L. W., and Bloch, F. A quantitative determination of the neutron moment in absolute nuclear magnetons. *Phys. Rev. 57* (Jan 1940), 111–122.

[8] Arbuznikov, A. V., Vaara, J., and Kaupp, M. Relativistic spin-orbit effects on hyperfine coupling tensors by density-functional theory. *The Journal of Chemical Physics 120*, 5 (2004), 2127–2139.

[9] Atkins, P., and Friedman, R. *Molecular Quantum Mechanics*, fourth edition ed. Oxford University Press, 2005.

[10] Avakian, P. Influence of magnetic fields on luminescence involving triplet excitons. *Pure and Applied Chemistry 37* (1974), 1–19.

[11] Avakian, P., and Merrifield, R. E. Triplet excitons in anthracene crystals - a review. *Molecular Crystals 5*, 1 (1968), 37–77.

[12] Barone, V. *Recent Advances in Density Functional Methods Part I.* World Scientific, 1996.

[13] Binhi, V. N. Microwave absorption by magnetic nanoparticles in the organism. *Biophysics 56*, 6 (2011), 1096–1098.

[14] Biskup, T. Magnetic field effects of *Xenopus laevis* cryptochrome-DASH. Unpublished, September 2012.

[15] Biskup, T., Paulus, B., Okafuji, A., Kenichi, H., Getzoff, E. D., and Weber, S. Variable electron transfer pathways in an amphibian cryptochrome. *Journal of Biological Chemistry 288* (2013), 9249–9260.

[16] Biskup, T., Schleicher, E., Okafuji, A., Link, G., Kenichi, H., Getzoff, E. D., and Weber, S. Direct observation of a photoinduced radical pair in a cryptochrome blue-light photoreceptor. *Angewandte Chemie International Edition 48* (2009), 404–407.

[17] Blake, N. W., and McClure, D. S. Delayed singlet-singlet emission from molecular crystals. *The Journal of Chemical Physics 29*, 4 (1958), 722–724.

[18] Bleifuss, G., Kolberg, M., Pötsch, S., Hofbauer, W., Bittl, R., Lubitz, W., Gräslund, A., Lassmann, G., and Lendzian, F. Tryptophan and tyrosine radicals in ribonucleotide reductase: a comparative high-field EPR study at 94 GHz. *Biochemistry 40*, 50 (2001), 15362–15368.

[19] Blum, K. *Density Matrix Theory and Applications*, 3rd ed. Springer, 2012.

[20] Boas, M. L. *Mathematical Methods in the Physical Sciences*, 2nd ed. John Wiley & Sons, 1983.

[21] Brazard, J., Usman, A., Lacombat, F., Ley, C., Martin, M. M., Plaza, P., Mony, L., Heijde, M., Zabulon, G., and Bowler, C. Spectro-temporal characterization of the photoactivation mechanism of two new oxidized cryptochrome/photolyase photoreceptors. *Journal of the American Chemical Society 132* (2010), 4935–4945.

[22] Bree, A., and Lyons, L. E. The intensity of ultraviolet light absorption by monocrystals. Part II. Absorption and reflection by anthracene of plane-polarised light. *J. Chem. Soc.* (1956), 2662–2670.

[23] Bree, A., and Lyons, L. E. The intensity of ultraviolet-light absorption by monocrystals. Part IV. Absorption by naphthacene of plane-polarized light. *J. Chem. Soc.* (1960), 5206–5212.

[24] Brettel, K., and Byrdin, M. Reaction mechanisms of {DNA} photolyase. *Current Opinion in Structural Biology 20*, 6 (2010), 693 – 701.

[25] Brooks, C. L., and Karplus, M. Solvent effects on protein motion and protein effects on solvent motion. *Journal of Molecular Biology 208*, 1 (1989), 159 – 181.

[26] Burdett, J. J., and Bardeen, C. J. Quantum beats in crystalline tetracene delayed fluorescence due to triplet pair coherences produced by direct singlet fission. *Journal of the American Chemical Society 134*, 20 (2012), 8597–8607.

[27] Campbell, R. B., Robertson, J. M., and Trotter, J. The crystal structure of hexacene, and a revision of the crystallographic data for tetracene. *Acta Crystallographica 15*, 3 (1962), 289–290.

[28] Challis, L. Mechanisms for interaction between rf fields and biological tissue. *Bioelectromagnetics 26*, S7 (2005), S98–S106.

[29] Chia, A., Tan, K. C., Pawela, L., Kurzyński, P., Paterek, T., and Kaszlikowski, D. Coherent chemical kinetics as quantum walks. I. Reaction operators for radical pairs. *Phys. Rev. E 93* (2016), 032407.

[30] Chow, T. L. *Introduction to Electromagnetic Theory: A Modern Perspective*. Jones & Bartlett Learning, 2006.

[31] Clark, L. B., and Philpott, M. R. Anisotropy of the singlet transitions of crystalline anthracene. *The Journal of Chemical Physics 53*, 10 (1970), 3790–3801.

[32] Coleman, T. F., and Li, Y. On the convergence of reflective newton methods for large-scale nonlinear minimization subject to bounds. *Mathematical Programming 67* (1994), 189–224.

[33] Coleman, T. F., and Li, Y. An interior, trust region approach for nonlinear minimization subject to bounds. *SIAM Journal on Optimization 6* (1996), 418–445.

[34] Collins, B., Mazzoni, E. O., Stanewsky, R., and Blau, J. Drosophila cryptochrome is a circadian transcriptional repressor. *Current Biology 16*, 5 (2006), 441 – 449.

[35] Daiyasu, H., Ishikawa, T., Kuma, K.-i., Iwai, S., Todo, T., and Toh, H. Identification of cryptochrome DASH from vertebrates. *Genes to Cells 9*, 5 (2004), 479–495.

[36] Dauxois, T., Ruffo, S., Arimondo, E., and Wilkens, M., Eds. *Dynamics and Thermodynamics of Systems with Long Range Interactions*. Springer, 2008.

[37] Davydov, A. S. *Izvestiya Akademii Nauk SSR, Seriya Fizicheskaya 15* (1951), 605.

[38] Efimova, O., and Hore, P. Evaluation of nuclear quadrupole interactions as a source of magnetic anisotropy in the radical pair model of the avian magnetic compass. *Molecular Physics 107*, 7 (2009), 665–671.

[39] Efimova, O., and Hore, P. J. Role of exchange and dipolar interactions in the radical pair model of the avian magnetic compass. *Biophysical Journal 94* (2008), 1565–1574.

[40] Egan, E. S., Franklin, T. M., Hilderbrand-Chae, M. J., McNeil, G. P., Roberts, M. A., Schroeder, A. J., Zhang, X., and Jackson, F. R. An extraretinally expressed insect cryptochrome with similarity to the blue light photoreceptors of mammals and plants. *Journal of Neuroscience 19*, 10 (1999), 3665–3673.

[41] El-Esawi, M., Glascoe, A., Engle, D., Ritz, T., Link, J., and Ahmad, M. Cellular metabolites modulate in vivo signaling of arabidopsis cryptochrome-1. *Plant Signaling & Behavior 10*, 9 (2015), e1063758.

[42] Emmons, R. C. *The Universal Stage*. Memoir 8. Geological Society of America, 1943.

[43] Engels, S., Schneider, N.-L., Lefeldt, N., Hein, C. M., Zapka, M., Michalik, A., Elbers, D., Kittel, A., Hore, P. J., and Mouritsen, H. Anthropogenic electromagnetic noise disrupts magnetic compass orientation in a migratory bird. *Nature 509* (2015), 353–356.

[44] Erickson, H. P. Size and shape of protein molecules at the nanometer level determined by sedimentation, gel filtration, and electron microscopy. *Biological Procedures Online 11* (2009), 32–51.

[45] Ern, V. Anisotropy of triplet exciton diffusion in anthracene. *Phys. Rev. Lett. 22* (Feb 1969), 343–345.

[46] Evans, E. W., Dodson, D. A., Maeda, K., Biskup, T., Wedge, C. J., and Timmel, C. R. Magnetic field effects in flavoproteins and related systems. *Interface Focus 3* (2013).

[47] Fedele, G., Green, E. W., Rosato, E., and Kyriacou, C. P. An electromagnetic field disrupts negative geotaxis in drosophila via a cry-dependent pathway. *Nature Communications 5* (July 2014), 4391.

[48] Ferguson, K. *An Investigation of Isotropic and Anisotropic Magnetic Field Effects in Fluorescent Systems.* DPhil thesis, University of Oxford, 2013.

[49] Fert, A., and Levy, P. M. Role of anisotropic exchange interactions in determining the properties of spin-glasses. *Phys. Rev. Lett. 44* (Jun 1980), 1538–1541.

[50] Feynman, R. P., Leighton, R. B., and Sands, M. *The Feynman Lectures on Physics.* Addison-Wesley, 1966.

[51] Field, T. R. Dynamical theory of spin noise and relaxation: Prospects for real-time nmr measurements. *Phys. Rev. E 90* (Nov 2014), 052144.

[52] Field, T. R., and Bain, A. D. Origins of spin noise. *Applied Magnetic Resonance 38*, 2 (2010), 167–178.

[53] Finney, J., Gellatly, B., Golton, I., and Goodfellow, J. Solvent effects and polar interactions in the structural stability and dynamics of globular proteins. *Biophysical Journal 32*, 1 (1980), 17 – 33.

[54] Fischer, K. H., and Hertz, J. A. *Spin Glasses*. Cambridge University Press, 1991.

[55] Frisch, M. J., Trucks, G. W., Schlegel, H. B., Scuseria, G. E., Robb, M. A., Cheeseman, J. R., Scalmani, G., Barone, V., Mennucci, B., Petersson, G. A., Nakatsuji, H., Caricato, M., Li, X., Hratchian, H. P., Izmaylov, A. F., Bloino, J., Zheng, G., Sonnenberg, J. L., Hada, M., Ehara, M., Toyota, K., Fukuda, R., Hasegawa, J., Ishida, M., Nakajima, T., Honda, Y., Kitao, O., Nakai, H., Vreven, T., Montgomery, Jr., J. A., Peralta, J. E., Ogliaro, F., Bearpark, M., Heyd, J. J., Brothers, E., Kudin, K. N., Staroverov, V. N., Kobayashi, R., Normand, J., Raghavachari, K., Rendell, A., Burant, J. C., Iyengar, S. S., Tomasi, J., Cossi, M., Rega, N., Millam, J. M., Klene, M., Knox, J. E., Cross, J. B., Bakken, V., Adamo, C., Jaramillo, J., Gomperts, R., Stratmann, R. E., Yazyev, O., Austin, A. J., Cammi, R., Pomelli, C., Ochterski, J. W., Martin, R. L., Morokuma, K., Zakrzewski, V. G., Voth, G. A., Salvador, P., Dannenberg, J. J., Dapprich, S., Daniels, A. D., Farkas, Ö., Foresman, J. B., Ortiz, J. V., Cioslowski, J., and Fox, D. J. Gaussian∼09 Revision D.01. Gaussian Inc. Wallingford CT 2009.

[56] Fuchs, M. R., Schleicher, E., Schnegg, A., Kay, C. W. M., Törring, J. T., Bittl, R., Bacher, A., Richter, G., Möbius, K., , and Weber, S. g-tensor of the neutral flavin radical cofactor of DNA photolyase revealed by 360-GHz electron paramagnetic resonance spectroscopy. *The Journal of Physical Chemistry B 106*, 34 (2002), 8885–8890.

[57] Gamliel, D., and Levanon., H. *Stochastic Processes in Magnetic Resonance*. World Scientific, 1995.

[58] García, A. E., and Hummer, G. Water penetration and escape in proteins. *Proteins: Structure, Function, and Bioinformatics 38*, 3 (2000), 261–272.

[59] Gauger, E. M., Rieper, E., Morton, J. J. L., Benjamin, S. C., and Vedral, V. Sustained quantum coherence and entanglement in the avian compass. *Phys. Rev. Lett. 106* (Jan 2011), 040503.

[60] Geacintov, N., Pope, M., and Vogel, F. Effect of magnetic field on the fluorescence of tetracene crystals: Exciton fission. *Phys. Rev. Lett. 22* (Mar 1969), 593–596.

[61] Gegear, R. J., Casselman, A., Waddell, S., and Reppert, S. M. Cryptochrome mediates light-dependent magnetosensitivity in drosophila. *Nature 454*, 7207 (Aug. 2008), 1014–1018.

[62] Geisselbrecht, Y., Frühwirth, S., Schroeder, C., Pierik, A. J., Klug, G., and Essen, L.-O. CryB from *Rhodobacter sphaeroides*: a unique class of cryptochromes with new cofactors. *EMBO Reports 13* (2012), 223–229.

[63] Giovani, B., Byrdin, M., Ahmad, M., and Brettel, K. Light-induced electron transfer in a cryptochrome blue-light photoreceptor. *Nat. Struct. Mol. Biol. 10*, 6 (June 2003), 489–490.

[64] Goudsmit, S. A. The discovery of the electron spin. *Nederlands Tijdschrift voor Natuurkunde 37* (1971), 386.

[65] Green, N. J. B. *Quantum Mechanics 2: The Toolkit.* Oxford Science Publications, 1998.

[66] Greene, F. D., Misrock, S. L., and Wolfe, Jr., J. R. The structure of anthracene photodimers. *Journal of the American Chemical Society 77*, 14 (1955), 3852–3855.

[67] Griffin, E. A., Staknis, D., and Weitz, C. J. Light-independent role of cry1 and cry2 in the mammalian circadian clock. *Science 286*, 5440 (1999), 768–771.

[68] Grivet, J.-P. Electron spin resonance of phosphorescent anthracene. *Chemical Physics Letters 4*, 2 (1969), 104 – 106.

[69] Groff, R. P., Avakian, P., and Merrifield, R. E. Coexistence of exciton fission and fusion in tetracene crystals. *Phys. Rev. B 1* (Jan 1970), 815–817.

[70] Haarer, D., Schmid, D., and Wolf, H. C. Elektronenspin-resonanz von triplett-exzitonen in anthrazen. *Physica Status Solidi B 23*, 2 (1967), 633–638.

[71] Haberkorn, R. Density matrix description of spin-selective radical pair reactions. *Molecular Physics 32*, 5 (1976), 1491–1493.

[72] Hansen, H. K., Riverol, C., and Acree, Jr., W. E. Solubilities of anthracene, fluoranthene and pyrene in organic solvents: Comparison of calculated values using UNIFAC and modified UNIFAC (Dortmund) models with experimental data and values using the mobile order theory. *The Canadian Journal of Chemical Engineering 78* (2000), 1168–1174.

[73] Hayward, S., Kitao, A., Hirata, F., and Gō, N. Effect of solvent on collective motions in globular protein. *Journal of Molecular Biology 234*, 4 (1993), 1207 – 1217.

[74] Henbest, K. B., Maeda, K., Hore, P. J., Joshi, M., Bacher, A., Bittl, R., Weber, S., Timmel, C. R., and Schleicher, E. Magnetic-field effect on the photoactivation reaction of *Escherichia coli* DNA photolyase. *Proceedings of the National Academy of Sciences 105*, 38 (2008), 14395–14399.

[75] Hidalgo, C., Ed. *Physical Properties of Biological Membranes and Their Functional Implications*. Springer Science & Business Media, 2012.

[76] Hiscock, H. G., Kattnig, D. R., Manolopoulos, D. E., and Hore, P. J. Floquet theory of radical pairs in radiofrequency magnetic fields. *The Journal of Chemical Physics 145*, 12 (2016), 124117.

[77] Hochstrasser, R. M. The luminescence of organic molecular crystals. *Rev. Mod. Phys. 34* (Jul 1962), 531–550.

[78] Hogben, H. J. *Coherent Spin Dynamics of Radical Pairs in Weak Magnetic Fields*. DPhil thesis, University of Oxford, 2011.

[79] Hogben, H. J., Efimova, O., Wagner-Rundell, N., Timmel, C. R., and Hore, P. J. Possible involvement of superoxide and dioxygen with cryptochrome in avian magnetoreception: Origin of Zeeman resonances observed by in vivo EPR spectroscopy. *Chemical Physics Letters 480* (2009), 118–122.

[80] Hore, P. J., Jones, J. A., and Wimperis, S. *NMR: The Toolkit*. Oxford University Press, 2000.

[81] Immeln, D., Weigel, A., Kottke, T., and Lustres, J. L. P. Primary events in the blue light sensor plant cryptochrome: Intraprotein electron and proton transfer revealed by femtosecond spectroscopy. *Journal of the American Chemical Society 134* (2012), 12536–12546.

[82] Ivanov, K. L., Petrova, M. V., Lukzen, N. N., and Maeda, K. Consistent treatment of spin-selective recombination of a radical pair confirms the Haberkorn approach. *The Journal of Physical Chemistry A 114*, 35 (2010), 9447–9455.

[83] Izmaylov, A. F., Tully, J. C., and Frisch, M. J. Relativistic interactions in the radical pair model of magnetic field sense in cry-1 protein of arabidopsis thaliana. *The Journal of Physical Chemistry A 113* (2009), 12276–12284.

[84] Johnson, R. C., and Merrifield, R. E. Effects of magnetic fields on the mutual annihilation of triplet excitons in anthracene crystals. *Physical Review B 1* (1970), 896–902.

[85] Johnson, R. C., Merrifield, R. E., Avakian, P., and Flippen, R. B. Effects of magnetic fields on the mutual annihilation of triplet excitons in molecular crystals. *Phys. Rev. Lett. 19* (Aug 1967), 285–287.

[86] Jones, J., and Hore, P. Spin-selective reactions of radical pairs act as quantum measurements. *Chemical Physics Letters 488*, 1–3 (2010), 90 – 93.

[87] Jortner, J., Rice, S. A., Katz, J. L., and Choi, S. Triplet excitons in crystals of aromatic molecules. *The Journal of Chemical Physics 42*, 1 (1965), 309–323.

[88] Justinek, M., Grampp, G., Landgraf, S., Hore, P. J., and Lukzen, N. N. Electron self-exchange kinetics determined by MARY spectroscopy: Theory and experiment. *Journal of the American Chemical Society 126* (2004), 5635–5646.

[89] Kalinowski, J., and Godlewski, J. Magnetic field effects on recombination radiation in tetracene crystal. *Chemical Physics Letters 36*, 3 (1975), 345 – 348.

[90] Kattnig, D. R., Evans, E. W., Dejean, V., Dodson, C. A., Wallace, M. I., Mackenzie, S. R., Timmel, C. R., and J., H. Chemical amplification of magnetic field effects relevant to avian magnetoreception. *Nat. Chem. 8*, 4 (Apr. 2016), 384–391.

[91] Kattnig, D. R., Solov'yov, I. A., and Hore, P. J. Electron spin relaxation in cryptochrome-based magnetoreception. *Phys. Chem. Chem. Phys. 18* (2016), 12443–12456.

[92] Kepler, R. G., Caris, J. C., Avakian, P., and Abramson, E. Triplet excitons and delayed fluorescence in anthracene crystals. *Phys. Rev. Lett. 10* (1963), 400–402.

[93] Khomskii, D. *Transition Metal Compounds.* Cambridge University Press, 2014.

[94] Khudyakov, I. V., Serebrennikov, Y. A., and Turro, N. J. Spin-orbit coupling in free-radical reactions: on the way to heavy elements. *Chemical Reviews 93*, 1 (1993), 537–570.

[95] Kimmich, R. *NMR: Tomography, Diffusometry, Relaxometry*. Springer Science & Business Media, 2012.

[96] Kirschvink, J. L. Microwave absorption by magnetite: A possible mechanism for coupling nonthermal levels of radiation to biological systems. *Bioelectromagnetics 17* (1996), 187–194.

[97] Klein, G., Voltz, R., and Schott, M. Magnetic field effect on prompt fluorescence in anthracene: evidence for singlet exciton fission. *Chemical Physics Letters 16*, 2 (1972), 340 – 344.

[98] Kodis, G., Liddell, P. A., Moore, A. L., Moore, T. A., and Gust, D. Synthesis and photochemistry of a carotene–porphyrin–fullerene model photosynthetic reaction center. *Journal of Physical Organic Chemistry 17*, 9 (2004), 724–734.

[99] Krishnan, V., and Cosman, M. An empirical relationship between rotational correlation time and solvent accessible surface area. *Journal of Biomolecular NMR 12*, 1 (1998), 177–182.

[100] Landau, L. D., and Lifshitz, E. M. *Fluid Mechanics*, vol. 6 of *Course of Theoretical Physics*. Pergamon Press, 1959.

[101] Langenbacher, T., Immeln, D., Dick, B., and Kottke, T. Microsecond light-induced proton transfer to flavin in the blue light sensor plant cryptochrome. *Journal of the American Chemical Society 121* (2009), 14274–14280.

[102] Lau, J. C. S. Restricted diffusion of radical pair magnetoreceptors. Master's thesis, University of Oxford, 2009.

[103] Lau, J. C. S., Wagner-Rundell, N., Rodgers, C. T., Green, N. J. B., and Hore, P. J. Effects of disorder and motion in a radical pair magnetoreceptor. *Journal of the Royal Society Interface 7* (2010), S257–S264.

[104] Lee, A. A., Lau, J. C. S., Hogben, H. J., Biskup, T., Kattnig, D. R., and Hore, P. J. Alternative radical pairs for cryptochrome-based magnetoreception. *Journal of The Royal Society Interface 11*, 95 (2014).

[105] Levitt, M. H. *Spin Dynamics: Basics of Nuclear Magnetic Resonance*. Wiley, 2001.

[106] Lewis, A. M., Manolopoulos, D. E., and Hore, P. J. Asymmetric recombination and electron spin relaxation in the semiclassical theory of radical pair reactions. *The Journal of Chemical Physics 141*, 4 (2014).

[107] Li, J. *Applications of Optical Cavity-Based Spectroscopic Techniques in the Condensed Phase*. DPhil thesis, University of Oxford, 2013.

[108] Lipsett, F. R. On the production of single crystals of naphthalene and anthracene. *Canadian Journal of Physics 35*, 3 (1957), 284–298.

[109] Liu, Z., Tan, C., Guo, X., Li, J., Wang, L., Sancar, A., and Zhong, D. Determining complete electron flow in the cofactor photoreduction of oxidized photolyase. *Proceedings of the National Academy of Sciences of the United States of America 110* (2013), 12966–12971.

[110] Lyons, L. E. Photoconductance in tetracene-type crystals: Theory of the spectral dependence. *The Journal of Chemical Physics 23*, 1 (1955), 220–220.

[111] Maeda, K., Henbest, K. B., Cintolesi, F., Kuprov, I., Rodgers, C. T., Liddell, P. A., Gust, D., Timmel, C. R., and Hore, P. J. Chemical compass model of avian magnetoreception. *Nature 453* (2008), 387–390.

[112] Maeda, K., Liddell, P., Gust, D., and Hore, P. J. Spin-selective recombination reactions of radical pairs: Experimental test of validity of reaction operators. *The Journal of Chemical Physics 139*, 23 (2013), 234309.

[113] Maeda, K., Robinson, A. J., Henbest, K. B., Hogben, H. J., Biskup, T., Ahmad, M., Schleicher, E., Weber, S., Timmel, C. R., and Hore, P. J. Magnetically sensitive light-induced reactions in cryptochrome are consistent with its proposed role as a magnetoreceptor. *Proceedings of the National Academy of Sciences of the United States of America 109* (2012), 4774–4770.

[114] Maeda, K., Storey, J. G., Liddell, P. A., Gust, D., Hore, P. J., Wedge, C. J., and Timmel, C. R. Probing a chemical compass: novel variants of low-frequency reaction yield detected magnetic resonance. *Phys. Chem. Chem. Phys. 17* (2015), 3550–3559.

[115] Maeda, K., Wedge, C. J., Storey, J. G., Henbest, K. B., Liddell, P. A., Kodis, G., Gust, D., Hore, P. J., and Timmel, C. R. Spin-selective recombination kinetics of a model chemical magnetoreceptor. *Chem. Commun. 47* (2011), 6563–6565.

[116] Manolopoulos, D. E., and Hore, P. J. An improved semiclassical theory of radical pair recombination reactions. *The Journal of Chemical Physics 139*, 12 (2013).

[117] Matsui, A., and Ishii, Y. Zone refining of anthracene. *Japanese Journal of Applied Physics 6*, 2 (1967), 127.

[118] McCord, E. F., Bucks, R. R., and Boxer, S. G. Laser chemically induced dynamic nuclear polarization study of the reaction between photoexcited flavins and tryptophan derivatives at 360 MHz. *Biochemistry 20*, 10 (1981), 2880–2888.

[119] McQuarrie, D. A., and SImon, J. D. *Physical Chemistry A Molecular Approach*. University Science Books, 1997.

[120] Merrifield, R., Avakian, P., and Groff, R. Fission of singlet excitons into pairs of triplet excitons in tetracene crystals. *Chemical Physics Letters 3*, 6 (1969), 386 – 388.

[121] Merrifield, R. E. Magnetic effects on triplet exciton interactions. *Pure and Applied Chemistry 27* (1971), 481–498.

[122] Misra, B., and Sudarshan, E. C. G. The zeno's paradox in quantum theory. *Journal of Mathematical Physics 18*, 4 (1977), 756–763.

[123] Miura, T., Maeda, K., and Arai, T. Effect of coulomb interaction on the dynamics of the radical pair in the system of flavin mononucleotide and hen egg-white lysozyme (HEWL) studied by a magnetic field effect. *The Journal of Physical Chemistry B 107*, 26 (2003), 6474–6478.

[124] Mohr, P. J., Taylor, B. N., and Newell, D. The 2014 codata recommended values of the fundamental physical constants, 2015. This database was developed by J. Baker, M. Douma, and S. Kotochigova.

[125] Mouritsen, H., and Hore, P. The magnetic retina: light-dependent and trigeminal magnetoreception in migratory birds. *Current Opinion in Neurobiology 22*, 2 (2012), 343 – 352. Neuroethology.

[126] Mouritsen, H., Janssen-Bienhold, U., Liedvogel, M., Feenders, G., Stalleicken, J., Dirks, P., and Weiler, R. Cryptochromes and neuronal-activity markers colocalize in the retina of migratory birds during magnetic orientation. *Proceedings of the National Academy of Sciences of the United States of America 101*, 39 (2004), 14294–14299.

[127] Mueller, P., Bouly, J.-P., Hitomi, K., Balland, V., Getzoff, E. D., Ritz, T., and Brettel, K. ATP binding turns plant cryptochrome into an efficient natural photoswitch. *Scientific Reports 4* (2014), 5175.

[128] Mueller, P., Brettel, K., Grama, L., Nyitrai, M., and Lukacs, A. Photochemistry of wild-type and N378D mutant *E. coli* DNA photolyase

with oxidized FAD cofactor studied by transient absorption spectroscopy. *ChemPhysChem 17*, 9 (2016), 1329–1340.

[129] Mueller, P., Yamamoto, J., Martin, R., Iwai, S., and Brettel, K. Discovery and functional analysis of a 4th electron-transferring tryptophan conserved exclusively in animal cryptochromes and (6-4) photolyases. *Chem. Commun. 51* (2015), 15502–15505.

[130] Nakada, I. The optical properties of anthracene single crystals. *Journal of the Physical Society of Japan 17*, 1 (1962), 113–118.

[131] Neil, S. R. T., Li, J., Sheppard, D. M. W., Storey, J., Maeda, K., Henbest, K. B., Hore, P. J., Timmel, C. R., and Mackenzie, S. R. Broadband cavity-enhanced detection of magnetic field effects in chemical models of a cryptochrome magnetoreceptor. *The Journal of Physical Chemistry B 118*, 15 (2014), 4177–4184.

[132] Nieman, G. C., and Robinson, G. W. Rapid triplet excitation migration in organic crystals. *The Journal of Chemical Physics 37*, 9 (1962), 2150–2151.

[133] Niessner, C., Denzau, S., Stapput, K., Ahmad, M., Peichl, L., Wiltschko, W., and Wiltschko, R. Magnetoreception: activated cryptochrome 1a concurs with magnetic orientation in birds. *Journal of The Royal Society Interface 10*, 88 (2013).

[134] Nohr, D., Franz, S., Rodriguez, R., Paulus, B., Essen, L.-O., Weber, S., and Schleicher, E. Extended electron-transfer in animal cryptochromes mediated by a tetrad of aromatic amino acids. *Biophysical Journal 111*, 2 (2016), 301 – 311.

[135] Norman, S. A. *Magnetic Field Effects on Radical Pair Reactions.* DPhil thesis, University of Oxford, 2006.

[136] Okafuji, A., Schnegg, A., Schleicher, E., Möbius, K., and Weber, S. G-tensors of the flavin adenine dinucleotide radicals in glucose ox-

idase: a comparative multifrequency electron paramagnetic resonance and electron−nuclear double resonance study. *The Journal of Physical Chemistry B 112*, 11 (2008), 3568–3574.

[137] Okumoto, K., Kanno, H., Hamada, Y., Takahashi, H., and Shibata, K. Organic light-emitting devices using polyacene derivatives as a hole-transporting layer. *Journal of Applied Physics 100*, 4 (2006), 044507.

[138] O'Neil, M. J. *The Merck Index: An Encyclopedia of Chemicals, Drugs, and Biologicals*. Royal Society of Chemistry, 2013.

[139] Oxborrow, M. Personnal communication.

[140] Oxborrow, M., Breeze, J. D., and Alford, N. M. Room-temperature solid-state maser. *Nature 488* (2012), 353–357.

[141] Ozturk, N., Selby, C. P., Annayev, Y., Zhong, D., and Sancar, A. Reaction mechanism of drosophila cryptochrome. *Proceedings of the National Academy of Sciences 108*, 2 (2011), 516–521.

[142] Paci, I., Johnson, J. C., Chen, X., Rana, G., Popović, D., David, D. E., Nozik, A. J., Ratner, M. A., and Michl, J. Singlet fission for dye-sensitized solar cells: can a suitable sensitizer be found? *Journal of the American Chemical Society 128*, 51 (2006), 16546–16553. PMID: 17177404.

[143] Park, H. W., Kim, S. T., Sancar, A., and Deisenhofer, J. Crystal structure of DNA photolyase from *Escherichia coli*. *Science 268* (1995), 1866–1872.

[144] Philpott, M. R. Dipole Davydov splittings in crystalline anthracene, tetracene, naphthalene, and phenanthrene. *The Journal of Chemical Physics 50*, 12 (1969), 5117–5128.

[145] Prigogine, I. *Les lois du chaos*. Flammarion, 2008.

[146] Robertson, J. M. Structure of naphthalene and anthracene. *Rev. Mod. Phys. 30* (Jan 1958), 155–158.

[147] Robertson, J. M., Sinclair, V. C., and Trotter, J. The crystal and molecular structure of tetracene. *Acta Crystallographica 14*, 7 (1961), 697–704.

[148] Robinson, A. J. *Magnetic Field Effects on Biological Systems.* DPhil thesis, University of Oxford, 2010.

[149] Rodgers, C. T. *Magnetic Field Effects in Chemical Systems.* DPhil thesis, University of Oxford, 2007.

[150] Rokeakh, A. I., Moskvin, A. S., Legkikh, N. V., and Sherstkov, Y. A. Experimental observation of the Dzyaloshinskii-Moriya electron-nuclear interaction by the electron-nuclear double resonance method. *Soviet Physics, Journal of Experimental and Theoretical Physics 5* (1987), 1021–1027.

[151] Sakurai, J. J., and Napolitano, J. *Modern Quantum Mechanics*, 2nd ed. Addison-Wesley, 2011.

[152] Scanes, C. G., Ed. *Sturkie's Avian Physiology.* Associated Press, 2015, ch. Magnetoreception in Birds and Its Use for Long-Distance Migration, pp. 113–133.

[153] Schillen, K., Brown, W., and Johnsen, R. M. Micellar sphere-to-rod transition in an aqueous triblock copolymer system. a dynamic light scattering study of translational and rotational diffusion. *Macromolecules 27*, 17 (1994), 4825–4832.

[154] Schulten, K., and Bittl, R. Probing the dynamics of a polymer with paramagnetic end groups by magnetic fields. *The Journal of Chemical Physics 84*, 9 (1986), 5155–5161.

[155] Schwarze, S., Schneider, N.-L., Reichl, T., Dreyer, D., Lefeldt, N., Engels, S., Baker, N., Hore, P. J., and Mouritsen, H. Weak

broadband electromagnetic fields are more disruptive to magnetic compass orientation in a night-migratory songbird (*Erithacus rubecula*) than strong narrow-band fields. *Frontiers in Behavioral Neuroscience 10* (2016), 55.

[156] Serdyuk, I. N., Zaccai, N. R., and Zaccai, J. *Methods in Molecular Biophysics: Structure, Dynamics, Function*, 1 ed. Cambridge University Press, 2007.

[157] Shushin, A. I. The effect of the spin exchange interaction on SNP and RYDMR spectra of geminate radical pairs. *Chemical Physics Letters 181* (1991), 274–278.

[158] Sivia, D. S., and Skilling, J. *Data analysis: a Bayesian tutorial*. Oxford University Press, 2006.

[159] Sponer, H., Kanda, Y., and Blackwell, L. A. Delayed fluorescence in naphthalene crystals at 4°K. *The Journal of Chemical Physics 29*, 4 (1958), 721–721.

[160] Stanford Research Systems. *MODEL SR830 DSP Lock-In Amplifier*, 2.5 ed. 1290-D Reamwood Avenue, Sunnyvale, CA 94089 U.S.A., 10 2011.

[161] Steiner, U. E., and Ulrich, T. Magnetic field effects in chemical kinetics and related phenomena. *Chemical Reviews 89*, 1 (1989), 51–147.

[162] Storey, J. G. *Magnetic Field Effects on Electron-Hole Recombination Reactions – Theoretical and Experimental Developments*. DPhil thesis, University of Oxford, 2014.

[163] Suna, A. Kinematics of exciton-exciton annihilation in molecular crystals. *Phys. Rev. B 1* (1970), 1716–1739.

[164] Suzuki, M. Convergence of general decompositions of exponential operators. *Communications in Mathematical Physics 163*, 3 (1994), 491–508.

[165] Swenberg, C. E. Theory of triplet exciton annihilation in polyacene crystals. *The Journal of Chemical Physics 51*, 5 (1969), 1753–1764.

[166] Tavazzi, S., Raimondo, L., Silvestri, L., Spearman, P., Camposeo, A., Polo, M., and Pisignano, D. Dielectric tensor of tetracene single crystals: The effect of anisotropy on polarized absorption and emission spectra. *The Journal of Chemical Physics 128*, 15 (2008).

[167] Tayebjee, M. J. Y., Clady, R. G. C. R., and Schmidt, T. W. The exciton dynamics in tetracene thin films. *Phys. Chem. Chem. Phys. 15* (2013), 14797–14805.

[168] Thorsmølle, V. K., Averitt, R. D., Demsar, J., Smith, D. L., Tretiak, S., Martin, R. L., Chi, X., Crone, B. K., Ramirez, A. P., and Taylor, A. J. Morphology effectively controls singlet-triplet exciton relaxation and charge transport in organic semiconductors. *Phys. Rev. Lett. 102* (2009), 017401.

[169] Thöing, C., Oldemeyer, S., and Kottke, T. Microsecond deprotonation of aspartic acid and response of the α/β subdomain precede c-terminal signaling in the blue light sensor plant cryptochrome. *Journal of the American Chemical Society 137*, 18 (2015), 5990–5999.

[170] Timmel, C. R., Cintolesi, F., Brocklehurst, B., and Hore, P. J. Model calculations of magnetic field effects on the recombination reactions of radicals with anisotropic hyperfine interactions. *Chemical Physics Letters 334*, 4-6 (2001), 387–395. Cited References Count:29|ELSEVIER SCIENCE BV|PO BOX 211, 1000 AE AMSTERDAM, NETHERLANDS.

[171] Timmel, C. R., and Henbest, K. B. A study of spin chemistry in weak magnetic fields. *Philosophical Transactions: Mathematical, Physical and Engineering Sciences 362* (2004), 2537–2589.

[172] Timmel, C. R., Till, U., Brocklehurst, B., McLauchlan, K. A., and Hore, P. J. Effects of weak magnetic fields on free radical recombination reactions. *Molecular Physics 95*, 1 (1998), 71–89.

[173] Tomkiewicz, Y., Groff, R. P., and Avakian, P. Spectroscopic approach to energetics of exciton fission and fusion in tetracene crystals. *The Journal of Chemical Physics 54*, 10 (1971), 4504–4507.

[174] Tsuchida, E., Miyake, Y., Kawagoe, T., and Shinohara, I. Solubilities of anthracene and anthraquinone in tetrahydrofuran, ethyl alcohol and methyl alcohol. *The Journal of the Society of Chemical Industry 71* (1968), 1572–1573.

[175] Turro, N. J., Scaiano, J. C., and Ramamurthy, V. *Principles of Molecular Photochemistry: An Introduction.* University Science Books, 2009.

[176] Tycko, Ed. *Nuclear Magnetic Resonance Probes of Molecular Dynamics.* Springer, 1994.

[177] Uhlenbeck, G. E., and Goudsmit, S. Spinning electrons and the structure of spectra. *Nature 117* (1926), 264–265.

[178] van Dijk, B., van der Vos, R., and Hoff, A. J. Rota-MARY, a novel way of measuring anisotropic magnetic field effects on reaction yield. *Chemical Physics Letters 226* (1994), 206–212.

[179] Vaubel, G., and Baessler, H. Diffusion of singlet excitons in tetracene crystals. *Molecular Crystals and Liquid Crystals 12*, 1 (1970), 47–56.

[180] Vaubel, G., and Kallmann, H. Diffusion length and lifetime of triplet excitons and crystal absorption coefficient in tetracene determined from photocurrent measurements. *Physica Status Solidi B 35*, 2 (1969), 789–792.

[181] Wagner-Rundell, N. *Electron Spin Relaxation Effects on Radical Recombination Reactions in Weak Magnetic Fields.* DPhil thesis, University of Oxford, 2008.

[182] Wedge, C. J. *Radiofrequency Magnetic Field Effects on Radical Pair Recombination Reactions*. DPhil thesis, University of Oxford, 2009.

[183] Weller, A., F., N., and Staerk, H. A quantitative interpretation of the magnetic field effect on hyperfine-coupling-induced triplet formation from radical ion pairs. *Chemical Physics Letters 96* (1983), 24–27.

[184] Wen, S.-W., Lee, M.-T., and Chen, C. H. Recent development of blue fluorescent oled materials and devices. *Journal of Display Technology 1*, 1 (Sept 2005), 90–99.

[185] Wu, H., and Zhou, J. Optical properties of anthracene single crystals grown by a simple solution technique. *International Journal of Modern Physics B 27*, 8 (2013), 1350022.

[186] Yamagata, H., Norton, J., Hontz, E., Olivier, Y., Beljonne, D., Brédas, J. L., Silbey, R. J., and Spano, F. C. The nature of singlet excitons in oligoacene molecular crystals. *The Journal of Chemical Physics 134*, 20 (2011).

[187] Yarmus, L., Rosenthal, J., and Chopp, M. EPR of triplet excitons in tetracene crystals: spin polarization and the role of singlet exciton fission. *Chemical Physics Letters 16*, 3 (1972), 477 – 481.

[188] Yong, C. K., Musser, A. J., Clark, J., Anthony, J. E., Beljonne, D., Friend, R. H., and Sirringhaus, H. Direct observation of entangled multiexciton states in organic semiconductors (conference presentation), 2016.

[189] Yu, X., Liu, H., Klejnot, J., and Lin, C. The cryptochrome blue light receptors. *The Arabidopsis Book 8* (2010), e0135.

[190] Zhang, P., Deng, J., Zeng, X., Liu, Z., Qiu, Y., Zhong, H., Fan, Y., Huang, J., Zhang, J., and Xu, K. Growth mechanism of large-size anthracene single crystals grown by a solution technique. *Journal of Crystal Growth 311*, 23–24 (2009), 4708 – 4713.

[191] Zimmerman, P. M., Bell, F., Casanova, D., and Head-Gordon, M. Mechanism for singlet fission in pentacene and tetracene: From single exciton to two triplets. *Journal of the American Chemical Society 133*, 49 (2011), 19944–19952.